Title

Behavior of piles in liquefied and laterally spreading ground, PhD Dissertation

Permalink

https://escholarship.org/uc/item/4kz886zf

Author

Brandenberg, Scott

Publication Date

2005-09-01

Peer reviewed

Behavior of Pile Foundations in Liquefied and Laterally Spreading Ground

By

Scott J. Brandenberg

M.S. (University of California, Davis) 2002

B.S. (Cal Poly, San Luis Obispo) 2000

DISSERTATION

Submitted in partial fulfillment of the requirements for the degree of

DOCTOR OF PHILOSOPHY

in

Civil and Environmental Engineering

in the
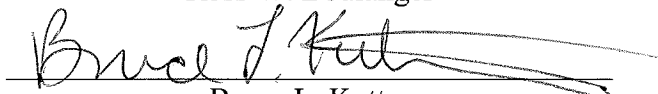
OFFICE OF GRADUATE STUDIES

of the

UNIVERSITY OF CALIFORNIA

DAVIS

Approved:

_____
Ross W. Boulanger

_____
Bruce L. Kutter

_____
I.M. Idriss

Committee In Charge

2005

i

Scott J. Brandenberg
September 2005
Civil and Environmental Engineering

Behavior of Pile Foundations in Liquefied and Laterally Spreading

Ground

Abstract

Pile foundations have suffered extensive damage in liquefiable soils during earthquakes around the world, particularly when a nonliquefied crust layer spreads laterally on top of underlying liquefied layers. Recent research has begun to clarify certain aspects of the problem, but many fundamental mechanisms have not yet been explored. As a result, designers are faced with making uninformed assumptions that could result in structural damage and the associated loss of life and money, or excessive conservatism in the design and the associated unnecessary high cost of construction.

A series of dynamic centrifuge model experiments was performed on a 9-m radius centrifuge to improve our understanding of these phenomena. One model contained a number of single piles and a two-pile group while the other models each contained a six-pile group. Soil profiles consisted of a nonliquefiable clay crust overlying liquefiable loose sand over dense sand. While the models spun on the centrifuge to simulate a large prototype, a servo-hydraulic shaker applied a sequence of realistic earthquake motions. Data was collected from dense arrays, and was subsequently archived and made publicly

available. The raw recorded data was processed to obtain time series of fundamental engineering behaviors, some of which had never before been measured or anticipated. The observed subgrade reaction loads between piles and liquefied sand, phasing of lateral spreading loads and inertia loads, and load transfer between pile groups and laterally spreading nonliquefiable crusts were all shown to be more complex than commonly assumed in design practice, and represent a challenge to our expanding numerical modeling capabilities. The complex observations were distilled into a simplified design guidelines and recommendations that can directly be implemented at a standard-of-practice computational level. Suites of hundreds of simplified analyses were performed to identify the potential accuracy of standard-of-practice methods, the influence of alternative assumptions and approximations, and the sensitivity of predicted bending moments to variations in the properties of the p-y materials, magnitude of inertia forces, magnitude and shape of ground displacements, axial capacities, flexibility of connections between piles and pile caps, and stiffness of the load transfer relation between the spreading crust and pile foundation.

ACKNOWLEDGEMENTS

Finally I would like to thank my wife Sarah for being there for me throughout graduate school, and my daughter Emelia for keeping me sane by distracting me occasionally from working on this dissertation while I took care of her in the mornings.

TABLE OF CONTENTS

CHAPTER ONE

1. INTRODUCTION

1.1 MECHANISMS OF DAMAGE TO PILE FOUNDATIONS IN LIQUEFIED AND LATERALLY SPREADING GROUND

Extensive damage to pile-supported bridges and other structures in areas of liquefaction and lateral spreading has been observed in many earthquakes around the world, and has been particularly intense when a strong nonliquefied crust spreads on top of liquefiable soils. Spreading of a rock fill on underlying liquefied hydraulic fill soils imposed loads on piles that supported a wharf at the Port of Oakland (Figs. 1-1 to 1-3) in the 1989 Loma Prieta earthquake. The battered piles that extended through the rock fill were stiffer than the vertical piles because some of the lateral loading was transmitted to axial loads through frame action, and because their unsupported length was smaller (i.e. the length of the segments of the piles between the wharf and the ground surface). The battered piles were not sufficiently strong to resist the loads and suffered extensive damage that rendered the cranes at the wharf unusable after the earthquake.

Fig. 1-4 shows damage to steel piles that occurred at Showa Bridge in the 1964 Niigata earthquake. Excessive deformations of the pile foundations caused the bridge decks to fall off of their seats and into the river. Fig. 1-5 illustrates a typical pier at the

Landing Road Bridge which was exposed to lateral spreading during the 1987 Edgecumbe earthquake in New Zealand. The estimated lateral spreading loads were close to the computed plastic capacity of the bridge piers, thereby creating a limit state in the foundation and bridge components.

Different mechanisms of damage to pile foundations are illustrated in Fig. 1-6 for cases with and without lateral spreading. Inertia loads caused by acceleration of structural masses (from the pile caps and the overlying structures) and kinematic loads caused by free field displacement demands from the soil can occur simultaneously during shaking. Kinematic loads may reach their peak values after shaking if delayed slope failure occurs, but may also reach their peak values during shaking if the transient, lurching components of ground displacements are significant. Designers must estimate a combination of kinematic and inertia loads to use for static-seismic design procedures, which involves considerable judgment because there are insufficient data to validate any theories for estimating the phasing of the loads. In addition to the mechanisms in Fig. 1-6, slender piles may buckle due to loss of confinement during liquefaction (Bhattacharya and Bolton 2004) and settlement of soil layers during reconsolidation could induce down-drag loads on piles (Boulanger and Brandenberg 2004).

1.2   OBSERVATIONS OF SUBGRADE REACTION LOADS IN LIQUEFIABLE SOIL PROFILES

Direct observations of "p-y" (subgrade reaction) behavior in liquefying soil were first provided by Wilson et al. (1998, 2000) by applying back-calculation procedures to the results of dynamic centrifuge model tests of pile-supported structures in level ground

models of loose to medium-dense sands (Fig. 1-7 to 1-9). They found that loose sand with D_r = 40% exhibited a very soft and weak p-y response, while medium dense sand with D_r = 55% exhibited an inverted s-shaped displacement-hardening behavior that is similar to the stress-strain response often observed in load-controlled undrained laboratory testing of saturated dilatant sands.

Tokimatsu et al. (2001) applied similar data processing procedures to the results of large-scale 1g shake table tests for piles embedded in a level ground soil profile (Fig. 1-10 and 1-11). They found that loose sand exhibited a very soft and weak p-y response, while more significant loads were mobilized for denser sands. Ashford and Rollins (2002) back-calculated p-y behavior for full-scale piles at Treasure Island that were laterally loaded after the level-ground site was liquefied by blasting (Fig. 1-12). Back-calculated p-y behavior in medium dense sand exhibited inverted s-shaped displacement hardening behavior that was similar to the responses observed by Wilson et al. (1998, 2000). Subsequent blast testing induced lateral spreading at a site on Tokachi Island, Japan where various piles and pipelines had been previously installed, and the piles behavior was analyzed by Ashford and Juirnarongrit (2005). Two-dimensional planar finite element model tests performed by Iai (2002) exhibited the same characteristic displacement-hardening p-y response (Figs. 1-13 and 1-14). Load rate was shown to contribute to p-y behavior in numerical studies conducted by Uzuoka et al. (2005), as summarized in Figs. 1-15 and 1-16. The rate dependence was found to depend on the consolidation characteristics of the sand expressed as a time factor, which in turn depends on pile diameter, loading rate, permeability and coefficient of volume compressibility.

Other physical modeling studies have provided valuable information on the lateral loads imposed on pile foundations by laterally spreading ground without necessarily presenting the results in terms of p or y time histories. Results of centrifuge testing by Abdoun et al. (2003) showed that peak bending moments induced during shaking can subsequently soften later in shaking in spite of increasing ground surface displacements (Fig. 1-17 and 1-18). Centrifuge testing by Haigh (2002) demonstrated that flexible piles may attract significantly smaller lateral spreading loads than stiffer piles with the same diameter (Figs. 1-19 and 1-20).

Significant research has been performed to characterize the subgrade reaction behavior between piles and liquefied ground, and many of the discrepancies among the different model tests have not yet been clarified. The combined findings from these physical modeling studies show that the p-y behavior of liquefied sand depends on the same factors that affect the monotonic and cyclic loading behavior of saturated sands, plus additional factors as expected. The factors are:

- Relative density (D_r).
- Prior displacement (strain) history.
- Excess pore pressure ratio in the far- and near-field.
    - Magnitude of cyclic stresses & number of loading cycles imposed on the free-field soil.
    - Magnitude and number of loading cycles between the pile & soil.
- Partial drainage and hence loading rate.
- Soil characteristics.
- Pile installation method.
- Pile foundation stiffness.
- Ground displacement profile.

While significant research has been devoted to studying the subgrade reaction behavior between liquefied soils and piles, relatively little has been done regarding loads between nonliquefied laterally spreading crust layers and pile foundations. The lack of research in this area is surprising considering that loads from nonliquefied crusts are often the critical loads that control the response of a pile foundation. Significant research has been performed on loads on piles and pile caps in static load testing in nonliquefied stationary ground. However, the loading conditions in static tests do not accurately represent the loading conditions in earthquake-induced lateral spreading. Research findings presented in this dissertation help to clarify many of the unknown issues regarding load transfer between pile foundations and nonliquefied laterally spreading crusts.

Another area in which significant research is needed is the phasing between lateral spreading loads and inertia loads during shaking. Often the peak lateral spreading loads are assumed to act at the end of shaking when the ground displacements are largest, and hence not simultaneously with inertia loads. However, if the transient lurching component of ground displacements are large enough during shaking, then crust loads and inertia loads might act in phase. Recommendations of load combinations for design were presented by Tokimatsu (2003), and are currently being studied by other researchers as well (e.g. Chang et al., 2005). More data is required to obtain robust, reliable design guidelines for combining loads in practice.

1.3 DESIGN PROCEDURES FOR PILE FOUNDATIONS IN LIQUEFIED AND LATERALLY SPREADING GROUND

Monotonic static-seismic design procedures for pile foundations in laterally spreading ground are intended to envelope the cyclic loading response that may occur during earthquake shaking by representing critical loading cycles using "statically-equivalent" loading conditions. Static design procedures include two alternative versions of the Beam on Nonlinear Winkler Foundation (BNWF) method, as depicted in Fig. 1-21. The first BNWF alternative requires the free-field soil movements (y_{soil}) as an input, with the resulting lateral soil reactions (p) being dependent on the relative displacement (y) between the free-field soil (y_{soil}) and the pile (y_{pile}), where $y = y_{soil} - y_{pile}$. The second BNWF alternative applies limit pressures on the pile over the depth of the laterally-spreading soil (with the p-y springs removed in this interval), and then uses p-y springs to model the response in the underlying competent soil. In this second alternative, the applied lateral pressures are independent of the free-field soil displacements since the soil movements are inherently assumed to be large enough to cause the lateral pressures to reach their limiting values (e.g. JRA 2002; Fig. 1-22). Boulanger et al. (2003) presented results of both types of BNWF pushover analyses on single piles, compared them to centrifuge tests results, and discussed the important factors for design practice.

Japanese design codes treat the influence of liquefaction on pile foundations differently for railway facilities, highway bridges, and buildings. The coefficient of subgrade reaction used in the various design codes varies considerably. Table 1-1 summarizes the approaches adopted in Japanese codes, and Table 1-2 summarizes the values of subgrade reaction adopted for highway bridges. Fig. 1-23 shows the relation

7

between p-multiplier and relative density or factor of safety against liquefaction for railway facilities and building foundations.

Table 1-1: Japanese codes for pile design in liquefied ground and for lateral spreading conditions (Uchida and Tokimatsu 2005).
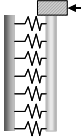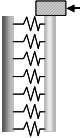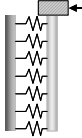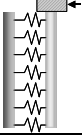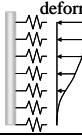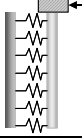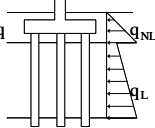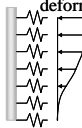
		Highway Bridges (JRA)	Railway Facilities (RTRI)	Building Foundations (AIJ)
Liquefaction	Inertia force	←P	←P	←P
	Ground movement force	Not consider	←P+α	deformation y_G
	Subgrade reaction	Reduce with • FL-value • Depth • Liquefaction strength • Earthquake Level	Reduce with • FL-value • Depth	Reduce with • Na-value • Depth
Lateral spreading	Inertia force	Not consider	Not consider	←P(liq)
	Ground movement force	Non-liq q_{NL} / Liq q_L	deformation y_G	deformation y_G
	Subgrade reaction	×	Liq.layer:1/1000 Non-liq.layer:No reduction	Same as liquefaction

Table 1-2: Reduction factors for highway bridges in Japanese code (Uchida and Tokimatsu 2005).

F_L	Depth	Liquefaction strength			
		$R \leq 0.3$		$0.3 < R$	
		Level 1	Level 2	Level 1	Level 2
$F_L \leq 1/3$	$0 \leq x \leq 10$	1/6	0	1/3	1/6
	$10 < x \leq 20$	2/3	1/3	2/3	1/3
$1/3 < F_L \leq 2/3$	$0 \leq x \leq 10$	2/3	1/3	1	2/3
	$10 < x \leq 20$	1	2/3	1	2/3
$2/3 < F_L \leq 1$	$0 \leq x \leq 10$	1	2/3	1	1
	$10 < x \leq 20$	1	1	1	1

Dobry et al. (2003) presented an alternative approach that utilized limit pressures along with elastic deformation characteristics of the soil-pile system to model the evolution of bending moment with increasing ground displacement without using any p-y elements (Fig. 1-24). Dobry et al. (1995) also presented a rational method for modeling p-y behavior in soils that do not fully liquefy (i.e. peak r_u-values do not reach 1.0; Fig. 1-25).

The concept of using a "free-field" soil deformation profile as an input into a pushover analysis is associated with the underlying assumption that the mass of laterally spreading soil is very large compared with the lateral restraining capacity provided by the pile group. In such cases, the free-field soil deformation can be calculated without considering the relatively small restraining force provided by the pile group. However, bridge abutments, which have a finite width and are often small compared with the restraining capacity of the pile group, may impose decreased displacement demands on the pile foundation as a result of the pinning action provided by the foundation and bridge components. A simple iterative coupling of the lateral spreading and pile response analyses has sometimes been used by designers (e.g., Martin et al. 2002) to take

advantage of the pinning effect (Figs. 1-27 to 1-30). Boulanger et al. (2005) performed a centrifuge test with pile foundations in granular abutments over liquefiable soils, and identified that the procedure produced reasonable predictions of abutment displacements provided the following previously unidentified factors were accounted for: 1. the tributary width abutment being pinned is larger than the width of the pile foundation, 2. the equivalent constant pile restraining force that acts throughout shaking is smaller than the pile restraining force at the end of shaking, 3. the size of the failure mass increases with increasing pile restraining force, and 4. shear strains in the abutment and in underlying nonliquefied layers reduce the pile pinning force associated with a given ground displacement. They suggested using caution when utilizing the design approach.

Dynamic finite element analyses (FEA) have the potential to better represent certain aspects of pile foundation behavior during earthquake loading and liquefaction-induced deformations. FEA can explicitly couple abutment deformation and pile foundation behavior, including the effects of progressive liquefaction on seismic response, ground deformations, and foundation stiffness. FEA can also model the kinematic and inertial loading that occur during shaking, whereas the quantities must be independently estimated in a static-seismic analysis. However, dynamic FEA methods are often not feasible for design of all but the most critical structures due to the time and effort required to perform a single analysis, and the difficulty involved in calibrating a model to exhibit reasonable response.

1.4   SCOPE OF DISSERTATION

The scope of this dissertation is to characterize the loading mechanics that occurred during the centrifuge tests, clarify and distill the complex dynamic behavior into simple concepts that can be utilized in simple design methods, and to evaluate the accuracy with which the complex loading can be enveloped using simplified static-seismic design methods. The body of this dissertation is organized into the following chapters:

- ***Chapter Two: Centrifuge Test Program, Typical Experimental Results, and Data Processing Methods.***

  Description of centrifuge test program with photos of models during excavation. Sample raw data results, methods of data processing used to obtain crust load, subgrade reaction, and pile and soil displacement, and sample p-histories obtained by double-differentiation of bending moment distributions from a heavily-instrumented pile.

- ***Chapter Three: Observations and Interpretation of Test Data.***

  Phasing of subgrade reaction loads from crust and liquefied layers for single piles and pile groups. Peak crust loads measured on single piles and pile groups, and methods for predicting crust loads. Measurements of softer-than-anticipated load transfer behavior between pile groups and laterally spreading crusts, and two simple models for predicting such behavior. Phasing of crust load and inertia loads for pile groups, and methods for estimating inertia loads to use in combination with crust loads for static-seismic design.

- ***Chapter Four: Static-Seismic Design Guidelines and Analyses.***

  Set of recommended design guidelines that were built upon existing guidelines and subsequently modified to account for liquefaction. Input parameters for analyses of six-pile groups from centrifuge tests that utilized the single set of recommended design guidelines. Numerical methods and tools developed to perform static-seismic analyses in OpenSees. Detailed example analyses of one

of the centrifuge models, and summary plots of measured versus predicted peak bending moments and pile cap displacements for five centrifuge tests. Influence of alternative guidelines and approximations on bending moments and cap displacements. Sensitivity study of which parameters most influence the analysis results.

- ***Chapter Five: Conclusions and Recommendations.***

    Recap of conclusions presented at the end of each chapter, and recommendations for future research in pile foundations in liquefied and laterally spreading ground.

Figure 1-1: Top of the wharf structure at the Port of Oakland following the 1989 Loma Prieta earthquake. The cranes could not operate due to separation of the rails caused by extension of the wharf. (Courtesy of John Egan, Geomatrix).
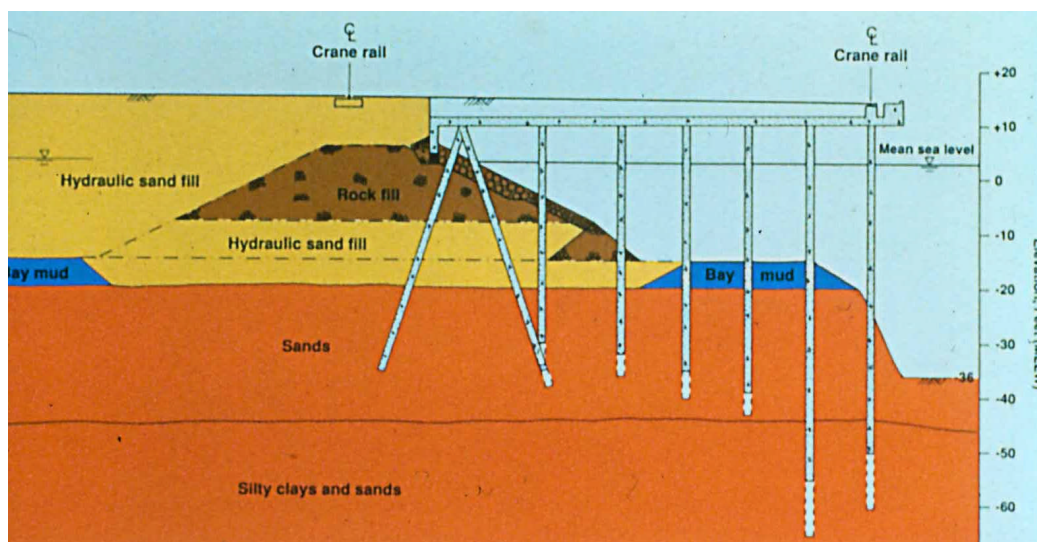
Figure 1-2: Section view of the soil stratigraphy and pile configuration supporting the damaged wharf at the Port of Oakland (Courtesy of John Egan, Geomatrix).

Figure 1-3: Damage to the battered piles that extended through the rock fill and liquefiable layers at the Port of Oakland after the 1989 Loma Prieta Earthquake. (Courtesy of John Egan, Geomatrix).

14
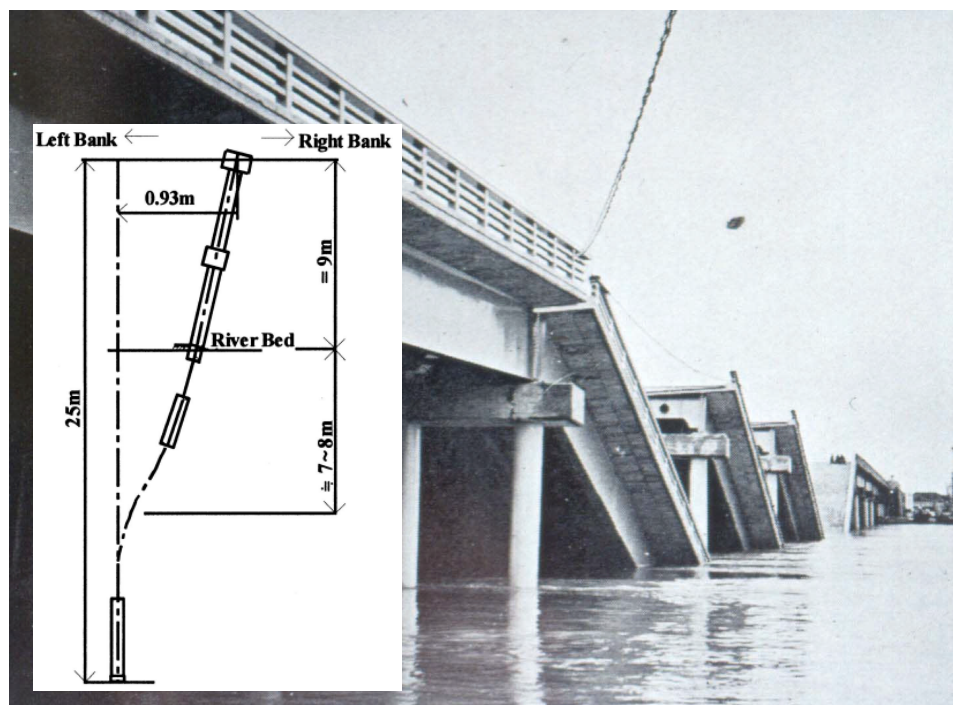
Figure 1-4: Damage to steel piles of Showa Bridge (PWRI; From Yasuda and Berrill 2000).
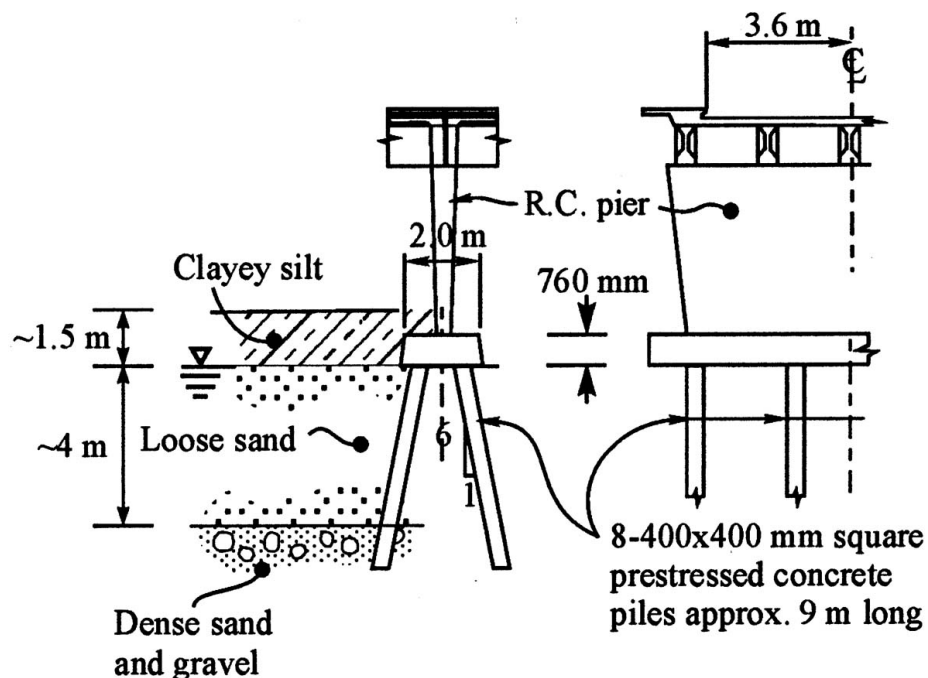
Figure 1-5: Typical pier foundation at Landing Road Bridge, 1987 Edgecumbe earthquake (Yasuda and Berrill 2000).
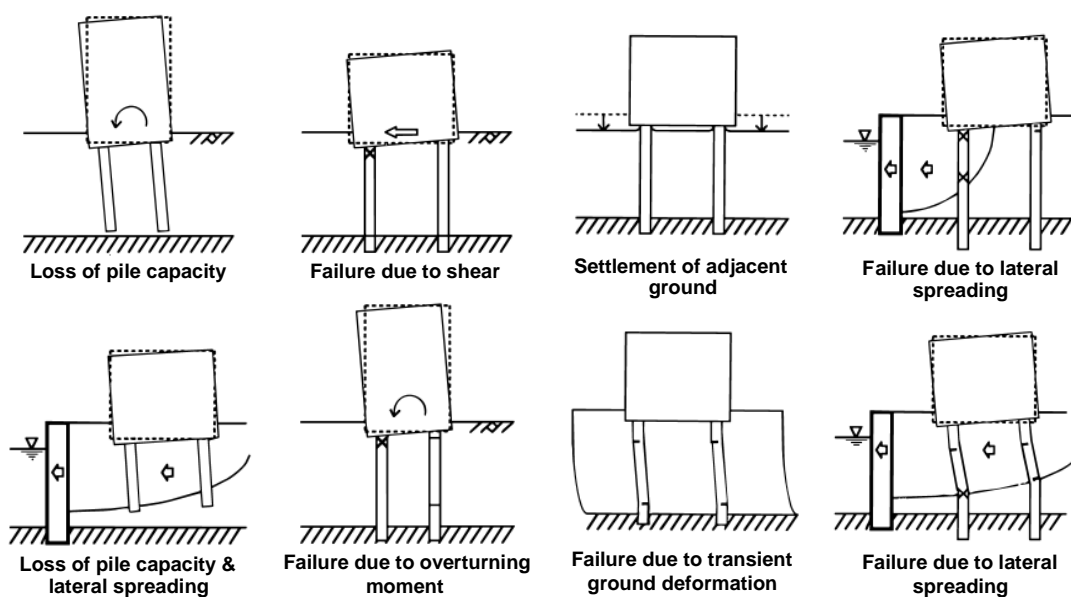
Figure 1-6: Schematic of pile damage mechanisms in liquefied ground (Tokimatsu et al. 1996).
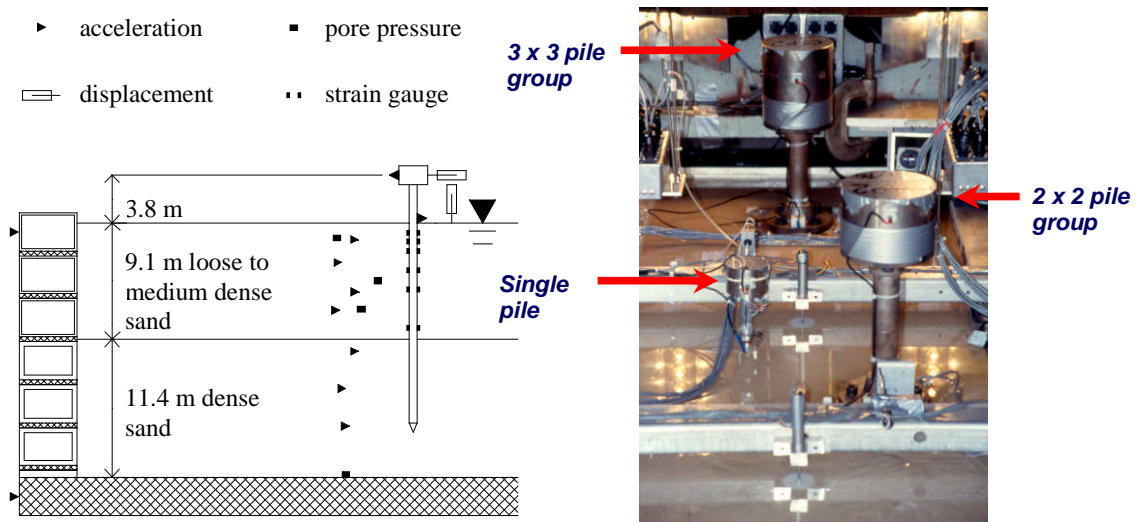
Figure 1-7: Schematic cross-section of centrifuge model and single-pile-supported structure used to back-calculate p-y behavior by Wilson et al. (2000).
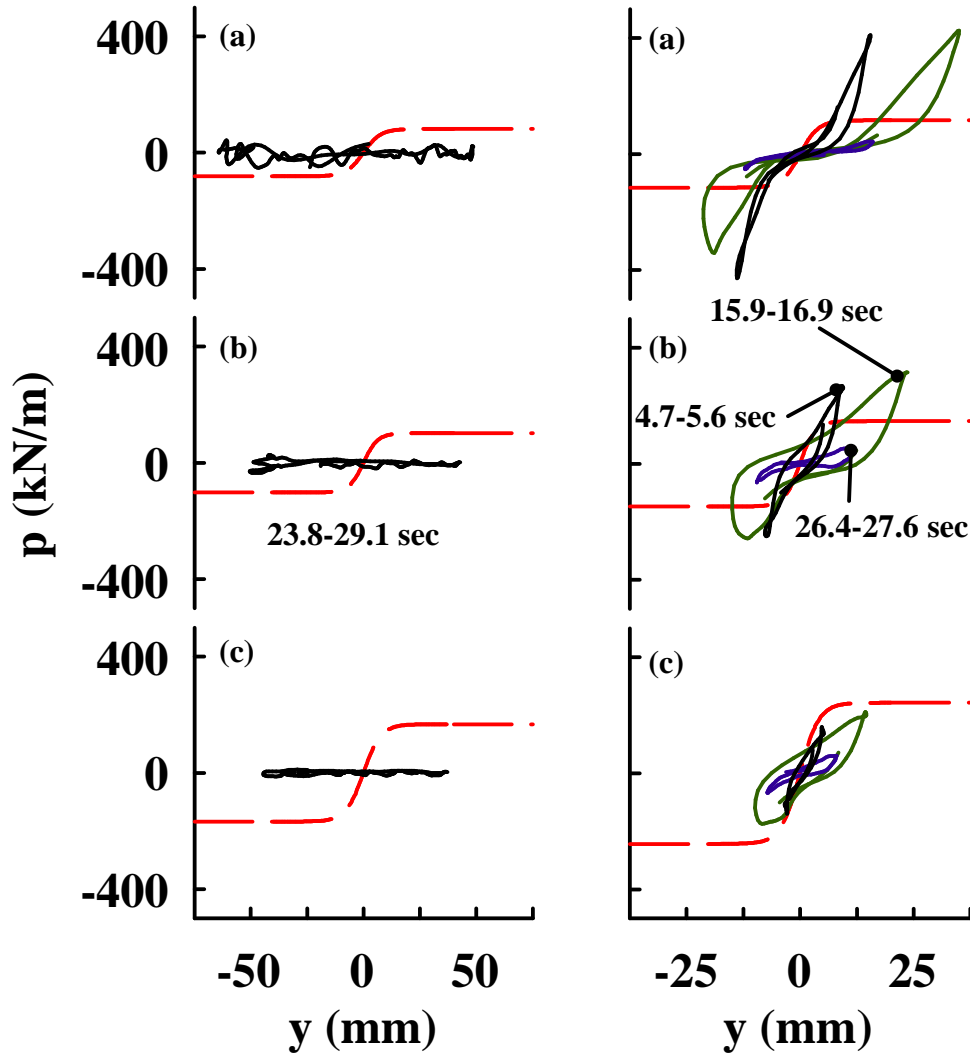
Figure 1-8: p-y loops in liquefying loose sand ($D_r \approx 40\%$) at depths (a) 2-D, (b) 3-D, and (c) 4-D (D = 0.67 m). Dashed lines per API (1993). (Wilson et al. 2000).

Figure 1-9: p-y loops in liquefying med. sand (Dr ≈ 55%) at depths (a) 2-D, (b) 3-D, and (c) 4-D (D = 0.67 m). Dashed lines per API (1993). (Wilson et al. 2000).
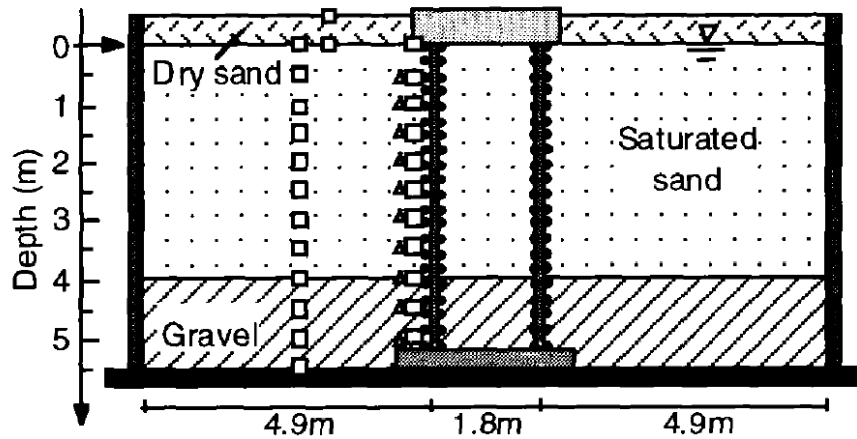
Figure 1-10: Layout of large shaking table tests by Tokimatsu et al. (2001).
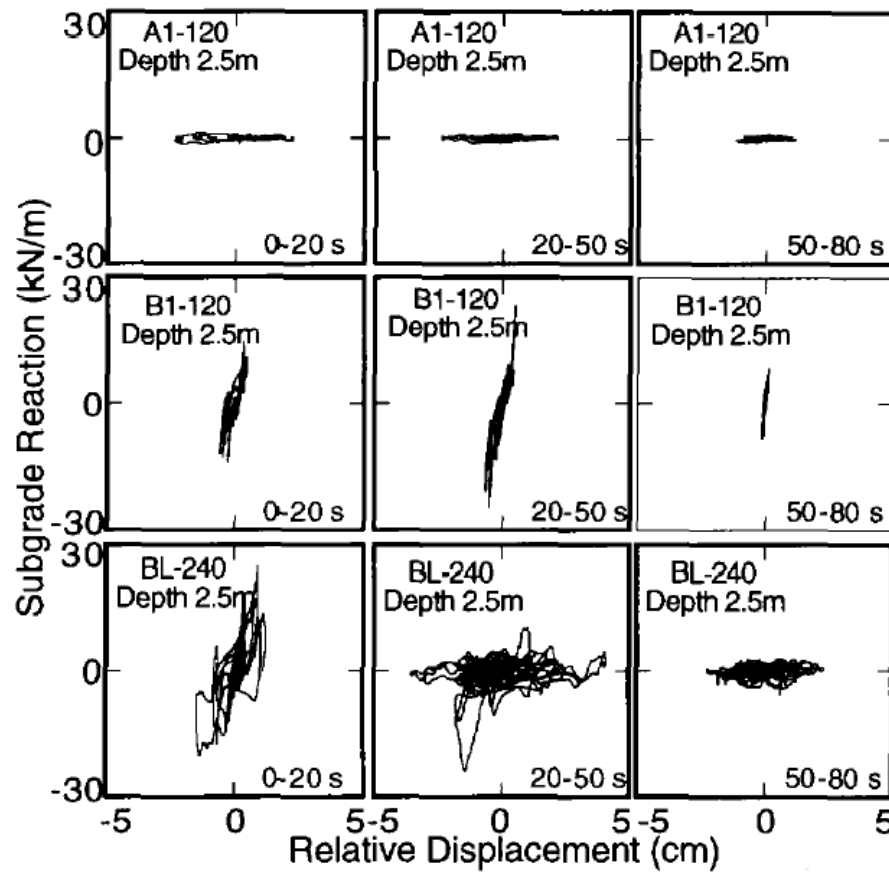
Figure 1-11: Back-calculated p-y behavior from large-scale shaking table tests (Tokimatsu et al. 2001): (a) Top row for A1-120 is for loose sand, (b) Middle row for B1 is for dense sand, and (c) Bottom row for BL is for medium dense sand.
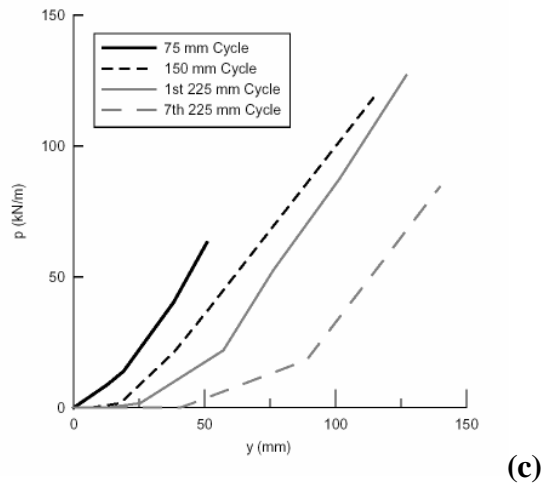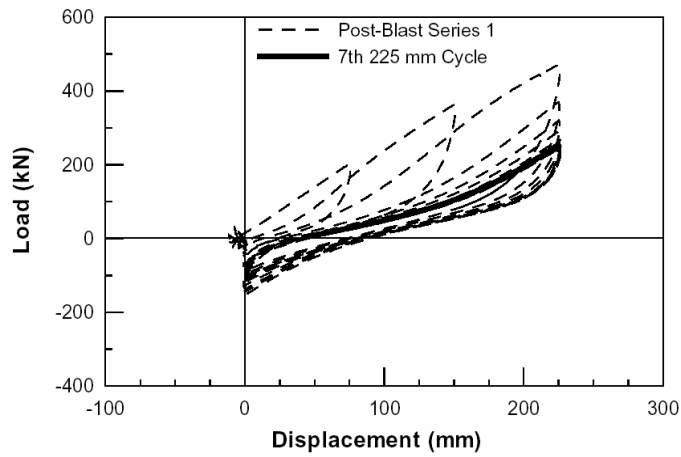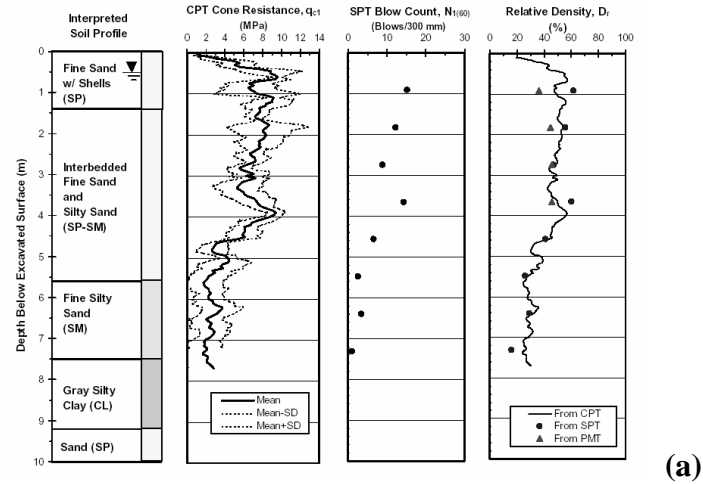
Figure 1-12: Lateral load tests on a 0.6-m-diameter CISS pile after blast-induced liquefaction at Treasure Island (Ashford and Rollins 2002): (a) Soil profile, (b) Load-displacement response, and (c) Back-calculated p-y response.
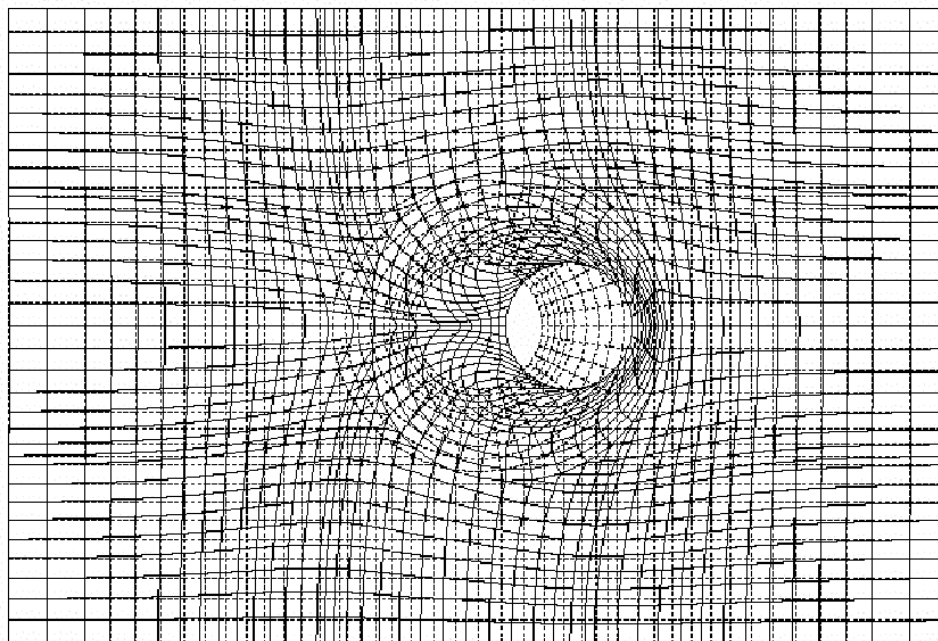
Figure 1-13: Finite element mesh for undrained cyclic loading of pile in saturated sand (Iai 2002).
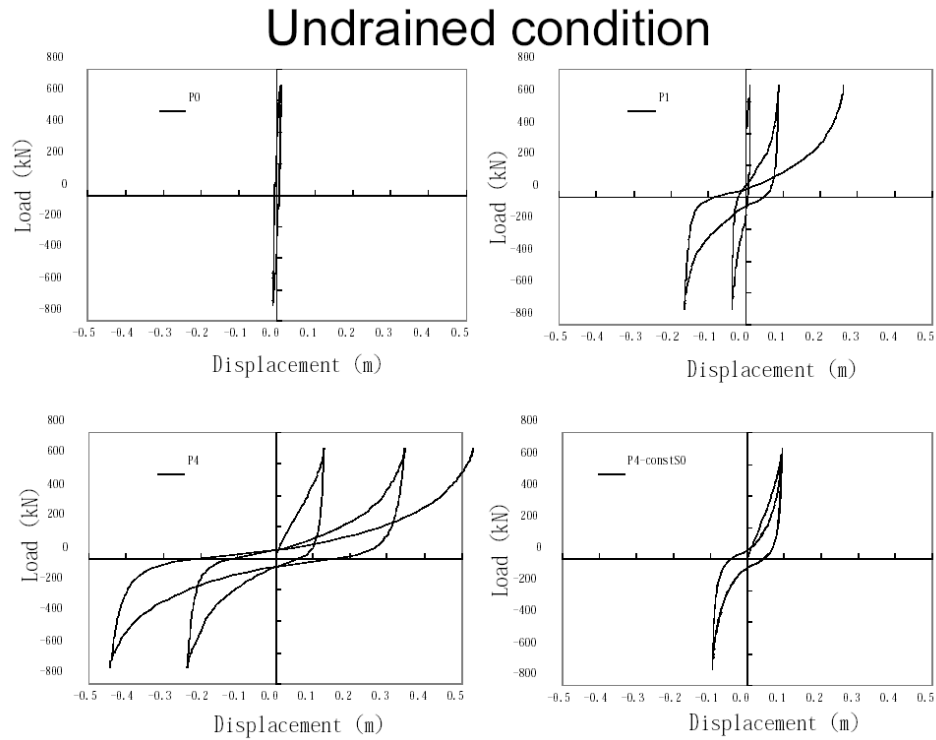
Figure 1-14: Predicted p-y behavior from FEM analysis of pile in liquefied soil (Iai 2002).
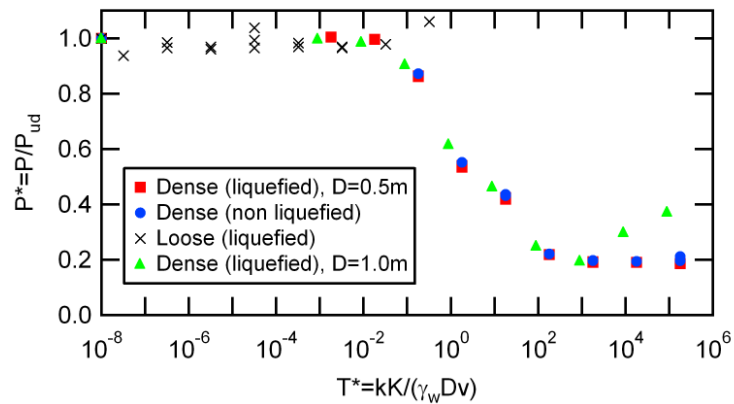
Figure 1-15: Relations between dimensionless subgrade reaction and time factor for a number of different numerical models with pile displacement = 0.25 m (Uzuoka et al. 2005)
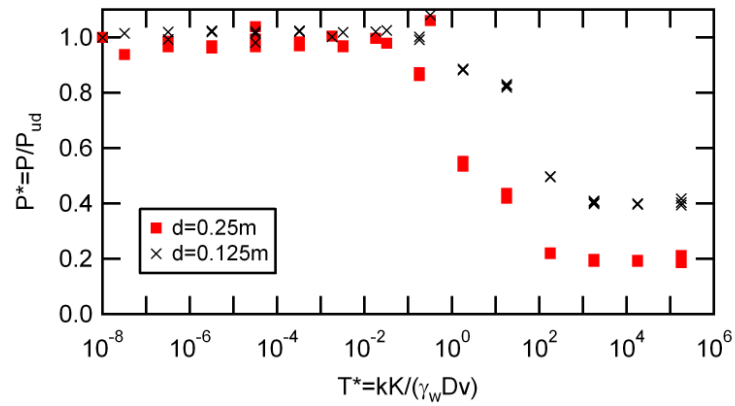
Figure 1-16: Influence of pile displacement on relations between dimensionless subgrade reaction and time factor (Uzuoka et al. 2005).
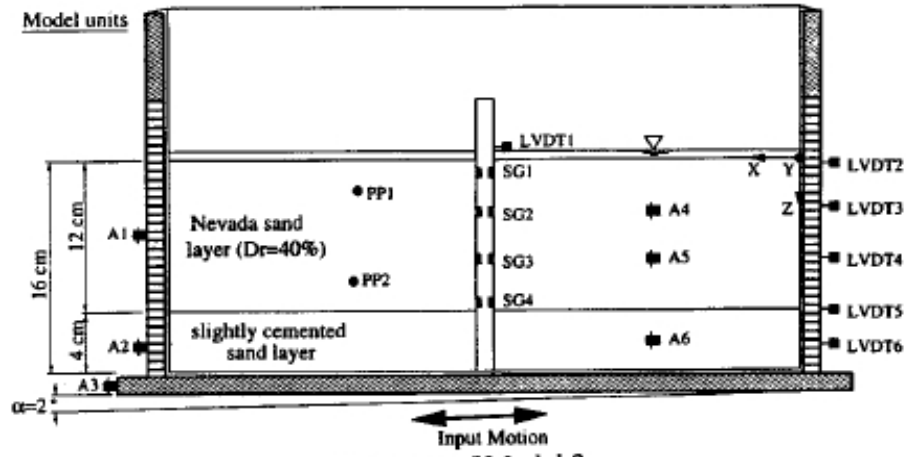
Figure 1-17: Schematic cross-sec. view of centrifuge model 3 (Abdoun et al. 2003).
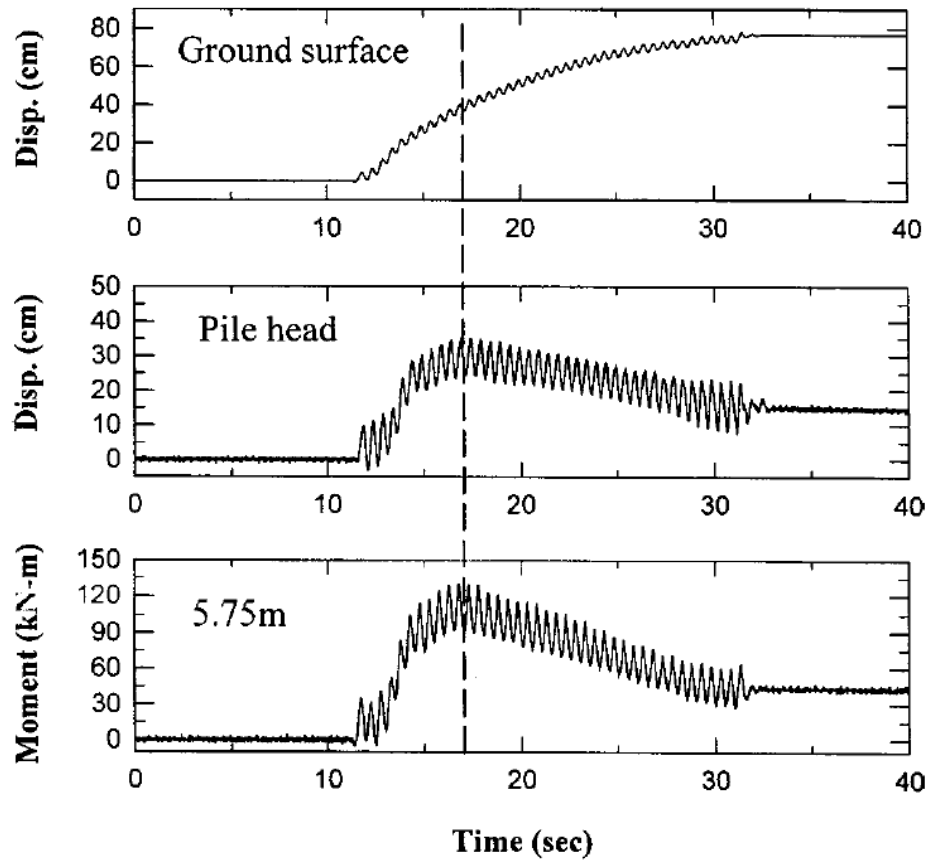
Figure 1-18: Ground displacement, pile head displacement and bending moment at the bottom of the liquefiable layer from centrifuge model 3 (Abdoun et al. 2003).
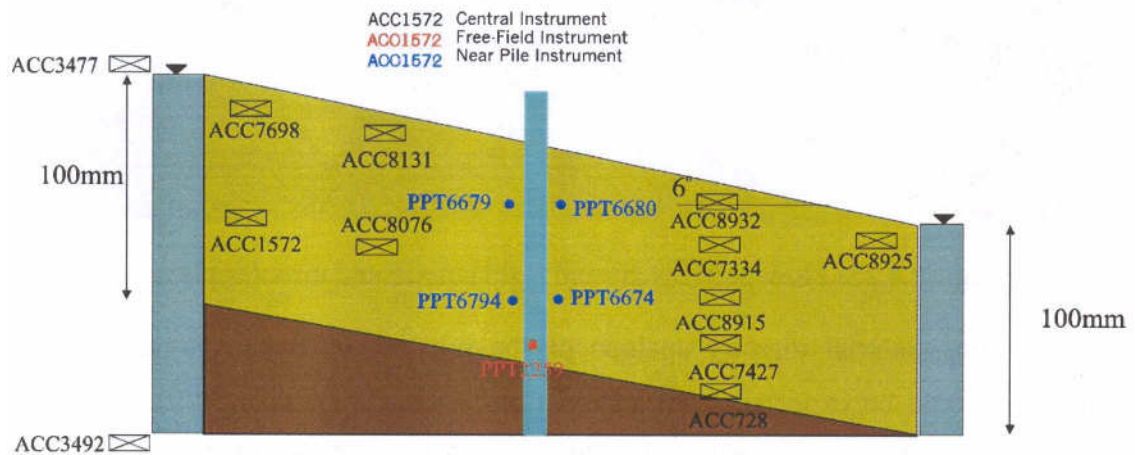
Figure 1-19: Schematic cross-section view of centrifuge tests to study lateral spreading loads on single piles of different flexibility (Haigh 2002).
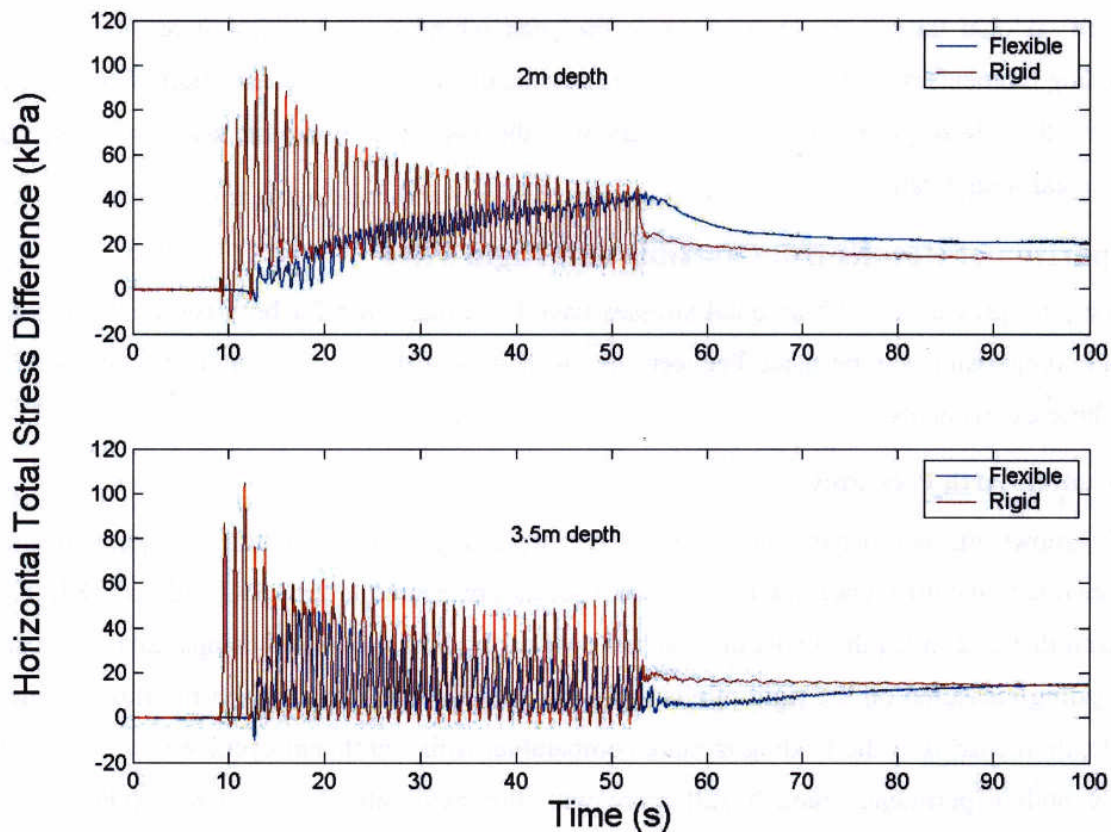
Figure 1-20: Time series of net horizontal stress against "flexible" and "rigid" piles in laterally spreading soil profile (Haigh 2002).
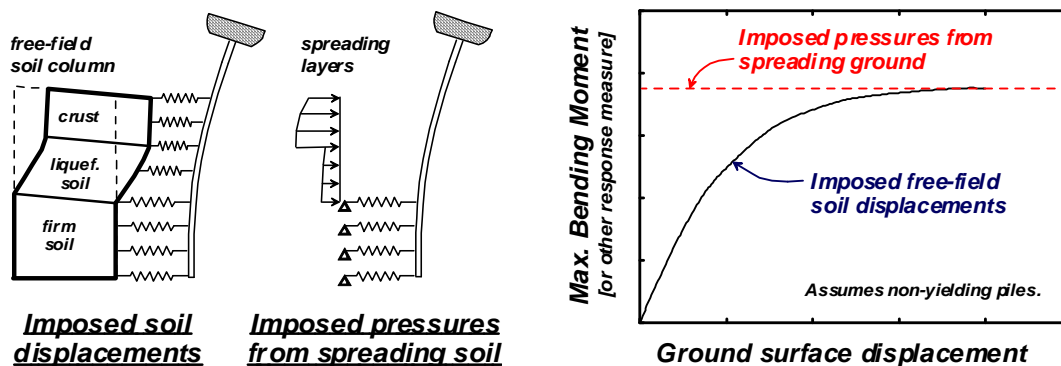
Figure 1-21: Schematic comparison of two methods for imposing loads from laterally spreading ground (Boulanger et al. 2003).
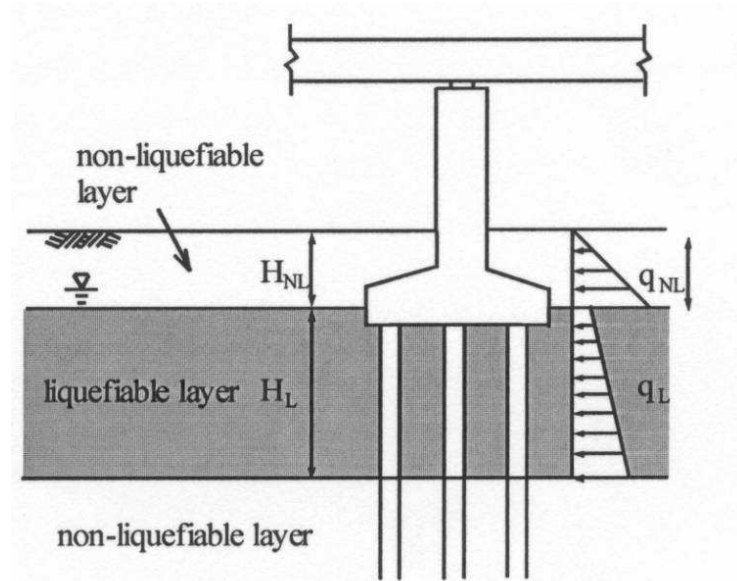
Figure 1-22: Representation of lateral spreading loads by JRA (2002).

(a)   **(b)**
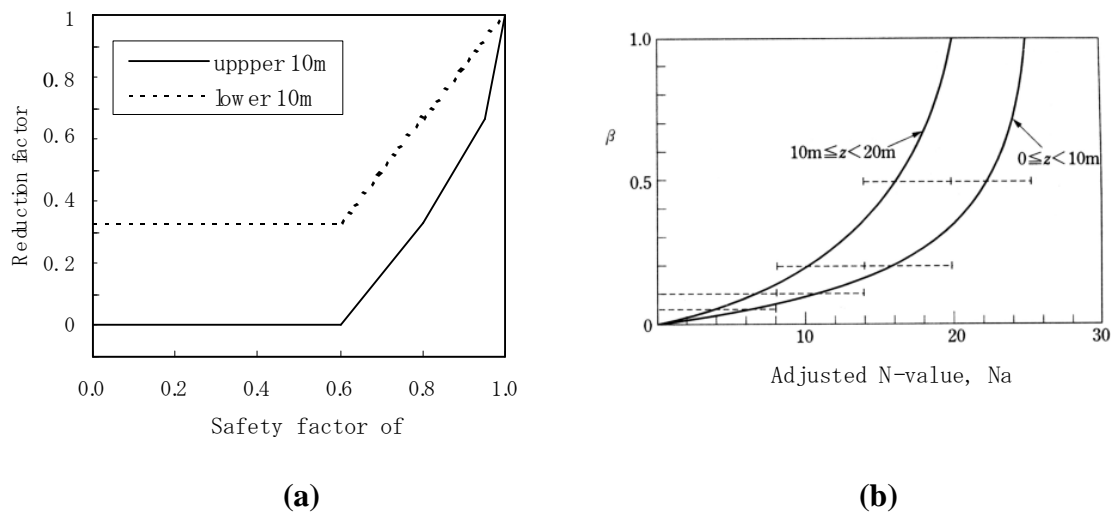
Figure 1-23: Reduction factors for p-y curves in liquefied ground for a) Railway facilities and b) Building foundations adopted in Japanese design code (Uchida and Tokimatsu 2005).
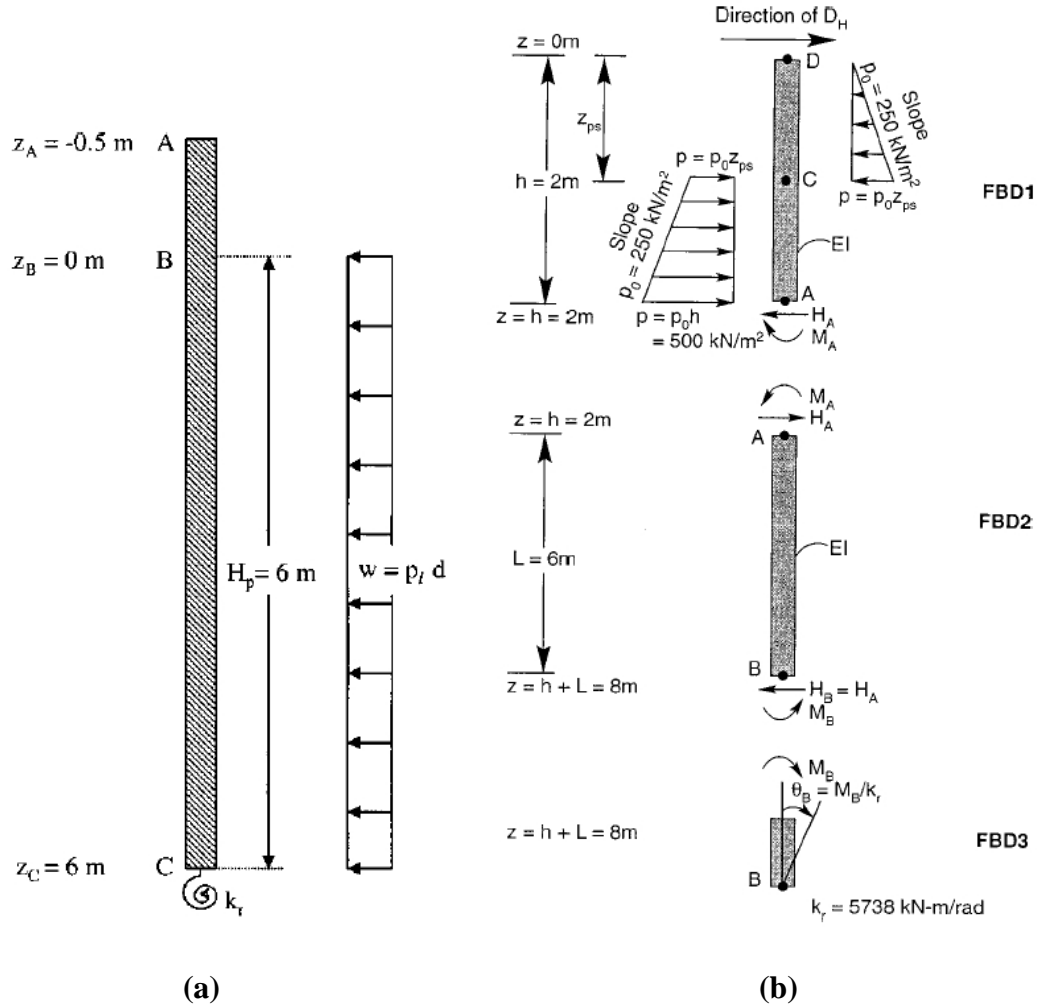
Figure 1-24: Free-body diagrams for limit pressures analysis for piles in soil profiles (a) without a nonliquefied crust, and (b) with a nonliquefied crust (Dobry et al. 2003).
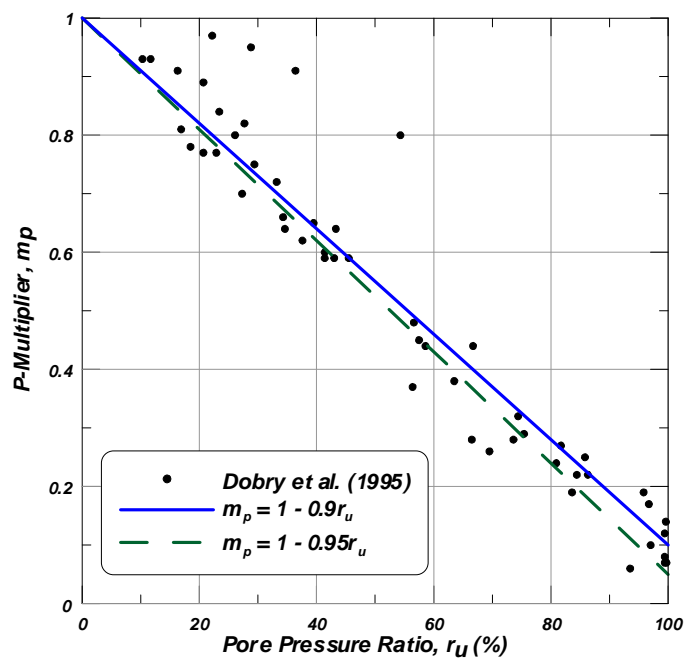
Figure 1-25: Effect of peak free-field excess pore pressure ratio on the ultimate capacity of p-y materials in liquefied sand (Dobry et al. 1995).
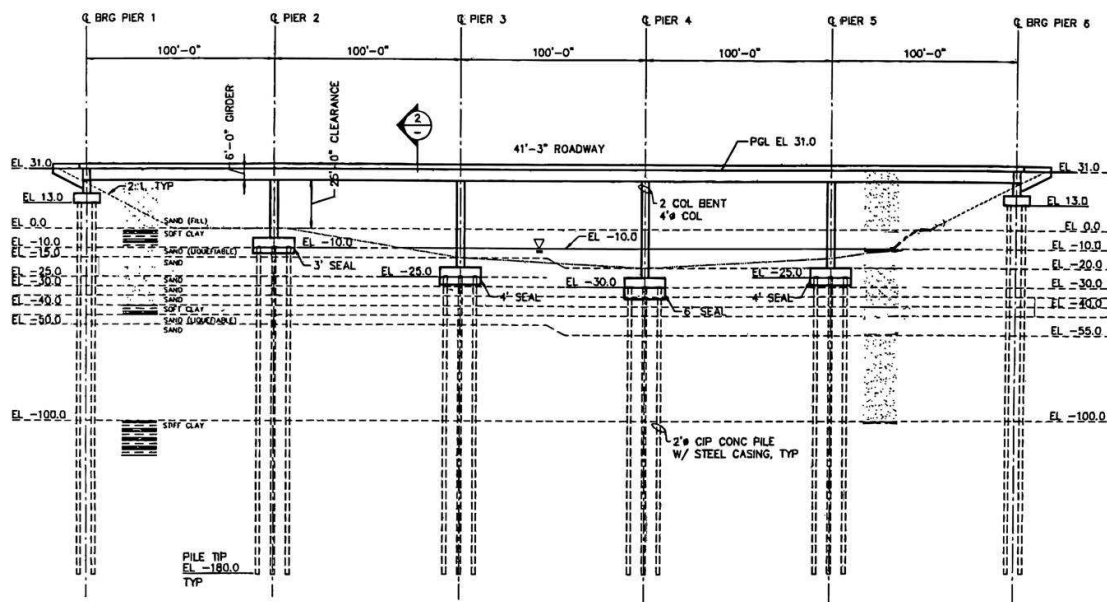
Figure 1-26: Schematic of a bridge supported on pile foundations with pile caps embedded in abutment fill with finite out-of-plane thickness and native soils with essentially infinite out-of-plane thickness (Martin et al. 2002).
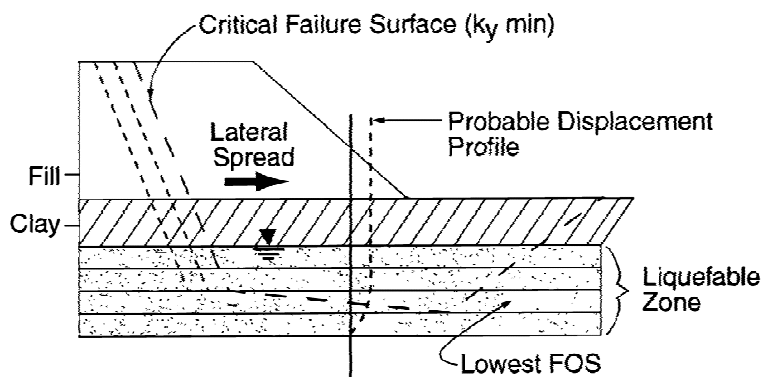
Figure 1-27: Sliding block analysis of a slope on liquefied soil to characterize pile pinning effect on finite-width abutment displacements (Martin et al. 2002).
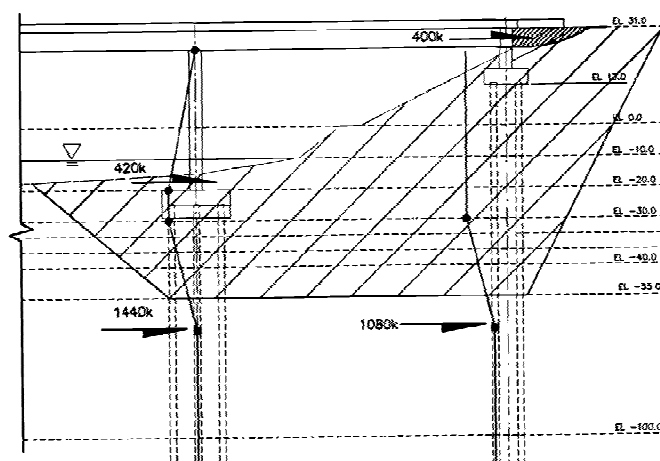
Figure 1-28: Example of pile foundation pinning forces and superstructure pinning forces that limit displacements of finite-width abutments (Martin et al. 2002).
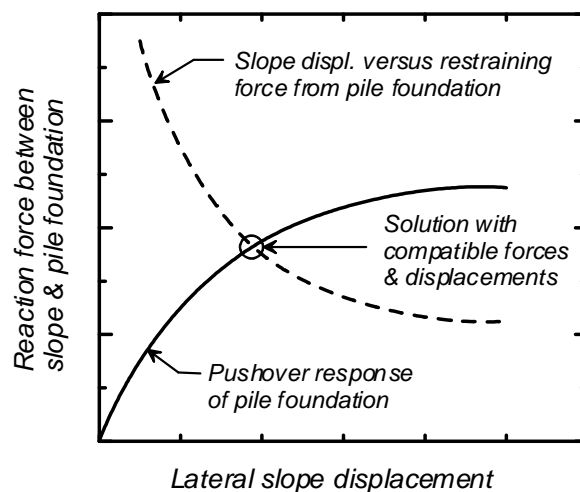
Figure 1-29: Schematic of iterative coupling procedure to account for the influence of pile pinning forces on abutment displacements (Boulanger et al. 2003).

CHAPTER TWO

2. CENTRIFUGE TEST PROGRAM, TYPICAL EXPERIMENTAL RESULTS AND DATA PROCESSING METHODS

This chapter presents the suite of eight dynamic centrifuge tests, including the configurations of each test, sample data that were collected during one of the tests, data processing methods, and sample time series that were obtained by processing the raw data. Each test is fully documented in data reports that can be found at http://nees.ucdavis.edu, along with all of the raw recorded data (Singh et al. 2001, 2000a, 2000b; Brandenberg et al. 2003, 2001a, 2001b). Only a fraction of the data is presented in this chapter. The next chapter contains additional raw and processed data recordings from which observations of loading mechanics are made.

2.1 CENTRIFUGE TEST PROGRAM

This section describes the centrifuge tests that were performed at the Center for Geotechnical Modeling (CGM) at UC Davis to study the behavior of pile foundations during earthquake-induced lateral spreading. The series of eight tests were performed on the 9.1-m radius geotechnical centrifuge at UC Davis (Fig. 2-1). Details of the centrifuge facility, including recent upgrades, are available at the CGM website

(http://nees.ucdavis.edu). A flexible shear beam container (FSB2) was used for the tests. Tests were performed at centrifugal accelerations varying from 36.2g to 57.2g. Table 2-1 presents the scaling factors relevant to the tests. Results are presented in prototype units unless stated otherwise. The first of these centrifuge tests (PDS01) involved three individual piles and one two-pile group, and the seven subsequent tests each contained a six-pile group.

Table 2-1: Centrifuge scaling factors.

Quantity	*Prototype Scale / Model Scale*
Stress	1
Acceleration	N^{-1}
Force	N^2
Moment	N^3
Young's Modulus	1
Length	N
Area	N^2
Moment of Inertia	N^4
Permeability[a]	N
Time	N

[a] Water was used as a pore fluid and its prototype viscosity is N times smaller than the actual viscosity of water.

2.1.1 Test configurations

The main variations in the eight centrifuge tests are listed in Table 2-2. The first centrifuge model, PDS01 (Fig. 2-2), had single pipe piles with prototype diameters of 0.36 m, 0.73 m, and 1.45 m, and one pile group of two 0.73-m diameter piles with an above group pile cap that provided a fixed-head connection. Tests PDS02, PDS03,

SJB01, and SJB02 (Figs. 2-3 to 2-6) each contained a pile group with six 0.73-m diameter pipe piles clamped tightly into a large embedded pile cap. Tests SJB03, DDC01 and DDC02 (Figs. 2-7 to 2-9) contained a pile group with six 1.17-m diameter pipe piles clamped tightly into a large embedded pile cap. Tests DDC01 and DDC02 each contained a mass supported on two columns connected to the top of the pile cap to simulate a single-degree-of-freedom superstructure. The main parameters varied in the tests were the input base motions, the shear strength of the clay crust, the thickness of the loose sand layer, the size of the pile group, and the presence of a superstructure attached to the pile foundation.

Table 2-2: Centrifuge test configurations and parameter variations.

Test	Centrifugal Acceleration	Pile Foundation	Soil	
PDS01	36.2 g	Single piles of dia. 0.36m, 0.73m, & 1.45m. Two-pile group of 0.73-m piles.	1.0 m Coarse Sand; Over 2.9 m Clay $s_u \approx 20$ kPa; Over 4.8 m Loose sand, $D_r \approx 26\%$; Over Dense sand, $D_r \approx 91\%$.	
PDS02	38.1 g	Six-pile group of 0.73-m diameter piles	0.3 m Coarse Sand; Over 4.0 m Clay, $s_u \approx 20$ kPa; Over 4.2 m Loose sand, $D_r \approx 32\%$; Over Dense sand, $D_r \approx 85\%$.	
PDS03	38.1 g	Six-pile group of 0.73-m diameter piles	4.2 m Clay, $s_u \approx 20$ kPa; Over 4.6 m Loose sand, $D_r \approx 35\%$; Over Dense sand, $D_r \approx 82\%$.	Different input base motion
SJB01	38.1 g	Six-pile group of 0.73-m diameter piles	4.2 m Clay, $s_u \approx 40$ kPa; Over 4.6 m Loose sand, $D_r \approx 33\%$; Over Dense sand, $D_r \approx 83\%$.	Increased crust strength
SJB02	38.1 g	Six-pile group of 0.73-m diameter piles	4.2 m Clay, $s_u \approx 40$ kPa; Over 2.3 m Loose sand, $D_r \approx 20\%$; Over Dense sand, $D_r \approx 78\%$.	Smaller thickness of loose sand layer
SJB03	57.2 g	Six-pile group of 1.17-m diameter piles	1.4 m Coarse Sand; Over 2.7 m Clay, $s_u \approx 40$ kPa; Over 5.4 m Loose sand, $D_r \approx 35\%$; Over Dense sand, $D_r \approx 75\%$.	Larger pile group
DDC01	57.2 g	Six-pile group of 1.17-m diameter piles	0.6 m Coarse Sand; Over 3.6 m Clay, $s_u \approx 30$ kPa; Over 5.4 m Loose sand, $D_r \approx 37\%$; Dense sand, $D_r \approx 75\%$.	Superstructure, T = 0.8 s
DDC02	57.2 g	Six-pile group of 1.17-m diameter piles	0.6 m Coarse Sand; Over 3.6 m Clay, $s_u \approx 20$ kPa; Over 5.4 m Loose sand, $D_r \approx 35\%$; Over Dense sand, $D_r \approx 80\%$.	Superstructure, T = 0.3 s

2.1.2   Soil properties

The soil properties for each test are summarized in Table 2-3. The soil profile for all of the models consisted of a nonliquefiable crust overlying loose sand ($D_r \approx$ 21-35%) overlying dense sand ($D_r \approx$ 69-83%). All of the layers sloped gently toward a river channel carved in the crust at one end of the model. The nonliquefiable crust consisted of reconstituted Bay mud (liquid limit ≈ 88, plasticity index ≈ 48) that was mechanically consolidated with a large hydraulic press, and subsequently carved to the desired slope. The sand layers beneath the crust consisted of air-pluviated uniformly-graded Nevada Sand (C_u = 1.5, D_{50} = 0.15 mm). A thin layer of coarse Monterey sand was placed on the surface of the Bay mud for some of the models.

The undrained shear strength of the clay, s_u, for each test was measured using a T-bar (Stewart and Randolph 1991). The s_u profile from the T-bar tests was reasonably consistent with the s_u profile estimated using a normalized strength ratio (e.g. Ladd and Foott 1974) according to:

$$s_u = 0.25 \cdot \sigma_{vc}' \cdot \left(\frac{\sigma_{vp}'}{\sigma_{vc}'}\right)^{0.8}$$

(2-1)

where σ_{vc}' = the vertical effective consolidation stress, and σ_{vp}' = the maximum vertical effective consolidation stress applied to the clay during model preparation. Average s_u values for the clay layers are reported in Table 2-2. The T-bar tests were conducted at a strain rate that was about an order of magnitude smaller than occurs

during shaking on the centrifuge, so the s_u values have been increased by 10% to account for rate effects (e.g. Ladd and Foott, 1974; Sheahan et al., 1996).

Water was used as a pore fluid for all of the models because some water permeated into the sand during consolidation of the clay slurry, and subsequent saturation with a viscous fluid would have resulted in a mixture of pore fluids in the sand layer. The prototype viscosity of the pore fluid was 1/N times that of water, and the permeability of the prototype soil was be N-times larger than if the prototype fluid was water. Hence, the permeability of the sand in the centrifuge models would be characteristic of a coarser sand. Although the sand was partially drained, it exhibited features of undrained response such as sharp drops in pore pressures caused by dilatancy, and the associated large high-frequency acceleration pulses. The rate of post-shaking pore pressure dissipation was very slow compared with the sharp drops in pore pressure, indicating that these drops were due to dilatancy behavior rather than drainage. Uzuoka et al. (2005) showed that subgrade reaction behavior between piles and saturated sand depends on time factor, which depends in part on the permeability of the soil. Permeability of the sand likely influenced the subgrade reaction behavior in the centrifuge tests, and this should be considered in interpreting the test results.

Table 2-3: Soil properties.

Parameter	Units	Nevada sand	Bay Mud
Specific gravity[a]		2.644	2.65
Mean grain size, D_{50}	(mm)	0.17	-
Coefficient of uniformity, c_u		1.64	-
Maximum dry unit weight, γ_{max}	(kN/m^3)	16.9 (17.3)	-
Minimum dry unit weight, γ_{min}	(kN/m^3)	13.9 (14.0)	-
PL	(%)	-	35-40
LL	(%)	-	88-93

[a] Cruz (1995) and Chen (1995)

2.1.3 Foundation properties

The properties of the pile foundations used in each test are provided in model scale in Table 2-3. The first test, PDS01, contained three single piles of various diameters (Pile A, B, and C) and a two-pile group (Pile B) with an above ground pile cap that provided nearly fixed-head conditions. Subsequent tests included a six-pile group (Pile B) with a large pile cap embedded in the nonliquefied crust. The pile caps for the six-pile groups provided a stiff rotational restraint at the connection between the pile and the cap with the measured rotational stiffness being about 7 kN·m/rad in model scale.

Table 2-4: Properties of aluminum tubing used for model piles.

Pile ID	Used in Test	Outer Diameter b (m)	Wall Thickness t (m)	Young's Modulus, E (kPa)	Moment of Inertia, I (m^4)	Yield Stress, σ_y (kPa)[a]	Yield Moment, M_y (kN·m)
SP	PDS01	0.00953	0.0009	39x10^6	2.30x10^{-10}	38000	0.00183
MP, GN, SEM	All	0.01905	0.0009	68.9x10^6	2.11x10^{-9}	216000	0.0478
BP	PDS01	0.03810	0.0017	68.9x10^6	3.23x10^{-8}	297000	0.5036

[a] Yield stress was determined from uniaxial tension testing of the model piles as described in Singh et al. (2000). SP exhibited extensive nonlinear material behavior after yield.

Each model scale pile was wrapped with protective plastic shrink tube that increased the diameter by about a millimeter. Strain gauge wires running along the outside of the pile produced irregularities in the shape of the piles, and the effect increased with increasing number of strain gauges. Therefore the roughness of the pile interface depended on how many strain gauges were affixed to a particular pile. Conical plastic tips with a 60° tip angle were attached to the tips of the piles.

2.1.4 Simulated earthquakes

Each test was subjected to a series of shaking events, with each event separated by sufficient time to allow full dissipation of any excess pore pressures. Shaking events were numbered sequentially for each test; e.g., the first shake in the test PDS01 was numbered PDS01_01, and so on. Table 2-4 lists the shaking events and the peak prototype base accelerations in parentheses. All the "Kobe" events are scaled versions of ground motions recorded at a depth of 83m at Port Island in the 1995 Hyogoken-Nambu (Kobe) Earthquake. The "Santa Cruz" events are scaled versions of the ground motion recorded during the 1989 Loma Prieta Earthquake at the UCSC/Lick Lab, Ch. 1-90°. The "Sine Wave" event is a synthetic motion consisting of 25 cycles of sinusoidal acceleration. The "Step Shake" events were small square wave displacement pulses intended to verify the data acquisition and shaking systems prior to the larger motions.

Table 2-5: Shaking events in the test series.

Shaking Event Number	Test Name							
	PDS01	PDS02	PDS03	SJB01	SJB02	SJB03	DDC01	DDC02
01	Step Shake (0.002g)	Step Shake (0.002g)	Step Shake (0.002g)	Step Shake (0.001g)	Step Shake (0.002g)	Step Shake (0.01g)	Step Shake (0.02g)	Step Shake (0.01g)
02	Small Kobe (0.20g)	Small Kobe (0.20g)	Small Santa Cruz (0.15g)	Small Santa Cruz (0.15g)	Small Santa Cruz (0.17g)	Small Santa Cruz (0.13g)	Small Santa Cruz (0.13g)	Small Santa Cruz (0.14g)
03	Large Kobe (0.70g)	Large Kobe (N.A.)	Medium Santa Cruz (0.46g)	Medium Santa Cruz (0.45g)	Medium Santa Cruz (0.52g)	Medium Santa Cruz (0.35g)	Medium Santa Cruz (0.35g)	Medium Santa Cruz (0.34g)
04	Large Kobe (0.70)	--	Large Santa Cruz (1.00g)	Large Santa Cruz (0.94g)	Large Santa Cruz (0.89g)	Large Santa Cruz (0.67g)	Large Santa Cruz (0.66g)	Large Santa Cruz (0.73g)
05	--	--	Large Kobe (0.74g)	Large Kobe (0.76g)	Large Kobe (0.67g)	Large Kobe (0.67g)	Large Kobe (0.66g)	Large Kobe (0.62g)
06	--	--	--	Large Kobe (0.76g)	Large Kobe (0.80g)	--	--	Sine Wave 1 (0.07g)
07	--	--	--	--	--	--	--	Sine Wave 2 (0.54g)

2.1.5 Instrumentation

Each centrifuge model contained about 100 instruments. Accelerations were recorded within the soil mass, on the base shaker, on the container rings and on the pile foundations. Pore water pressures were measured in the soil. Displacements were measured at the soil surface, on the pile foundations, and on the rings of the container. Bending moments, axial loads, and shear loads were measured in the piles using

Wheatstone full bridge strain gauge configurations. Details of the instrumentation can be found in the data reports on the project website (http://nees.ucdavis.edu).

2.1.6   Photos of the centrifuge models

Fig. 2-10 shows model PDS01 on the centrifuge prior to testing. The large-diameter single pile and small-diameter single pile are shown in the photo. The surface of the model was covered with coarse Monterey sand to prevent desiccation of the clay caused by wind currents during spinning. The open river channel is visible at the bottom edge of the photo. Displacement transducers and accelerometers are attached to the piles, and wires emerging from the tops of the piles are attached to strain gauge bridges located at depth on the piles.

Fig. 2-11 shows a cross section of model PDS01 during excavation of the model after testing. The small-diameter single pile yielded extensively during the test, with a displacement profile that followed the sand layers. The pile sliced through the clay crust as it spread downslope, and the pile head displacement was slightly larger than the ground surface displacement. Paper markers inserted through the soil layers prior to shaking show the pattern of deformation induced in the soil during the simulated earthquakes. Small shear strains were induced in the lower part of the loose sand layer, and large shear strains were induced at the top of the loose sand layer. The clay crust slid on top of the loose sand layer, causing a displacement discontinuity at the interface between the two layers. This behavior was characteristic of all of the centrifuge tests, and was caused by pore water in the liquefied sand becoming trapped beneath the low-

permeability crust, thereby causing a weakened plane due to re-distribution of voids in the sand, or possibly even a water film (Kulasingam et al. 2004).

Fig. 2-12 shows model SJB01 off of the centrifuge after testing. The lateral cracking (in a direction parallel to the river channel) of the clay layer is characteristic of lateral spreads, and the large cracks that extend outward from the upslope edge of the pile cap indicate that the pile group restrained the downslope movement of the crust. The extent of lateral spreading is evident by the gap that was left in the clay on the downslope side of the pile cap. The gap is about 75 mm wide in model scale, which corresponds to about 3 meters in prototype at 38.1 g. Colored paper markers are visible protruding at the surface of the crust layer, and some of the markers provided a drainage path for sand boils to flow to the surface during liquefaction.

Fig. 2-13 shows a cross-section of model SJB02 during excavation after testing. Strains in the dense and loose sand layers were smaller than in test PDS01, but the displacement of the clay crust was large due to the displacement discontinuity at the interface with the loose sand layer. The horizontal black line in the sand marks the contact between the loose and dense sand. The horizontal white line in the clay crust marks the contact between the two lifts that were placed during consolidation of the clay slurry.

2.2 *TYPICAL EXPERIMENTAL RESULTS*

Raw data are presented herein to illustrate typical recordings taken during testing. Data from every instrument for every test is plotted in the data reports, and are therefore not plotted in this dissertation. Fig. 2-14 shows a vertical array of accelerometers near

the center of the model container for PDS01, and Fig. 2-15 shows a vertical array of pore pressure transducers. The acceleration recordings exhibit high frequency large spikes of acceleration that correspond with transient drops in pore pressure caused by the dilatancy of the sand. Excess pore pressures and accelerations were small for the first motion (small Kobe), but the two subsequent motions both liquefied the loose sand layer and induced large accelerations in the soil. The excess pore pressures dissipate relatively quickly after shaking because the pore fluid was water, which diffuses through the soil more quickly than a fluid with the prototype viscosity of water would.

Pile SEM in test SJB03 was instrumented with 21 Wheatstone full bridges to measure bending moments. The dense instrumentation was desired for double-differentiating the bending distributions to obtain subgrade reaction loads, as explained later. Fig. 2-16 contains records of seven of the bending gauges that were nearest to the pile cap for the large Santa Cruz and large Kobe motions from SJB03.

2.3   DATA PROCESSING METHODS

Numerical processing of the raw data can often provide better insights into the fundamental mechanisms than studying the raw recorded data alone. This section presents the methods that were used to process the raw data to obtain measured loads on the pile caps, subgrade reaction loads between the piles and the soil, and displacements of the piles and soil layers.

2.3.1   *Measured loads on pile caps*

Strain gauges oriented in Wheatstone full bridges to measure shear (hereafter called shear gauges) located on the piles near the interface between the loose sand and clay provided a measure of the shear forces, V_s, V_n and V_c, as shown in the free-body diagram in Fig. 2-17. The sign conventions used throughout the dissertation are also defined in Fig. 2-17. These shear forces had contributions from loads imposed on the foundation by the clay crust and pile cap inertia. For tests DDC01 and DDC02, the superstructure inertia provided an extra contribution to the loading imposed on the cap. The loading imposed on the pile group by the crust, F_{crust}, was calculated as the difference between the total shear and the cap inertia force using Eq. 2-2.

$$F_{crust} = \left(2V_s + 2V_n + 2V_c\right) + a_h \cdot m_{cap} \tag{2-2}$$

where the cap inertia force is $-a_h \cdot m_{cap}$. The pile cap acceleration was measured for every test except PDS03 and the cap inertia was therefore estimated for PDS03, as described later. In addition to pile cap inertia, the superstructure inertia force was also subtracted from the measured shear to obtain the crust load imposed on the pile groups in tests DDC01 and DDC02.

The calculated crust load includes the passive resistance on the upslope face, friction on the sides and base of the cap, and loads on the pile segments between the shear gauges and the bottom of the cap as shown in Fig. 2-17.

$$F_{crust} = F_p + F_2 + F_4 + 2F_s + 2F_c + 2F_n \qquad\qquad (2\text{-}3)$$

The components of horizontal soil loading on the right side of Eq. 2-3 could not be calculated separately based on the test data, therefore estimates of the various components were made analytically as described in a later section. Active loading on the downslope face of the cap was excluded from the free-body diagram because large gaps formed along this face when the soil spread laterally downslope, and are believed to have remained open during the large earthquake motions. However, during the small earthquake motions, the gap was small and may have closed during transient upslope displacement cycles.

The lateral loading mechanism in Fig. 2-17 assumes that the clay beneath the pile cap flows around the piles, thereby mobilizing lateral loads on the pile segments and friction loads at any contact between the crust and the base of the cap. However, there is another possible mechanism in which the clay crust beneath the pile caps becomes trapped between the piles, thereby acting as an equivalent block. In such cases, the passive force and side friction forces would act along the entire thickness of the nonliquefied crust layer, while the lateral loads on the pile segments and base of the pile cap would be considered internal forces (i.e. not external to a free body of the equivalent block). The controlling mechanism is that which produces the smaller total lateral load. The pile groups in the centrifuge tests all exhibited the failure mechanism in Fig. 2-17 in which the clay crust flowed around the pile segments, which was verified both by photos taken after the tests during excavation of the models and by comparison of theoretical predictions of the total lateral loads for each mechanism.

2.3.2   Lateral subgrade reaction between piles and soil

Back-calculation of the load-transfer or subgrade reaction behavior between the laterally spreading ground and the piles and pile caps provides a clearer expression of the mechanisms of soil-pile interaction than can be obtained from studying the raw recorded data alone. Dynamic subgrade reaction behavior was back-calculated using the recorded bending moment distribution M(z) along a pile using simple beam theory according to the equation:

$$p = \frac{d^2}{dz^2} M(z)$$

(2-4)

where p is the lateral reaction on the pile, z is depth, and M(z) is the recorded bending moment at location z.

The distribution of lateral resistance (p) was obtained by double differentiating the bending moment distribution with respect to depth at each time step of an event. Discrete numerical differentiation can be very sensitive to relatively small errors in the moment distribution, and tends to amplify high frequency noise in discretely sampled data. Hence the method of differentiation and careful signal processing are important considerations. Wilson (1998) evaluated the various methods used to double differentiate bending moment distributions, and subsequently developed a weighted-residual technique that had certain advantages over more traditional approaches because there is some smoothing inherent to the method. Wilson (1998) also developed signal processing techniques (e.g.

filtering, base line corrections) specific to the instrumentation that was used, which provided the basis for signal processing in this study.

The large amount of data collected during the centrifuge tests sometimes provides an opportunity to compare different measurements of the same quantity, which indicates the reliability of the various measurements and data processing techniques. In addition to the measurements of shear taken directly from the shear strain gauges, the total shear could be estimated using elastic beam theory by single-differentiation of bending moment distributions:

$$V(z) = \frac{dM(z)}{dz} \tag{2-5}$$

where V(z) is the shear distribution, M(z) is the moment distribution, and z is the depth along the pile. By differentiating the moment distribution at every time step, time series of shear can be obtained at a number of depths along the piles. Fig. 2-18 shows a comparison between the shear time history obtained directly from readings from the shear gauges, and the shear time history obtained by differentiating the moment distribution for SJB03, both near the same depth but on different piles. The close agreement between the two shear time histories validates the accuracy of the shear gauges and the accuracy of the numerical differentiation technique. An independent verification of the second derivative of bending moment could not be obtained from the measured data, but

verification of the accuracy of the first derivative at least qualitatively validates the accuracy of the second derivatives.

Subgrade reaction (p) time series are shown in Figs. 2-19 to 2-22 for the large Kobe motion for test SJB03. The p-histories are believed to be of high quality given the dense array of 21 bending moment transducers on the piles (p-histories were obtained at the midpoints of the gauges, hence there are 20 p-histories), and the close agreement between the shear recording obtained by differentiation and the one that was measured directly with the shear gauges. However, some errors are likely to be caused at the boundaries of the pile (near the cap and tip) during differentiation, and also at the interface between the clay crust and the loose sand due to the sharply varying change in p across the interface. Furthermore, the values of p are sensitive to the various assumptions involved in computing the second derivatives. The trends, however, are qualitatively correct. These p-histories permit a detailed examination of many of the assumptions used in design of laterally loaded piles, as will be discussed in a later chapter.

2.3.3   Pile displacement

The displacement of the piles, y_{pile}, was calculated from measured boundary conditions and the recorded curvature distribution along the pile using the equation:

$$\frac{d^2}{dz^2} y_{pile}(z) = \phi(z) \qquad\qquad (2\text{-}6)$$

where ϕ is curvature, which was measured using the Wheatstone full bridges that were calibrated to measure bending moment (for linear elastic material behavior, $M = EI \cdot \phi$). Integrating to solve for y_{pile} requires specification of two boundary conditions. The measured pile head displacement relative to the container base was used for one of the boundary conditions, and the pile tip displacement relative to the container base was assumed to be zero for the other. The measured pile head rotation provided an independent check on the reasonableness of the computed shape. The calculated pile displacement profiles contained contributions from curvature along the piles and rotation at the pile tips.

2.3.4 Soil displacement

The free-field soil displacement, y_{soil}, ranged from relatively high-frequency dynamic movement to relatively low-frequency permanent displacement. Horizontal displacement transducers attached to vertical anchor plates that extended down into the crust layer provided the low frequency part of the crust displacement, but the high frequency component was inaccurate due to transient rotation of the anchor plates during shaking. The dynamic component of the soil displacement was calculated by double integration of acceleration records, but the permanent displacement could not be obtained in this way because double integration is sensitive to very small noise levels in the low-frequency portion of the signals containing the permanent displacement data. The displacement of the crust relative to the base was therefore calculated by adding together the low frequency component from the displacement transducers and the high frequency component obtained from the accelerometers. The low-frequency component of the

deeper sand displacements was not measured during shaking, but the permanent displacement profile was measured when the model was dissected after all of the shaking events. The low-frequency component of the deeper sand layers was obtained by scaling the measured low-frequency portion of the crust displacement to the permanent soil deformation profile taken at each accelerometer location (i.e. the shape of the low-frequency component of displacement was assumed to be the same at all depths). This assumption likely introduces some error into the data, but permits qualitative assessments of the displaced shape of the soil profile at different times during shaking, and is believed to be a reasonable method for extrapolating deep low-frequency displacements. All displacement values were calculated relative to the base.

2.3.5   Relative displacement between piles and soil

The subgrade reaction is related to the relative displacement between the piles and the soil ($y = y_{pile} - y_{soil}$). The calculated time histories of y were difficult to accurately determine because they contained measurement errors that were attributed primarily to assumptions regarding the boundary conditions required to calculate y_{pile} and the low frequency part of y_{soil}. The results do, however, permit qualitative observations of the relative displacement profiles at snapshots in time. Hence, time histories are presented for p, but not for y, while snapshots of the displaced shapes of the soil and piles are presented for critical loading cycles.

2.4 SUMMARY

A series of eight dynamic centrifuge tests was performed to study the behavior of pile foundations in liquefied and laterally spreading ground. The first of these centrifuge tests involved three individual piles and one two-pile group, and the seven subsequent tests each contained a six-pile group with a large pile cap embedded in the nonliquefiable crust layer. A sequence of realistic earthquake motions was imposed on the base of the models, generally with larger motions following smaller ones.

Data were collected from about 100 sensors placed in each model to measure accelerations, pore pressures, displacements, bending moments, axial forces and shear forces. Pore pressure records showed that the loose sand layer liquefied for the large earthquake motions, and that the sand exhibited dilatancy behavior in which the pore pressures transiently dropped as the sand layer became temporarily stiff and strong. The dilatancy behavior is also evident in the high-frequency large acceleration spikes that occurred simultaneously with the drops in pore pressure. Bending moments measured along the piles showed that the peak moments occurred at the connection with the pile cap, and the profile exhibited the reverse curvature characteristic of deeply-embedded fixed-head piles in lateral spreads.

Measurements of the model geometries taken before and after testing identified a displacement pattern in which the clay crust slid on top of the liquefiable sand layer. This discontinuity was caused by upward-seeping pore water becoming trapped beneath the low-permeability clay crust layer, thereby causing an increase in the void ratio of the sand underlying the crust layer. This displacement profile was not seen in other

centrifuge studies by Abdoun et al. (2003) in which the crust was perforated to increase its permeability.

Processing of the raw recorded data provided fundamental engineering behaviors that cannot be observed directly in the raw data itself. Methods used to compute subgrade reaction loads, crust loads, pile displacements and soil displacements were presented. Validation for the differentiation and data processing techniques used in this dissertation was provided by the close agreement between shear forces measured directly using shear gauges, and those obtained by single differentiation of bending moment distributions. Detailed p-histories from a pile that was heavily-instrumented with bending moment gauges were presented, and provide a high-quality understanding of loading mechanisms in the various layers.

Figure 2-1: 9-m radius centrifuge at the center for geotechnical modeling.

Dimensions: model - mm [prototype - m]

Monterey
Sand

Clay

Loose Sand

580 [22]

Dense Sand

North

South

1.2°

MP

BP

790 [30]

GN GS

SP

1650 [63]

Accelerometer

Pore Pressure
Transducer

Linear
Potentiometer
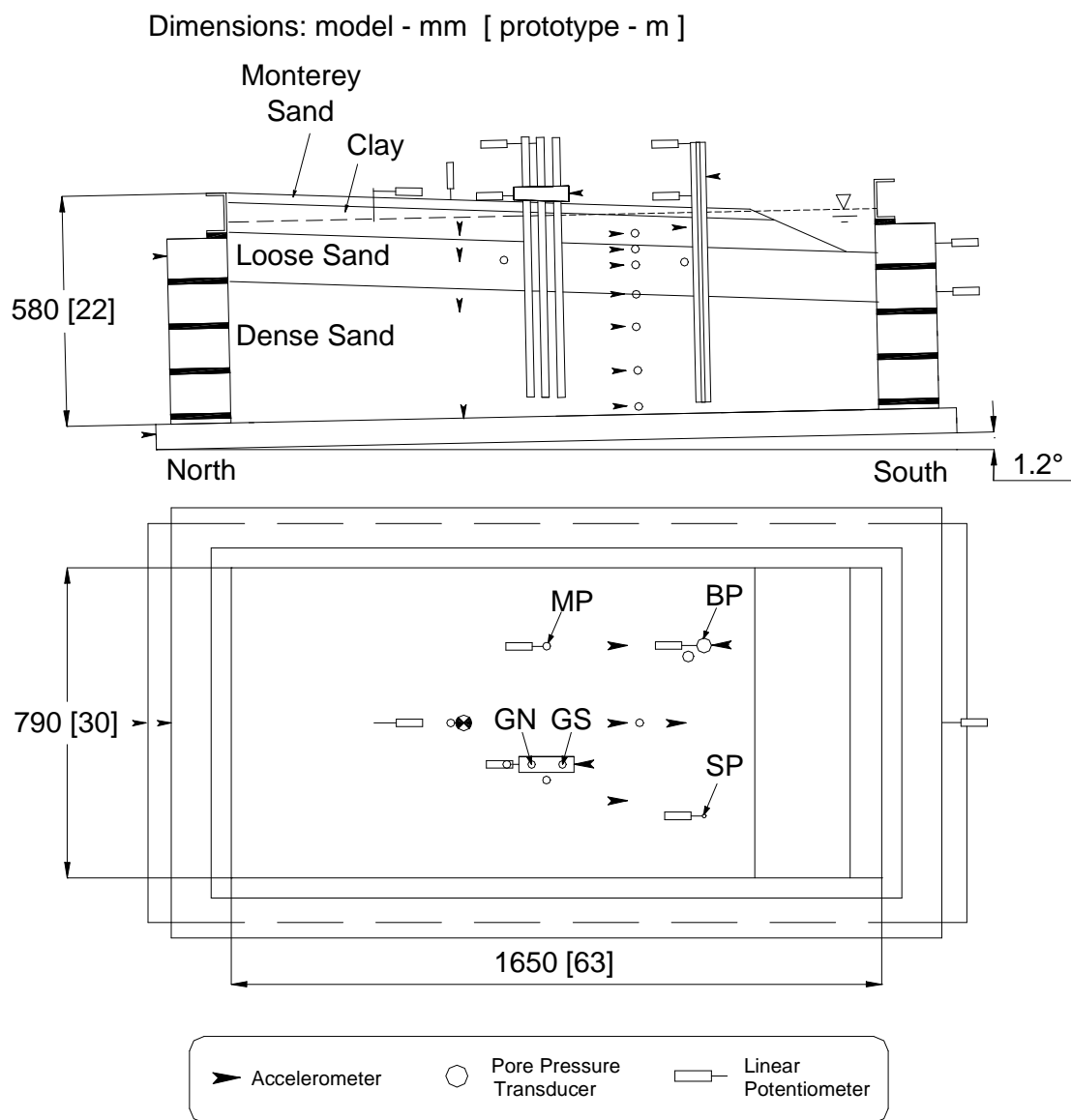
Figure 2-2: PDS01 model layout.

Dimensions: model - mm [prototype - m]
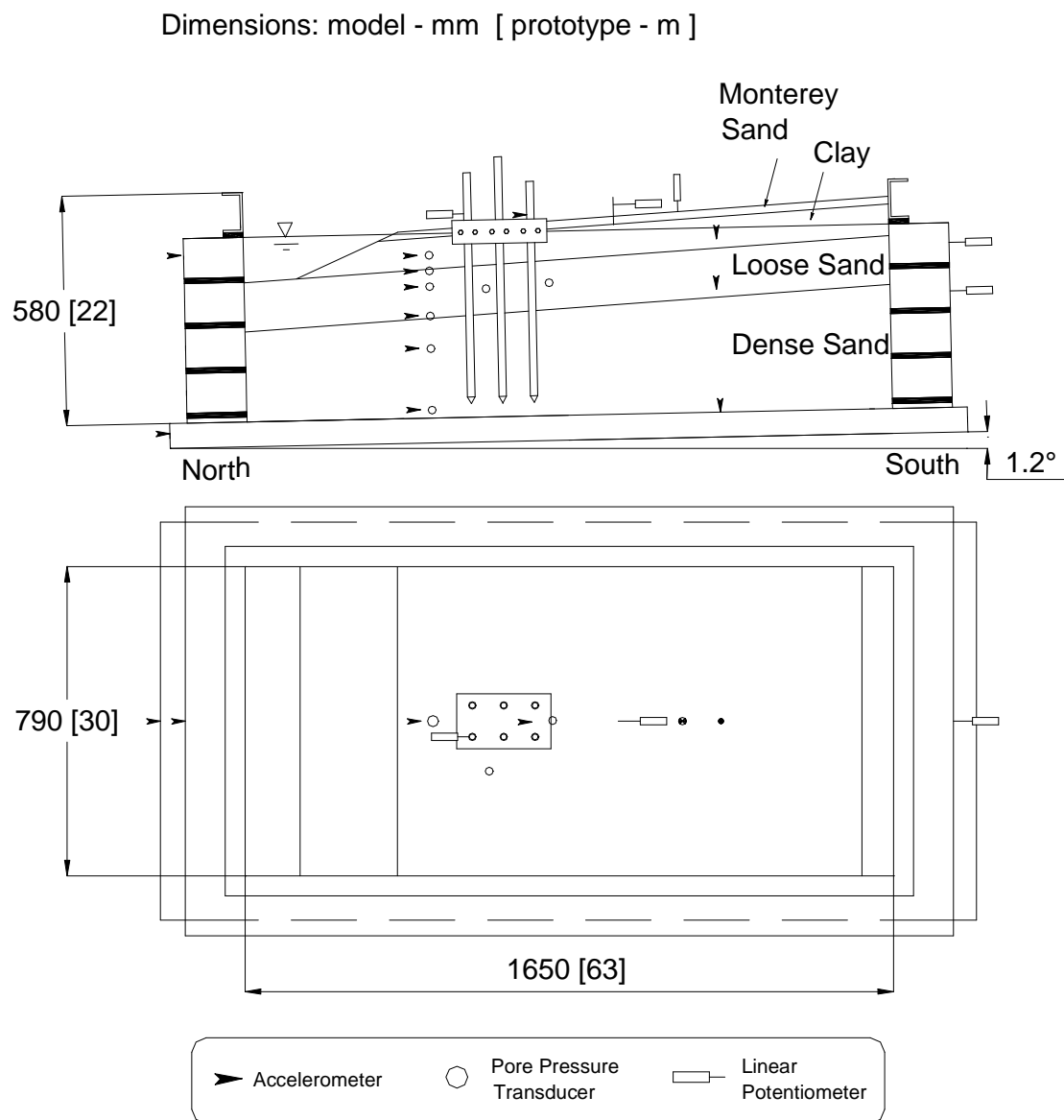
Figure 2-3: PDS02 model layout.

Dimensions: model - mm [prototype - m]
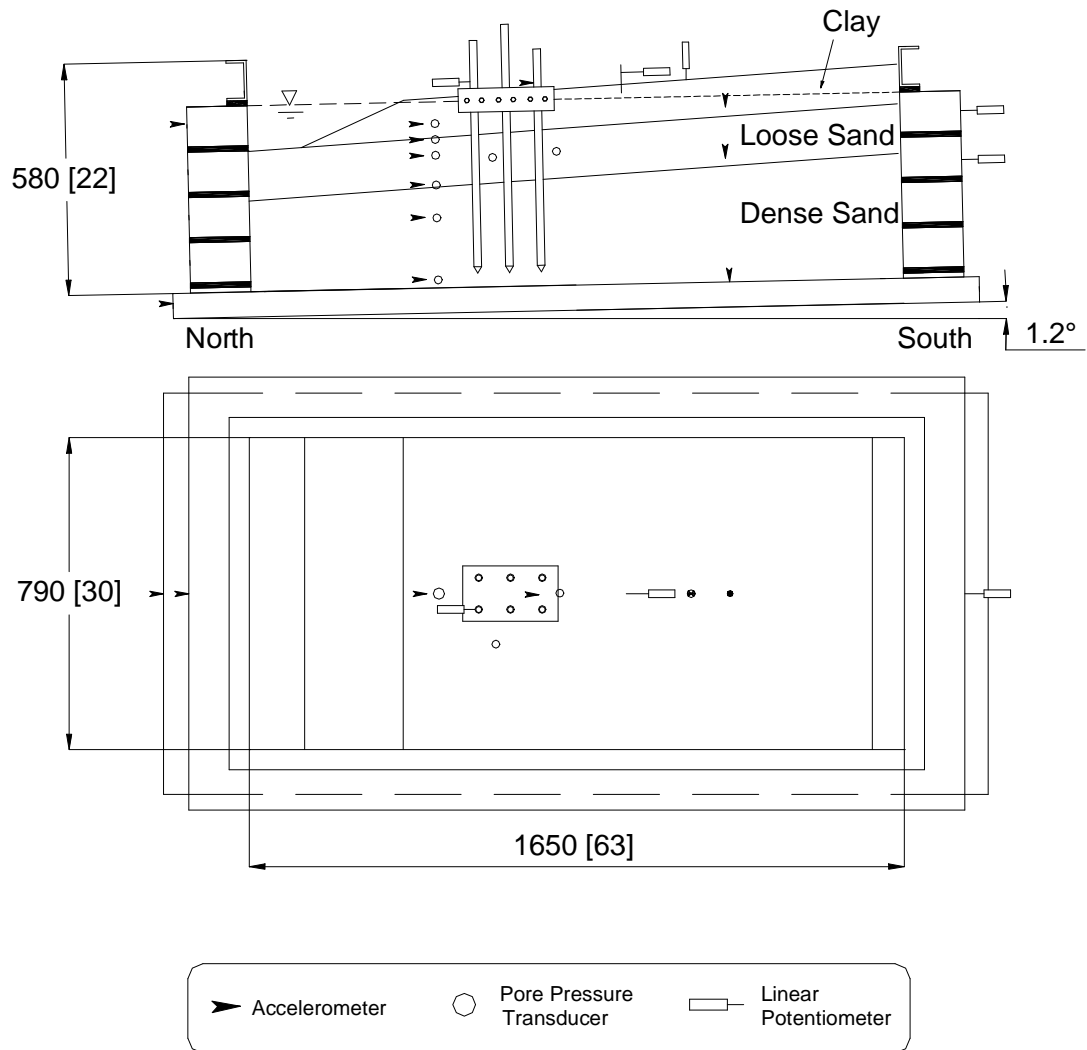
Figure 2-4: PDS03 model layout.

Dimensions: model - mm [prototype - m]

Clay

Loose Sand

Dense Sand

580 [22]

North

South

1.4°

790 [30]

1650 [63]

➤ Accelerometer   ⬡ Pore Pressure Transducer   ▭ Linear Potentiometer
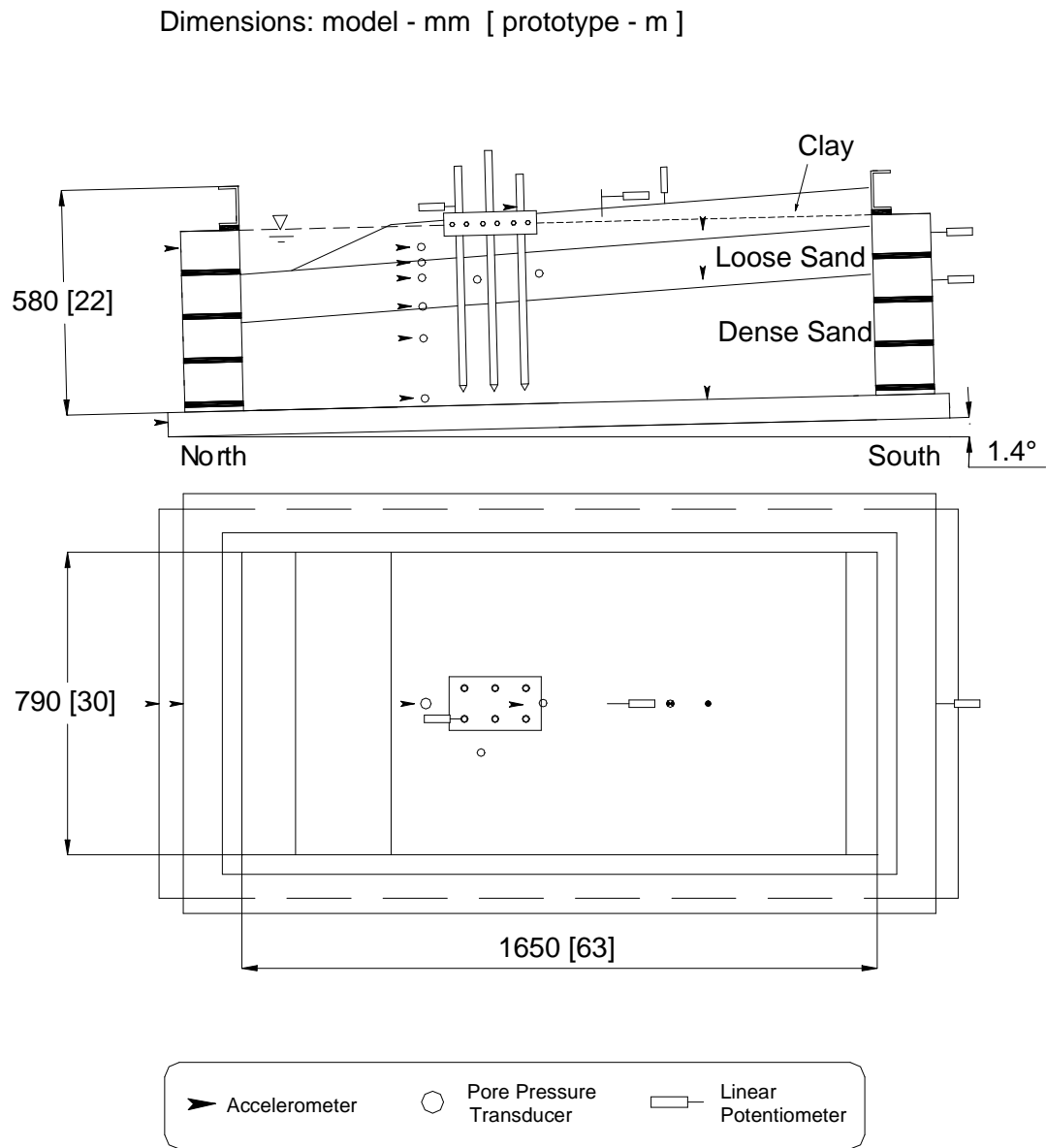
Figure 2-5: SJB01 model layout.

Dimensions: model - mm [prototype - m]

Clay

580 [22]

Loose Sand

Dense Sand

North

South

1.4°

790 [30]

1650 [63]

Accelerometer

Pore Pressure
Transducer

Linear
Potentiometer
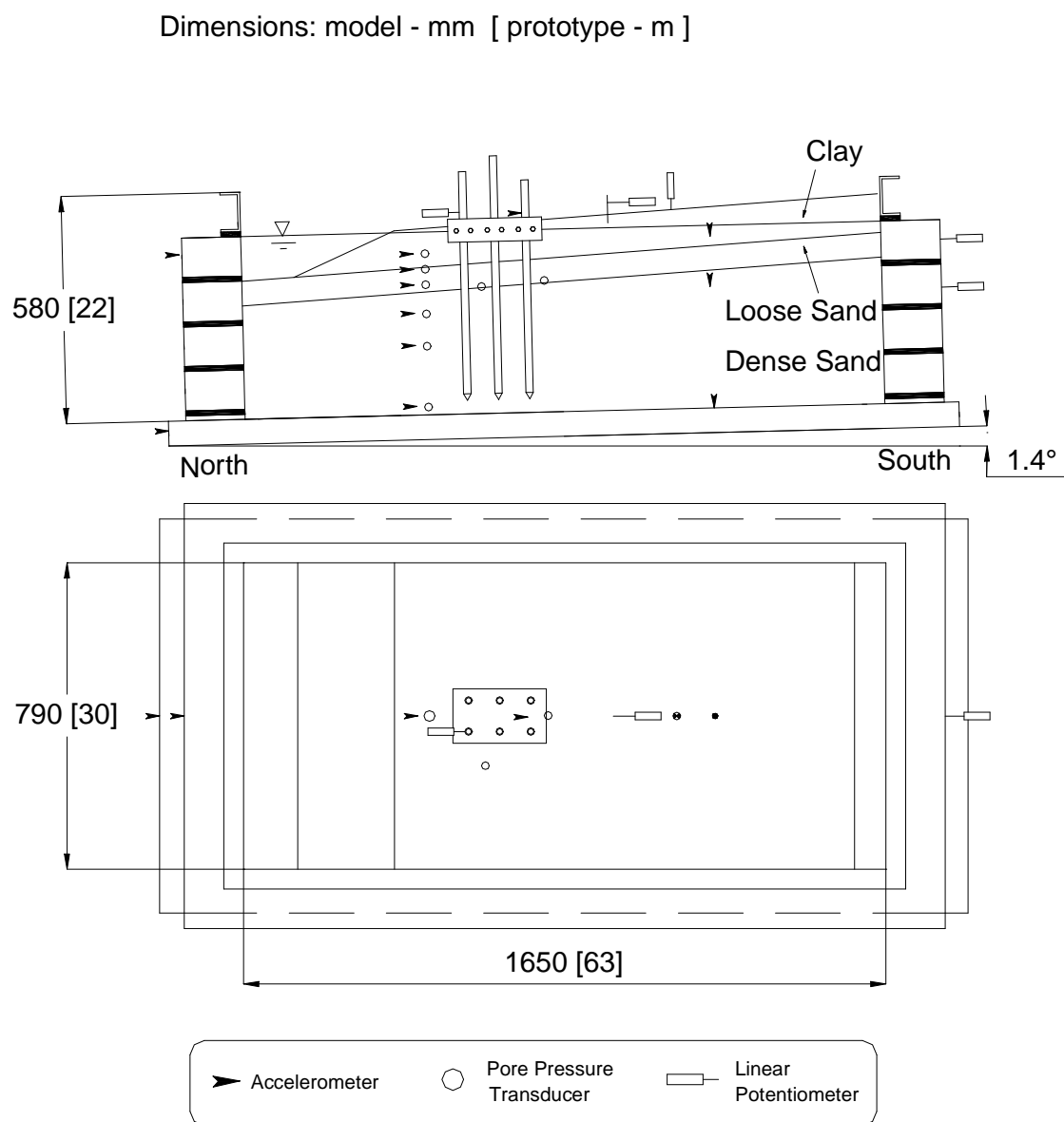
Figure 2-6: SJB02 model layout.

Dimensions: model - mm [prototype - m]
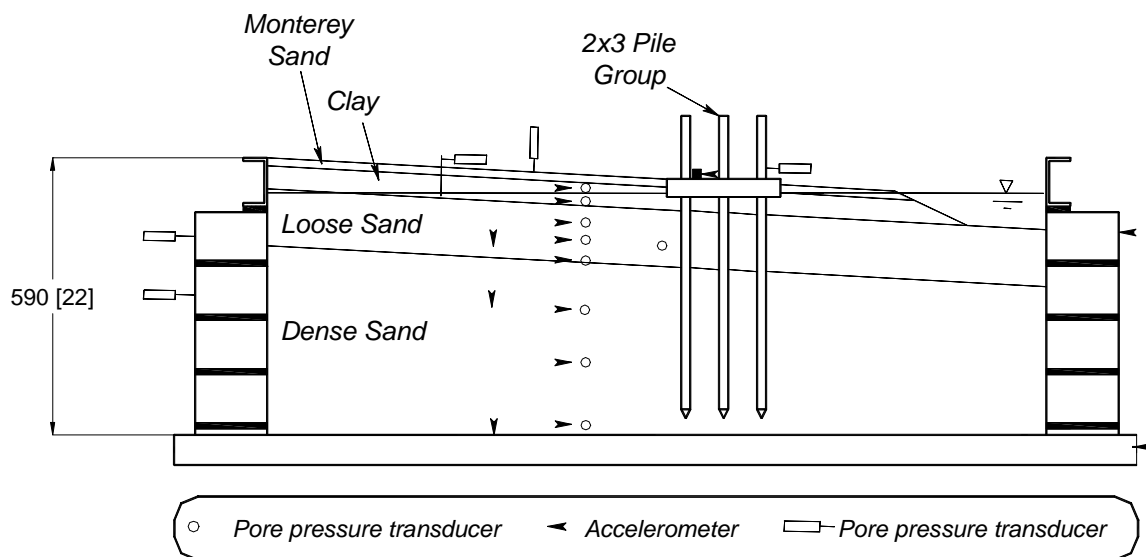
Figure 2-7: SJB03 model layout.

Dimensions: model - mm [prototype - m]
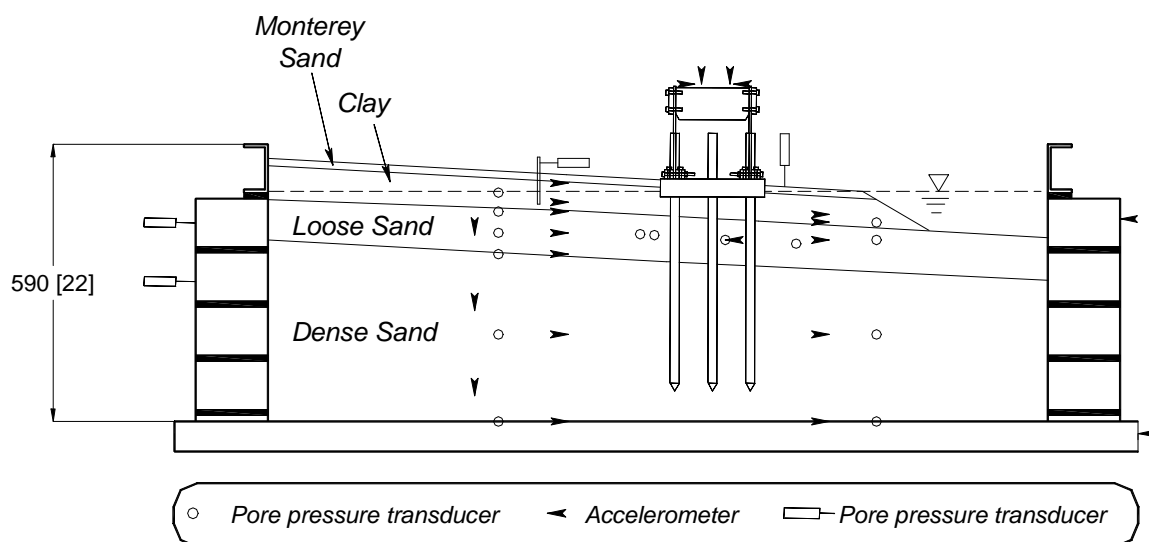
Figure 2-8: DDC01 model layout.

Dimensions: model - mm [prototype - m]

Monterey
Sand

Clay

590 [22]

Loose Sand

Dense Sand

○ *Pore pressure transducer* ◄ *Accelerometer* ▭—*Pore pressure transducer*
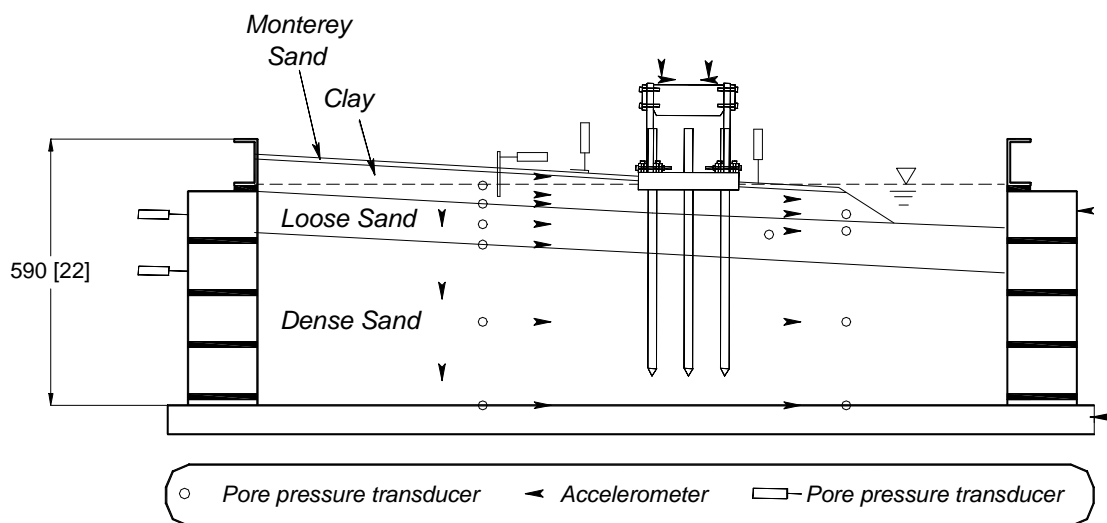
Figure 2-9: DDC02 model layout.
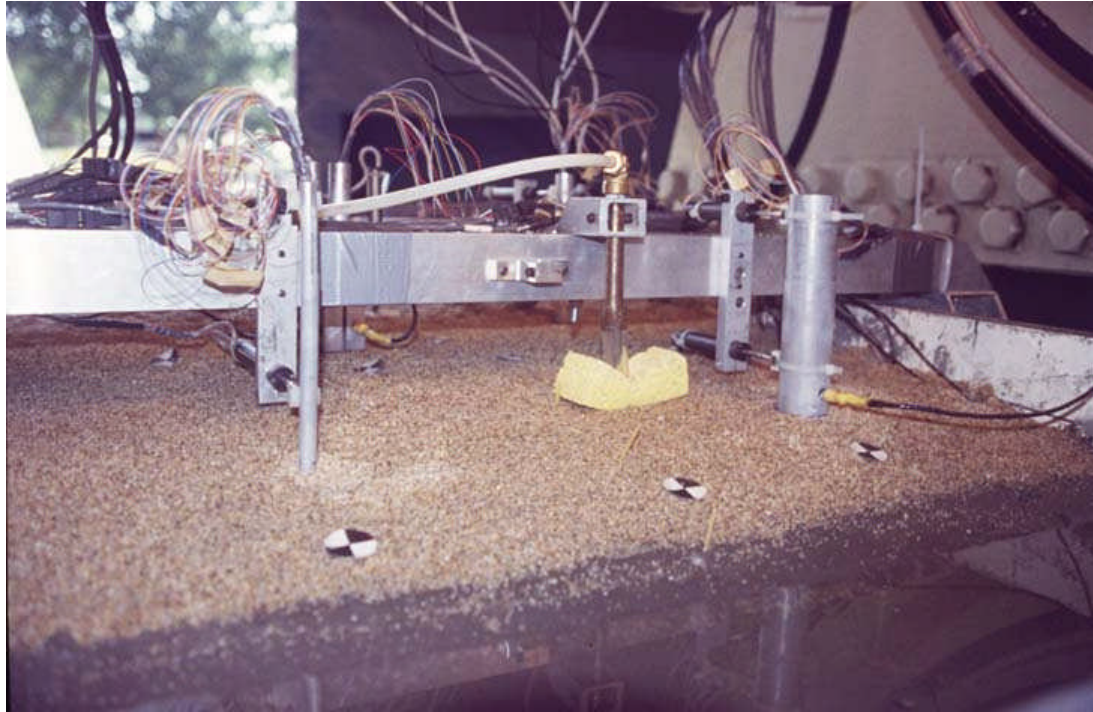
Figure 2-10: Photo of model PDS01 on the centrifuge prior to shaking showing small- and large-diameter piles near the channel at the down-stream toe. The channel exposes the darker colored clay, while the above-water ground surface has a thin layer of protective sand on it.
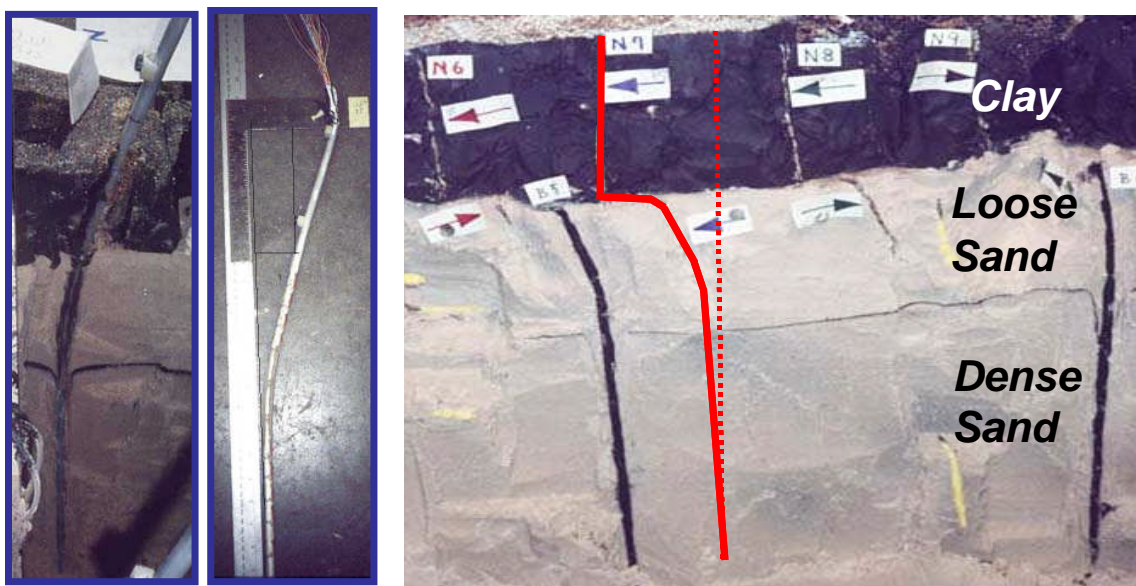
Figure 2-11: Excavation photos from PDS01 showing the small-diameter pile that yielded extensively and the localized ground deformation between the clay and loose sand.

Figure 2-12: Photo of model SJB01 off of the centrifuge after testing with external instrumentation and wiring removed, showing the ground's cracking pattern from spreading toward the open channel (bottom of photo).

Figure 2-13: Excavation of SJB02 showing the strong localized deformation at the interface between the loose sand and overlying clay layer (paper markers highlighted in white for clarity).
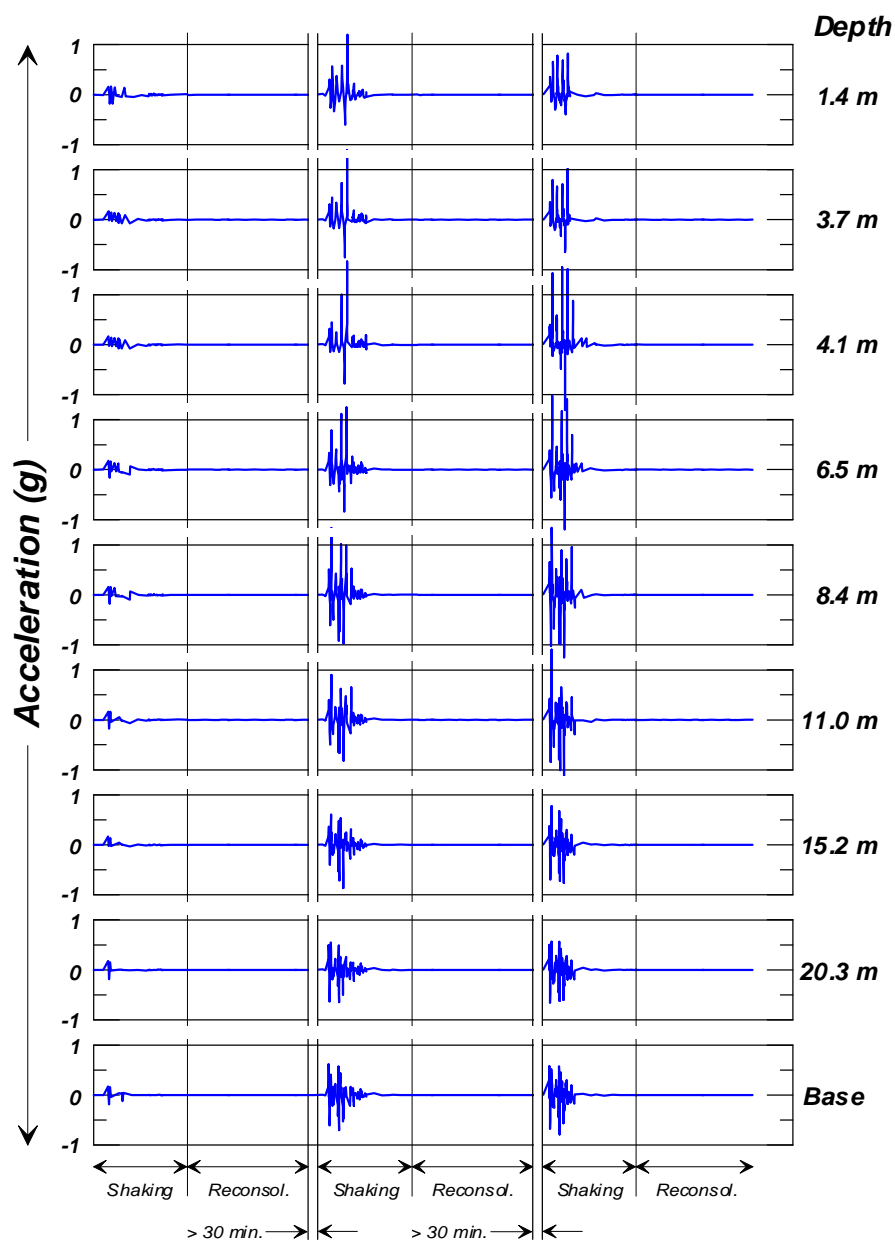
Figure 2-14: Acceleration time series for a vertical array of horizontal accelerometers in test PDS01.
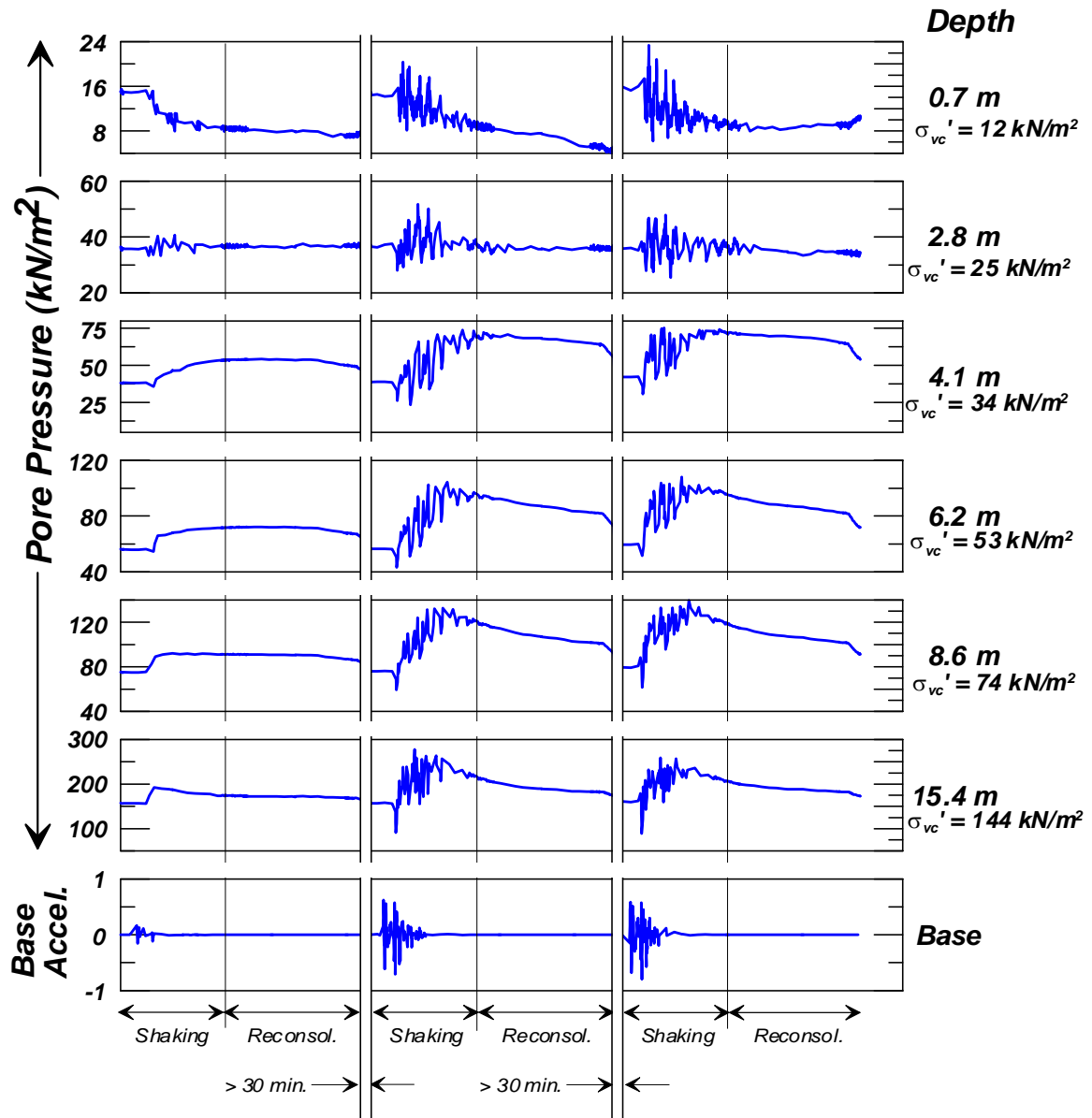
Figure 2-15: Pore pressure recordings from a vertical array of pressure transducers in test PDS01.
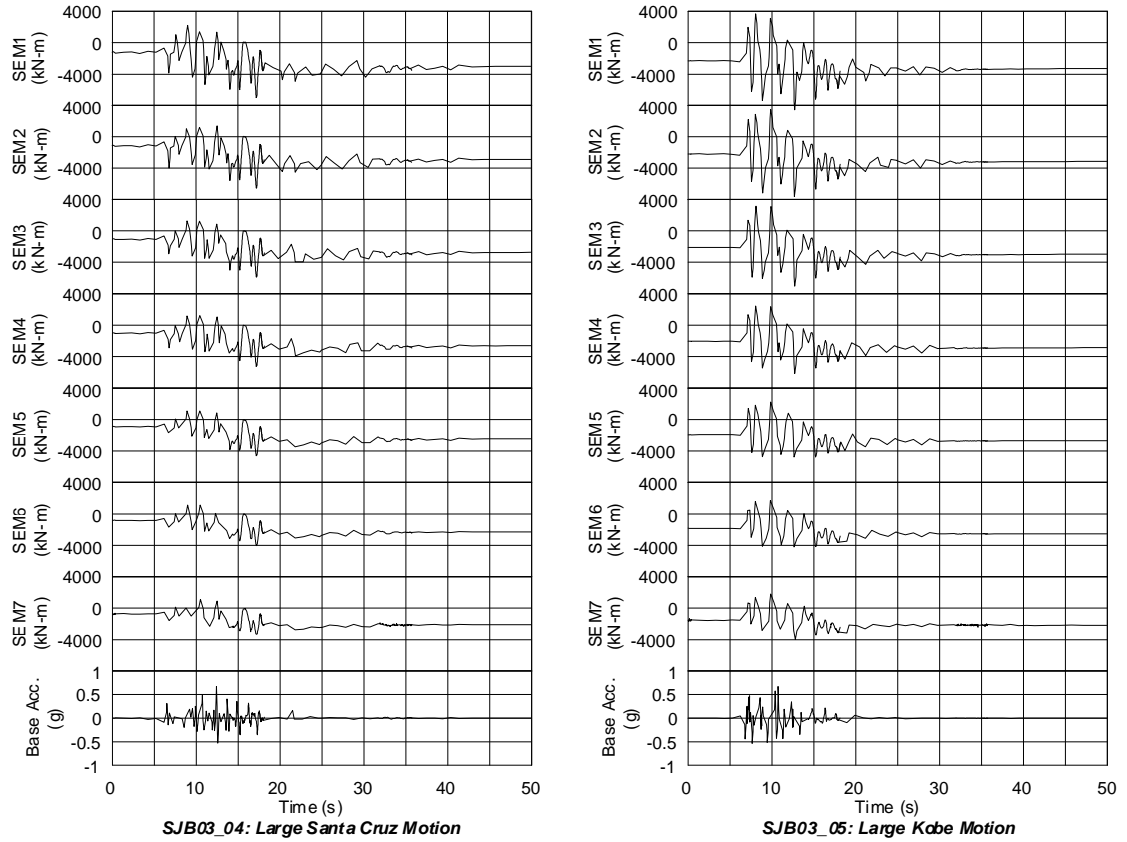
Figure 2-16: Time series from the densely instrumented pile SEM from test SJB03. SEM1 is nearest to the pile cap, where peak bending moments were measured.
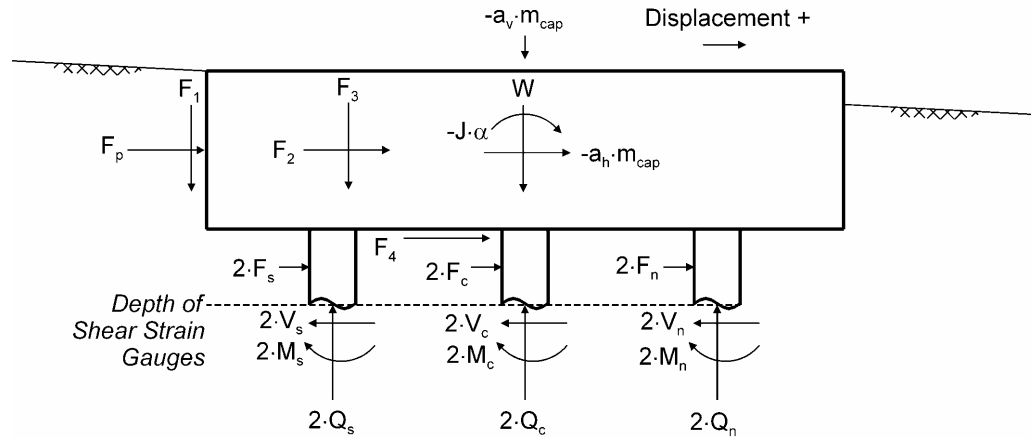
Horizontal forces	Non-horizontal forces
F_p = Passive force on upslope face of pile cap.	F_1 = Vertical friction on upslope face of pile cap.
F_2 = Horizontal friction on sides of pile cap.	F_3 = Vertical friction on sides of pile cap.
F_4 = Horizontal friction on base of pile cap.	W = Weight of pile cap.
$-a_h \cdot m_{cap}$ = Horizontal inertia of pile cap mass.	$-a_v \cdot m_{cap}$ = Vertical inertia of pile cap mass (in addition to weight).
$2 \cdot F_s$, $2 \cdot F_c$, $2 \cdot F_n$ = Lateral force on south, center and north pile segments.	$-J \cdot \alpha$ = Rotational inertia of pile cap mass.
$2 \cdot V_s$, $2 \cdot V_c$, $2 \cdot V_n$ = Shear force in south, center and north piles.	$2 \cdot M_s$, $2 \cdot M_c$, $2 \cdot M_n$ = Bending moment in south, center and north piles.
	$2 \cdot Q_s$, $2 \cdot Q_c$, $2 \cdot Q_n$ = Axial force in south, center and north piles.

Figure 2-17: Free-body diagram of pile group above Wheatstone full-bridge shear strain gauges affixed to piles.
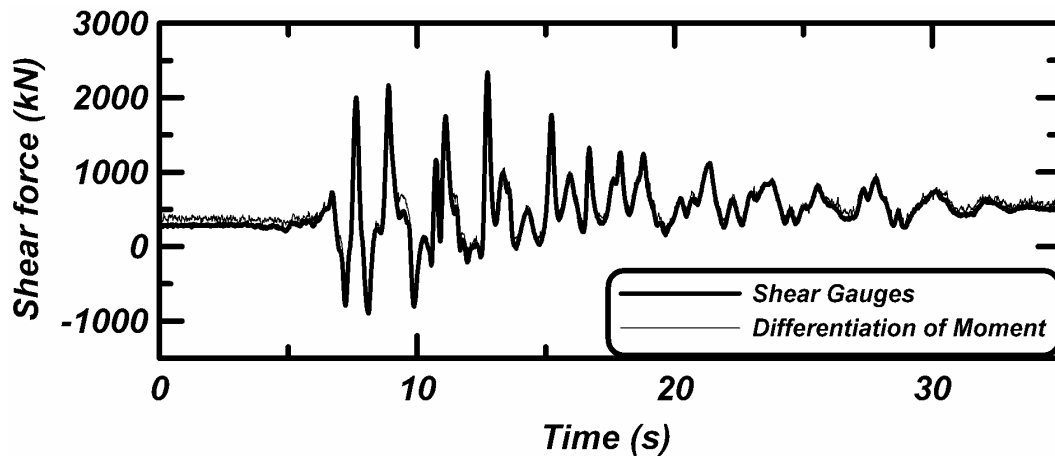
Figure 2-18: Comparison of shear time series obtained by single-differentiation of bending moments and by direct recording from a shear strain gauge bridge.
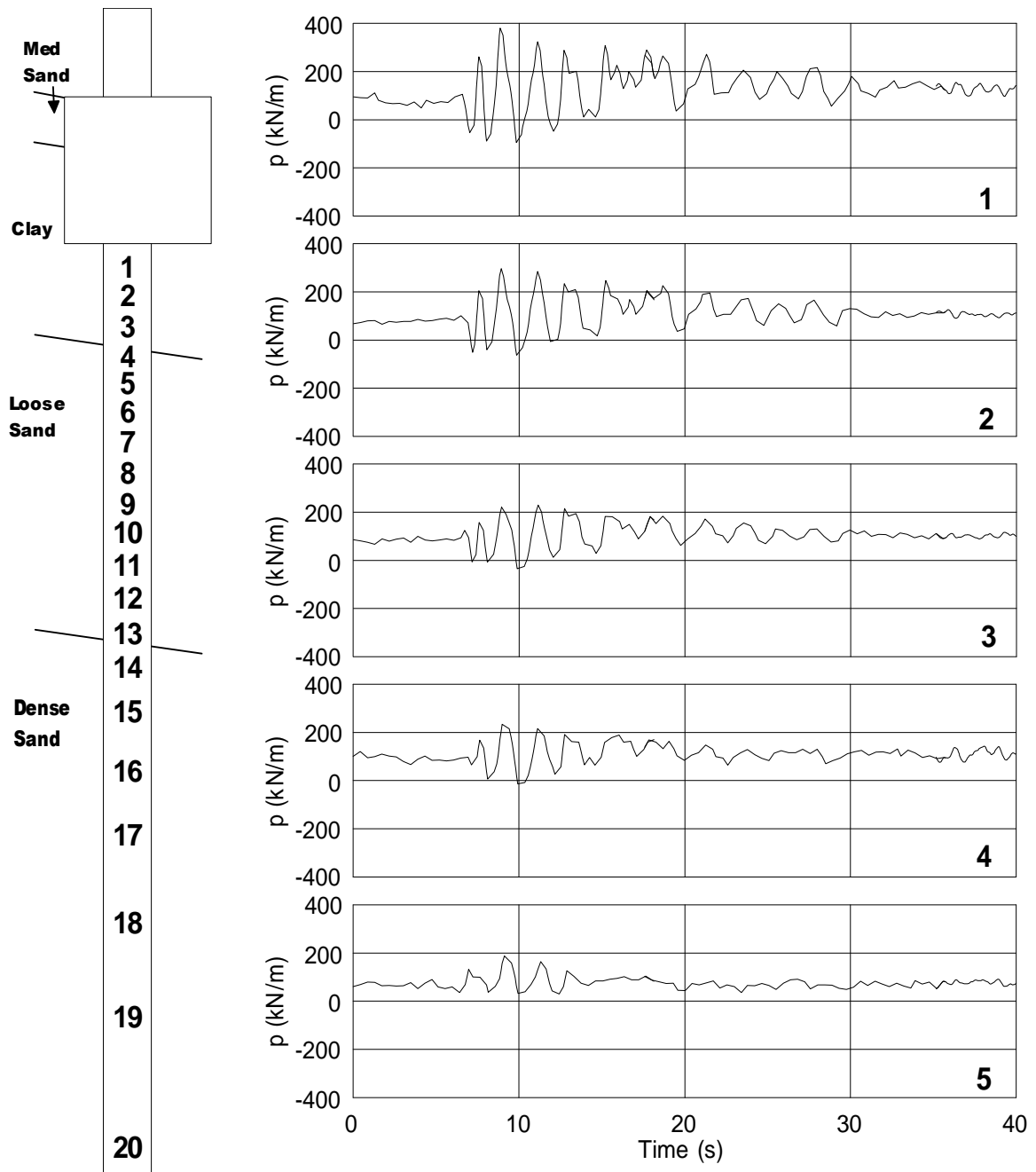
Figure 2-19: Time series of subgrade reaction, p, in the clay and the top of the loose sand obtained by double-differentiation of bending moment distributions for a large Kobe motion from test SJB03.

67
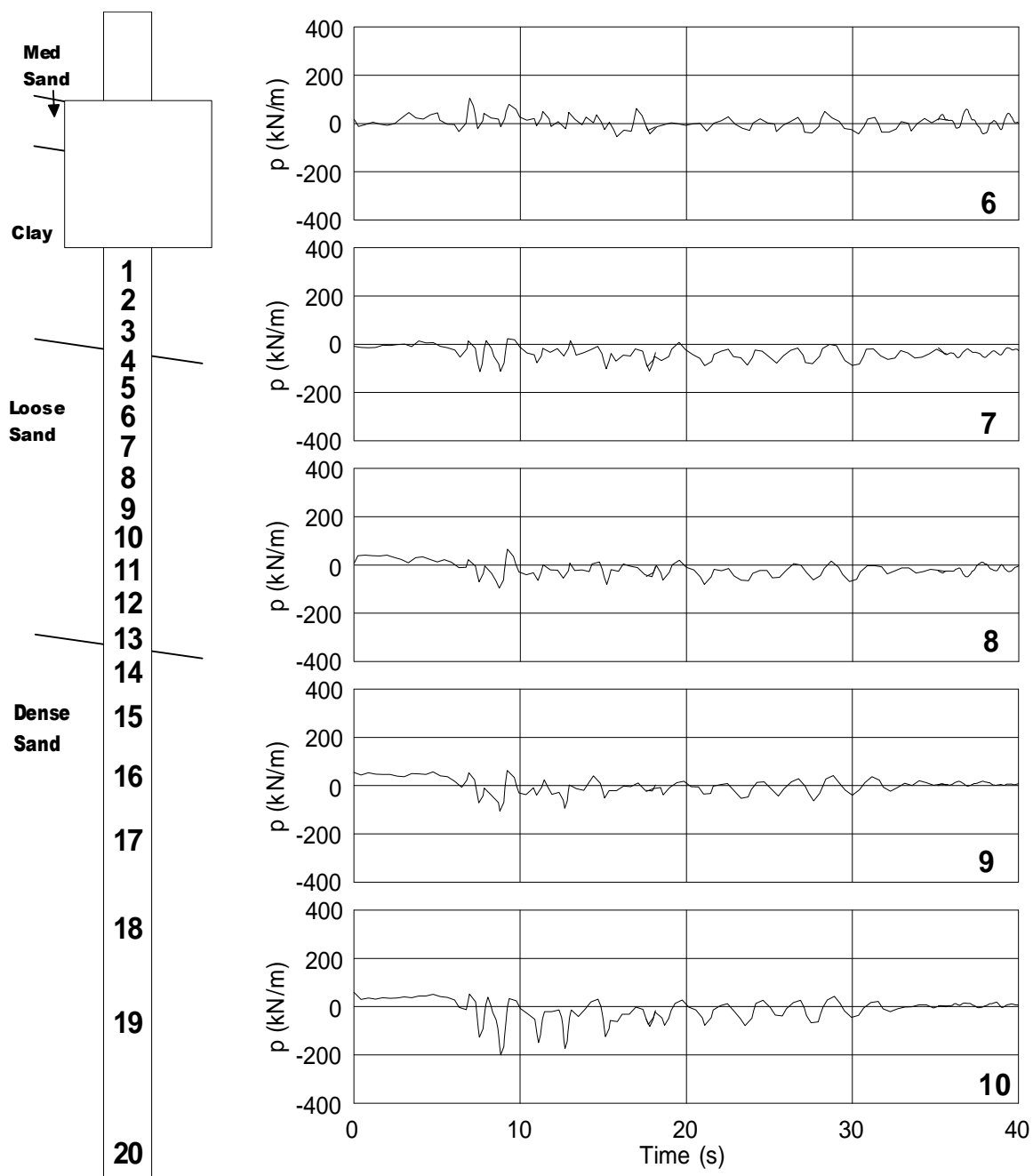
Figure 2-20: Time series of subgrade reaction, p, in the loose sand obtained by double-differentiation of bending moment distributions for a large Kobe motion from test SJB03.
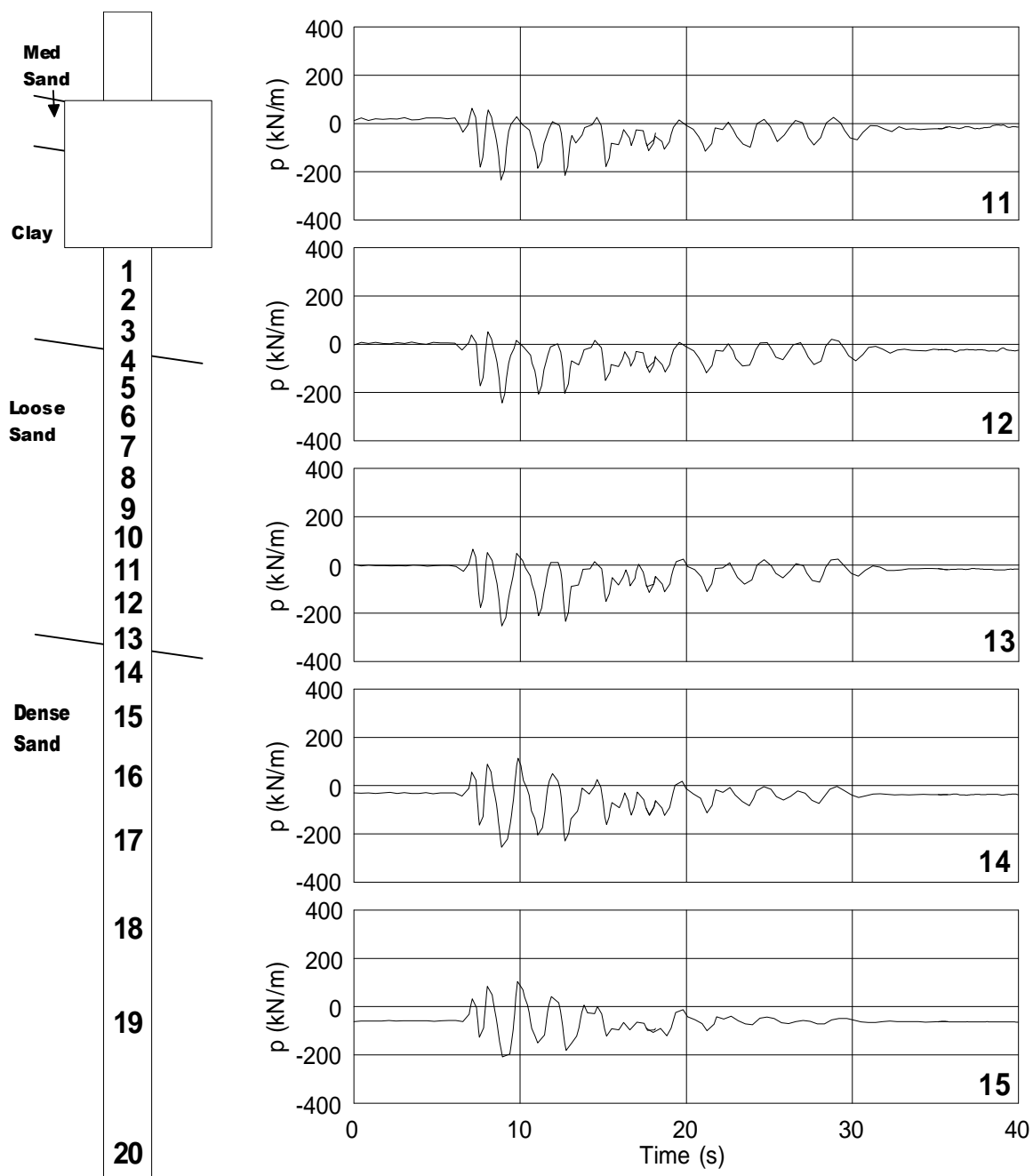
Figure 2-21: Time series of subgrade reaction, p, in the loose sand and dense sand obtained by double-differentiation of bending moment distributions for a large Kobe motion from test SJB03.
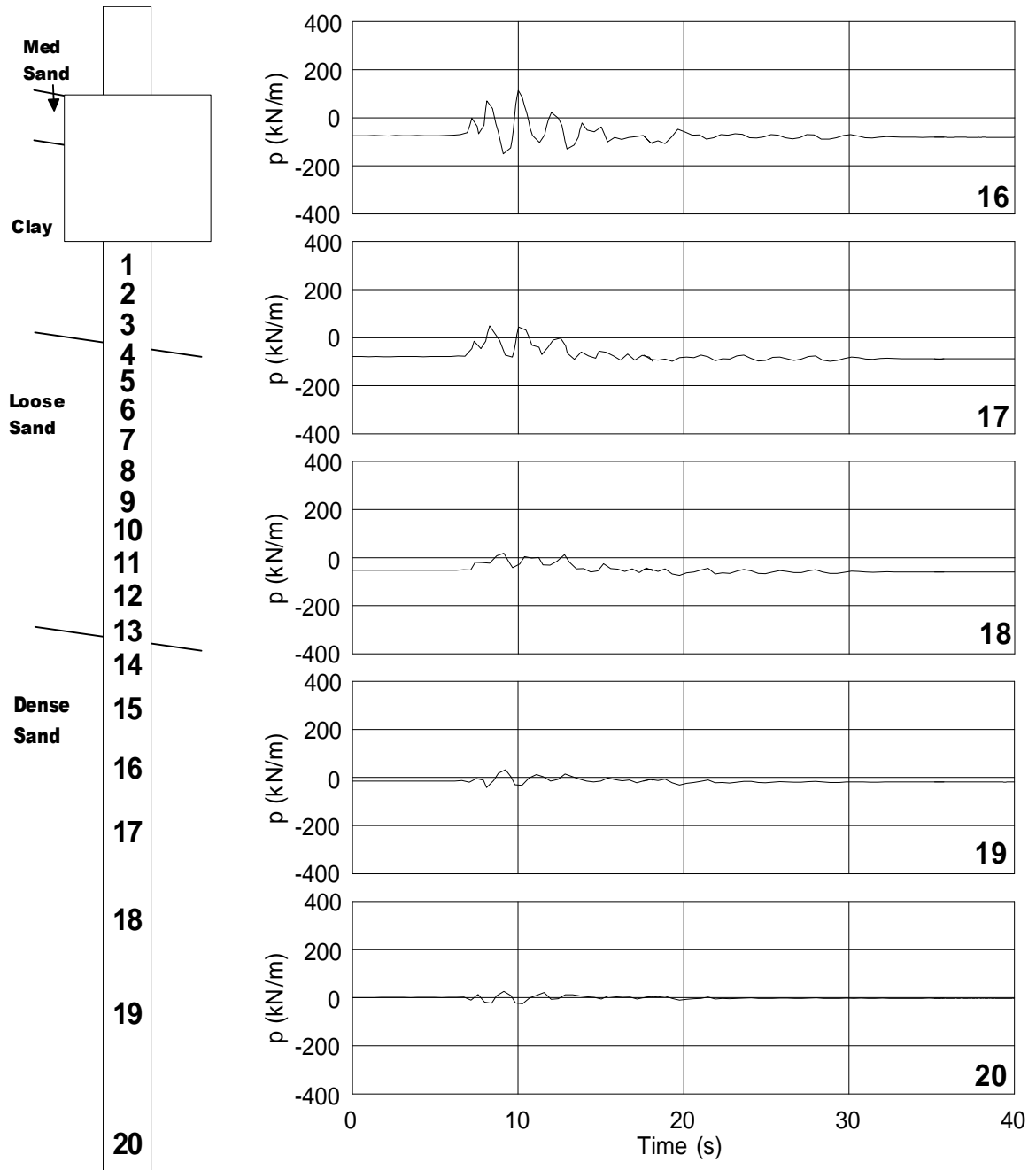
Figure 2-22: Time series of subgrade reaction, p, in the dense sand obtained by double-differentiation of bending moment distributions for a large Kobe motion from test SJB03.

CHAPTER THREE

3. OBSERVATIONS AND INTERPRETATION OF TEST DATA

This chapter presents observations from the centrifuge test data that provide insight into the load transfer behavior between pile foundations and laterally spreading ground. Some of the observations were based on raw instrument recordings, while others were the result of data processing that helps clarify certain aspects of foundation behavior. The data processing procedures were described in Chapter 2. Data for the single piles and two-pile group from test PDS01 are presented first, followed by data for the six-pile group in SJB03, then data for the six-pile groups in the other tests. Comparisons among the tests are made, including subgrade reaction loads from the liquefiable sand layer, and the phasing of the subgrade reaction loads from the liquefied sand and nonliquefiable crusts. Theoretical explanations for some of the important observations are presented, including crust load magnitude, load transfer behavior between the crusts and pile groups, and phasing and magnitude of inertia loading. These theoretical explanations serve as the basis for some of the design guidelines presented in Chapter 4.

3.1 SINGLE PILES AND TWO-PILE GROUP IN PDS01

Experiment PDS01 involved three single piles of various diameter and a two pile group with an above ground pile cap that provided fixed-head conditions (Fig. 2-2). The single piles were BP with a diameter of 1.45 m, MP with a diameter of 0.73 m, and SP with a diameter of 0.36 m. The two pile group consisted of GN on the north side and GS on the south side, both of which had 0.73-m diameters. The two pile group was oriented perpendicular to the slope, with GN being further upslope than GS.

Time series for BP during a large Kobe motion are shown in Fig. 3-1, including bending moment 9.5 meters below the ground surface (where peak bending moments were measured), subgrade reaction 2.4 meters below the ground surface (in the clay crust), subgrade reaction 6.2 meters below the ground surface (in the loose sand), excess pore pressure ratio 6.2 meters below the ground surface (in the loose sand), displacement of the crust surface and of the pile head, and the base acceleration. Sign conventions for the single pile and two-pile group were the same as those for the six-pile groups shown in the free-body diagram in Fig. 2-17. The Kobe motion was the third and final motion in a sequence, and was preceded by a small and large Kobe motion. Nearly identical peak bending moments occurred at two different times during the ground motion: once during the first cycle, before liquefaction occurred, and again later in the motion after excess pore pressures had reached their peak values. In spite of the fact that the sand had not yet liquefied for the first peak bending moment, but had liquefied for the second peak (or at least r_u values had reached their peaks), the loading mechanisms during the two cycles were very similar. At the time that the peak bending moments were measured for both critical loading cycles:

- Subgrade reaction in the crust layer was near a peak value and acted downslope.

- Subgrade reaction in the loose sand layer acted downslope, but was not at or near a peak downslope value.

- Excess pore pressure ratios were smaller than they had been immediately prior to the loading cycle. The drops in pore pressure are caused by dilatancy of the sand.

- The pile displacement and crust displacement were both at or near peak values. The pile was stiff relative to the ground profile, and the crust spread downslope around the pile, creating significant relative displacements between the crust and the pile.

Time series for GN are shown in Fig. 3-2, including bending moment at the ground surface (where peak bending moments were measured), subgrade reaction 1.9 meters below the ground surface (in the crust), subgrade reaction 6.2 meters below the ground surface (in the loose sand), excess pore pressure ratio 6.2 meters below the ground surface (in the loose sand), and displacement of the crust surface and of the pile cap. The peak bending moment was recorded during the first loading cycle prior to liquefaction of the sand, but several bending moments nearly as large as the peak were recorded later in shaking after excess pore pressures had reached substantial values. In spite of differences in the amount of excess pore pressure that had been generated by shaking during the first loading cycle (before liquefaction) and subsequent loading cycles (after excess pore pressures had been high), the loading mechanics during the loading cycles were similar. At the time that the peak bending moments were recorded:

- Subgrade reaction load in the clay crust were near a peak value, and acted downslope on the pile.

- Subgrade reaction load in the loose sand was near a peak in magnitude, but was negative, which means that the loose sand restrained downslope movement of the piles by providing an upslope resisting force.

- Excess pore pressure ratios had transiently dropped to values that were lower than existed prior to the loading cycle.

- Displacements of the clay crust and pile cap were both at or near local maxima, though the peak crust and cap displacements occurred later during the ground motion.

Time series for MP are shown in Fig. 3-3, and include bending moment at 8.6 meters below the ground surface (where the peak bending moments were measured), subgrade reaction at 2.4 meters depth (in the clay crust), subgrade reaction at 6.2 meters depth (in the loose sand), excess pore pressure ratio at 6.2 meters depth (in the loose sand), displacements of the pile head and of the crust surface, and base acceleration. The p recordings for the MP pile have some erroneous drift that was caused by drift in the bending moment gauges. The p-history in the clay starts at about +100 kN/m, which is believed to be too high, and the p-history in the loose sand starts at about -50 kN/m, which is believed to be too low. In spite of these offset errors, the transient portions of the recordings are believed to accurately represent the trends that occurred during shaking. At the time that the peak bending moment cycles occurred:

- Subgrade reaction in the clay layer was at its peak value, and acted downslope on the pile.

- Subgrade reaction in the loose sand was at its maximum magnitude, and acted upslope on the pile (i.e. the loose sand restrained downslope movement of the pile).

- Excess pore pressures had transiently dropped to values that were smaller than they had been immediately prior to the loading cycle.

- Displacements of the pile head and of the ground surface were both at local maxima.

Comparing subgrade reaction in the loose sand layer at the time that the peak bending moments were measured in the three piles, BP attracted a small downslope load, GN attracted a moderate upslope resisting load, and MP attracted a large upslope resisting load (Table 3-1). In this regard, the response of BP most closely matches the loading conditions that are expected based on commonly-used static design procedures in which the loose sand is represented as being very soft and weak, and exerting a downslope pressure on the pile. However, the response of the other two piles was different than commonly expected because they attracted upslope resisting loads from the loose sand layer during critical loading cycles. The reason for this behavior will be shown later in this chapter to be caused by the mode of displacement of the pile relative to the soil, which depends on a number of factors including crust load magnitude, pile stiffness and the deformed shape of the ground (both permanent and transient). Singh's (2002) static analyses of these three single piles (BP, GN and MP) showed that the bending moments

were most accurately predicted for BP, less accurately for GN, and yet less accurately for MP. Subgrade reaction loads in the loose sand layer were softened in his analyses, and tended to act downslope due to the large permanent free-field ground displacement profile. The accuracy of his predictions are related to how well the simplified static loading conditions matched the more complex dynamic loading conditions measured during the centrifuge tests.

Table 3-1: Summary of measurements from test PDS01 for the first large Kobe motion.

Pile Foundation	Pile Diameter (m)	Peak Incremental Soil Surface Displacement (m)[a]	Peak Incremental Pile Displacement (m)[a]	Yielding of Pile	Peak Crust Load (kN)[b]	p_l [c] (kN/m)
BP	1.45	0.99	0.29	None	550	90
GN	0.73	0.55	0.48	None	280	-60
MP	0.73	0.55	0.55	None	280	-190
SP	0.36	0.99	1.29	Extensive	n.a	n.a.

[a] Displacements continued to accumulate through the earthquake sequence. Incremental displacements are relative to the displacements existing before each earthquake event.
[b] Estimated from p recordings at the middle of the clay layer, and extrapolated to boundaries using theoretical models for variation of p with depth.
[c] Subgrade reaction mobilized in middle of liquefied sand at time of peak moment.

3.2   SIX-PILE GROUP IN SJB03

The data from SJB03 was studied in more detail than for any other test, in part because the test contained a pile that was heavily-instrumented to measure bending moments at 21

discrete locations along the pile and permitted accurate p time series by double differentiation. Many of the observations made from the data for SJB03 were similar to observations from other centrifuge tests containing the six-pile groups, and repeating data plots from every earthquake motion for every test is not necessary to support the observations and conclusions made from SJB03. Hence, time series of raw and processed data are presented in this section for each earthquake from SJB03, and discussed in detail. In subsequent sections regarding other tests with six-pile groups, time series are presented for one earthquake only, and time series from each earthquake are presented in Appendix B.

Experiment SJB03 contained a group of six piles, connected by a pile cap embedded within the nonliquefiable crust. The pile diameters were 1.17 m, and the connection between the piles and the cap was nearly rigid, with a rotational stiffness of about 1.3×10^6 kN·m/rad. SJB03 was spun to a centrifugal acceleration of 57.2 g.

Time series for test SJB03 are shown for four shaking events in Figs. 3-4 through 3-7. The bending moment 2.7 m below the ground surface was the recording from the moment bridge on the southeast pile (SEM) that was closest to the pile cap connection, where the peak moments were measured during the test. SEM was on the upslope side of the pile cap, and was therefore a leading pile with regard to crust load. The time series of p and r_u were near the middle of the loose sand layer, and r_u was in the free-field (about 13 m downslope of the pile group). The sign conventions for bending moment, crust load, pile cap inertia, subgrade reaction and displacement are shown in Fig. 2-17. The displacement of the clay crust was measured at a location to the side of the pile cap between the side face of the cap and the wall of the model container, and was influenced

by the walls of the container and the pile cap. A truly "free-field" crust displacement could not be obtained during the tests, but the crust displacement was measured at a location where these influences are believed to be small, and will be treated as "free-field" in this report.

A series of four simulated earthquake events were applied to model SJB03. The first was a small Santa Cruz motion with a peak acceleration of 0.13g. Subsequent motions were a medium Santa Cruz ($a_{max,base} = 0.35g$), a large Santa Cruz ($a_{max,base} = 0.67g$) and a large Kobe ($a_{max,base} = 0.67g$). The amount of time between shaking events was sufficient to allow full dissipation of excess pore pressures in the model prior to the next shaking event. Observations will be presented for each shaking event in chronological order.

The small Santa Cruz motion exhibited a peak base acceleration, $a_{max,base} = 0.13g$, and produced peak r_u values of about 0.4. Soil deformation, excess pore pressure ratio, pile cap displacement and bending moments were all relatively small during the small Santa Cruz motion compared with the larger motions that followed. Selected time series from the small Santa Cruz motion are shown in Fig. 3-4.

The medium Santa Cruz motion exhibited a peak base acceleration, $a_{max,base} = 0.35g$, and produced a peak r_u value of about 0.7. Selected time series from the medium Santa Cruz motion are shown in Fig. 3-5. At the time that the peak bending moment occurred in the piles during the medium Santa Cruz motion:

- The peak lateral load from the clay crust occurred.
- The subgrade reaction was near a local minimum, and the loose sand restrained downslope movement of the piles.
- The excess pore pressure ratio was near a local minimum due to dilatancy.

The transient drops in pore pressure in the loose sand during shaking are a commonly observed behavior that arises from the dilatancy of the sand during portions of the applied cyclic loading. Dilatancy will be defined as the tendency of sand to dilate during drained shear loading, which is manifested as an increase in effective stress during undrained shear loading. As cyclic loading is producing a net progressive increase in excess pore pressure, a sand can cyclically transition between incrementally contractive and incrementally dilative behavior, with the transition from contractive to dilative behavior often called phase transformation. This cyclic transitioning in behavior is why r_u =100% only develops when sand is under an isotropic state of stress, with r_u subsequently dropping below 100% as shear stresses are applied. The result is the inverted s-shaped stress-strain behavior commonly observed in cyclic undrained loading of sand, which has also been called cyclic mobility.

The displacement of the clay crust was about 0.35 m at the end of shaking, while the displacement of the pile cap was only about 0.03 m. The relative displacement of 0.32 m is about 16% of the pile cap height, and would generally be considered sufficient to mobilize the passive resistance of the clay crust against the upslope face of the pile cap based on static loading concepts. However, the peak crust load for the medium Santa Cruz motion was 4403 kN, which is only about 2/3 of the peak load observed during the subsequent large shakes. The relation between crust load and relative displacement between the pile cap and free-field crust is different during lateral spreading than during static loading, as addressed in a later section.

The large Santa Cruz motion had a peak base acceleration, $a_{max,base} = 0.67g$ and r_u values in the loose sand layer reached 1.0. Selected time series from the large Santa Cruz motion are shown in Fig. 3-6. At the time that the peak bending moment occurred in the piles during the large Santa Cruz motion:

- The peak lateral load from the clay crust was 6696 kN, which was the maximum for the test.

- The subgrade reaction in the loose sand was near a local minimum, and the loose sand restrained downslope movement of the piles.

- The excess pore pressure ratio was near a local minimum due to dilatancy.

- The displacement of the clay crust was 1.2 m, which was less than the residual crust displacement of 1.8 m after strong shaking.

- The relative displacement between the crust and the pile cap was 1.6 m after shaking, which was large enough to mobilize passive resistance on the upslope face of the pile cap.

In spite of the fact that the loose sand liquefied ($r_u = 1.0$) during the large Santa Cruz motion, and did not liquefy during the medium Santa Cruz motion ($r_u < 1.0$), the behavior observed during the two motions has many similarities. For example, the loose sand layer provided a relatively large upslope resisting force to the piles during the critical cycle that produced the peak bending moment for each event.

The large Kobe motion had a peak base acceleration, $a_{max,base} = 0.67g$ and r_u values in the loose sand layer reached 1.0. Selected time series from the large Kobe motion are

shown in Fig. 3-7. At the time that the peak bending moment was measured during the large Kobe motion (8838 kN·m), the following also occurred:

- The lateral load from the clay crust was 6327 kN, which was the maximum for the large Kobe motion.

- The pile cap inertia force was 5295 kN, which was the maximum for the test.

- The subgrade reaction, p, 6.7 m below the ground surface was –389 kN/m, which was a local minimum. Note that the subgrade reaction was negative; the loose sand restrained the pile from moving downslope.

- The excess pore pressure ratio was 0.54, near a local minimum, in spite of having been close to 1.0 earlier in the shake.

- The displacement of the pile cap was 0.35 m, and was approaching a local maximum.

- The displacement of the clay crust was 2.3 m, which was less than the permanent crust displacement of nearly 3.5 m.

- The relative displacement between the crust and the pile cap was 3.2 m by the end of the large Kobe motion, which was sufficient to develop passive pressure against the upslope face of the pile cap.

The peak base acceleration was the same for the large Santa Cruz motion as for the large Kobe motion. However, the different shaking characteristics resulted in some differences in the pile group response. The pile cap inertia force was 2560 kN at the time of peak bending moment during the large Santa Cruz motion, which only about 50% of the cap inertia during the critical cycle from the Kobe motion. The peak bending moment

during the large Santa Cruz motion was 7082 kN·m, which is only 80% of the peak moment from the Kobe motion. The total shear force exerted on the piles was larger for the Kobe motion than for the Santa Cruz motion due to the larger pile cap inertia force, hence larger bending moments were induced during the Kobe motion. The dips in r_u due to dilatancy were not as large, and the loads imposed on the piles by the loose sand were not as large during the large Santa Cruz motion as during the Kobe motion. Key quantities measured at the time of peak bending moment are in Table 3-2 for each shake for test SJB03.

Table 3-2: Summary of important quantities recorded at the time of the peak measured bending moment for each base motion for test SJB03

Motion	Bending Moment (kN·m)[a]	Crust Load (kN)	Pile Cap Inertia (kN)	p at 6.7 m depth (kN/m)[b]	r_u at 6.7 m depth[b]	Pile Cap Displacement (m)	Crust Displacement (m)[c]
Small Santa Cruz	-1550	1560	1570	-50	0.2	0.04	0.1
Medium Santa Cruz	-3070	2870	1400	-150	0.5	0.08	0.2
Large Santa Cruz	-7080	6380	2560	-310	0.7	0.3	1.3
Large Kobe	-8840	5730	5790	-370	0.5	0.5	2.3

[a] Bending moments were measured near the connection between the pile and the pile cap.
[b] Depth = 6.7 meters is near the center of the loose sand layer. r_u values correspond to the transient dips at this instance in time, and were generally much greater immediately before and after.
[c] Crust displacement was measured at a location to the side of the pile cap.

Given that the peak base acceleration amplitudes for the large Santa Cruz and large Kobe motions were the same, the differences in the responses indicate that the frequency content of the base motion significantly influences the behavior of the pile groups.

Hence, reproducing realistic earthquake shaking with a wide range of frequency content is a critical for relating observations from model studies to design practice.

The loading mechanisms observed during testing are further illustrated by the snapshots of soil displacement, pile displacement, bending moment, p, and r_u shown in Fig. 3-8 for the Kobe motion at the time of peak bending moment and at the time of peak pile cap displacement. At the time of peak bending moment, r_u values were low across nearly the entire depth of the loose sand layer in spite of high values earlier and later in the shake. Some of the peaks in r_u reported in Fig. 3-8 are larger than 1.0, which may be due to transducer movements or changes in total stress caused, for example, by transient stress waves or the movement of the clay crust layer. The r_u values were highest near the interface between the clay and the sand, likely due to pore water becoming trapped beneath the low-permeability crust layer. The trapping of pore water beneath the clay can cause the loose sand layer to become looser in a zone near the top of the loose sand due to void redistribution (Kulasingam et al. 2004), thereby enabling the clay crust to slide on top of the loose sand. The resulting large displacement discontinuity allowed development of passive pressure of the crust against the pile cap with relatively small soil displacement in the loose sand layer. The temporarily stiffened loose sand layer resisted nearly the entire lateral crust load (as illustrated by the moment and p profiles in Fig. 3-8), with only small loads mobilized against the portion of the piles in the dense sand.

Phasing of crust load, bending moment, cap displacement and r_u with p near the center of the loose sand layer can be more closely examined in the cross-plots in Fig. 3-9. The peak shear loads and peak magnitude bending moments are mobilized when p in the loose sand is small (i.e. a large magnitude, negative sign, upslope restraining force).

Furthermore, crust load and bending moment are fairly well correlated with p in the loose sand layer, which indicates that the responses are coupled together. Every time that p in the loose sand layer drops to a small value, crust loads become large and bending moment magnitudes become large as well. Positive values of p are associated with unloading cycles in which crust load is negative (acts upslope) and bending moments are positive. The coupling of crust load and subgrade reaction in the loose sand layer is facilitated by the displacement discontinuity that occurs at the interface between the crust and underlying liquefiable sand because the soil serves as a discontinuous shear beam. It is not clear how the coupling would change if the discontinuity did not occur.

Cap displacement is not as well correlated with p in the loose sand layer, but one interesting trend is that the peak cap displacements occur during unloading cycles in p in the loose sand. As p in the loose sand layer drops, cap displacement increases to near its peak, then as p begins to approach zero during unloading, cap displacement continues to increase until it reaches its peak. The unloading of p is the result of increasing r_u, which is also shown in the cross plots. The plot of r_u versus p is similar to a q-p' plot, in which p (subgrade reaction) is analogous to q and r_u is inversely related to p' (mean effective stress), with $r_u = 1$ corresponding to p' = 0. The minimum p-values are always associated with small r_u values, and the p-values decrease as r_u returns to 1. The unloading cycle is associated with a softening of the force-displacement stiffness of the pile foundation. Hence, the peak crust loads and bending moments were observed during a time when the stiffness of the pile group was large due to the dilation of the loose sand layer and associated large resisting forces provided by the dilatant sand. In contrast, the peak pile cap displacements were not associated with the peak loads from the crust layer, but rather

with slightly smaller loads from the crust layer being imposed at a time when the force-displacement response of the pile foundation was smaller because the loose sand layer had unloaded to a higher r_u value.

3.3   SIX-PILE GROUPS IN OTHER TESTS

3.3.1   PDS03

Experiment PDS03 contained a single group of six 0.73-m diameter piles connected by a pile cap embedded within the clay layer. As before, the soil profile consisted of a nonliquefiable crust overlying a liquefiable layer of loose Nevada sand overlying nonliquefiable dense Nevada sand. The nonliquefiable crust and liquefiable layers sloped gently toward an open channel at the downslope end of the models. Time series are shown for the large Kobe event for test PDS03 in Fig. 3-10, and are comparable to the time series that were presented for test SJB03. The large Kobe motion was preceded by one small, one medium and one large Santa Cruz motion.

Many observations from the large Kobe earthquake for PDS03 were similar to observations from SJB03. The peak bending moment for the pile occurred in the moment gauge closest to the pile cap connection at about $t \approx 13$ s. This peak bending moment coincided with:

- The peak lateral load from the clay crust, which acted downslope (positive);

- A local peak in the |p| for the loose sand, which acted upslope (negative p).

- The r_u in the loose sand transiently dipped to a local minimum less than 30%, despite having been up to 100% immediately beforehand;

Ground displacements reached their maximum value of about 3.5 m near the end of shaking, with peak r_u values of about 100% in the loose sand. The pile cap displacement increased to about 0.6 m by the end of shaking, so the ground surface moved about 2.9 m relative to the pile cap. The peak lateral load from the clay crust was about 3600 kN, which was the peak value measured for the test (i.e. for all four shakes).

3.3.2   SJB01

Experiment SJB01 contained a single group of six 0.73-m diameter piles connected by a pile cap embedded within the clay layer. As before, the soil profile consisted of a nonliquefiable crust overlying a liquefiable layer of loose Nevada sand overlying nonliquefiable dense Nevada sand. The nonliquefiable crust and liquefiable layers sloped gently toward an open channel at the downslope end of the models. Time series are shown for the second large Kobe event for test SJB01 in Fig. 3-11, and are comparable to the time series that were presented for test SJB03. The second large Kobe motion was preceded by one small, one medium and one large Santa Cruz motion and one large Kobe motion.

Many of the trends observed during the second large Kobe motion for SJB01 were similar to the trends observed during motions from the other tests, as previously discussed. The peak bending moment for the pile occurred at the moment gauge closest to the pile cap connection at about $t \approx 7$ s. This peak bending moment coincided with:

- The peak lateral load from the clay crust, which acted downslope (positive);

- A local peak in the |p| for the loose sand, which acted upslope (negative p).

- The r_u in the loose sand transiently dipped to a negative value less than -30%, despite having been up to 100% immediately beforehand;

Ground displacements reached their maximum value of about 2.0 m near the end of shaking, with peak r_u values of about 100% in the loose sand. The pile cap displacement increased to almost 0.8 m by the end of shaking, so the ground surface moved about 1.2 m relative to the pile cap. The peak lateral load from the clay crust was about 5500 kN, which was the peak value measured for the test (i.e. for all five shakes), and was larger than the value recorded during PDS03 because the undrained shear strength of the crust was higher (s_u = 44 kPa compared with 22 kPa).

One important difference between SJB03 and SJB01 was that the pile cap inertia force acted in phase with the downslope crust loads for SJB03, but was not in phase with the downslope crust loading from SJB01. The nature of this phasing is not yet clearly understood, but a primary factor is believed to be that the smaller diameter piles in SJB01 caused that pile foundation to be laterally more flexible than the pile group in SJB03 with the larger piles. Phasing between crust loads and inertia loads is discussed in more detail in a later section.

3.3.3   DDC01

Time series are shown in Fig. 3-12 for model DDC01 during a large Kobe motion, and the focus of the time series is to show the phasing of crust loads with inertia loads.

Together, the time series for the earthquakes showed attributes that are similar to the attributes from the other tests with the stiffer pile group (SJB03 and DDC02). Those attributes are:

- The critical cycle that produced the peak total shear on the pile foundation always occurred during shaking and coincided with transient reductions in r_u in the liquefiable sand.

- The inertia and crust loads were simultaneously at, or near, their respective peak values at the critical loading cycle (at the time of maximum shear).

- The cap inertia and crust loads were acting in-phase at the critical loading cycles.

- The relative displacement between cap and crust kept increasing after shaking, but the crust load was still smaller than its peak value during shaking.

Note that the arrows pointing to the peaks of the various quantities occur at different times. Pile cap inertia acted in-phase with the crust loads, but superstructure inertia forces were not as in-phase with peak superstructure accelerations following shortly after peak pile cap accelerations and crust loads.

3.3.4 DDC02

Time series are shown in Fig. 3-13 for model DDC02 during a large Kobe motion, and are similar to the time series shown for DDC01. Together, the time series for the earthquakes showed attributes that are similar to the attributes from the other tests with the stiffer pile group (SJB03 and DDC01). Those attributes are:

- The critical cycle that produced the peak total shear on the pile foundation always occurred during shaking and coincided with transient reductions in r_u in the liquefiable sand.

- The pile cap inertia, superstructure inertia, and crust loads were simultaneously at, or near, their respective peak values at the critical loading cycle (at the time of peak bending moments in the piles).

- The relative displacement between cap and crust kept increasing after shaking, but the crust load was still smaller than its peak value during shaking.

3.4 SUBGRADE REACTION BEHAVIOR IN LIQUEFIED SAND

This section explains the differences in subgrade reaction loads that were observed at the time that the peak bending moments were recorded during the centrifuge tests. Fig. 3-14 shows p recorded in the loose sand layer for piles BP, GN and MP from PDS01 and pile SEM from SJB03, all during a large Kobe motion. At the time that the peak bending moments were recorded in each pile, BP attracted a downslope load in the loose sand layer, GN attracted an upslope resisting load, MP attracted a larger upslope resisting load, and SEM attracted the largest upslope resisting load. The magnitude and direction of subgrade reaction loading is related to the mode of displacement of the pile relative to the soil, with downslope loads being attracted by piles that displaced less than the sand layer, and upslope resisting loads being attracted by piles that displaced more than the sand layer. Pile BP had a large diameter and was stiff relative to the other single piles in test PDS01. Hence, the loads applied by the nonliquefied crust layer were small relative to the stiffness of the pile, and the displacement of the pile in the loose sand layer was

less than that of the loose sand. Regarding the other two single piles, GN was stiffer than MP because some of the lateral loading was resisted through frame action of the pile group. The loads applied by the nonliquefied crust induced pile displacements in the loose sand layer for GN that were larger than the displacement of the loose sand, but that were not as large as the displacements of the MP pile relative to the free-field loose sand layer. Hence, both piles attracted upslope resisting loads from the liquefiable sand layer, and GN attracted a smaller upslope load than MP.

The six-pile group from SJB03 consisted of fairly stiff piles, but the but the piles in SJB03 attracted much larger upslope resisting loads from the liquefiable sand layer than the piles in PDS01. The primary reason for the large upslope resisting loads in the liquefied sand were the large downslope driving loads attracted by the embedded pile cap. Additionally, compared with PDS01, the strains in the loose sand layer were small in SJB03. Hence, although the stiffness of the piles in SJB03 were larger than MP and GN in PDS01, the large loads attracted by the embedded pile cap caused the piles to displace considerably further downslope through the liquefiable sand. The upslope resisting force is essentially reacting against the downslope driving force from the nonliquefied crust and the imposed inertia loading. Hence, the magnitude of resisting subgrade reaction loads in the loose sand layer are limited to the magnitude of total loading exerted on the pile group. For example the peak total load (crust load and inertia) exerted on the six-pile group in SJB03 at the time of peak bending moment was about 11600 kN. The peak p-value in the loose sand layer was about -400 kN/m, the thickness of the liquefiable sand layer was about 4.5 m, and there were six piles. Hence, the total resisting load from the liquefiable sand layer can be roughly estimated as (-400

kN/m)·(4.5 m)·(6) = -10800 kN, which is reasonably close to the peak total load. This observation is congruous with the observation in Fig. 3-8 that the subgrade reaction loads in the loose sand layer provided the bulk of the resistance, with only negligible loads being mobilized in the dense sand.

The mechanisms of loading observed in the centrifuge tests can be clarified by considering the schematic of a pile and soil shown in Fig. 3-15. Three different loading scenarios are considered in the figure. Case A is characterized by a pile that is stiff relative to the clay crust and the loose sand layer, similar to BP from PDS01. The pile displacement is smaller than the free-field displacement of the crust and of the loose sand, hence the pile attracts downslope loading from both layers. Case B is characterized by a pile that is stiff enough to resist the full downslope loading imposed by the nonliquefied crust, but not stiff enough to exhibit smaller displacements than the free-field liquefiable sand, similar to piles GN, MP and SEM. The pile displacement is smaller than the crust displacement and attracts downslope loading along its length in the crust, but pile displacement is larger than the liquefiable sand displacement and attracts upslope loading along its length within the liquefiable sand. Case C is characterized by a pile that is too flexible and/or weak to mobilize the full downslope crust load, and is similar to the 0.36-m diameter pile SP from PDS01. Case C is also similar to piles tested by Abdoun et al. (2003), and subsequently analyzed by Dobry et al. (2003). The pile is too flexible to mobilize the full downslope loading of the nonliquefied crust layer, and as a result the crust provides a gripping action on the pile characterized by a depth of transition where the pile displacement and free-field soil displacement are equal [called z_{ps} by Dobry et al. (2003)]. Above the transition depth the crust exerts an upslope

loading on the pile and below the transition depth the crust exerts a downslope loading on the pile. The pile head displacement is larger than the ground surface displacement in such cases, and the pile behavior is essentially controlled by the free-field ground displacement profile.

Differences in Cases A, B, and C in Fig. 3-15 can help explain some of the negligible subgrade reaction loads were observed in the liquefied sand in tests by Abdoun et al. (2003) in which a nonliquefiable crust spread downslope on top of a liquefiable layer. Their crust layer was perforated to prevent the displacement discontinuity caused by void redistribution at layers with permeability contrasts, hence their displacement profile was continuous. Furthermore, their pile was very flexible since it was designed to replicate the hollow concrete piles that supported the Niigata Family Courthouse Building. The flexible piles closely followed the displacement profile within the liquefiable sand layer, and significant relative displacements between the piles and free-field soil profile were never mobilized. As a result, negligible lateral loads were observed in the liquefiable sand. The negligible lateral loads do not imply that the liquefiable sand had no strength as it flowed past the pile, but rather reflect the fact that the pile was too flexible to resist the displacement demands imposed by the ground. A stiffer pile that was able to resist the displacement demands imposed by the free-field soil would likely have attracted some loading from the liquefiable layer because it would have mobilized some displacement relative to the free-field soil profile.

3.5 PILE CAP LOADING THEORIES

This section describes the theories that were used to estimate the various contributions to the loading imposed on the pile groups by the laterally spreading crust (i.e. passive pressures on the upslope face of the caps, friction between the caps and the crusts, and loads on the pile segments in the crust beneath the caps). The contributions of lateral loading were not measured independently of each other, so assessing the accuracy of the estimates of each component is not possible. In light of this limitation, commonly-accepted theories were used to estimate the load components and subsequent comparisons with measured test data provide some guidance regarding the fractional contributions of the various force components.

3.5.1 Passive earth pressure on upslope face of pile cap

A Coulomb-based passive earth pressure theory was used to calculate the passive loading exerted on the upslope face of the pile cap. The Coulomb method is limited to application in uniform soil deposits, but the crusts in the centrifuge tests often contained a layered profile consisting of sand over clay. Hence, the Coulomb method was modified to account for layering, as shown in Fig. 3-16. Furthermore, the inertia of the failure wedge was included in the calculation using the method first proposed by Okabe (1926) and Mononobe and Matsuo (1929) for cohesionless soils. For the sand layer, the passive force, $F_{p,sand}$, and the force on the failure wedge, R, were assumed to be the same as for a pile cap with height H_1 in a uniform sand layer:

$$F_{p,sand}(\theta) = \frac{\gamma_{sand} \cdot H_{sand}^{2}}{2} \cdot \frac{\cos(\beta) \cdot \cos(\theta) \cdot [\sin(\theta + \phi) + k_{h} \cdot \cos(\theta + \phi)]}{\sin(\theta - \beta) \cdot \cos(\theta + \phi + \delta)} \qquad (3\text{-}1)$$

$$R(\theta) = \frac{\gamma_{sand} \cdot H_{sand}^{2}}{2} \cdot \frac{\cos(\beta) \cdot \cos(\theta) \cdot [\cos(\delta) + k_{h} \cdot \sin(\delta)]}{\sin(\theta - \beta) \cdot \cos(\theta + \phi + \delta)} \qquad (3\text{-}2)$$

where γ_{sand} = unit weight of sand layer,

           H_{sand} = thickness of sand layer in contact with pile cap,

           θ = angle of inclination of failure surface,

           ϕ = friction angle of sand material,

           β = angle of inclination of backfill,

           δ = angle of interface friction between pile cap and sand material.

           k_{h} = horizontal inertia coefficient (equal to horizontal acceleration in g)

The passive force in the clay layer was then calculated by force equilibrium:

$$F_{p,clay} = N(\theta) \cdot \sin(\theta) + T(\theta) \cdot \cos(\theta) + R(\theta) \cdot \sin(\theta + \phi) + k_{h} \cdot W(\theta) - F_{p,sand}(\theta) \cdot \cos(\delta) \qquad (3\text{-}3)$$

$$W(\theta) = \left[\frac{\gamma_{sand} \cdot \left(H_{sand}^{2} + 2 \cdot H_{sand} \cdot H_{clay} \right)}{2} + \frac{\gamma_{clay} \cdot H_{clay}^{2}}{2} \right] \cdot \left[\frac{\cos(\theta) \cdot \cos(\beta)}{\sin(\theta - \beta)} \right] \qquad (3\text{-}4)$$

$$F_{f,clay} = \alpha \cdot s_{u} \cdot H_{clay} \qquad (3\text{-}5)$$

$$T(\theta) = s_u \cdot H_{clay} \cdot \frac{\cos(\beta)}{\sin(\theta - \beta)}$$

(3-6)

$$N(\theta) = \frac{W(\theta)}{\cos(\theta)} + \frac{F_{f,clay}}{\cos(\theta)} + T(\theta) \cdot \frac{\sin(\theta)}{\cos(\theta)} - R(\theta) \cdot \frac{\cos(\theta + \phi)}{\cos(\theta)} + F_{p,sand}(\theta) \cdot \frac{\sin(\delta)}{\cos(\theta)}$$

(3-7)

where γ_{clay} = unit weight of clay layer

                  H_{clay} = thickness of clay layer in contact with pile cap

                  s_u = undrained shear strength of clay

                  α = adhesion coefficient between clay and pile cap

Finally, the total lateral earth pressure was calculated as the sum of the horizontal components from the sand and from the clay.

$$F_p(\theta) = F_{p,sand}(\theta) \cdot \cos(\delta) + F_{p,clay}(\theta)$$

(3-8)

Eqs. 3-1 to 3-8 are all functions of the failure angle, θ, and the solution is associated with the θ that results in the minimum F_p. For uniform soil deposits, closed-form solutions can be constructed for the θ that produces the minimum F_p, and tables of values can be found in many foundation engineering textbooks. However, such closed-form solutions are not available for pile caps in layered soil profiles. Hence, calculating passive force using Eqs. 3-1 to 3-8 requires iteration to obtain the θ that produces the minimum F_p. Planar failure surfaces, as assumed in Coulomb earth pressure analyses, can be very inaccurate for granular soils in which the failure surface more is more closely

approximated using a log-spiral method. For the layered profile in Fig. 3-16, the influence of curvature of the failure surface within the sand layer is believed to be small since the sand layer is at the top of the profile, where the failure mechanism is nearly linear.

An additional correction can be applied to account for three-dimensional effects of the finite-width pile cap on the passive pressures on the upslope face. Three-dimensional corrections are larger for sandy soil than for clays, and corrections for cohesionless soils were presented by Mokwa and Duncan (2000). In their study, three-dimensional effects in cohesive soils were not explicit functions of the shape of the pile cap, but were rather intrinsically included in an empirical equation based on field test data. Three-dimensional effects were not included in the calculation of passive forces for the pile caps in the centrifuge tests in this study because they are believed to be small since the crusts were composed primarily of clay and because the pile caps had a large width compared with their height. Uncertainty in the undrained shear strength of the crust during shaking (due to load rate), areas of contact between the pile caps and spreading crusts, and computing passive resistance in layered soil systems, are believed to overshadow three-dimensional effects caused by the finite width of the pile caps.

3.5.2   *Horizontal friction between pile cap and crust*

The horizontal friction forces between the Monterey sand and the sides of the pile cap ($F_{2,sand}$) were estimated as:

$$F_{2,sand} = \tfrac{1}{2} \cdot \gamma_1 \cdot K_o \cdot H_1 \cdot \tan(\delta) \cdot A_{sides1} \tag{3-9}$$

where: K_o, the coefficient of earth pressure at rest, was taken as $1-\sin(\phi')$, and A_{sides1} is the contact area between the Monterey sand and the pile cap.

The horizontal friction forces between the sides of the pile caps and the clay portion of the crusts ($F_{2,clay}$) were estimated using an α-method, in which α was estimated based on undrained shear strength [as in e.g. Terzaghi et al. (1996)], and the friction force was estimated as:

$$F_{2,clay} = \alpha \cdot s_u \cdot A_{sides2} \tag{3-10}$$

where: A_{sides2} is the contact area between the sides of the pile cap and the clay.

Horizontal friction between the base of the pile cap and the clay (F_4) was calculated using the equation:

$$F_4 = \alpha \cdot s_u \cdot R_{base} \cdot A_{base} \tag{3-11}$$

where: A_{base} is the area of the base of the pile cap minus the area of the piles, and R_{base} is the base reduction coefficient. R_{base} is an empirical factor that accounts for reduction in contact area between the base of the cap and the clay crust as the soil settles away from the cap during lateral spreading, and for reduction in friction stresses caused by interaction between base friction and the stresses induced by the pile segments beneath the pile cap. Values of R_{base} for the centrifuge tests are presented later.

3.5.3   *Lateral loads on pile segments in crust beneath pile caps*

The horizontal forces acting on the pile segments between the pile caps and the shear gauges were estimated using the method for calculating p_u for piles in clay developed by Matlock (1970) for static loading conditions:

$$p_u = \left(3 + \frac{\sigma_v{'}}{s_u} + J \cdot \frac{x}{b}\right) \cdot s_u \cdot b \qquad\qquad for \qquad x < x_{cr} \qquad\qquad (3\text{-}12)$$

$$p_u = 9 \cdot s_u \cdot b \qquad\qquad for \qquad x < x_{cr} \qquad\qquad (3\text{-}13)$$

where:

p_u = ultimate soil resistance per unit depth

$\sigma_v{'}$ = effective overburden pressure

s_u = undrained shear strength of soil

b = pile diameter

J = empirical constant

The force acting on each pile was calculated by integrating p_u (units force/length) along the length of the pile segment in the crust.

Matlock suggested modifications to p-y curves to account for cyclic degradation of the clay stress-strain response. However, these modifications were based on highly sensitive clays (Matlock, personal communication), and for piles exposed to lateral loading at the pile head. These modifications for cyclic loading are not appropriate to use in the case of

lateral spreading because significant degradation would not be expected due to the permanent component of lateral spreading displacements, and because the clay used in the centrifuge tests did not have a high sensitivity. The static relations for p_u produced very reasonable agreement with the measured ultimate crust loads for the single piles in test PDS01 (Table 3-3).

Table 3-3: Predicted and measured peak lateral crust loads on single piles.

Pile	Peak measured p (kN/m)	Predicted p_u with static loading relations[a] (kN/m)	Predicted p_u with cyclic loading relations[a] (kN/m)
BP	169	175	36
GN	82	90	22

[a] Using Matlock's (1970) p-y relations for static or cyclic loading as appropriate.

Matlock's bearing equations were developed for single piles in clay with a free ground surface such that a failure wedge on the passive side of the pile could exhibit some upward vertical displacement at shallow depths. If a gap exists between the base of a pile cap and the underlying clay, then failure wedges against the piles can move upwards. In this case, the depth x in Matlock's equations would be best taken as relative to the base of the pile cap. If the base of a pile cap is in contact with the underlying clay, then the clay may be restrained to fail in plain strain against the piles, producing larger bearing factors (i.e. Eq. 3-13 versus 3-12). Back-calculated values for the peak subgrade reaction loads on the pile segments at mid-depth in the clay beneath the pile cap for

SJB03 at the time of peak moment (Fig. 3-8) ranged from about 200 kN/m to about 450 kN/m (neglecting the top p-recording, which was erroneous due to the influence of boundaries on double differentiation), which corresponds to quite reasonable bearing factors of $N_p = 3.9$ to $N_p = 8.7$, respectively. The accuracy of these back-calculated values is limited by the small number of strain gauges in the clay layer beneath the cap, and so the comparison with Matlock's bearing equations really only represents a qualitative check on the consistency of the data. Consequently, in the absence of a suitable equation for bearing factors on piles beneath pile caps, the loads on the pile segments beneath the caps were estimated using Matlock's equations with the depth x being relative to the adjacent ground surface, which gives N_p values intermediate to those calculated for plane strain and for a gap beneath the cap.

3.5.4   *Comparing recorded lateral loads to theoretical calculations*

The procedures described in the previous section were performed for five of the tests to estimate the lateral loads acting on the pile groups. The base reduction coefficient, R_{base}, was varied to provide a match between the predicted loads and the measured peak crust loads. The results of the study are summarized in Table 3-4.

Table 3-4: Summary of back-calculated lateral load components for pile groups in centrifuge tests.

Test ID	Undrained Shear Strength, s_u (kPa)	Adhesion Factor, α	Base Friction Reduction Factor, R_{base} [a]	Passive Force (kN)	Side Friction (kN)	Base Friction (kN)	Pile Segment Force (kN)	Total Crust Load (kN)	Peak Measured Crust Load (kN)
PDS03	22	0.6	0.5	1090	490	410	560	2550	≈ 2530 [b]
SJB01	44	0.5	0.4	2320	950	700	1020	4990	4980
SJB03	44	0.5	0.0	3500	450	0	2990	6940	6380
DDC01	33	0.55	0.3	2600	650	680	2160	6090	6150
DDC02	22	0.6	0.0	2090	480	170	1540	4280	4330

[a] Base friction force is defined as $\alpha \cdot R_{base} \cdot s_u \cdot A_{base}$
[b] Crust load is total measured load from the nonliquefied crust minus structural inertia load(s). Pile cap acceleration was not measured for PDS03, so the pile cap inertia was assumed equal to that measured in SJB01 at the time that the peak pile bending moments were recorded (approximately 620 kN).

The following observations can be drawn from the data summarized in Table 3-4:

- The base friction reduction factor, R_{base}, ranged from 0 to 1/2, with an average of about 1/4.

- Passive pressures contributed only 43% to 50% of the total loads on the pile groups. Friction between the crust and the pile caps contributed 15% to 39% of the predicted lateral load, and forces on the pile segments beneath the cap contributed 22% to 43%.

- Reasonable predictions of the peak measured crust loads were obtained, provided that some friction forces were included in the estimates.

The back-calculated R_{base} values correspond qualitatively with the amount of contact between the crusts and pile caps (i.e. more contact was observed for tests with higher R_{base} values). Fig. 3-17 shows photos of the gaps at the downslope face of two different

pile groups. A large gap was observed beneath the cap for test SJB03 ($R_{base} = 0$), which is evident because significant portions of the piles can be seen beneath the cap and above the ground surface. Gapping beneath the cap was not nearly as significant for test SJB02 as it was for SJB03, which is evident because portions of the downslope edge of the pile cap is still in contact with the clay crust. The contact between the cap and crust for SJB02 was similar to the contact for tests PDS03 and SJB01 ($R_{base} = 0.5$ and 0.4, respectively). Unfortunately, the contact was not clearly shown in the photos taken during excavation of those models. Higher R_{base} values were back-calculated for groups of small-diameter piles that exhibited significant cap rotations. One potential mechanism that can occur during lateral spreading is that the spreading soils becomes wedged beneath the caps, thereby maintaining contact between the cap and crust during shaking, or potentially even creating contact where a gap existed prior to shaking. Flexible pile groups that exhibit significant cap rotations, and hence significant downward displacement of the downslope edge of the cap, could potentially maintain contact with the soil along a larger portion of base of the pile cap compared with stiffer pile groups where the soil settles away from the base of the cap.

3.6 OBSERVED LOAD VERSUS RELATIVE DISPLACEMENT BETWEEN PILE GROUPS AND LATERALLY SPREADING CRUSTS

The total lateral load from the crust is plotted versus the relative displacement at virgin loading peaks (i.e. crust load peaks that exceed the maximum past crust load) in Fig. 3-18. Each virgin peak load was normalized by the greatest overall peak load measured for that specific model test. The relative displacement was taken as the soil displacement to

the side of the pile cap (point A in Fig. 3-19) minus the pile cap displacement (point B in Fig. 3-19). This relative displacement was then normalized by the thickness of the nonliquefiable crust. The resulting data show that the overall peak lateral loads were mobilized at relative displacements of 25% to over 70% of the crust thickness, which is about an order of magnitude larger than trends observed in static load tests of pile groups in nonliquefied soil profiles.

Static loading of retaining walls and pile caps have shown that full passive resistance is mobilized when the wall displacement is more than about 1% to 7% of the wall height, depending on soil type and density. For example, Rollins and Sparks (2002) performed static load tests on a pile group in granular soil and reported that the peak load was mobilized at a pile cap displacement of about 2.5% to 6% of the pile cap height. Duncan and Mokwa (2001) and Mokwa and Duncan (2001) describe load tests on bulkheads and pile groups embedded in sandy silt/sandy clay and in gravel/sand backfills and showed that passive loads were mobilized at displacements of about 1% to 4% of the pile cap height. In design practice for lateral spreading loads, it is commonly assumed that the load transfer relation is similar to those observed from static loading tests.

The softer-than-expected relation between lateral loads and relative cap-soil displacement, as observed from the centrifuge tests may be influenced by several factors. For example, cyclic degradation of the clay stress-strain response would cause the lateral load transfer behavior to be softer than for static lateral loading. However, the differences between the static load tests and the centrifuge tests are too large to be explained by cyclic degradation alone.

The softer lateral load transfer behavior during lateral spreading as opposed to static loading is primarily attributed to the effects of liquefaction beneath the surface crust. In particular, liquefaction of the underlying soils has a strong effect on the distribution of stresses in the nonliquefied crust. For static loading of a pile cap without any liquefaction in the underlying soils, some of the stress imposed on the clay by the pile cap would geometrically spread down into the sand and thus stresses in the clay crust would decrease sharply with distance away from the pile cap. For the case where the underlying sand is liquefied, the stress imposed on the clay by the pile cap would not be able to spread down into the liquefied sand (assuming it has essentially zero strength compared to the crust), and thus the lateral stress in the clay crust would decrease more slowly with distance away from the pile cap. Spreading of lateral stress to greater distance back from the pile cap causes larger strains in the clay soil away from the pile cap. The spreading of lateral stress is evident in Fig. 3-19, where the light-colored clay markers show that the pile cap induced strains in the clay at a large distance upslope from the cap. Since relative cap-soil displacement represents an integral of strains between two reference points, the result is a much softer load versus relative displacement response for the crust over liquefied soil than for the crust supported on nonliquefied soil.

Terzaghi (1936) asserted that the Rankine states of stress (active and passive) are not realistic for natural soil deposits because frictionless boundaries are required to produce a uniform stress distribution throughout the soil deposit (Fig. 3-20). He postulated that elimination of friction between the base of a soil deposit and the underlying soils cannot occur in practice, hence Rankine theory is valid only "in our imaginations." Furthermore, Terzaghi noted that these "imaginary" boundary conditions would result in mobilization

of Rankine stress states at very large lateral displacements that are proportional to the length of the soil deposit rather than its height. Although Terzaghi's intent was to describe a practical limitation of Rankine earth pressure theory for static loading problems, his assertions turned out to be useful in explaining the soft load-versus-relative-displacement response observed for the case of a nonliquefied crust spreading laterally over a liquefiable deposit where friction at the bottom of the crust is small due to liquefaction of the underlying sand (Brandenberg et al. 2004).

3.7 THREE-DIMENSIONAL SIMPLIFIED LOAD TRANSFER MODELS FOR PILE GROUPS IN LATERALLY SPREADING GROUND

This section presents models for predicting load transfer behavior between pile groups and nonliquefied crust overlying liquefied sand for conceptual cases wherein 1. the pile cap moves horizontally into a stationary soil mass, and 2. the nonliquefied crust layer spreads laterally into a stationary pile group. The first might occur, for example, during an inertia loading cycle when transient ground displacements are small, or during a static load test of a pile foundation in a soil profile that has been liquefied by blast charges (e.g. Ashford and Rollins 2002). The second occurs when laterally spreading soil fails in the passive mode and flows around a stiff pile foundation that exhibits little cap displacement. Actual loading conditions are more complicated than these simplified conceptual cases, and field conditions likely involve some combination of pile cap displacement and ground displacement. The conceptual division into inertia loading and lateral spreading cases is intended to envelope the actual response.

3.7.1 *Inertia Loading Model*

This section presents the derivation of the load transfer behavior for inertia loading conditions in which the pile cap displaces into the soil mass (Fig. 3-21a). The assumptions of the load transfer model are:

1. Inertia of the nonliquefied crust is neglected.

2. The residual strength of the liquefied sand is fully mobilized along the base of the nonliquefied crust, and acts in the downslope direction against the force imposed by the pile group.

3. Stresses attenuate within a block of stress influence that geometrically extends at an angle α from the back face of the pile cap in plan view (Fig. 3-22).

The solution proceeds by first assuming an interaction force between the pile group and the nonliquefied crust, F_{crust}, and subsequently solving for strains induced in the soil mass, then integrating those strains in the zone of influence to obtain relative displacement between the pile cap and crust. F_{crust} is defined as the change in interaction force between the pile group and the nonliquefied crust (Fig. 23c). The plane on the left edge of the slices in Fig. 23 is assumed to be the plane of contact with the pile group. Force equilibrium in the x-direction of Fig. 23c dictates the following equation:

$$\Delta F(x) = F_{crust} - \Delta T(x) \qquad\qquad (3\text{-}14)$$

Assuming that the shear force in the final condition is equal to the residual strength of the liquefied sand layer times the area of the base of the slice, the magnitude of the change in shear force is computed from force equilibrium in the z-direction in the following equation:

$$\Delta T(x) = T_f(x) - T_i(x) = s_r \cdot \left[W \cdot x + x^2 \cdot \tan \alpha \right] + \gamma \cdot H \cdot \sin \beta \cdot \left[W \cdot x + x^2 \cdot \tan \alpha \right] \qquad (3\text{-}15)$$

The two terms in Eq. 2 add together because the vectors $T_f(x)$ and $T_i(x)$ point in opposite directions. Substituting $\Delta T(x)$ from Eq. 3-15 into Eq. 3-14 results in the following expression:

$$\Delta F(x) = F_{crust} - \left[s_r + \gamma \cdot H \cdot \sin \beta \right] \cdot \left[W \cdot x + x^2 \cdot \tan \alpha \right] \qquad (3\text{-}16)$$

The change in horizontal stress at the right edge of the slice, $\Delta\sigma(x)$, is equal to $\Delta F(x)$ divided by the section area of the right edge of the slice. The strain at the right edge is equal to the stress divided by the modulus, and is presented in the following Eq.:

$$\varepsilon(x) = \frac{1}{E} \left[\frac{F_{crust} - \left[s_r + \gamma \cdot H \cdot \sin \beta \right] \cdot \left[W \cdot x + x^2 \cdot \tan \alpha \right]}{H \cdot \left[W + 2 \cdot x \cdot \tan \alpha \right]} \right] \qquad (3\text{-}17)$$

The relative displacement between the pile cap and the free-field soil mass (equal in magnitude to the pile cap displacement since the soil mass is stationary) is equal to the integral of strain within the zone of influence, which extends a distance x_{cr} upslope from

the pile cap. The length of the zone of influence can be found by setting $x = x_{cr}$ and $F(x_{cr})$ $= 0$, and subsequently solving Eq. 3-16 for x_{cr}. The positive part of the quadratic solution for x_{cr} is presented in the following Eq's:

$$x_{cr} = \frac{1}{2 \cdot C_1} \cdot \left[-C_2 + \sqrt{\left(C_2^{\,2} + 4 \cdot C_1 \cdot F_{crust} \right)} \right] \tag{3-18}$$

$$C_1 = \left[s_r + \gamma \cdot H \cdot \sin \beta \right] \cdot \tan \alpha \tag{3-19}$$

$$C_2 = \left[s_r + \gamma \cdot H \cdot \sin \beta \right] \cdot W \tag{3-20}$$

Finally, the relative displacement, equal to the integral of strain in the zone of influence, is given in the following Eq.:

$$\Delta_{rel} = \int_0^{x_{cr}} \varepsilon(x) \cdot dx \tag{3-21}$$

A closed-form solution for Δ_{rel} can be obtained by substituting the appropriate expressions for $\varepsilon(x)$ and x_{cr}, provided that the modulus, E, is constant. However, the resulting expression is too long to be practically useful, and it is often desirable to use a nonlinear stress-strain relationship, in which secant modulus depends on strain, for the crust material. The following incremental approach was utilized for the load transfer relations presented in this dissertation:

1. Compute x_{cr} using Eqs. 3-18 through 3-20, and discretize the zone of influence into thin slices,

2. beginning with the slice adjacent to the pile group, impose F_{crust} as a known force on

   the left edge of the slice,

3. compute the strain on the left edge of the slice as F_{crust} / (W·H·E),

4. solve for the force on the right edge of the slice using Eq. 3-16,

5. solve for the strain at the right edge of the slice using Eq. 3-17,

6. impose the force on the right edge of the current slice as being equal to the force on

   the left edge of the next slice, and repeat the procedure for all of the slices,

7. compute the displacement by summing the strains times tributary widths,

8. repeat steps 2. through 7. for a sufficient number of different F_{crust} values to define

   the load transfer relation.

The load transfer relation is demonstrated using an example problem later in this dissertation.

3.7.2   *Lateral Spreading*

This section presents the derivation of the load transfer behavior for lateral spreading conditions in which the nonliquefied crust spreads downslope into the pile group (Fig. 3-21b). The assumptions of the load transfer model are:

1. Pile cap displacement is zero,

2. the residual strength of the liquefied sand is fully mobilized along the base of the

   nonliquefied crust, and acts in the upslope direction to resist lateral spreading of the

   crust,

3. stresses attenuate within a block of stress influence that geometrically extends at an angle α from the back face of the pile cap in plan view (Fig. 3),

4. horizontal accelerations and horizontal displacement at a given location in the nonliquefied crust layer must be compatible with the acceleration versus Newmark displacement relation obtained for a given ground motion.

The solution for the lateral spreading model follows the same logic as for the inertia loading case, with the only differences being the addition of a crust inertia force, and the change in direction of the shear force from the liquefied sand layer. Horizontal force equilibrium from Fig. 3-24c dictates that:

$$\Delta F(x) = F_{crust} + \Delta T(x) - k_h(x) \cdot \gamma \cdot H \cdot \sin \beta \cdot \left[W \cdot x + x^2 \cdot \tan \beta \right] \cdot \cos \beta \tag{3-22}$$

Assuming that the shear force in the final condition is equal to the residual strength of the liquefied sand layer times the area of the base of the slice, the magnitude of the change in shear force is computed from force equilibrium in the z-direction in the following equation:

$$\Delta T(x) = T_f(x) - T_i(x) = s_r \cdot \left[W \cdot x + x^2 \cdot \tan \alpha \right] - \gamma \cdot H \cdot \sin \beta \cdot \left[W \cdot x + x^2 \cdot \tan \alpha \right] \tag{3-23}$$

The second term is subtracted from the first term in Eq. 3-23 because vectors $T_f(x)$ and $T_i(x)$ point in the same direction. Substituting Eq. 3-23 into Eq. 3-22 results in the following expression:

$$\Delta F(x) = F_{crust} + (s_r - \gamma \cdot H \cdot \sin \beta - k_h(x) \cdot \gamma \cdot H \cdot \cos \beta) \cdot \left[W \cdot x + x^2 \cdot \tan \beta \right] \qquad (3\text{-}24)$$

The change in horizontal stress at the right edge of the slice, $\Delta\sigma(x)$, is equal to $\Delta F(x)$ divided by the section area of the right edge of the slice. The strain at the right edge is equal to the stress divided by the modulus, and is presented in the following Eq.:

$$\varepsilon(x) = \frac{1}{E} \left[\frac{F_{crust} + (s_r - \gamma \cdot H \cdot \sin \beta - k_h(x) \cdot \gamma \cdot H \cdot \cos \beta) \cdot \left[W \cdot x + x^2 \cdot \tan \beta \right]}{H \cdot \left[W + 2 \cdot x \cdot \tan \alpha \right]} \right] \qquad (3\text{-}25)$$

A closed-form solution for the length of the zone of influence cannot be obtained for the lateral spreading model because the horizontal acceleration is an unknown function of x. The horizontal acceleration of each slice must be compatible with the displacement of the slice obtained from a Newmark sliding block analysis. The solution procedure used to solve the lateral spreading load transfer model are:

1. Define a ground motion, and compute Newmark sliding block analyses to define yield acceleration versus block displacement,
2. select a length of the zone of influence, and discretize the crust inside the zone of influence into thin slices,
3. beginning with the slice adjacent to the pile group, select a guess value of F_{crust} that will produce a compatible solution,

4. obtain the k_h-value for the slice from the Newmark sliding block results based on the displacement of the left side of the slice (zero displacement for the first slice),

5. solve for the force on the right edge of the slice using Eq. 11,

6. solve for the strain in the slice using Eq. 12, and compute the displacement of the right edge of the slice by multiplying the strain by the slice thickness,

8. set the force and displacement on the right edge of the current slice equal to the force and displacement on the left edge of the next slice, and repeat the procedure for all of the slices,

9. check if the force on the right edge of the last slice is reasonably close to zero, and if it is not, repeat steps 3 through 9 until it is,

10. repeat steps 1 through 9 for a sufficient number of different ground motions (or scaled versions of a single motion) to define the load transfer relation.

The length of the zone of influence selected in step 2 depends on the boundary conditions, and may be geometrically limited to the length of spreading soil. In cases where a large lateral extent of spreading soil exists upslope from the pile group, x_{cr} should be sufficiently large that the solution becomes insensitive to further increases in x_{cr}. A single Newmark displacement versus yield acceleration relation will give a single crust load (F_{crust}) and relative displacement (displacement at the right edge of the last slice). To define the entire load transfer relation, the procedure must be repeated for a number of different ground motions, or scaled versions of a single ground motion. In this dissertation, load transfer curves that correspond to a given ground motion will be

obtained by scaling that motion to various peak acceleration values and subsequently solving the load transfer equations for each scaled value.

3.7.3   Example Solutions

In this section, load transfer relations are computed for an example pile group and soil profile using both the inertia loading and lateral spreading models. Distributions of stress and displacement are presented first using a baseline set of input parameters, then some of the parameters are systematically varied to demonstrate their influence. Finally, comparisons between the predicted load transfer relations with centrifuge observations provide validation for the models. The baseline parameters are given in Table 3-5. The Newmark sliding block solutions for the Kobe ground motion is in Fig. 3-25, along with solutions for three other motions that will be used later. The motions are scaled to $a_{max} =$ 1.0 g, and scaling to any other a_{max} can be achieved by simply multiplying the x- and y- axes by the desired a_{max} value in units of g. The value of $F_{crust,ult}$ was computed using Rankine passive earth pressure theory as $F_{crust,ult} = \frac{1}{2} \cdot \gamma \cdot H^2 + 2 \cdot s_u \cdot H$. The stress-strain relation used for the models is shown in Fig. 3-26. Note that the ultimate stress is equal to the ultimate crust load divided by the pile cap cross-sectional area, and that the stress is assumed to be constant with depth for a given slice for simplicity.

Table 3-5: Input parameters for baseline case

Parameter	Value
W	10 m
H	2.5 m
γ	16 kN/m3
s_r	3 kPa
s_u	40 kPa
$F_{crust,ult}$	2500 kN
α	26.6 degrees
β	3 degrees
ε_{ult}	20 %
Motion	Kobe

3.7.3.1 Distributions of Displacement and Stress

Distributions of relative displacement, stress and inter-slice force are shown in Fig. 3-27 for $F_{crust} = F_{crust,ult}$. The length of the zone of influence, x_{cr}, for the inertia loading model was found to be about 20 meters, while $x_{cr} \approx 100$ m was appropriate for the lateral spreading model. The relative displacement at x_{cr} was 0.38 m for the inertia loading model and 0.56 m for the lateral spreading model. Soil stresses extended further upslope for the lateral spreading model than for the inertia loading model, and the integral of horizontal strains within this larger zone of influence caused larger relative displacements.

3.7.3.2 Influence of Residual Strength of Liquefied Sand

The influence of the residual strength of the liquefied sand layer on the computed load transfer relations is presented in Fig. 3-28. The curve for $s_r / s_u = 0.1$ is for the baseline case, with the other curves corresponding to increasing s_r / s_u. As s_r / s_u increases, the load transfer relation stiffens for both models because the increasing restraining force

provided by the liquefiable layer causes stresses to attenuate more rapidly with distance away from the pile group. The load transfer curves were softer for the lateral spreading model than for the inertia loading model because of the larger zone of influence demonstrated in the previous section. For the case with $s_r / s_u = 1.0$, the ultimate lateral load is mobilized at a relative displacement of 5.5% of the crust thickness for the inertia loading model. The loading conditions for this case are similar to static load testing of a pile foundation in nonliquefied ground, and the load transfer curve reasonably reflects such loading conditions. The shape of the load transfer curves for the lateral spreading model were not as sensitive to s_r as those for the inertia model. However, the peak ground acceleration required to mobilize $F_{crust,ult}$ (a_{ult}) increased significantly as s_r increased (inset of Fig. 3-28b) due to the large yield accelerations associated with high s_r values. A Kobe motion with $a_{ult} = 0.4$ g would be required to mobilize $F_{crust,ult}$ for $s_r / s_u = 0.1$, while $a_{ult} = 2.4$ g would be required for $s_r / s_u = 1.0$. This is consistent with the observation that large yield accelerations must be overcome for high s_r / s_u values to compress the spreading crust layer against the pile group.

3.7.3.3 Influence of Pile Cap Width

The influence of pile cap width on computed load transfer relations is presented in Fig. 3-29. The case with $W / H = 4$ is the baseline case, and $W / H = 1$ and 10 are also presented. As the width to height ratio increases, the load transfer behavior becomes softer for both models because the length of the zone of influence increases with pile cap width. The peak accelerations required to mobilize $F_{crust,ult}$ for the lateral spreading model increase with increasing W / H because larger accelerations are required to

compress the soil within the larger zone of influence. For the Kobe motion, $a_{ult} = 0.25$ g for W / H = 1, while $a_{ult} = 0.63$ g for W / H = 10. Comparing the influence of W / H relative to s_r / s_u, W / H more significantly influences the shape of the load transfer relations, but less significantly influences a_{ult}.

3.7.3.4   Influence of Angle of Stress Attenuation

The influence of the angle of stress attenuation, α, on load transfer behavior is presented in Fig. 3-30. The case with $\alpha = 26.6^o$ (2:1) is the baseline case, and curves are also presented for $\alpha = 0$ and $\alpha = 45^o$. The load transfer relations become stiffer as α increases because the length of the zone of influence decreases as strains are distributed into larger out-of-plane soil zones. The case with $\alpha = 0^o$ corresponds to, for example, a long constant-width bridge abutment, and is associated with a very soft load transfer relation. The accelerations required to mobilize $F_{crust,ult}$ for the lateral spreading model increase with decreasing α because large a_{ult} values are required to mobilize the requisite ground displacements.

3.7.3.5   Influence of Strain at Ultimate Stress

The influence of soil strain at the ultimate stress is presented in Fig. 3-31. The case with $\varepsilon_{ult} = 20\%$ is the baseline case, and curves are also presented for $\varepsilon_{ult} = 10\%$ and 30%. As ε_{ult} increases, the load transfer relation softens as expected. Larger a_{ult}-values are required to mobilize the larger displacements required for the higher ε_{ult} values for the lateral spreading model. Compared with the influence of W/H and α, ε_{ult} had

significantly less influence on the shape of the load transfer relations, and influenced a_{ult} less than any of the other parameters studied thus far.

3.7.3.6 Influence of Ground Motion

The influence of the ground motion on the lateral spreading load transfer model is presented in Fig. 3-32. The Kobe motion is the baseline case, and curves are also presented for the Santa Cruz motion, and a sine wave motion with 5 and 40 uniform 2-Hz cycles (Sine 05 and Sine 40, respectively). The shape of the curves is nearly identical for all four motions, but the a_{ult} values vary considerably. $F_{crust,ult}$ is reached at $a_{ult} = 0.18$ g for the Sine 40 motion, 0.38 g for the Sine 05 motion, 0.40 g for the Kobe motion, and 0.54 g is required for the Santa Cruz motion. Comparing the Sine 40 and Sine 05 motions demonstrates how duration affects the load transfer results, and comparing the Kobe and Santa Cruz motion demonstrates the influence of frequency content since these motions had nearly the same duration. Comparing the sine wave motions with the Kobe and Santa Cruz motions demonstrates the importance of using realistic earthquake motions in model tests to accurately simulate field conditions.

3.7.3.7 Correction for Point of Reference Within Lateral Spread

A stiffness correction may be applied to the load transfer curves for the lateral spreading model to change the point of reference within a lateral spread. Typically lateral spreading displacements are largest at the open face and decrease with distance upslope (e.g. Tokimatsu and Asaka 1998). The load transfer curves derived in this dissertation relate F_{crust} with displacement between the pile cap and the soil surface at a

distance x_{cr} upslope from the pile cap. However, the traditional approach is to relate F_{crust} to the free field soil displacement that would occur at the pile group location in the absence of any influence from the pile group. The example in Fig. 3-33 illustrates an actual ground displacement profile that occurs with the influence of the pile group, and a free-field ground displacement that would occur without the pile group. The two soil displacements are the same at $x_a = x_{cr}$ because the pile group does not influence the ground displacements at this location. The relative displacement between the pile cap and the soil at point a is $\Delta_{rel,a} = 0.56$ m, while $\Delta_{rel,b} = 1.12$ m. Both relative displacements are associated with the same crust load value, in this case $F_{crust} = F_{crust,ult}$. Hence, a correction to the load transfer relation is required to shift the point of reference from point a (point of reference in the load transfer model) to point b (conventional point of reference). In this case, a y-multiplier of 2 is required ($m_y = \Delta_{rel,b} / \Delta_{rel,a} = 2$) to soften the load transfer relation.

3.7.3.8   *Comparisons With Centrifuge Data*

Backbone load transfer relations were developed from the centrifuge test data by recording virgin crust loads and the associated relative displacement between the pile cap and the soil surface, and the normalized relations are shown in Fig. 3-34. The observed relations were significantly softer than the range of responses commonly observed in static load tests. Load transfer relations were predicted using the inertia loading model and the lateral spreading model, and a y-multiplier of 2 was subsequently applied to the lateral spreading model to account for the ground displacements being measured at the pile group location rather than further upslope at the edge of the zone of influence. This

y-multiplier was based on measurements of crust displacements near the pile cap location compared with displacements further upslope. The inertia loading model provides a reasonable upper bound to the observed load transfer data, while the lateral spreading model more closely fits the softer data points. Some of the points are softer than the predicted range and the cause is not well understood, but could be related to cyclic degradation or cracking of the crust material. Nevertheless, the two load transfer models presented in this dissertation provide a much better match with the observed behavior than the static load test results.

3.8   PILE CAP AND SUPERSTRUCTURE INERTIA LOADS

Designers often assume that peak inertia loads and peak lateral spreading loads do not act simultaneously based on the assumption that inertia loads occur during strong shaking while lateral spreading loads peak at the end of or after strong shaking when ground displacements are largest.   The centrifuge test data showed that this assumption is incorrect because peak inertia loads and peak lateral spreading loads can occur simultaneously due to large lurching ground displacements during shaking (Fig. 3-35). Therefore, estimating inertia loads to use in combination with lateral spreading loads is a critical component of design.   However, the problem is complicated because of the difficulty in estimating site response in liquefied ground, and because of soil-foundation-structure interaction.   Reliable methods for estimating inertia loads in liquefied, laterally spreading ground have not yet emerged, and designers are faced with a series of difficult assumptions.

To further demonstrate the complexity in site response and soil-foundation-structure interaction, consider the time series of accelerations of the crust, the liquefied sand, and the pile cap shown in Fig. 3-36 for the large Kobe motion for test SJB03. Regarding site response, the acceleration of the loose sand is dominated by the sand's dilatancy response because the large downslope (positive) acceleration pulses occur simultaneously with the transient drops in pore water pressure.   These acceleration pulses also influence the motion of the clay crust by inducing similar acceleration spikes a short time later after the waves have propagated upward into the crust.   The large dilatancy-induced acceleration spikes are contrary to the common expectation that liquefied sand serves as an isolator, limiting the accelerations transmitted to overlying layers.   Regarding soil-foundation

interaction, the motion of the pile cap more closely resembles the motion of the loose sand layer than the motion of the crust layer. The explanation is again the dilatancy behavior of the loose sand layer. As the pore pressures transiently drop and the loose sand gains strength and stiffness, it provides stiff subgrade reaction load transfer behavior that causes the pile foundation to follow the deformation of the loose sand. Using ground surface motion as an input into a structure neglects this important dynamic soil-foundation-structure interaction, but is common in design practice.

Site response and dynamic soil-foundation-structure interaction in liquefied, laterally spreading ground are complex, yet it is important to incorporate their effects into simplified design methods. Hence, the following sections will lay out a simplified method for estimating pile cap and structural accelerations based on equivalent linear site response analysis methods. The method consists of three parts: 1. Estimate the ground surface motion, 2. Estimate the pile cap motion 3. Estimate the superstructure motion.

3.8.1   *Estimate ground surface motion*

Ground motions are often estimated by first estimating the rock motion for the site, and second by performing a site response analysis. The site response analysis is especially important for soft soil sites because the dynamic properties of the soil can cause the motion to change significantly as it propagates upward through the soil profile. Liquefaction complicates the estimate of ground surface accelerations because the dynamic properties of liquefying soil are difficult to characterize, and change throughout the motion. Equivalent-linear methods that are commonly used in site response analyses (e.g. in SHAKE, Idriss and Sun 1992) do not capture the material response exhibited by

liquefying soils. Nonlinear site response analyses can conceivably capture the influence of liquefaction on ground motion, but are limited by the accuracy of the constitutive modeling, and have not been proven reliable.

Equivalent linear site response analyses of the centrifuge tests are presented in this section. The limitations of such analyses are acknowledged from the outset, with anticipation that the analyses cannot capture the influence of liquefaction, but rather predict the ground motion that would occur in the absence of liquefaction. This is important because design response spectra do not account for liquefaction, but are used extensively. Hence, relating pile cap and superstructure accelerations measured in the centrifuge tests to the ground accelerations predicted in the absence of liquefaction is valuable.

3.8.1.1 *Input parameters calibrated for site response analysis*

Site response analyses were performed using SHAKE, and the soil properties were calibrated to provide a reasonable estimate of ground surface acceleration for the small and medium motions imposed on the models since those motions did not induce liquefaction in the sand layers. Stress strain behavior of the sand layers was modeled using the depth-dependent modulus reduction curves recommended by EPRI (1993), and clay layers were modeled using the PI=50 modulus reduction and damping curves recommended by Vucetic and Dobry (1991). Damping of the sand layers was modeled based on the findings of Elgamal et al. (2005) and Lai et al. (2001) from their site response studies of sand on the large centrifuge. They found that the damping values required to analytically match site response measurements were significantly larger than

published values. The reason for this increase in the required damping values is not well understood, but can likely be attributed to energy dissipation occurring in the model container and through the base shaker rather than to actual material damping in the soil. The container base was modeled as a stiff elastic half-space with material properties characteristic of rock.

Shear wave velocities for the Nevada sand layers were computed based on measurements of travel time of small-strain shear waves induced using mini air hammers (Arulnathan et al. 2000). The wave forms were sampled at high frequency using accelerometers. For the sand layers in the SHAKE analyses, a continuous small strain shear modulus profile was computed using Eq. 3-26.

$$G_{mx} = p_a \cdot 21.79 \cdot k_{2,max} \cdot \sqrt{\frac{\sigma_m}{p_a}} \qquad (3\text{-}26)$$

The value of $k_{2,max}$ was calibrated to 30 for the loose sand and 40 for the dense sand, and the resulting shear wave velocity profile is shown in Fig. 3-37. These values of $k_{2,max}$ are smaller than those reported by Seed and Idriss (1970), but are in reasonable agreement with the values presented by Arulnathan et al. (2000) for Nevada sand. Ideally, the average measured shear wave velocity profile would provide reasonable predictions of site response, but the back-calculated values are near the low end of the measured data. The reasons for this trend are not entirely understood, though one likely cause is that there were significant vertical accelerations recorded in the centrifuge tests, caused primarily by rocking of the model container, that are not modeled in the site response

analysis. The combination of horizontal and vertical accelerations would have the influence of softening the soil compared with horizontal accelerations alone.

The shear wave velocity for the clay layer could not be determined from centrifuge test data because the recorded shear wave response from the mini air hammer was too small compared with the noise in the signal. So the small strain shear modulus of the clay was instead estimated as $G_{max} = 700 \cdot s_u$, where $V_s^2 = G_{max}/\rho$. The shear strains in the clay layer measured in the centrifuge tests were small, and those predicted in the SHAKE analyses were small as well. Hence the analysis is not sensitive to the properties of the clay layer within the range of properties tested in the centrifuge test.

The influence of the model container is an important consideration when extrapolating centrifuge observations to field cases with different boundary conditions. The masses of the container rings were included in the analysis by increasing the unit weight of the soil layers in proportion to the increase in mass contributed by each container ring. The stiffness of the container was incorporated into the analysis by increasing the soils' stress-strain relations based on the following steps:

1. Apply a static force on the soil deposit alone (without the container) at the ground surface that corresponds to a known stress,

2. use the modulus reduction curves to compute the strains in each soil layer, and compute the ground surface displacement,

3. compute the force required to displace the container the distance obtained from step 2,

4. divide the container force from step 3 by the plan-view area of the soil profile to obtain an equivalent increase in soil stress,

5. add the stress computed in step 4 to the stress applied in step 1,

6. compute a modified shear modulus by dividing the stress computed in step 5 by the strain for a given soil layer computed in step 2,

7. repeat steps 1 – 6 for a number of different values of applied force to obtain stress-strain relations at desired depths. Compute new small-strain shear moduli and new modulus reduction curves from these stress-strain relations.

An example of the influence of container stiffness on the composite stress-strain response of the material used in the SHAKE analyses is shown in Fig. 3-38 for a location near the center of the loose sand layer. Wilson (1998) noted that significant sloshing occurred when the soil liquefied in his models, which indicates that the container significantly influences liquefied soils.   The container influence varies throughout shaking as excess pore pressures vary, and likely is small when the liquefied soil is temporarily de-liquefied during dilatancy behavior.

3.8.1.2   Results of SHAKE analyses

Measured and predicted response spectra (5% damped) for the recorded and predicted ground surface motion are shown in Fig. 3-39, and predicted versus measured peak ground surface accelerations are presented in Fig. 3-40. The motion from the centrifuge test was measured upslope from the pile cap from an accelerometer embedded within the crust. The SHAKE analyses reasonably predicted the site response for the small and medium base motions because the input parameters were selected to reasonably match the measured data for these motions.   The match was not as accurate for the large

motions using those input parameters, which was expected since liquefaction was not modeled in the analyses.

The Kobe motion produced significant scatter in the peak ground surface accelerations, with PGA's at 57.2 g being about double those at 38.1 g. The difference in peak ground accelerations was not predicted by the SHAKE analyses, which indicates that the contributing factors lie outside of the mechanics included in SHAKE (e.g. the larger thickness of the dense sand for the tests at 57.2 g does not contribute to the larger accelerations). The cause of the scatter is not completely understood, but could be the influence of the container (which has a different prototype natural period at 57.2 g than at 38.1 g), rocking of the container and associated vertical accelerations, the influence of the pile group on structural accelerations, and friction between the container and the sides of the crust.

Liquefaction is commonly assumed to influence ground motion by 1. Decreasing peak ground accelerations because transmitted shear stresses are limited to the small strength of the liquefied sand, and 2. increasing long period accelerations because the softening of the liquefied sand increases the natural period of the site. The first assumption was not substantiated by the test data and analyses because the measured peak ground accelerations were sometimes much larger than predicted. This behavior is attributed to the shock wave phenomenon observed by Kutter and Wilson (1999), in which large high-frequency acceleration spikes are caused by the dilatancy behavior of the sand during transient drops in pore pressure. The container also likely influenced the motion of the crust since the stiffness of the container was substantial compared with the stiffness of the liquefied soil deposit, and because the container exhibited some rocking behavior. The

measured data did contain more long-period content than predicted in the shake analyses, which corresponds well with common expectation.

3.8.2   Estimate pile cap acceleration

Imposing a predicted free-field ground surface motion on the bottom of a structure inherently assumes that the foundation motion will be the same as the ground motion, and that the foundation will not interact with the ground nor with the structure. Soil Foundation Structure Interaction (SFSI) can be a particularly important consideration in liquefying and laterally spreading ground because it is desirable for the foundation to be stiff and strong relative to the ground so that the foundation displacement is smaller than the free-field lateral spreading displacement. Hence, the motion of the foundation must be different from the free-field motion of the ground (Fig. 3-36), and relating the two motions is desirable.

Fig. 3-41 shows the measured peak pile cap acceleration compared with the peak measured ground acceleration and the peak predicted ground acceleration for each motion for five centrifuge tests. There is significant dispersion in the relation between measured cap acceleration and measured ground acceleration, which further demonstrates that the pile caps do not move in compliance with the ground, but rather interact with the ground and exhibit their own motion. The relation between peak cap acceleration and peak ground acceleration predicted from equivalent linear dynamic analysis shows similar dispersion. The relation between peak pile cap acceleration and predicted peak ground acceleration in the absence of liquefaction has a coefficient of variation of 0.44, and plus or minus a factor of two would correspond to about $2.0 \cdot \sigma$.

Estimating the peak pile cap acceleration is only the first step in estimating a pile cap inertia load to use in a static-seismic foundation design analysis; the second step is estimating the timing of the inertia loading and lateral spreading loading. Fig. 3-42 shows the pile cap acceleration measured during the critical cycle when the peak crust load occurred versus the peak upslope cap acceleration measured for the test (upslope acceleration is associated with downslope inertia force). The cap acceleration during the critical cycle was close to the peak acceleration for the tests with the 1.17-m diameter piles, while the cap acceleration during the critical cycle was considerably smaller than the peak accelerations for the smaller 0.73-m diameter piles. Essentially, the peak downslope cap inertia forces acted at the same time as the peak downslope crust loads for the larger, stiffer pile foundations, while a smaller fraction of the peak downslope cap inertia acted at the same time as the peak downslope crust loads for the smaller, more flexible pile foundations.

The influence of pile stiffness on the cap acceleration during peak downslope crust loads is not entirely understood, though the phasing can be qualitatively explained by considering what would happen if the pile stiffness was zero, and there was no superstructure attached to the cap. In the absence of pile resisting forces, the downslope crust loads would be resisted entirely by upslope inertia forces from the pile cap. Hence, the cap inertia forces would always be out-of-phase with the crust load. Adding in some pile stiffness changes the equations of dynamic equilibrium, thereby complicating the phasing of the crust load and inertia load. Nevertheless, another clarifying qualitative observation can explain conditions in which the crust load and inertia forces act in phase. Downslope inertia loading is associated with upslope cap acceleration, and for a

harmonic cap motion (for simplicity) the peak upslope acceleration occurs when the pile cap decelerates and comes to a stop. Hence, if the piles are stiff enough to bring the pile cap to a complete stop during a large downslope displacement cycle of the crust, the crust will fail and flow around the cap thereby exerting a peak crust load, while at the same time the peak downslope cap inertia load will occur. The larger diameter piles in the centrifuge tests were sufficiently stiff to cause the pile cap to come to a stop during large crust displacement cycles, while the more flexible smaller diameter piles were not. Note that the stiffness of the piles relates to the section properties of the piles themselves, and also to the nonlinear, time-varying properties of the liquefying sand layer. The dilatancy of the sand contributed to the pile response, and hence also to the phasing between the crust loads and inertia loads.

In designing pile groups that are stiff and exhibit limited displacements during lateral spreading (like the larger diameter piles in the centrifuge tests), the cap inertia load in a static-seismic design should be the based on the peak predicted pile cap acceleration; a reduction to account for the inertia forces being out-of-phase with the crust load is not justified. More flexible pile foundations that displace significantly with the imposed lateral spreading demands could result in peak cap inertia forces that are not in phase with peak crust loads (like the smaller diameter pile foundations in the centrifuge tests), or even in pile cap accelerations that are out-of-phase with the crust loads for pile foundations that are very flexible relative to the crust. However, such flexible pile foundations are often not desirable due to the large foundation displacements and associated structural damages. The focus of this dissertation is to propose design methods for stiff pile foundations that exhibit small displacements in lateral spreads, and

reduction in inertia loads to account for out-of-phase behavior is not recommended in such cases.

3.8.3   Estimate superstructure acceleration

Estimating accelerations of structures on pile foundations in liquefied and laterally spreading ground is complicated by the fact that 1. The motion of the foundation is different from the motion of the free-field ground, and 2. the structure influences the motion of the foundation. The typical approach to treat the predicted ground motion as an input to the base of the structure neglects these two complications, which introduces error into the prediction of structural acceleration. Fig. 3-43 shows 5% damped response spectra for the predicted and measured crust motions and also for the measured pile cap motions for the large Kobe motion for tests DDC01 and DDC02. The measured fixed-base natural period and measured peak structure accelerations are also shown in Fig. 3-43. The measured peak accelerations are in the vicinity of the recorded cap spectrum and the recorded crust spectrum for both DDC01 and DDC02. The predicted crust response spectrum provides a reasonably accurate prediction of peak acceleration for the 0.8s structure, but under-predicts the response of the 0.3s structure. However, an increase in the natural period of the structure would be expected to accompany liquefaction of the soil layers, and lengthening the natural period of the 0.3s structure could provide an accurate prediction of its acceleration. Care must be taken in estimating inertia loads for structures with fixed-base natural periods that lie to the left of the peak of the response spectrum because there is danger that SFSI will increase the natural period of the system, thereby increasing the structural accelerations.

Fig. 3-44 shows predicted 5% damped spectral acceleration versus peak measured structural acceleration for each motion for tests DDC01 and DDC02. The best correlation is obtained using the measured cap motion, which is not surprising since the only source of error in that case is the influence of the structure on the foundation rotations. A slightly worse prediction is obtained using the response spectra from the measured crust motion, with additional error coming from the difference between the crust motion and the cap motion. Finally, the prediction of structural acceleration using the response spectra from the predicted crust motion is the worst of the three, but still generally lies within a factor of two from the measured values.

Fig. 3-45 shows the relation between the peak structural acceleration and the structural acceleration measured at the same time as the peak crust load. The stiffer structure with $T_{FixedBase} = 0.3$ s exhibited accelerations during the critical cycle that were very near the peak accelerations, while the more flexible structure with $T_{FixedBase} = 0.8$ s exhibited accelerations that were not as in phase with the crust load. Tokimatsu (2003) observed that stiff structures with a natural period shorter than the natural period of the ground will exhibit accelerations that are in phase with the crust loads, while accelerations of more flexible structures with natural periods longer than the natural period of the ground will not be in phase with crust loads. A similar trend was observed in the centrifuge test data, with accelerations of the stiffer structure being more in phase with the crust load than accelerations of the more flexible structure.

The fundamental mechanisms involved in the phasing of crust loads and structural inertia loads appear to depend significantly upon pile section properties, structural mass, and dilatancy behavior of liquefiable sand. Ongoing and future nonlinear dynamic finite

element analyses are being calibrated to the centrifuge test data, and will be used to refine the prediction of pile cap acceleration and structural acceleration to use in simplified static-seismic design methods (Chang et al. 2005). Reductions in inertia loads may be justified in certain cases once the fundamental mechanisms are better understood.

3.9 SUMMARY

In this chapter, observations from centrifuge test data provided insight into the load transfer behavior between pile foundations and laterally spreading ground. Raw data provided some of the observations, while back-calculated quantities obtained from data processing provided others. Single piles and pile groups were studied. Comparisons among the different tests were made, and theoretical explanations of the fundamental loading mechanisms were presented.

Subgrade reaction loads in the liquefiable sand layer were often found to act in the opposite direction as the loads from the spreading nonliquefiable crust during critical loading cycles when the peak bending moments were measured in the piles. This is contrary to the downslope loading direction commonly anticipated in design, and the magnitude of the observed loads was often an order of magnitude larger than commonly assumed in static design approaches. The fundamental mechanisms that caused this behavior were 1. the displaced shape of the pile compared with the displaced shape of the ground, and 2. the dilatancy response of the sand layers during critical cycles. Piles that were flexible relative to the soil exhibited large displacements than the liquefiable sand layer, thereby attracting upslope restraining forces from that layer. Piles that were stiff relative to the soil exhibited smaller displacements than the liquefiable sand, thereby

attracting a downslope load. The liquefiable sand layer exhibited transient drops in pore pressure caused by dilatancy, and the associated increase in strength and stiffness of the liquefiable layer resulted in large-magnitude subgrade reaction loads.

Peak crust loads were observed during strong shaking rather than at the end of shaking when ground displacements were largest. This is contrary to the common expectation that crust load depends only on the total relative displacement between the pile foundation and the spreading crust. Incremental displacements that occurred when the crust lunged downslope during strong shaking were sufficiently large to mobilize the peak crust loads, while crust loads did not return to these large values after strong shaking when incremental displacements were smaller.

Lateral loads exerted on the single piles by the laterally spreading crust layer were reasonably predicted using Matlock's (1970) static bearing factors for piles in soft clay. His relations for cyclic loading were found to significantly under-predict the measured subgrade reaction loads, and are not appropriate to use in lateral spreading loading conditions.

The components of loading exerted on the pile groups by laterally spreading crusts were 1. passive force on the upslope face of the pile cap, 2. friction forces between the sides of the pile cap and the spreading crust, 3. friction forces between the base of the pile cap and the spreading crust, and 4. loads on the pile segments in the spreading crust beneath the pile cap. An additional upslope active force may act on the downslope face of the pile cap if a gap does not exist along this face. Friction along the sides and base of the pile caps were observed to contribute significantly to the lateral loading, which is

contrary to the common expectation that passive force on the upslope face is the dominant component.

Load transfer between pile groups and laterally spreading non-liquefied crusts was about an order of magnitude softer than commonly observed and assumed for static loading conditions. Horizontal strains were distributed through a large block of crust soil upslope from the pile group. Since relative displacement is the integral of horizontal strain through some zone of influence, the spreading of significant strains throughout a large zone of crust soil was associated with a soft load versus relative displacement response. Simple models were developed to envelope load transfer behavior between pile groups and nonliquefied laterally spreading crusts, and captured the centrifuge test results.

Pile cap inertia forces were often at or near their peak downslope values at the same time that the crust load values were at or near their peak values. This is contrary to the common design expectation that inertia forces and kinematic forces do not act simultaneously (e.g. TRB 2002). The cause of this behavior is not yet well understood, though pile foundation stiffness was observed to contribute to the magnitude and phasing of pile cap accelerations. Stiffer pile foundations exhibited cap accelerations that were in-phase with crust loads, while more flexible pile foundations exhibited cap inertia forces that were a smaller fraction of their peak values during peak crust loads. Pile cap accelerations were reasonably estimated as being equal to the peak ground surface acceleration predicted in the absence of liquefaction from an equivalent-linear site response analysis. Superstructure accelerations were reasonably predicted as the spectral

acceleration associated with the natural period of the superstructure. Uncertainty in both predictions was quantified.
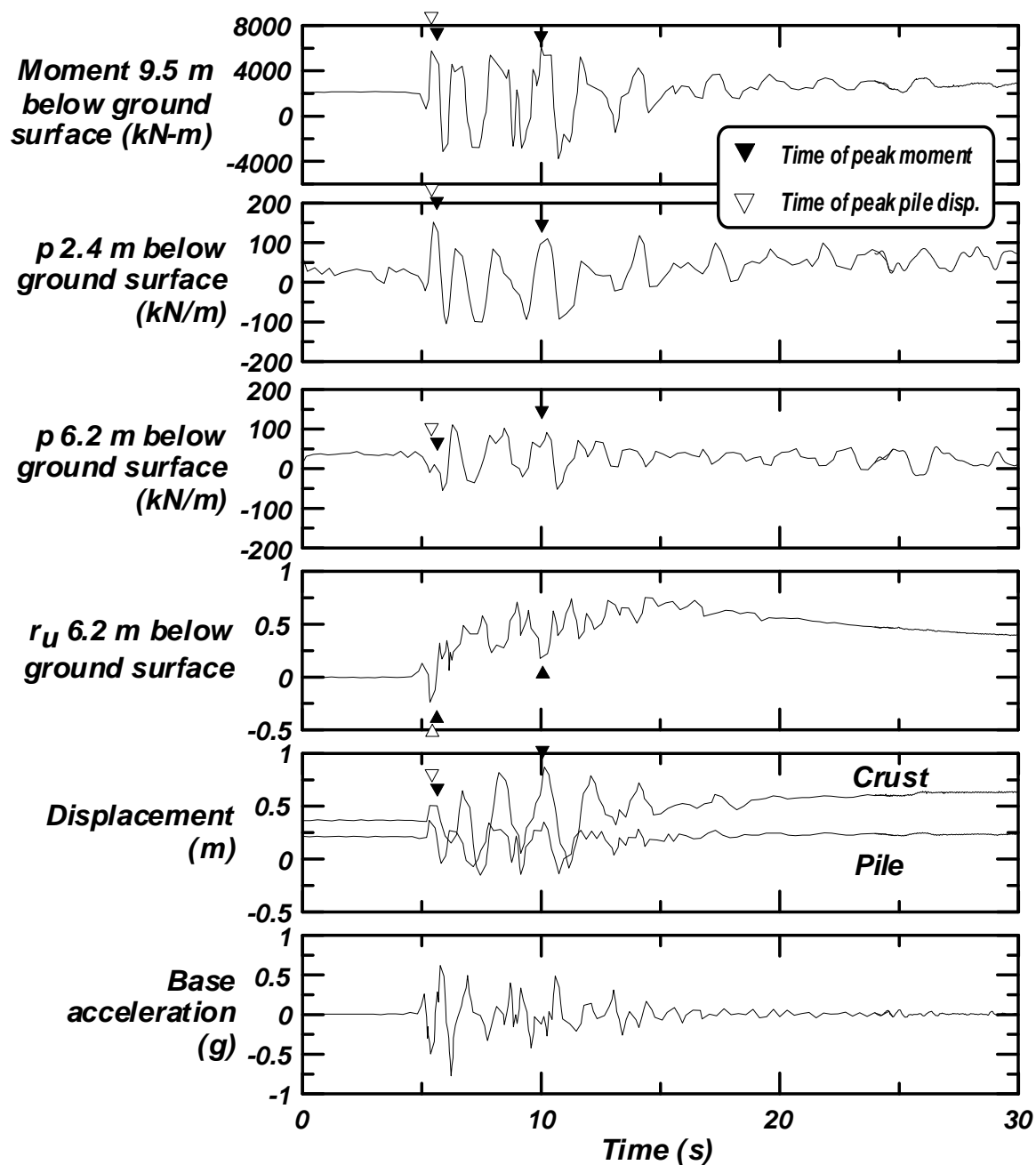
Figure 3-1: Representative time series from PDS01 for the large-diameter single pile, BP, for a large Kobe motion.
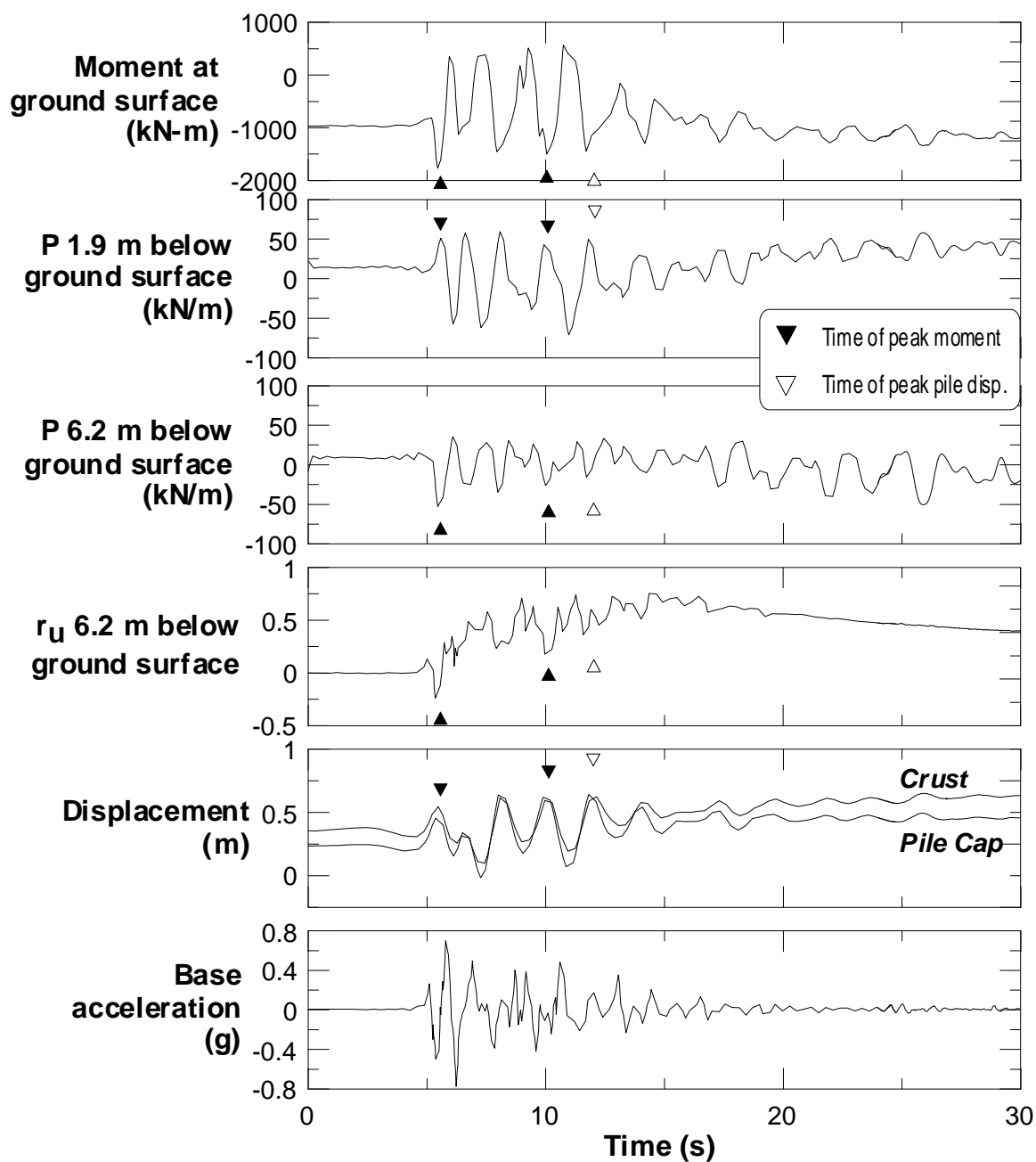
Figure 3-2: Representative time series from PDS01 for the medium-diameter pile on the upslope (north) side of the two-pile group, GN, for the large Kobe motion.
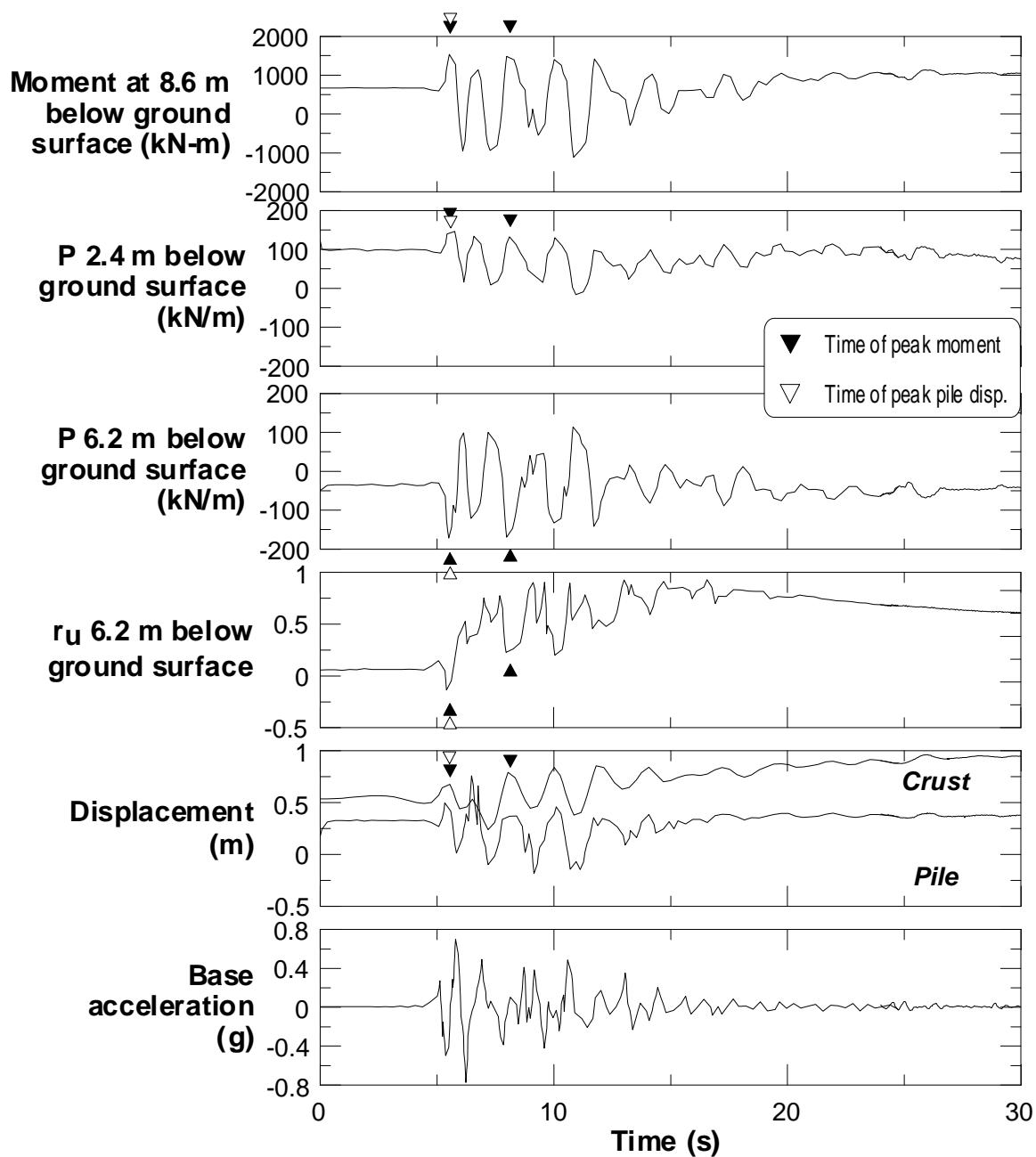
Figure 3-3: Representative time series from PDS01 for the medium-diameter single pile, MP, for the large Kobe motion.
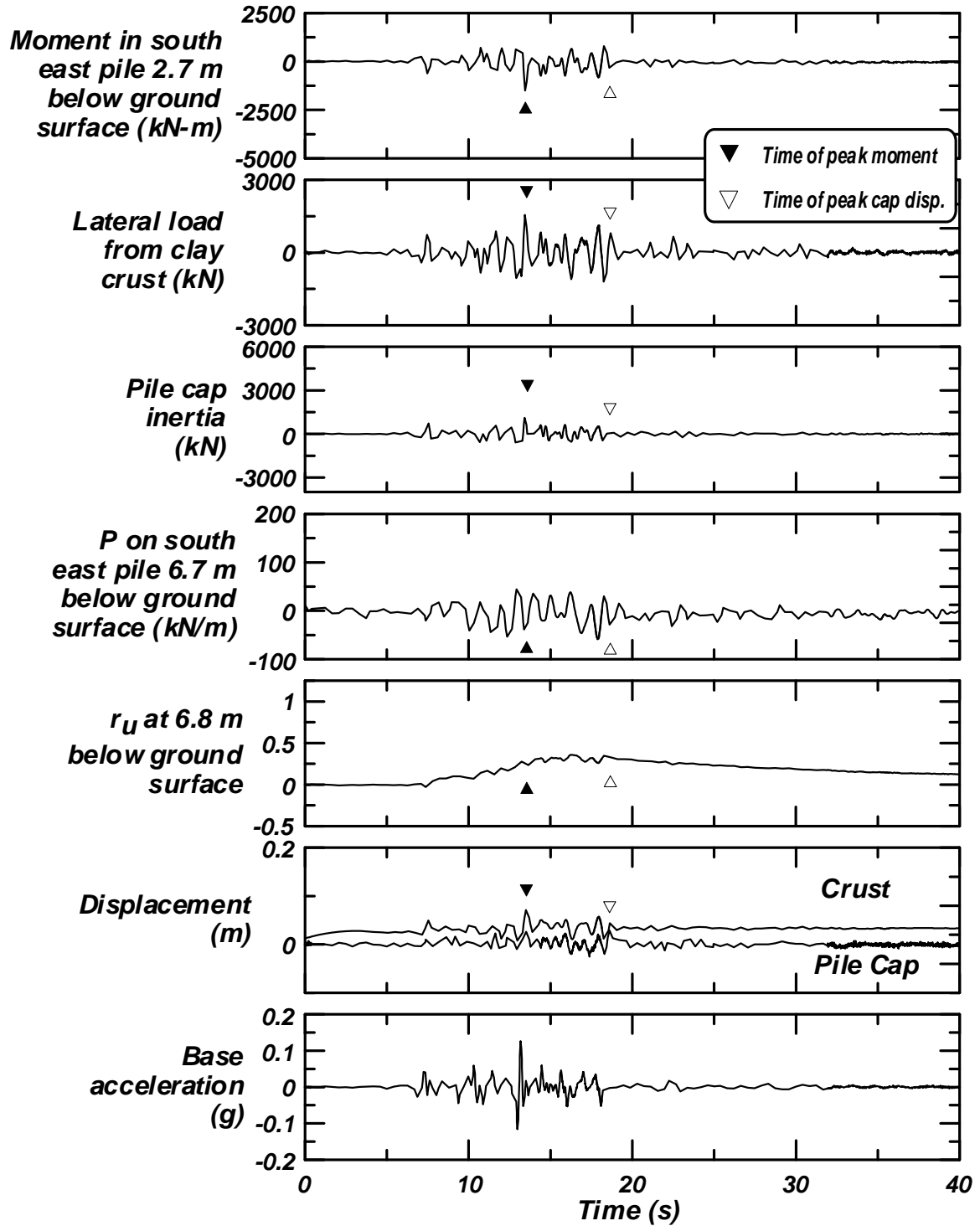
Figure 3-4: Representative time series from SJB03 for the small Santa Cruz motion.
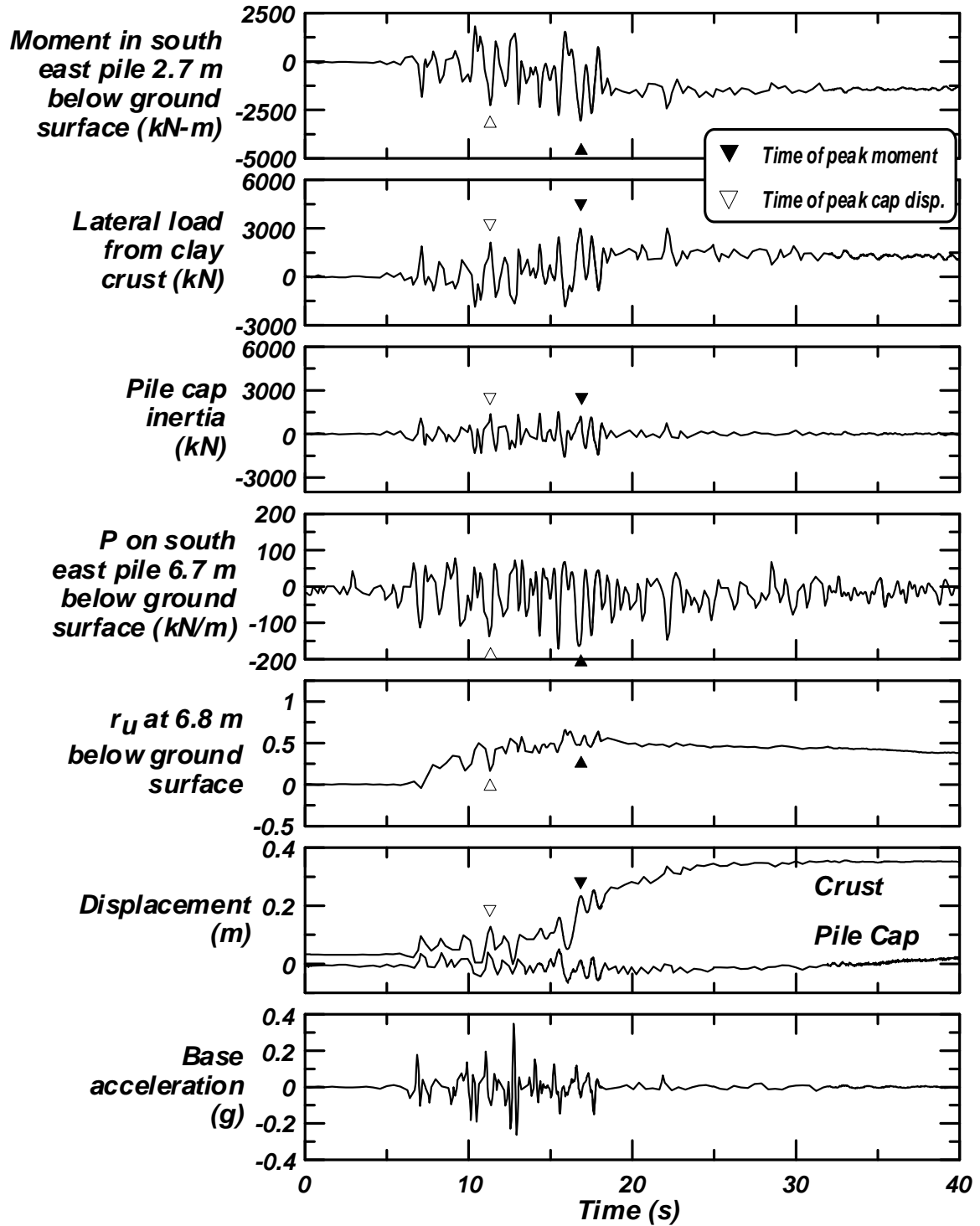
Figure 3-5: Representative time series from SJB03 for the medium Santa Cruz motion.
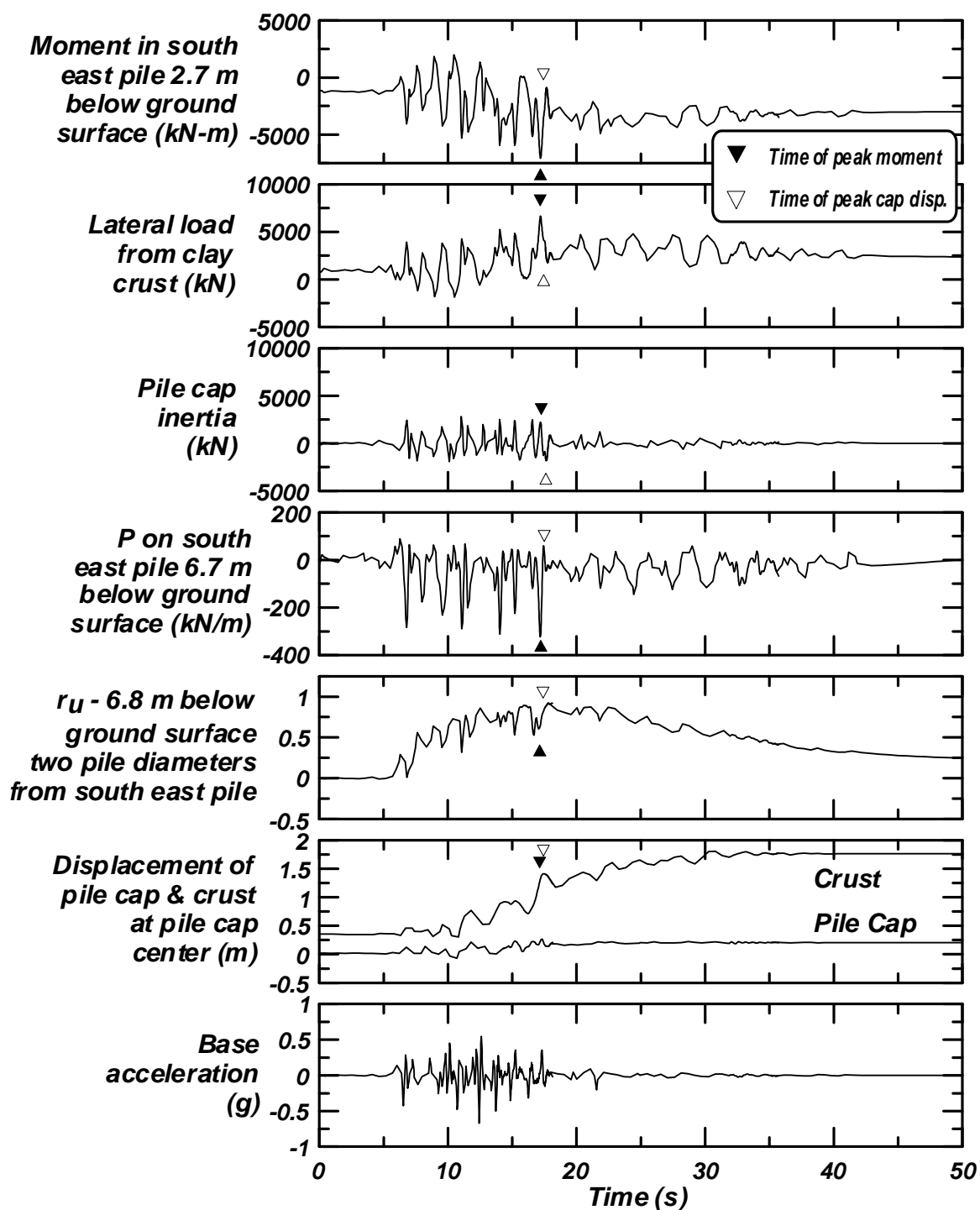
Figure 3-6: Representative time series from SJB03 for the large Santa Cruz motion.
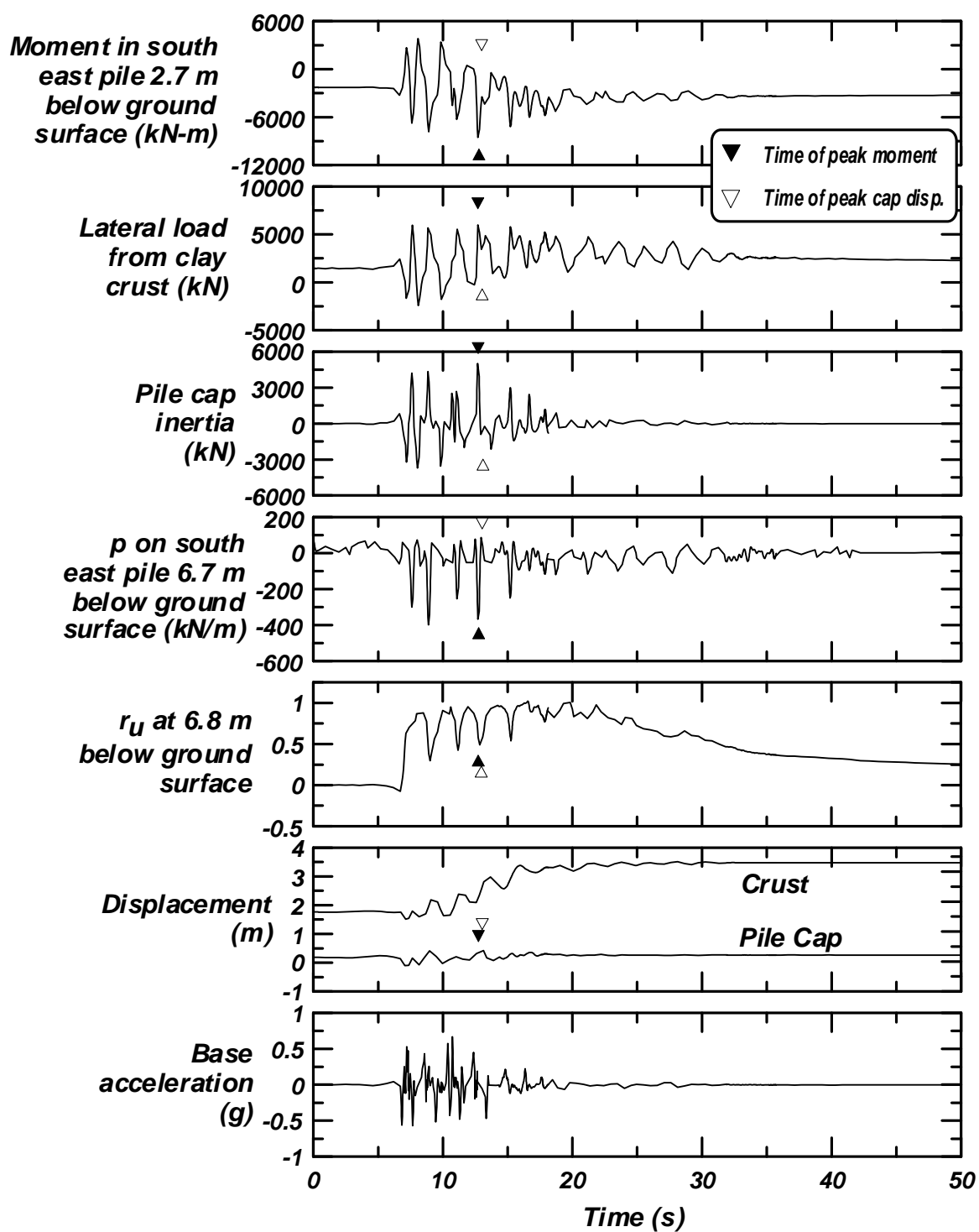
Figure 3-7: Representative time series from SJB03 for the large Kobe motion.
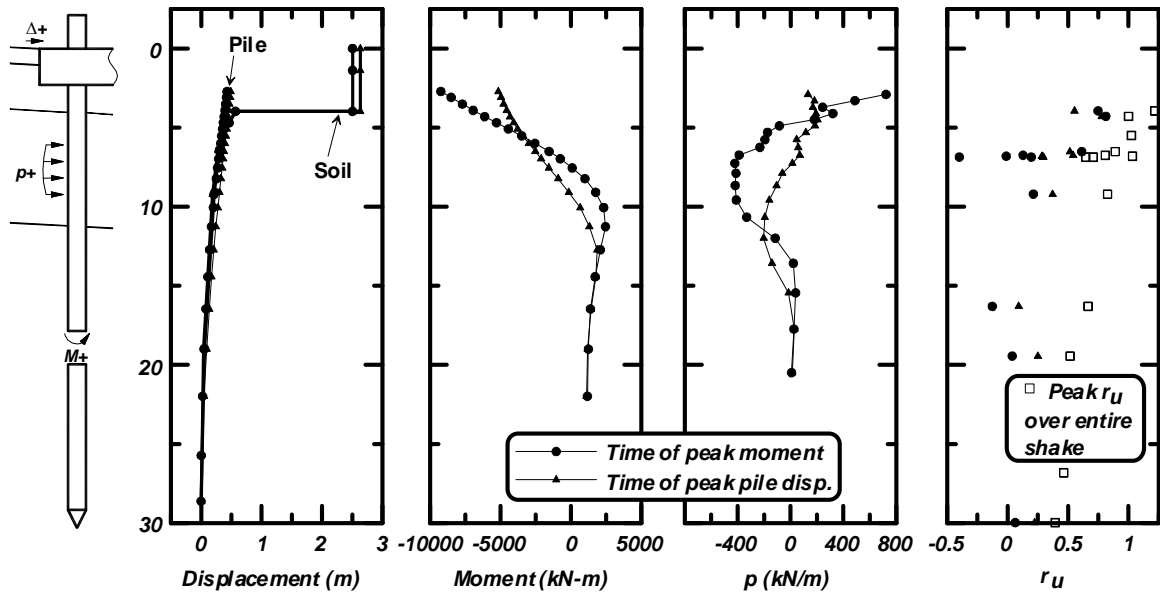
Figure 3-8: Snapshots of displacement, bending moment, p and r_u at the time of peak bending moment and at the time of peak pile cap displacement from SJB03 during the large Kobe motion.
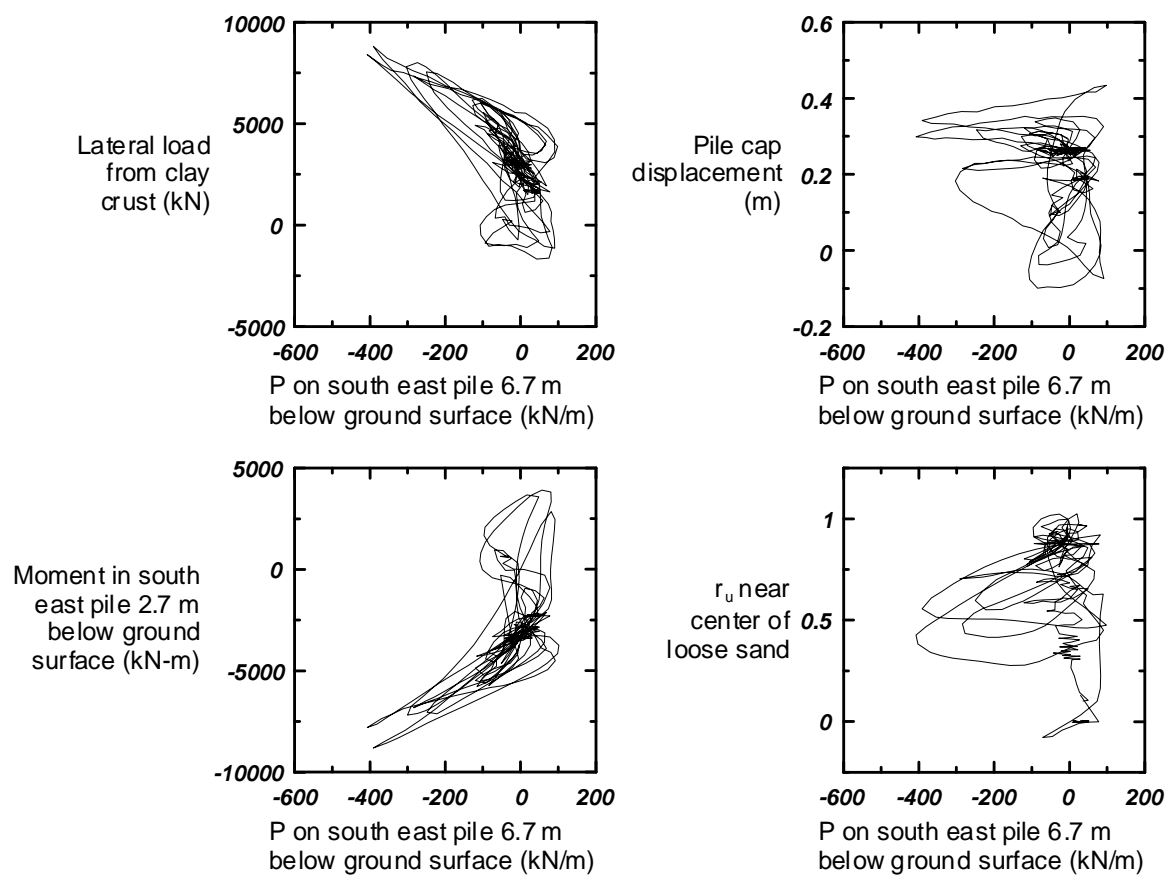
Figure 3-9: Cross-plots of crust load, cap displacement, bending moment and r_u with subgrade reaction between pile and liquefied sand.
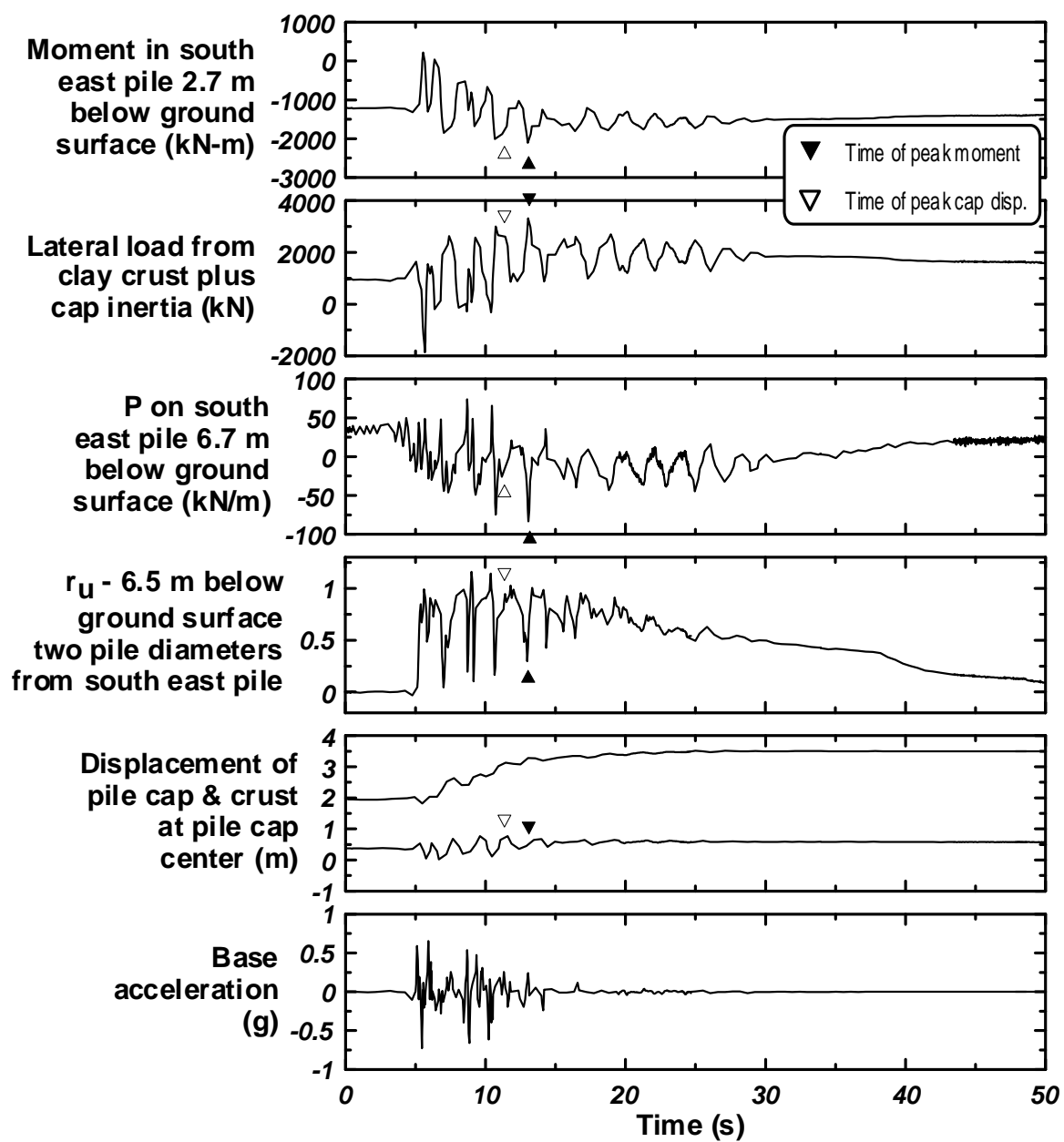
Figure 3-10: Representative time series from PDS03 for a large Kobe motion.
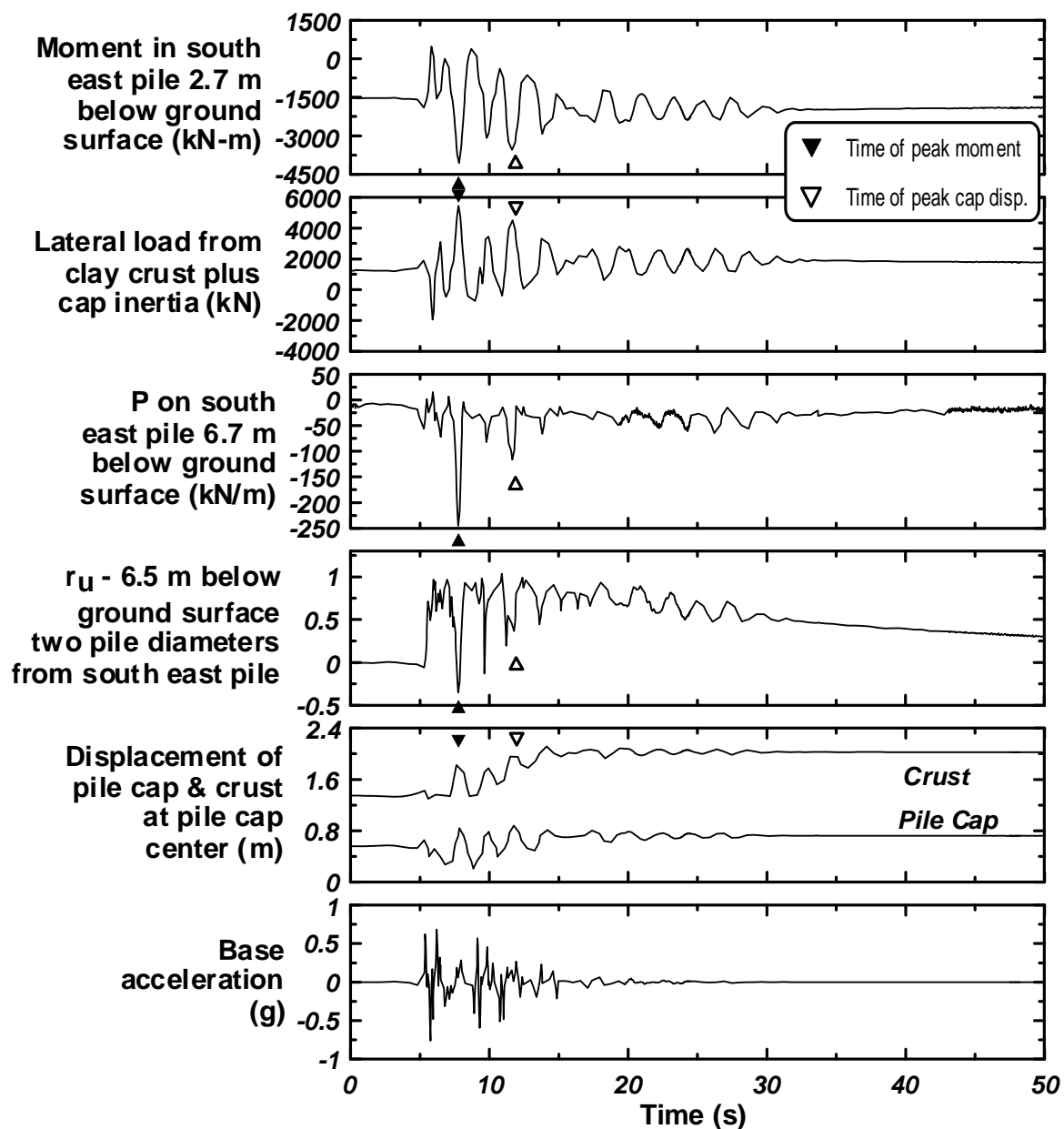
Figure 3-11: Representative time series from SJB01 for the second large Kobe motion.
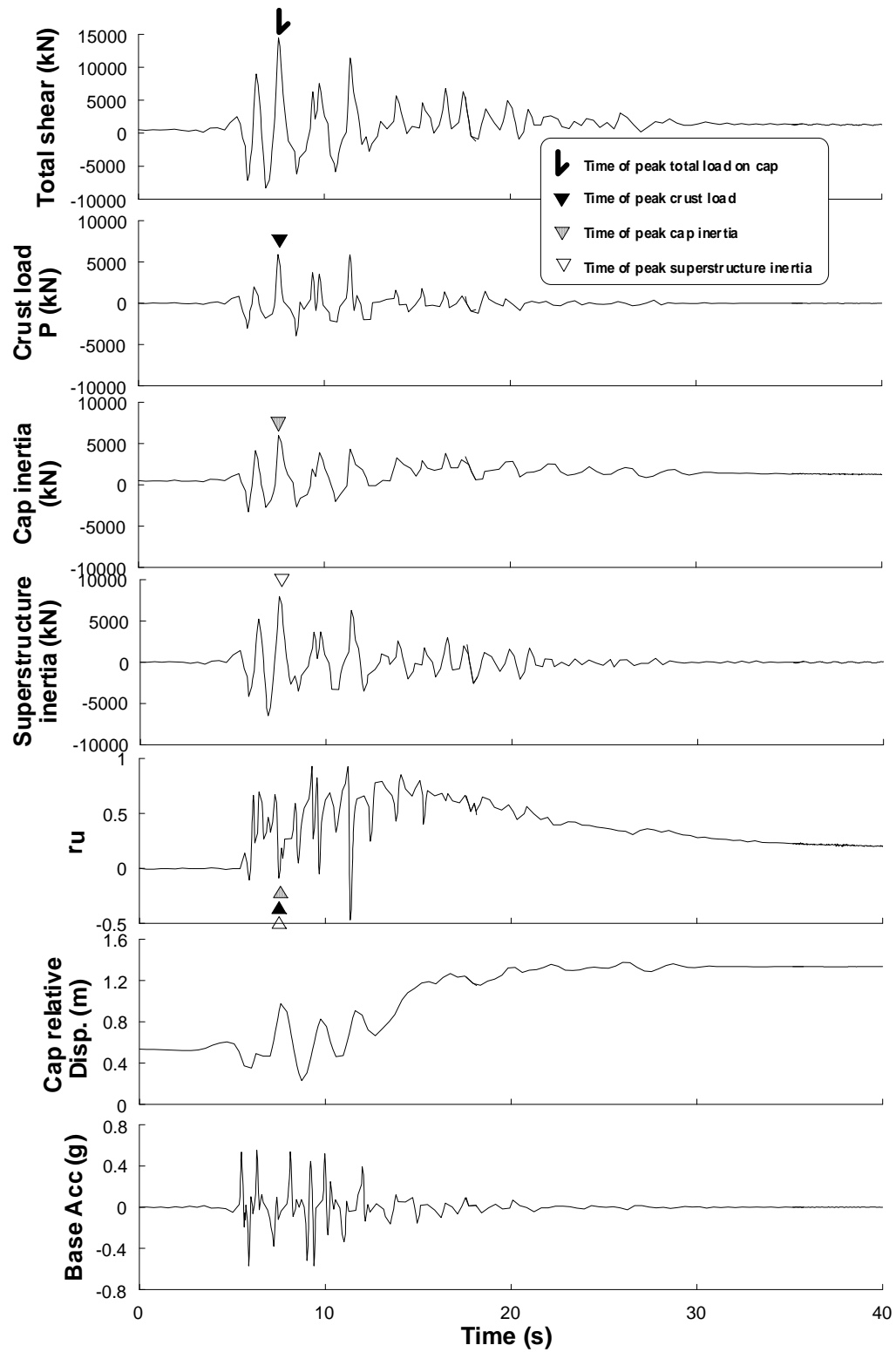
Figure 3-12: Representative time series from DDC01 for the large Kobe motion.
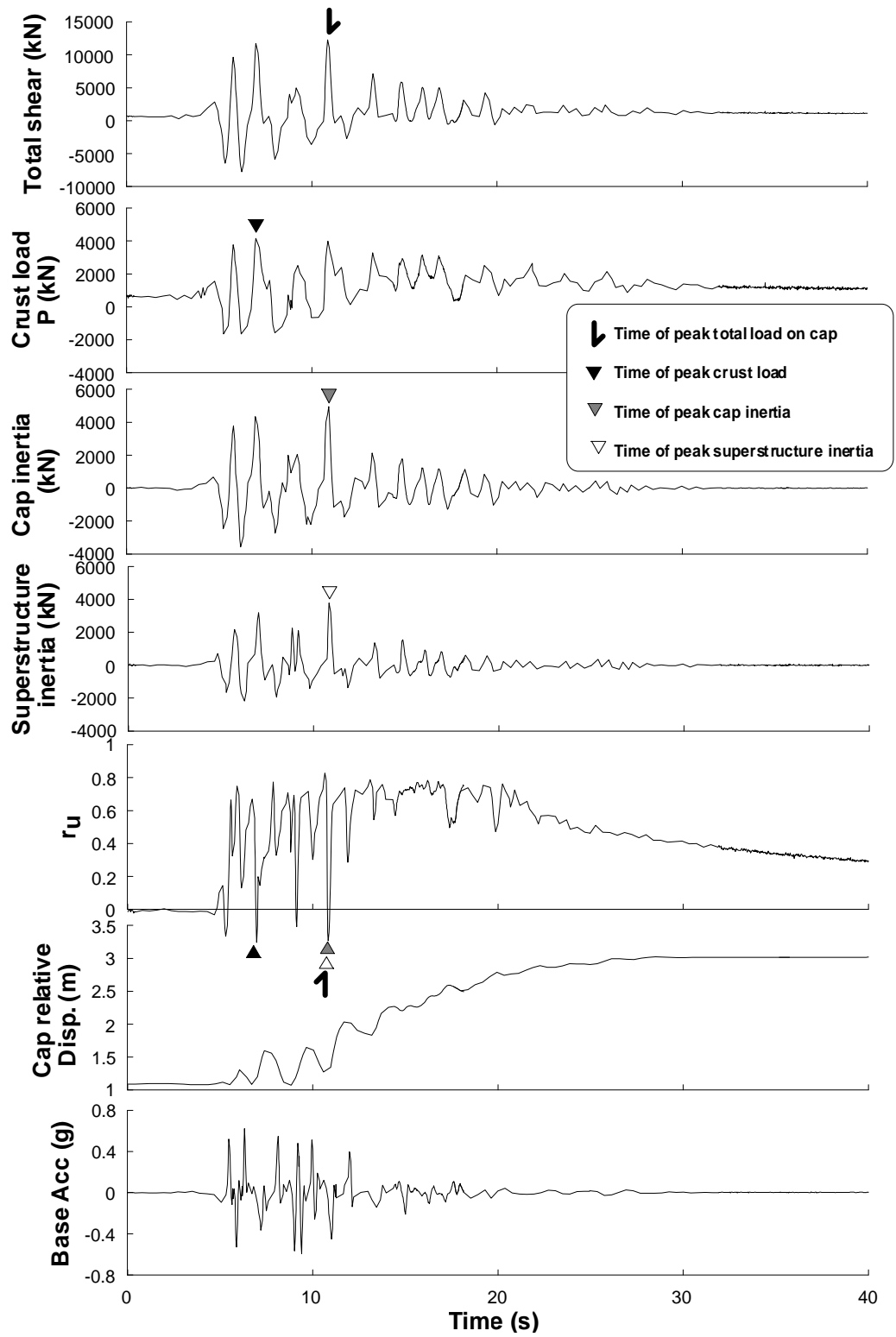
Figure 3-13: Representative time series from DDC02 for the large Kobe motion.
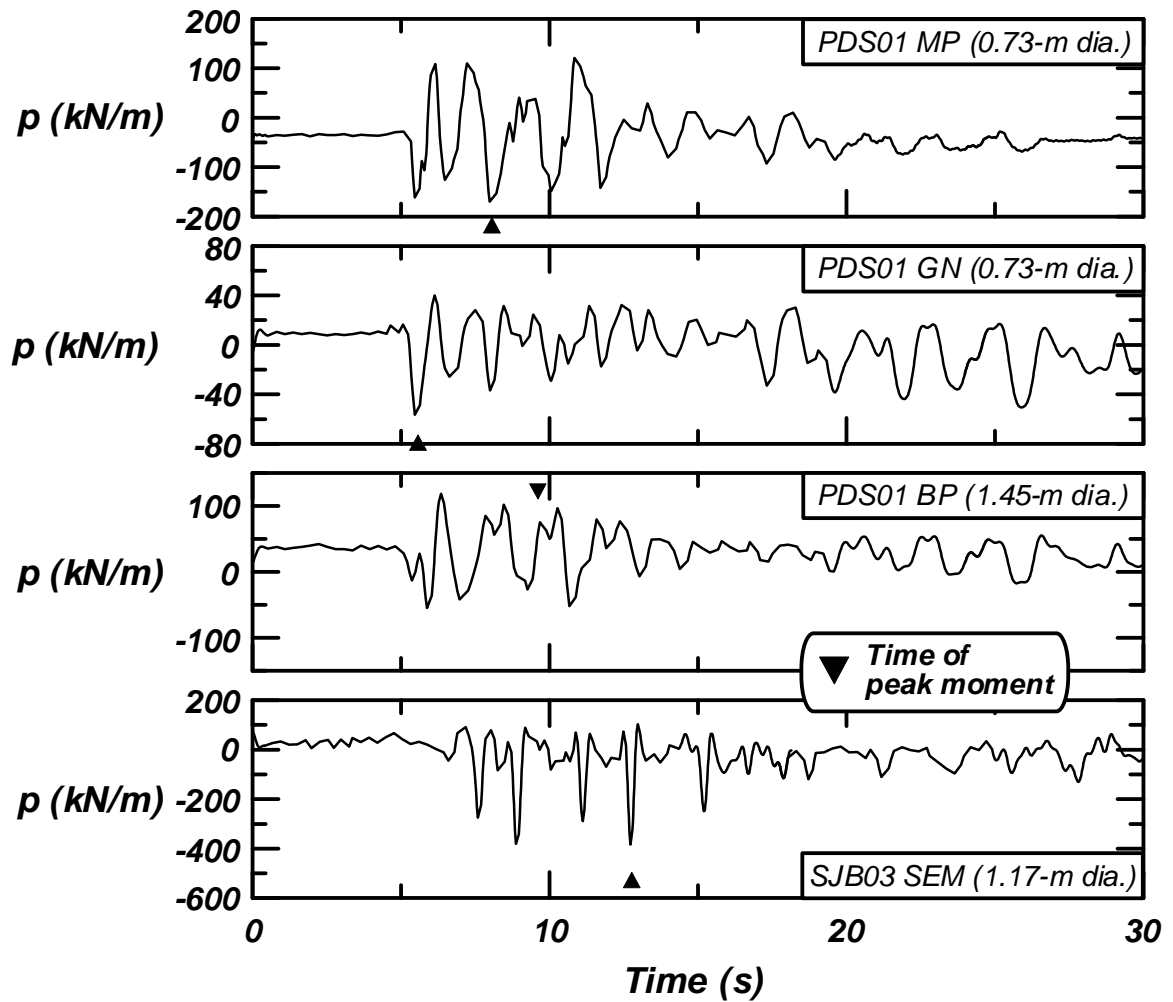
Figure 3-14: Time series of subgrade reaction between piles and liquefiable sand for MP, GN and BP from PDS01 and SEM from SJB03 for a large Kobe motion.
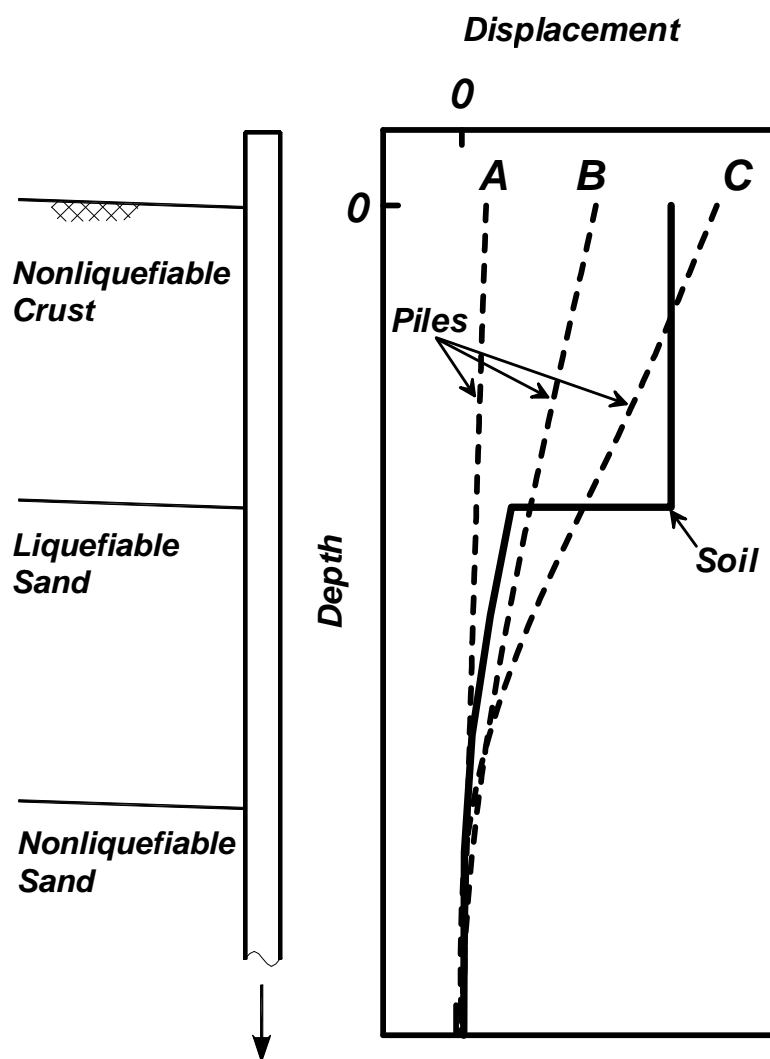
Figure 3-15: Schematic of soil and pile displacements for cases where piles resisted the full downslope crust load and (A) mobilized downslope driving loads in the liquefied sand or (B) mobilized upslope resisting loads in the liquefied sand, and a case where the pile (C) was too flexible and/or weak to mobilize the full downslope crust load.
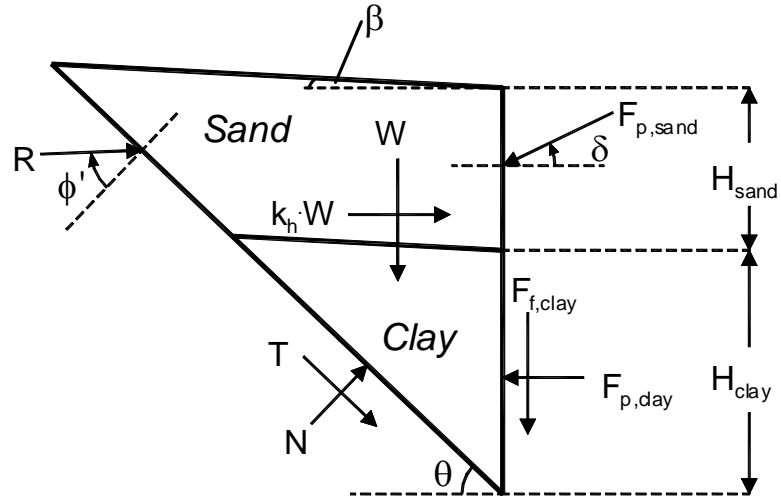
Figure 3-16: Free-body diagram of passive failure wedge for Coulomb-based analysis of passive earth pressure in a layered soil deposit.
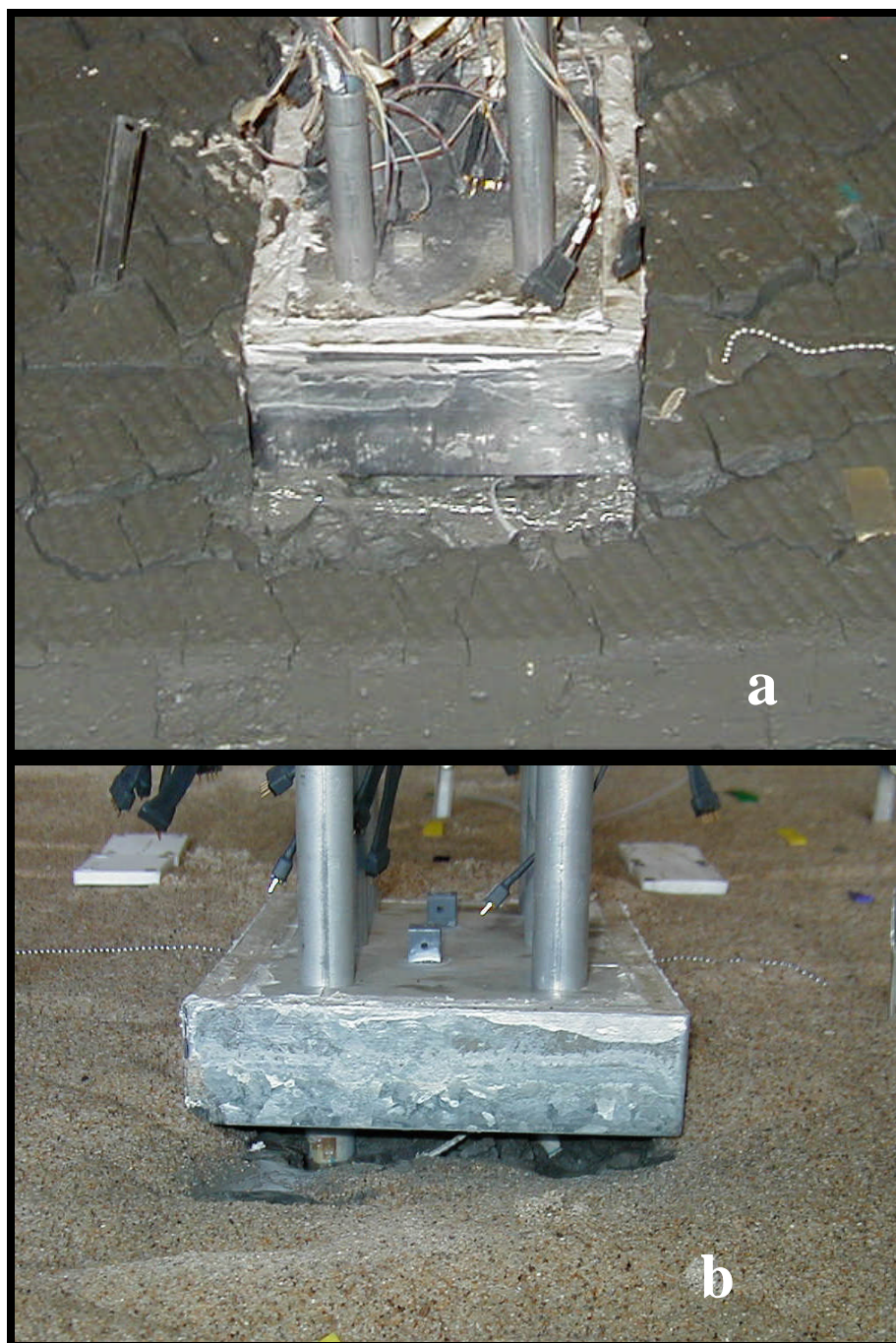
Figure 3-17: Gaps at downslope face of pile caps during model dissection after shaking for (a) SJB02 and (b) SJB03.
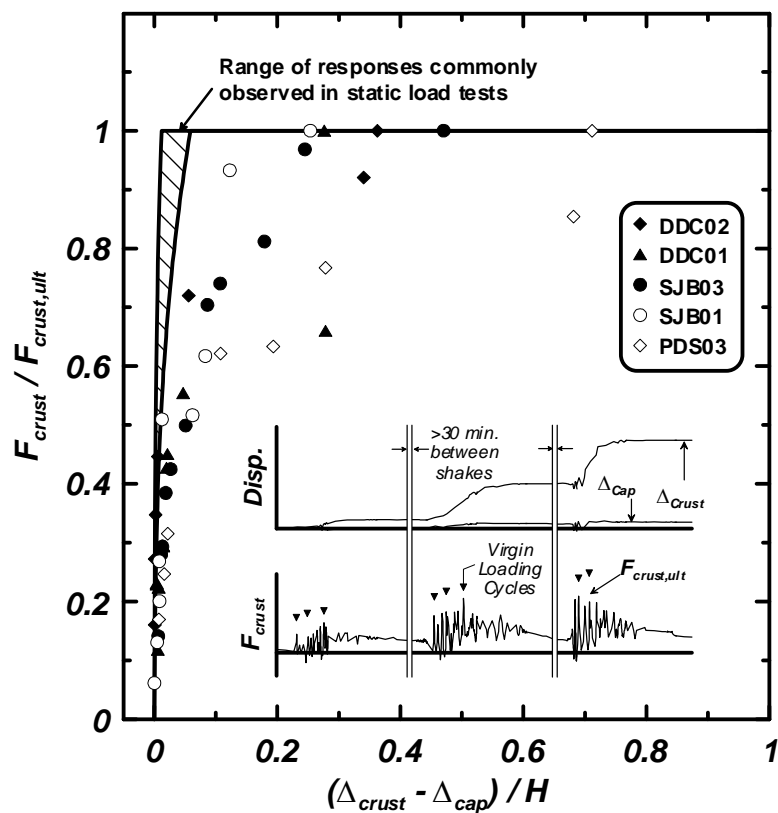
Figure 3-18: Normalized lateral load from the surface crust versus relative cap-soil displacement.
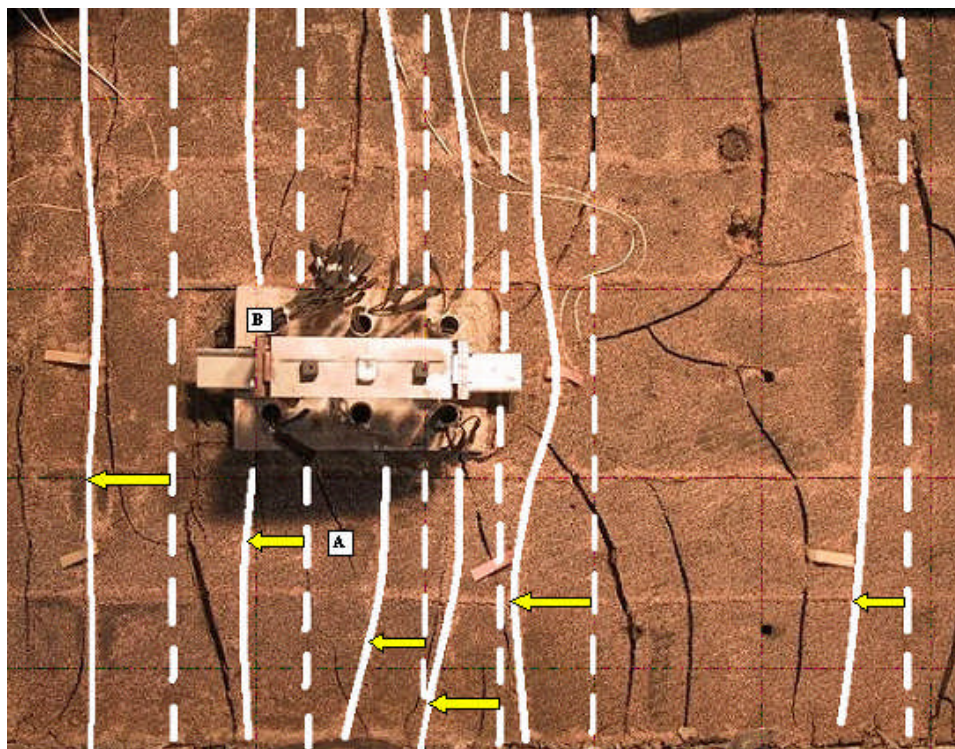
Figure 3-19: Photograph looking down onto model DDC02 after the surface layer of sand had been removed (thin white lines show the positions before shaking while thick white lines show the positions after shaking.
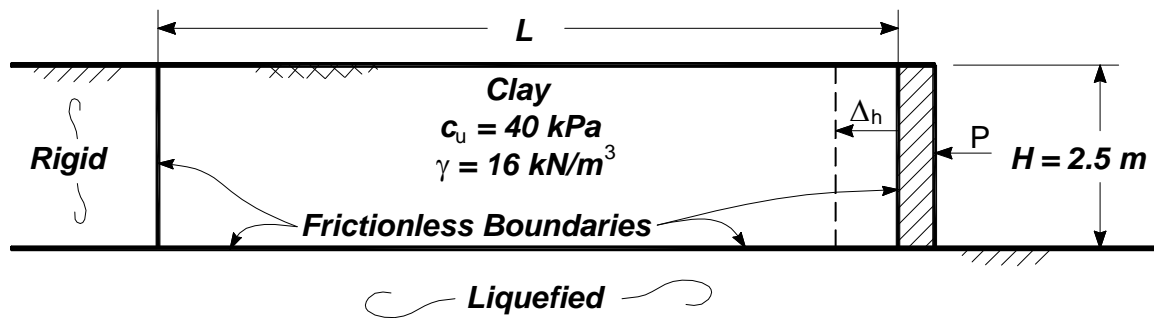
Figure 3-20: Two-dimensional idealization for illustrating the boundary conditions required for uniform Rankine stresses (after Terzaghi 1936), and the associated soft load transfer behavior.
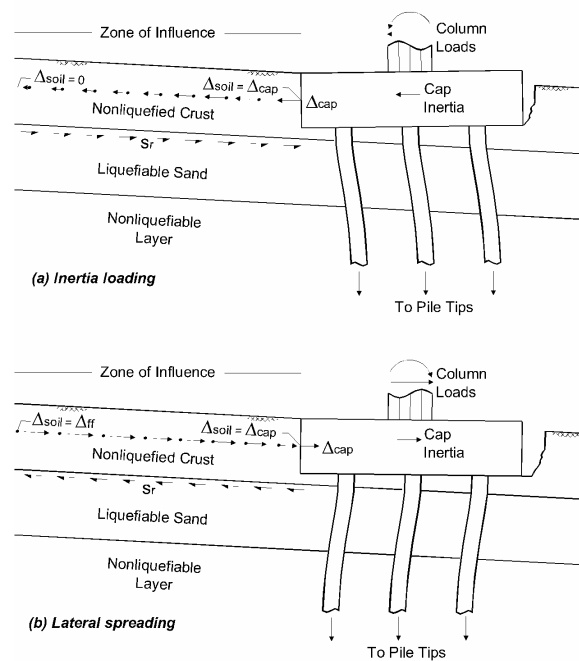
Figure 3-21: Schematic of load mechanisms between pile group and nonliquefied crust for (a) inertia loading in non-laterally spreading ground, and (b) a nonliquefied crust spreading downslope against a pile group.
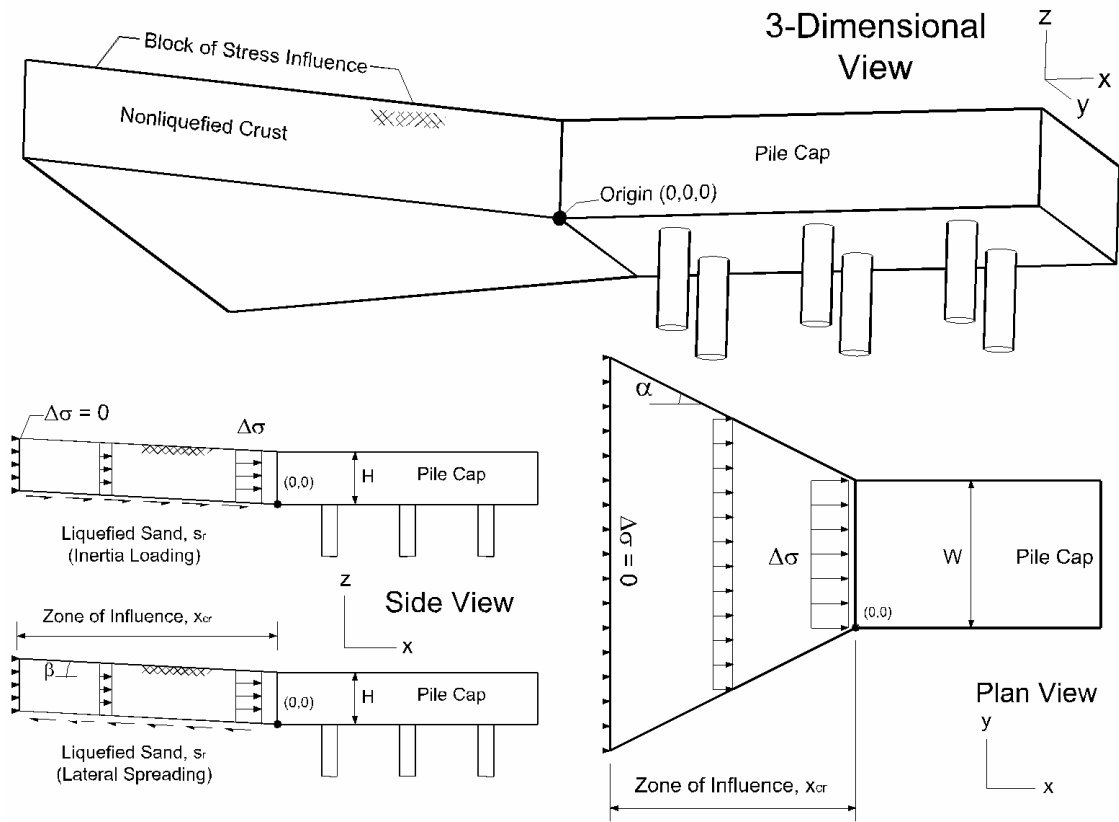
Figure 3-22: Simplified load transfer relation accounting for liquefied sand's residual strength and out-of-plane spreading of stresses in the crust.
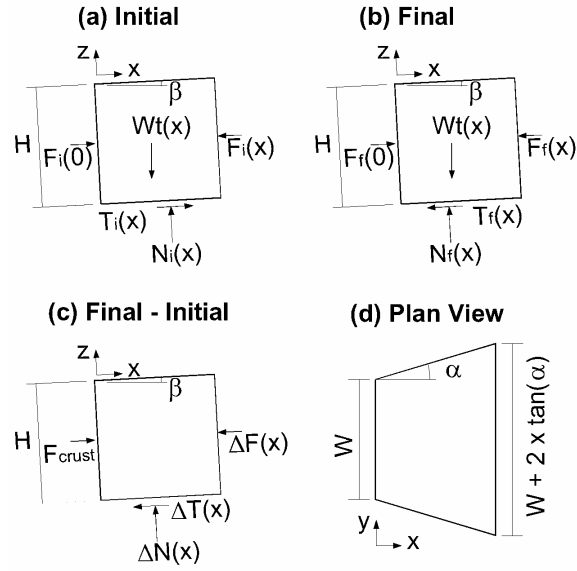
Figure 3-23: Free-body diagrams of nonliquefied crust layer for load transfer model for inertia loading.
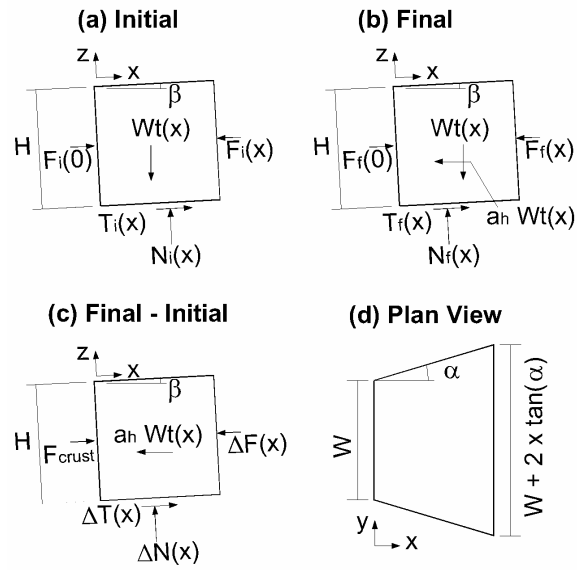

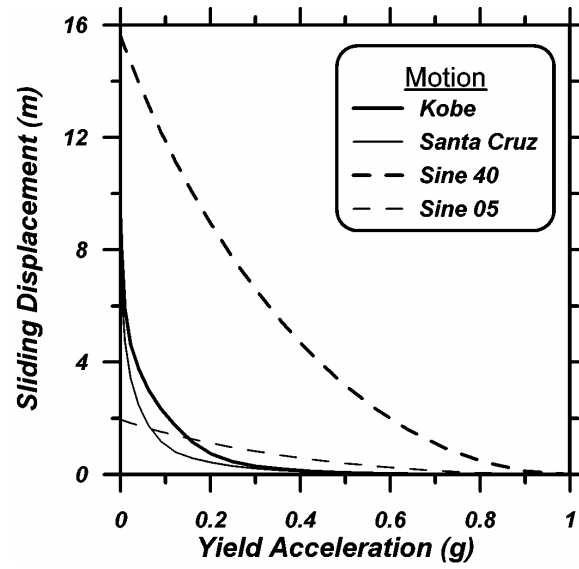**Figure 3-24: Free-body diagrams of nonliquefied crust layer for load transfer model for lateral spreading.**

Figure 3-25: Newmark sliding block solutions of sliding displacement versus yield acceleration with a_{max} scaled to 1.0 g.
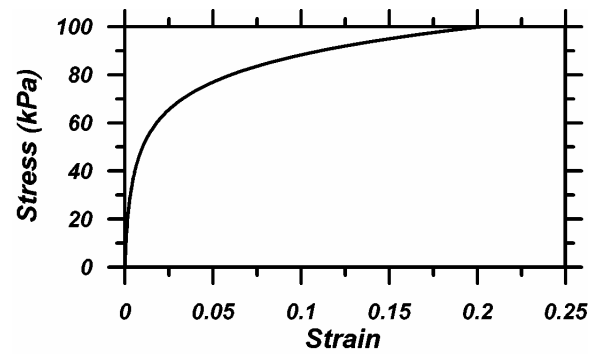

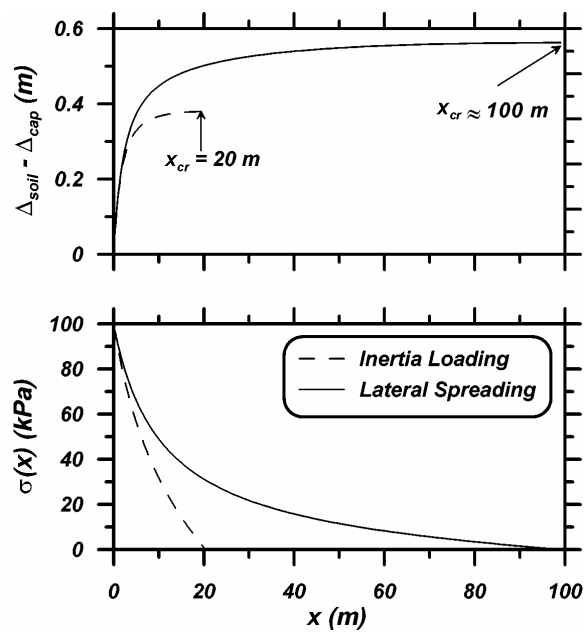**Figure 3-26: Stress-strain relation for baseline case.**

Figure 3-27: Distributions of soil / pile group relative displacement and horizontal stress from baseline case solutions.
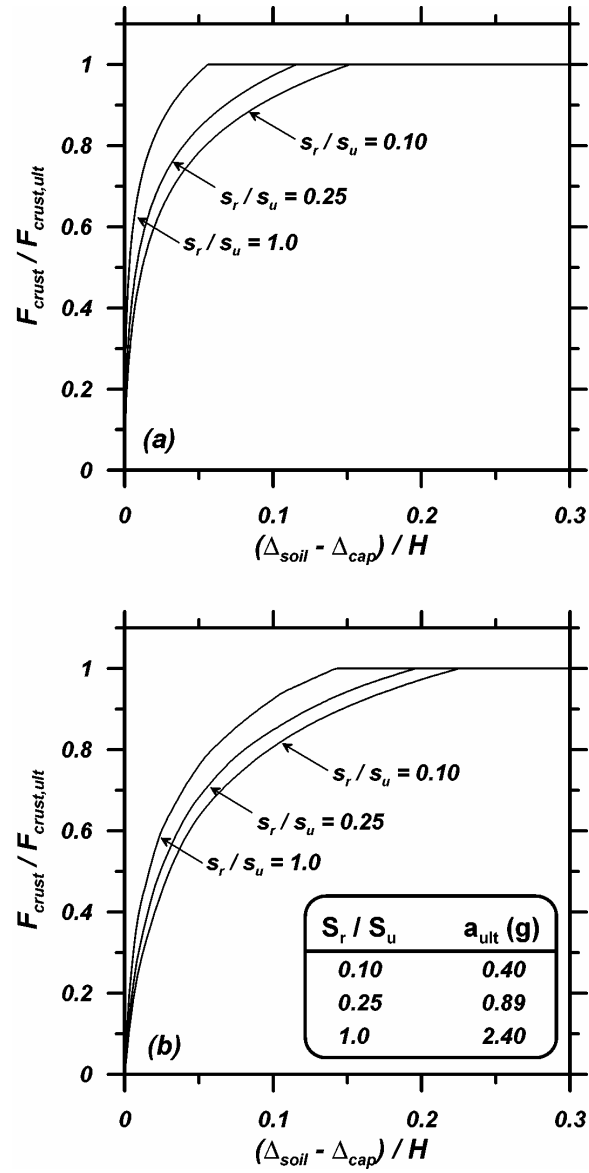
Figure 3-28: Influence of ratio of liquefied sand residual strength to crust undrained shear strength (s_r / s_u) on load transfer relation for (a) inertia loading and (b) lateral spreading.
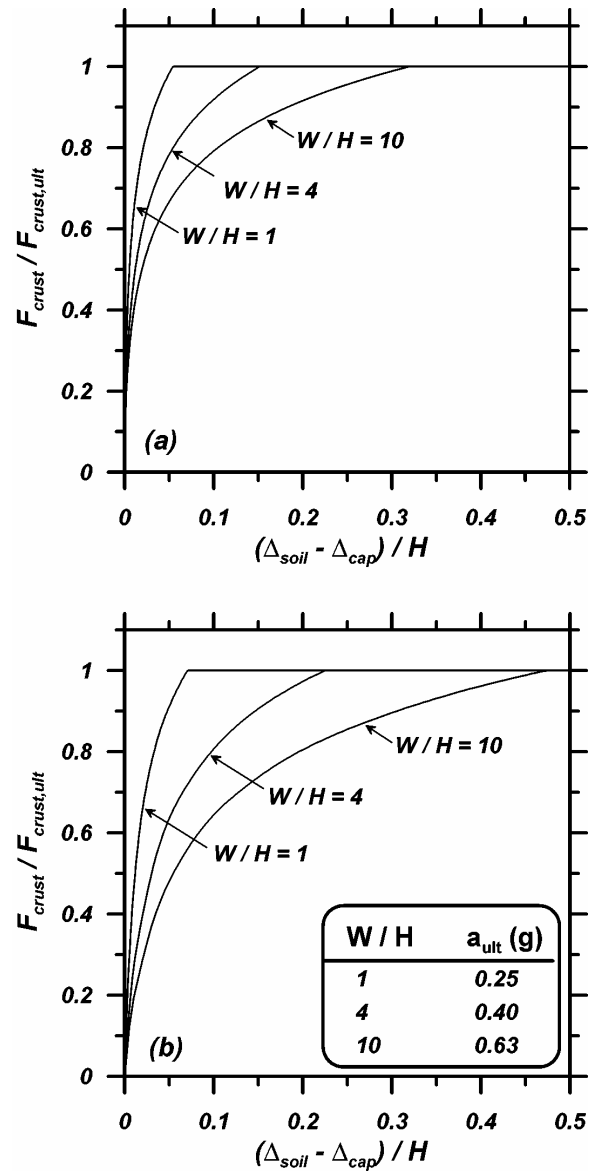
Figure 3-29: Influence of ratio of pile cap width to layer thickness on load transfer relation for (a) inertia loading and (b) lateral spreading.
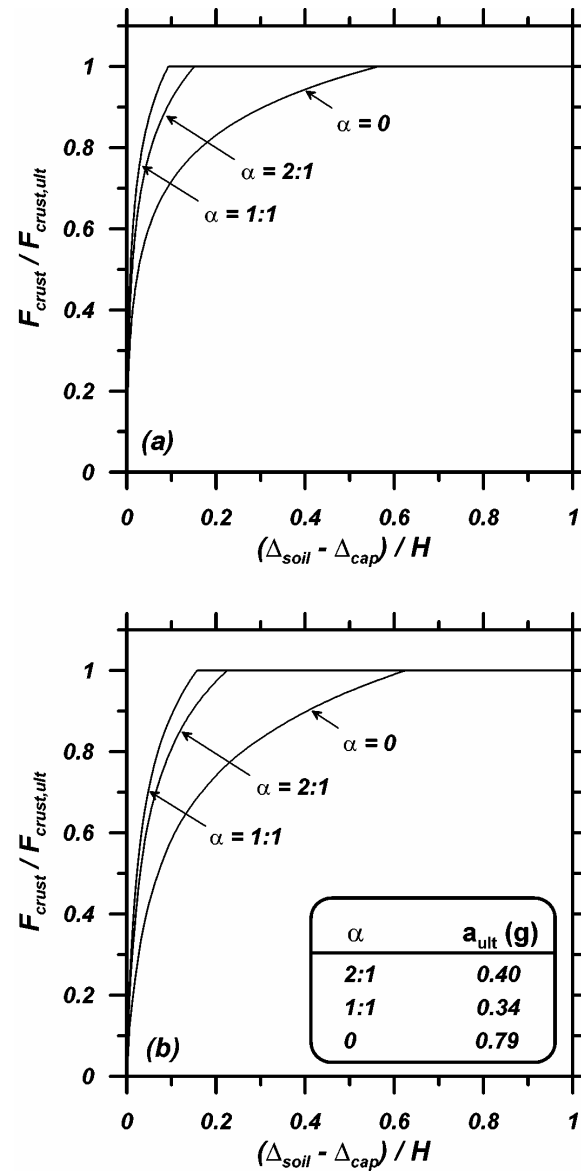
Figure 3-30: Influence of angle of out-of-plane stress spreading on load transfer relation for (a) inertia loading and (b) lateral spreading.
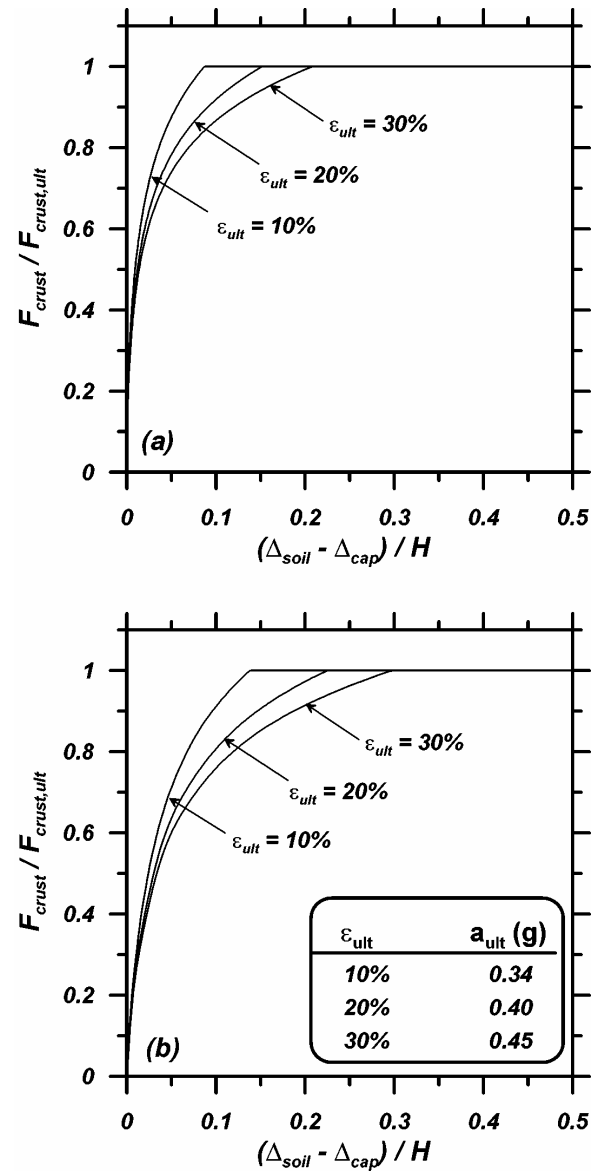
Figure 3-31: Influence of strain at ultimate stress on load transfer relation for (a) inertia loading and (b) lateral spreading.
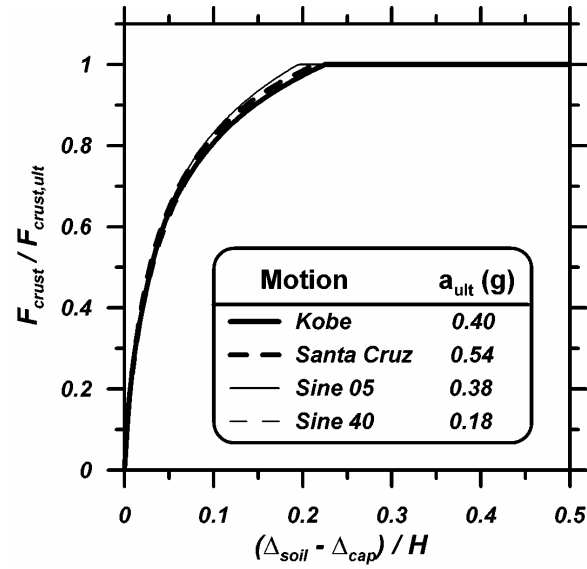
Figure 3-32: Influence of ground motion on load transfer relation for lateral spreading conditions.
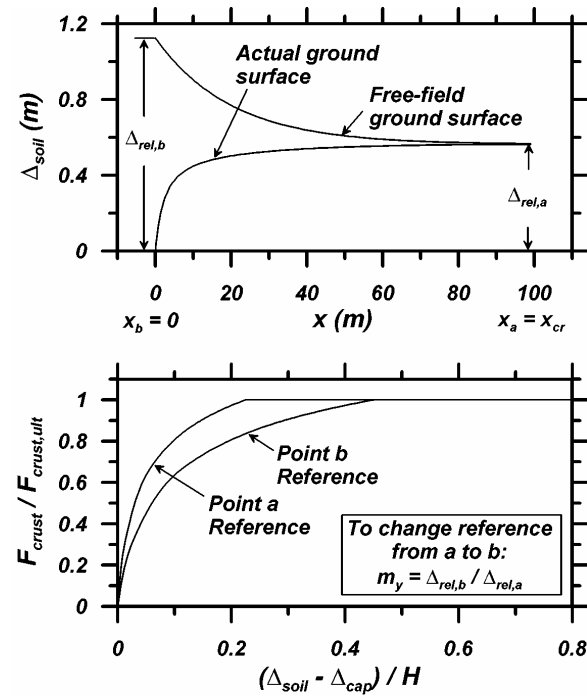
Figure 3-33: Influence of point of reference within lateral spread on load transfer relation.
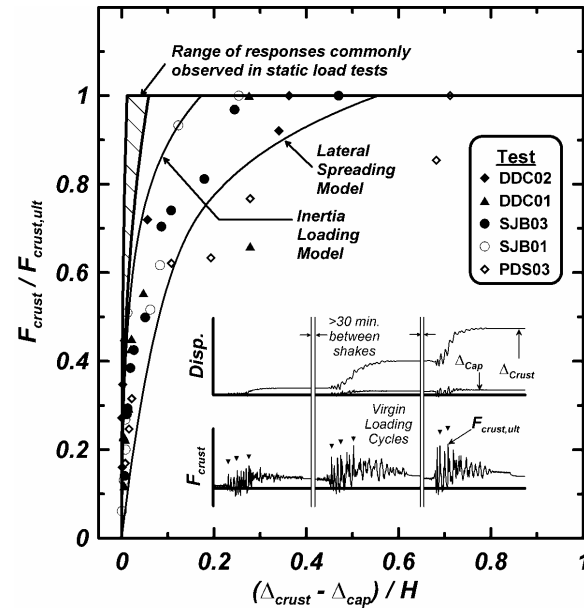
Figure 3-34: Comparison between measured and predicted load transfer behavior.
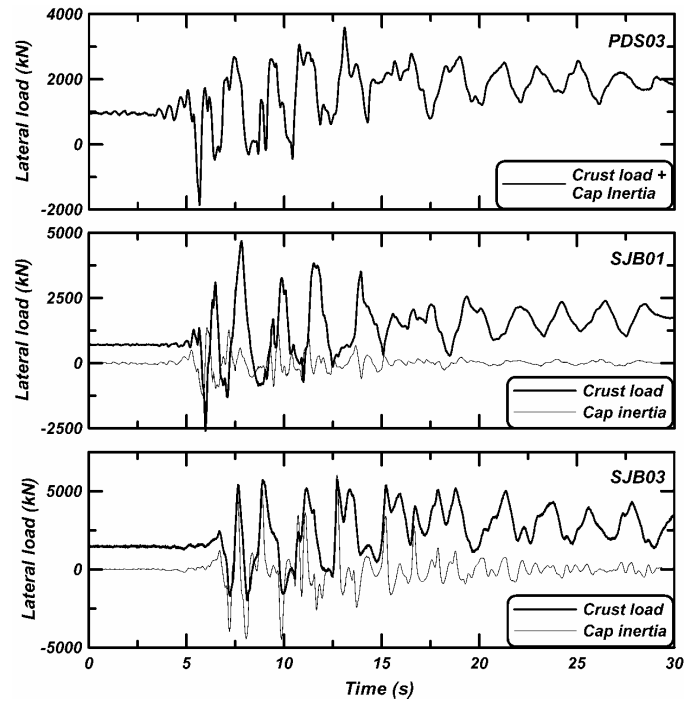
Figure 3-35: Time series of lateral crust load for PDS03, SJB01 and SJB03 for a large Kobe motion.
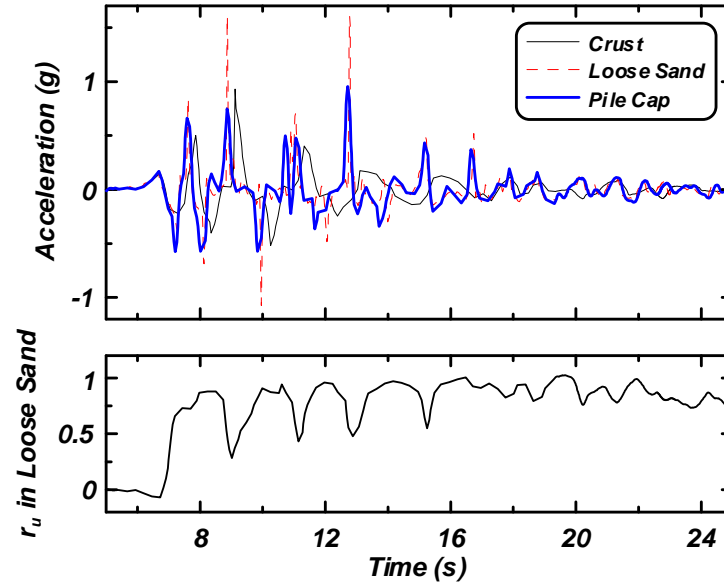
Figure 3-36: Time series of acceleration and excess pore pressure ratio that demonstrate complex dynamic soil-foundation interaction.
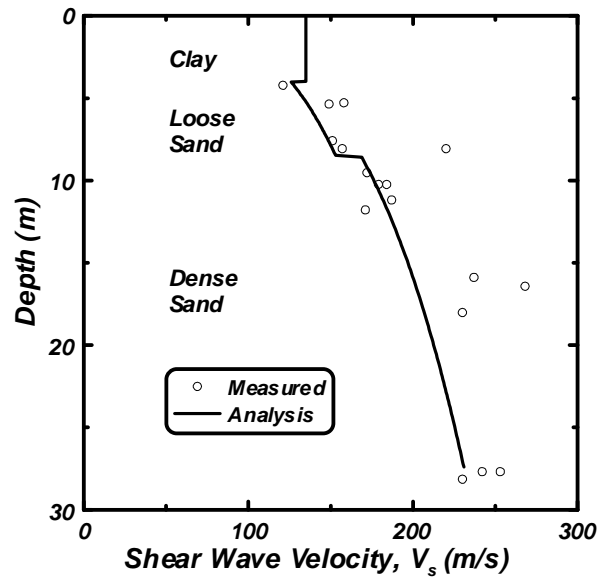
Figure 3-37: Shear wave velocity profile measured during centrifuge tests and used in SHAKE analyses.
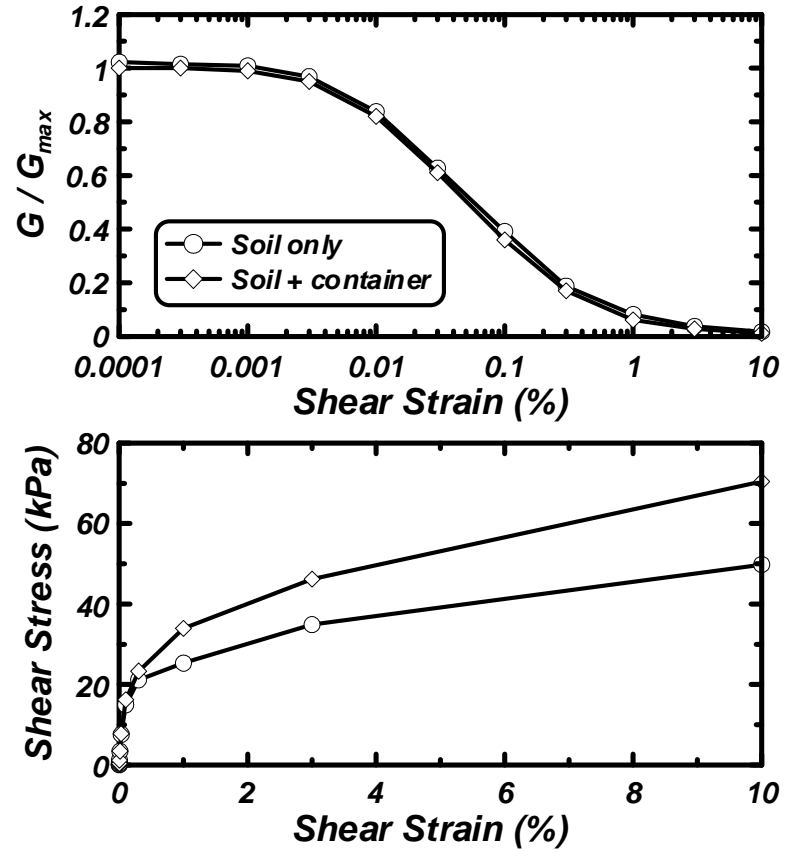
Figure 3-38: Influence of container stiffness on composite stress-strain response.
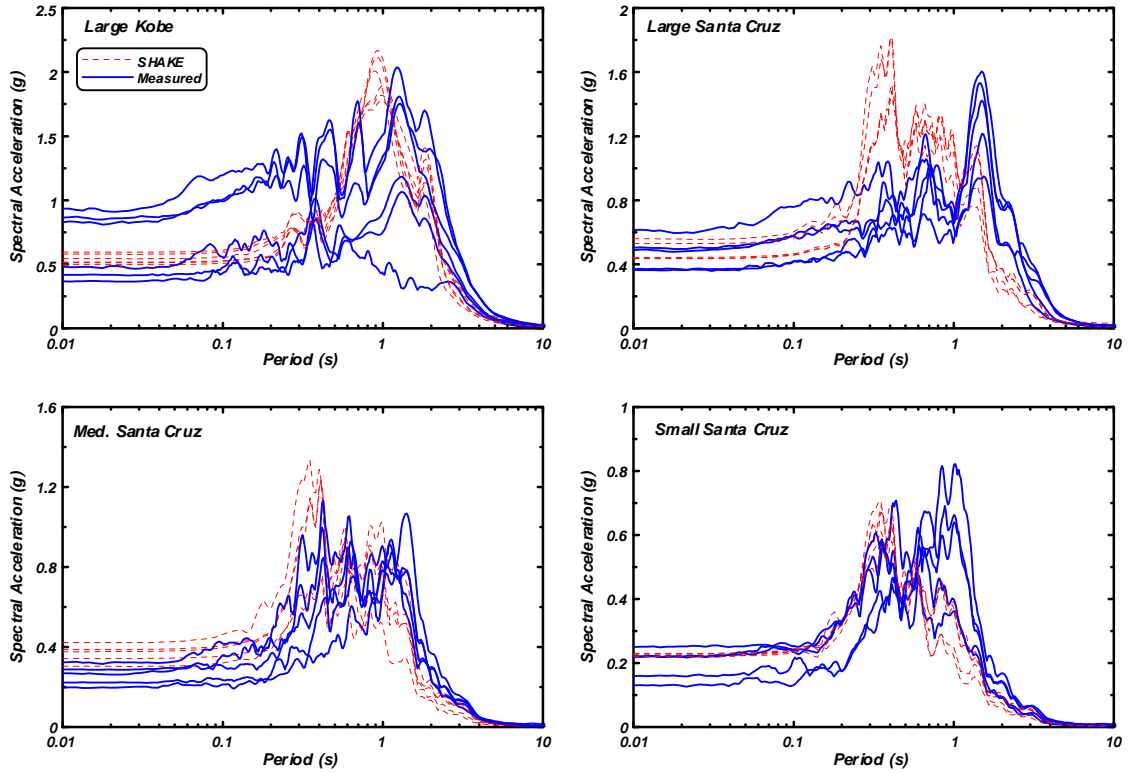
Figure 3-39: Acceleration response spectra (5% damping) for ground surface motions for five centrifuge tests.
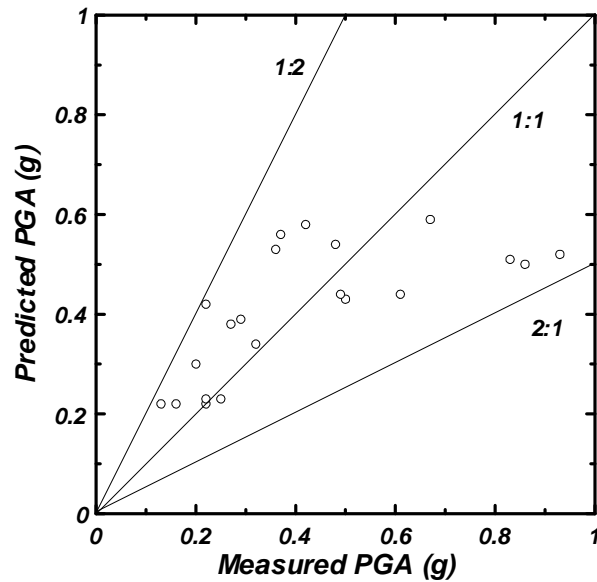
Figure 3-40: Peak ground acceleration measured during centrifuge tests versus peak ground acceleration predicted from SHAKE analyses.
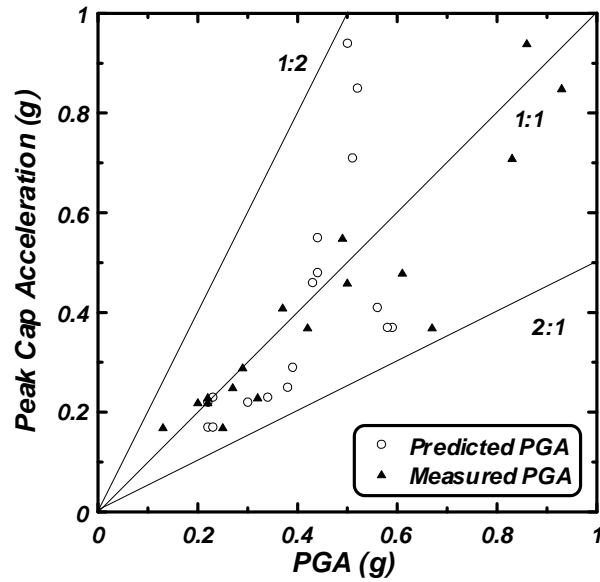
Figure 3-41: Peak pile cap acceleration versus measured peak ground surface acceleration (PGA) and predicted PGA.
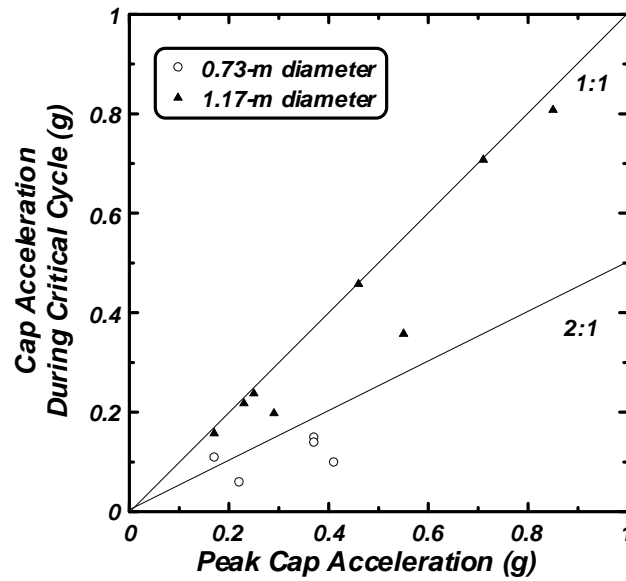
Figure 3-42: Pile cap acceleration during critical cycle versus peak measured pile cap acceleration.
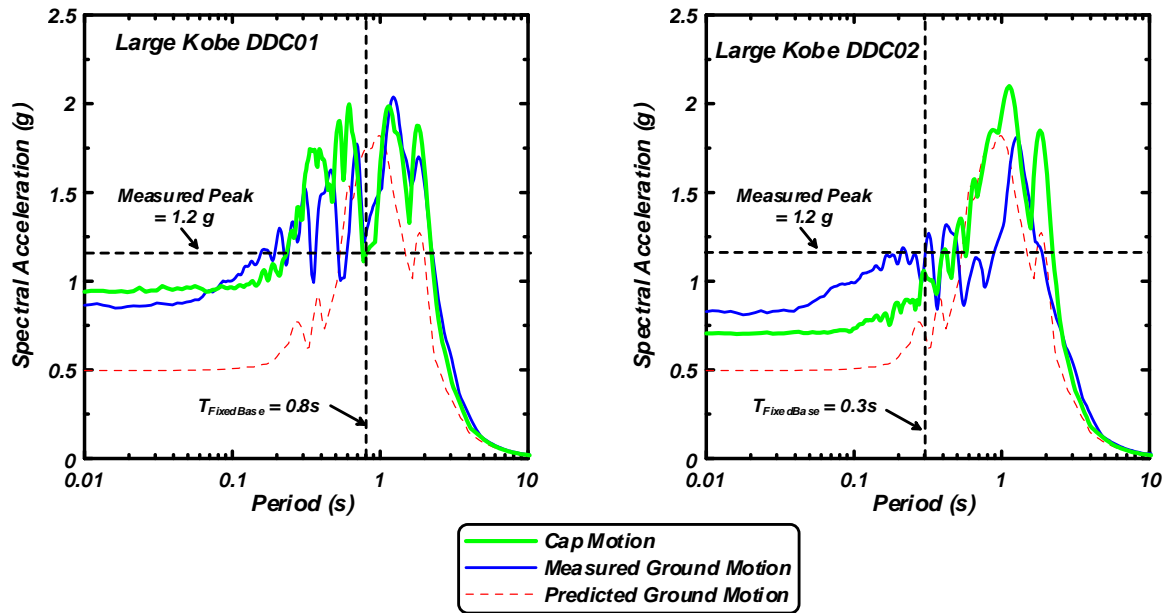
Figure 3-43: Response spectra from measured cap motion, measured ground motion, and predicted ground motion.
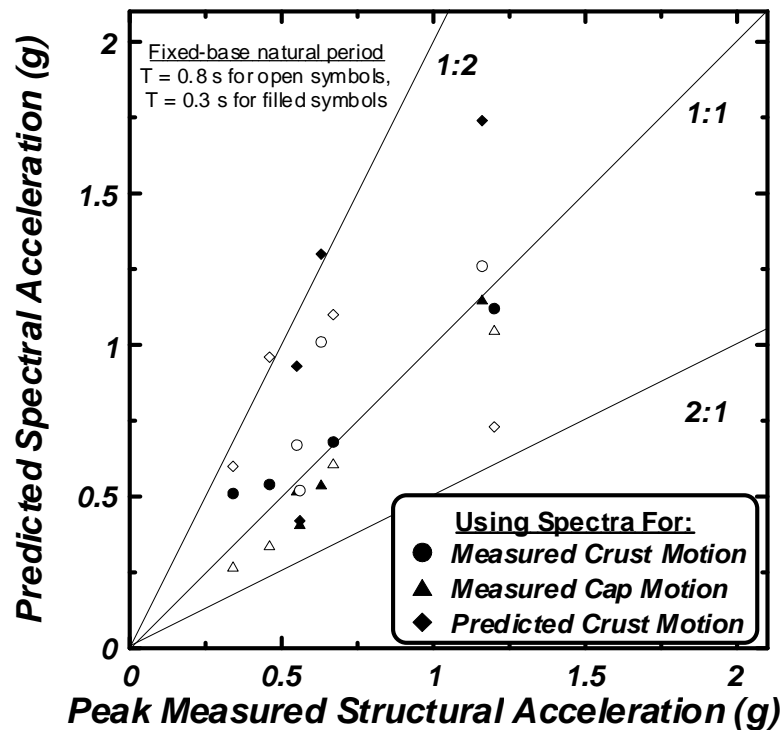
Figure 3-44: Predicted spectral acceleration versus peak measured structural acceleration from three different response spectra.
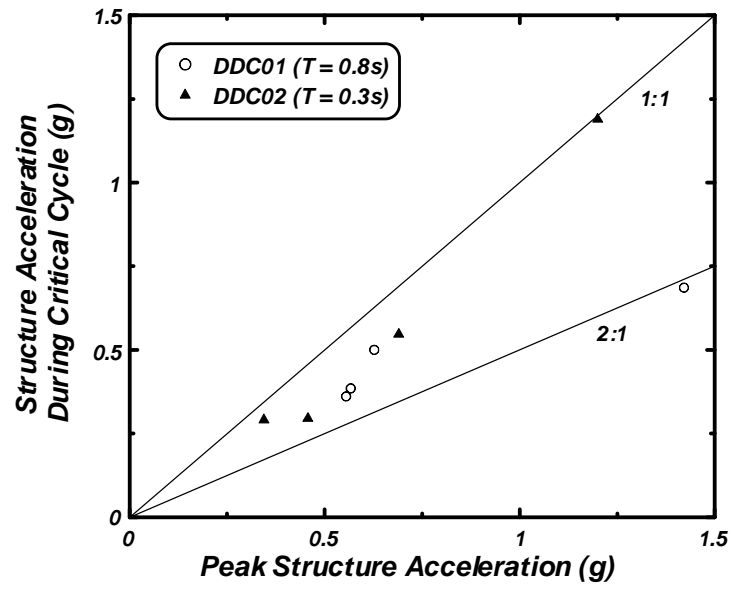
Figure 3-45: Structural acceleration during critical cycle (peak bending moment in piles) when peak crust load occurred versus peak structural acceleration.

CHAPTER FOUR

4. STATIC-SEISMIC DESIGN GUIDELINES AND ANALYSES

In this chapter, the purpose and objectives of the static-seismic analyses are presented first, followed by the procedures and parameters adopted in this study. Next, the numerical methods utilized in the study are presented, along with the computational tools developed to perform the analyses. A detailed example analysis of one of the pile foundations with the baseline parameter set is then presented to thoroughly demonstrate the analysis approach. Results from all of the pile foundations with the baseline set of input parameters are then summarized. The influence of alternative approximations or assumptions that differ from the baseline set of parameters is explored, and a sensitivity study is performed to identify the input parameters that most influence the analysis results.

4.1 PURPOSE AND OBJECTIVES

The purpose of performing static-seismic analyses of the pile foundations in the centrifuge tests is to assess the potential accuracy of such methods using a single set of adopted design guidelines, to identify the influence of alternative approximations that are different from the adopted guidelines, and to identify the input parameters that most

influence the results of the analyses. This section provides background information and sets the context in which the analyses were performed.

Two types of Beam on Nonlinear Winkler Foundation (BNWF) analyses were performed in this dissertation: BNWF_SD analyses with imposed Soil Displacements used to represent lateral spreading displacements, and BNWF_LP analyses with Limit Pressures used to represent lateral spreading loads (Fig. 4-1). The BNWF_LP approach inherently assumes that ground displacements are large enough to mobilize passive pressures of the spreading soil layers. The BNWF_SD approach more accurately represents lateral spreading demands than the BNWF_LP approach, but is often more difficult to implement because it requires imposing displacement boundary conditions on the free-ends of the soil springs. Hence, soil displacements in deep nonliquefiable layers are typically not included in BNWF_LP analyses. BNWF_LP analyses are often used at Caltrans, and similar analysis methods have been recommended by JRA (2002), and Dobry et al. (2003). Because both methods are widely used in design practice, studying them and comparing with the centrifuge test data is valuable.

From the outset, static analyses are acknowledged as simple, crude representations of complex dynamic conditions. Previous chapters of this dissertation identified many complex loading conditions that cannot be captured using static analysis methods (e.g. the influence of dilatancy on p-y behavior). Nevertheless, static methods have the advantage of being computationally simple to perform, while dynamic analyses that can conceptually more realistically capture complex seismic loading conditions are often too computationally intense to be justified for all but the most important projects, and typically lack the validation required to demonstrate they are more accurate than static

methods. Hence, static methods will continue to be a staple of design practice, and validating static methods with model studies and case histories is very valuable.

As an example of the complexity of the dynamic problem of pile foundations in liquefied and laterally spreading ground, Fig. 4-2 shows a cross-section of one of the centrifuge model pile foundations that was exposed during post-test excavation of the model. Part of the clay crust was dragged down into the sand layer during pile driving such that the piles contacted clay along much of their length in the sand layers. During shaking, gaps formed downslope of the piles and liquefied sand flowed up into the gaps. Therefore the downslope sides of the piles beneath the cap were in contact with sand rather than clay. In a typical analysis, static or dynamic, the soils in contact with a pile at a given depth are assumed to be the same as the soils that existed at that same depth prior to pile driving and earthquake shaking. During the centrifuge tests, however, the soils in contact with the piles were not necessarily the same as the soils in the vicinity of the piles prior to shaking, and movement of the soils adjacent to the piles caused by earthquake shaking further complicated the problem. These observations demonstrate the difficulty involved in accurately predicting the response of a pile foundation, and underscore the importance of accounting for uncertainty in design.

Singh (2002) performed static-seismic analyses of the single piles and two-pile group from test PDS01 with the intention of identifying a set of design guidelines that would reasonably capture the peak bending moments and pile displacements observed in the centrifuge tests. However, he found that different piles required different input parameters to match the test data. This finding was important because it prompted an understanding of the complex fundamental mechanisms that occurred in the centrifuge

models (Chapter 3 of this dissertation), but these fundamentals could not be distilled into rational static design guidelines that account for all of the various complexities. Hence, an objective of the analyses in this dissertation is to adopt a single set of design guidelines, apply them to static analyses of the entire suite of centrifuge tests, and subsequently observe the errors in predicting pile bending moments and pile cap displacements. Many of the guidelines used in this study were developed by first adopting existing guidelines for static pile loading conditions, and subsequently modifying them for the influence of liquefaction as observed in the centrifuge test data.

A number of different approximations and assumptions may be used in static-seismic analyses of pile foundations in lateral spreads, and it is therefore important to identify the influence of alternative approaches that differ from the guidelines adopted in this dissertation. For example, inertia forces and lateral spreading forces are sometimes assumed to act in phase, but sometimes assumed to act out of phase. An objective of this dissertation is to compare results of analyses that use different approximations and assumptions with the observations from the centrifuge tests to validate or demonstrate limitations of various assumptions commonly used in static-seismic analyses.

Uncertainty in the various input parameters in static-seismic analyses of pile foundations in lateral spreads will influence predicted bending moments and pile cap displacements to varying degrees. Variations in some input parameters may heavily influence analysis results, while variations in others may affect analysis results very little. Knowing which input parameters most influence the results of the analyses is important because effort can be focused on better characterizing the most important properties. An

objective of this dissertation is to identify the sensitivity of the analysis results to reasonable variations in input parameters.

4.2   *ADOPTED PROCEDURES AND PARAMETERS*

This section presents the procedures and input parameters that were adopted as the baseline parameter set for the analyses. Guidelines are presented for accounting for the following:

- Load transfer between pile groups and nonliquefied laterally spreading crusts.

- Influence of liquefaction on soil springs (p-y, t-z and q-z).

- Free-field ground displacements.

- Inertia forces.

The general guidelines are presented first, and tables containing the values of the input parameters used in the analyses in this dissertation are presented together at the end of this section.

4.2.1   *Load transfer between pile groups and nonliquefied laterally spreading crusts*

Estimating a curve representing the load transfer behavior in nonliquefied laterally spreading crusts involves first estimating the magnitude of the crust load, and second estimating the shape of the load transfer relation.

4.2.1.1   Magnitude of crust load

Two possible mechanisms can control the maximum lateral loads exerted on the pile caps (Fig. 4-3). The first mechanism is characterized by the crust spreading in between the piles beneath the cap thereby flowing around each pile, and the second mechanism is characterized by the crust becoming trapped between the piles beneath the cap, in which case the group acts as an equivalent block. The governing mechanism is the one that produces the lower estimate of crust load. The following lateral load components exerted on a pile cap by a laterally spreading crust must be estimated:

1. Passive force on upslope face of pile cap.

2. Friction force between sides of pile cap and spreading crust.

3. Friction force between base of pile cap and spreading crust.

4. Lateral loads on pile segments.

Each of these load components is discussed in more detail in the sections that follow, and the parameters used to compute the crust loads for analyses of the centrifuge test foundations are summarized at the end of this chapter.

Passive force on the upslope face of the cap should be computed using an appropriate earth pressure theory. Equations for computing passive pressures were included in Chapter 3, so they are not repeated in this section. For clay crusts, Coulomb earth pressure theory is appropriate, while for cohesionless soils a log-spiral approach more accurately represents the failure mechanism. For layered crusts consisting of sand overlying clay, the Coulomb-based approach developed in Chapter 3 can be used. Those equations are also appropriate for uniform clay crusts (i.e. by setting the sand layer height

to zero and subsequently solving the passive force), but should not be used for uniform sands or for profiles with clay overlying sand since log-spiral methods would be more appropriate.

Earth pressure theories are typically two-dimensional, and inherently assume that the out-of-plane dimension of the pile cap is infinite. Three-dimensional loading effects should be included in the estimate, particularly for granular soils and pile caps with small width-to-height ratios (e.g. Ovesen 1964). Three-dimensional effects might be small for pile caps with large width-to-height ratios in cohesive soils (i.e. like the pile caps in the centrifuge tests).

Friction between the sides of the pile cap and the laterally spreading crust should be computed using an appropriate interface friction approach. Equations for computing side friction forces were included in Chapter 3, so they are not repeated in this section. For clay crusts, an α-based approach originally derived for piles was used for pile caps (values of α for piles may be found in a number of different foundation engineering text books). For cohesionless soils, the interface strength may be characterized by an interface friction angle, δ, that relates the normal effective stress to interface shearing resistance. For the "equivalent block" mechanism, the contact friction, f_s, between soil and pile cap should be characterized as soil-to-structure contact [$f_s = \alpha \cdot s_u$ or $\sigma_h' \cdot \tan(\delta)$], and the contact between the spreading crust and the soil trapped beneath the cap should be characterized as soil-to-soil contact [$f_s = s_u$ or $\sigma_h' \cdot \tan(\phi)$].

The contribution of side friction to the total load exerted on the pile caps in the centrifuge tests was quite large because the pile cap length was large relative to its width and because the clay soils exerted large interface friction stresses. Typical pile caps for

bridge foundations have a short length compared to their width, so the influence of side friction would likely be smaller than was observed in the centrifuge tests. However, friction forces between the sides of the pile cap and spreading crust should never be dismissed outright based on the assumption that lateral loading is dominated by passive pressures. The forces should first be estimated, with the importance of the contribution relative to passive loading subsequently observed.

Friction between the base of the pile cap and laterally spreading crust should be computed in a fashion similar to the method for estimating side friction [i.e. α-method for clay, $\tan(\delta)$ for sand]. Equations for computing base friction forces were included in Chapter 3, so they are not repeated in this section.

There is the possibility that the soil will settle away from the base of the pile cap due to consolidation, with the axial loads being supported entirely by the piles. If settlement of the soils beneath the pile cap is anticipated, then a base reduction coefficient, R_{base}, may be applied to reduce the friction forces exerted on the cap. The amount by which the base friction is reduced is left to the discretion of the designer. One phenomena that should be considered when selecting an R_{base} value is that a gap that exists prior to lateral spreading might subsequently close as the soil spreads downslope and becomes wedged beneath the pile cap, thereby creating interface stresses in zones of contact. Base friction may be neglected when 1) a gap exists beneath the cap, and 2) the gap will remain open during lateral spreading. The average R_{base} value observed from the centrifuge test data was ¼, with a range of 0 to ½.

Lateral loads on pile segments in the crust beneath the pile cap should be estimated using appropriate bearing factors for laterally loaded piles. In this dissertation, loads on

piles in clay were computed using Matlock's (1970) bearing factors for piles in soft clay, as discussed in Chapter 3. Equations for computing bearing factors for piles in sands using the API (1993) recommendations are presented later in this chapter, along with modifications for the influence of liquefaction.

Lateral loading mechanisms for piles beneath pile caps might be different from mechanisms for piles with a free ground surface. Bearing factors at shallow depths are typically controlled by a wedge-type mechanism in which the soil failure wedge exhibits some vertical displacement. The boundary condition imposed by a pile cap might impede the upward displacement required to mobilize the wedge-type mechanism, thereby resulting in a plane-strain type mechanism in which failure occurs in a horizontal plane with no vertical deformation. Additionally, if a gap exists beneath the pile cap, then the bearing factors should be computed with the ground surface referenced from beneath the cap rather than at the actual ground surface. There was some uncertainty regarding whether gaps existed beneath the caps in the centrifuge tests, so the free-field ground surface was used to compute the bearing factors, which resulted in values intermediate to the plane-strain mechanism that would occur in the absence of a gap, and the localized wedge mechanism that would occur if a gap did exist.

Pile group effects could influence the distribution of lateral loading to the various piles within a pile group, particularly for cases in which the equivalent block mechanism controls the lateral loading. In particular, leading piles have been shown to attract more load than trailing piles, and within a given row of piles, those on the edge of the pile group attract more load than interior piles. For example, Duncan and Mokwa (2000) recommend using shadow factors in which a given trailing row of piles attracts about 2/3

of the load that the preceding row of pile attracted, with the shadowing influence extending only to the third trailing row (i.e. trailing rows after the third trailing row all attract the same load). These shadow factors are commonly used to account for the fact that a pile group may exhibit larger deformations for a given head loading than would be predicted by summing the responses from all of the individual piles. Hence, using shadow factors for the case in which a pile group is loaded at the head may result in a more accurate estimate of cap displacement. Furthermore, ignoring the shadow factors would be unconservative for such loading conditions because the cap displacement would be underestimated.

Using shadow factors for pile groups exposed to laterally spreading soil may be unconservative because the magnitude of lateral crust load could be underestimated. Values of shadow factors for design were developed for pile cap lateral loading conditions in stationary ground. Using small shadow factors would result in larger cap displacements, and design values tend to deliberately use small values to incorporate some conservatism. However, the trend is reversed for lateral spreading conditions. Using small shadow factors would result in an under-estimate of lateral loads exerted on the pile foundation. Hence, for the case in which the lateral loading mechanism is controlled by the individual load components on the cap, and not by the equivalent block mechanism, shadow factors should not be used. However, for the case in which the equivalent block mechanism controls, the total load on the equivalent block must be distributed to the individual components of the pile foundation for analysis. In such cases, the lateral load for the leading piles (i.e. the upslope piles) should be computed without any reduction for group effects. Lateral loads for trailing pile rows should then

be progressively decreased, for example based on the inter-row ratios suggested by Mokwa and Duncan (2000), until the computed total load on the group matches that for the equivalent block.

Shadow factors are typically applied to the p-y springs on a given pile at every depth (i.e. the shadow factors are taken as a property of the pile itself), which is not appropriate for loading conditions encountered during lateral spreading. "Leading piles" and "trailing piles" do not exist under lateral spreading loading conditions because the direction of significant subgrade reaction loads varies along the pile length. For example, a pile in the upslope row would be a "leading" pile with respect to the downslope acting crust load, but a "trailing" pile with respect to the upslope acting subgrade reaction loads in deeper sand layers. In this regard, the influence of shadowing would be better represented using p-y springs with direction-dependent capacities rather than applying p-multipliers to the p-y springs along an entire pile. Reversal of load direction also occurs under static head load conditions, but the response of the pile foundation is dominated by subgrade reaction loads at shallow depths with only small loads mobilized in deeper soils.

4.2.1.2 Shape of load transfer relation

The load transfer relation between pile groups and laterally spreading crusts can be significantly softer than the load transfer relation that would exist during a static load test of the same pile group in the absence of liquefaction of underlying layers. Liquefaction of soil beneath the crust influences the distribution of stresses and strains within the crust, resulting in a large zone of influence and a soft load transfer relation. Derivation of a load transfer model was presented in Chapter 3, so the equations are not repeated in this

section. Properties of the load transfer relation used in the analyses of the centrifuge pile foundations are summarized at the end of this chapter.

Designers might prefer to implement the load transfer relation predicted by the model in Chapter 3 using existing p-y relations, but with the stiffness adjusted such that the resulting p-y material reasonably matches the predicted load transfer behavior. In the analyses presented in this dissertation, the shape of the p-y materials closely matched the shape suggested by Matlock (1970) for soft clay, with the y_{50} value adjusted to account for the softening of the load transfer caused by liquefaction.

4.2.2   p-y relations

p-y relations were defined for pile caps, for piles in clay, for piles in nonliquefied sand, for piles in fully-liquefied sand (i.e. when peak r_u-values reach 1.0), and for piles in sand with intermediate peak r_u-values (i.e. $0 < r_u < 1$). Input parameters used in the analyses of the centrifuge pile foundations are summarized in at the end of this chapter.

4.2.2.1   p-y relations for pile caps

The p-y relations for pile caps represented the total crust load exerted on the pile caps, and are shown in Table 4-5. For example, a total load of 4640 kN was exerted on the pile cap for test SJB03 (Table 4-4). The pile cap height was 2.2 meters, so the value of p_u is 4640 kN / 2.2 m = 2109 kN/m.

4.2.2.2 *p-y relations for clay*

The p-y curves for the pile segments in the clay crust beneath the pile cap were based on the relations presented by Matlock (1970). The equations for the ultimate resistance, p_u, were presented in Chapter 3, so they are not repeated in this section. The shape of the p-y curve for soft clay is defined in Eq. 4-1.

$$p = 0.5 p_u \left(\frac{y}{y_{50}} \right)^{0.33} \tag{4-1}$$

Based on static load tests of model piles in uniform clay soil, Matlock found that $y_{50} = 2.5 \cdot \varepsilon_{50} \cdot b$ appropriately characterized the shape of the p-y curve, where ε_{50} is the axial strain associated with half of the ultimate deviator stress in a triaxial compression test. This value of y_{50} is not appropriate for clay layers spreading over liquefiable layers, and the value of y_{50} to use for lateral spreading clay crusts should be selected based on the softer load transfer relation predicted by the model defined in Chapter 3.

4.2.2.3 *p-y relations for sand without liquefaction*

The p-y curves for sand were based on the relations presented in API (1993), which do not include the effects of liquefaction, plus adjustments for the effects of liquefaction as described in the following section. The ultimate resistance in the sand, assuming a wedge shaped mechanism that extends to the ground surface can be expressed as:

$$p_{u_1} = (c_1 x + c_2 b) \gamma' x \tag{4-2}$$

where

γ' is the effective unit weight.

$$c_1 = \frac{k_0 \tan\phi \sin\beta}{\tan(\beta-\phi)\cos\alpha} + \frac{\tan^2\beta \tan\alpha}{\tan(\beta-\phi)} + k_0 \tan\beta(\tan\phi\sin\beta - \tan\alpha) \qquad (4\text{-}3)$$

$$c_2 = \frac{\tan\beta}{\tan(\beta-\phi)} - k_a \qquad (4\text{-}4)$$

where,

K_a = coefficient of active lateral earth pressure.

$$K_a = \tan^2\left(45 - \frac{\phi}{2}\right) \qquad (4\text{-}5)$$

For horizontal plane strain failure,

$$p_{u_2} = c_3 b\gamma'x \qquad (4\text{-}6)$$

where

$$c_3 = K_0 \tan\phi \tan^4\beta + k_a\left(\tan^8\beta - 1\right) \qquad (4\text{-}7)$$

$$\beta = 45 + \frac{\phi}{2} \qquad (4\text{-}8)$$

$$\alpha = \frac{\phi}{2} \qquad (4\text{-}9)$$

$$K_o = 0.4 \qquad (4\text{-}10)$$

The smaller of the two p_u values, p_{u1} and p_{u2}, is used to determine the ultimate soil resistance at any depth. The shape of the p-y curve is based on the Hyperbolic method:

$$p = Ap_u \tanh\left(\frac{kx}{Ap_u}y\right)$$ (4-11)

where

A = Factor to account for cyclic or static loading

$A = 0.9$ *for cyclic loading* (4-12)

$A = 3 - 0.8\dfrac{x}{b} \geq 0.9$ *for static loading* (4-13)

k = modulus of subgrade reaction

The values of k given in Fig. 4-4, which are commonly used to derive p-y relations, are known to overestimate the stiffness at depths more than a few pile diameters. This is because the values for k are based on lateral load tests that are dominated by the soil behavior at shallow depths (e.g., a few pile diameters). Since the elastic modulus of sand approximately increases with the square root of confining stress, the result will be an overestimate of stiffness at larger depths. Such an overestimate may not be important for lateral loading at a pile head where loads are small in deeper soil layers, but may affect the response to lateral spreading in which large loads are mobilized in deep layers. Consequently, an approximate correction for overburden effects was used in this study. The corrected modulus of subgrade reaction was obtained as:

$$k^* = c_\sigma k$$ (4-14)

$$c_\sigma = \sqrt{\frac{\sigma_{ref}'}{\sigma_v'}} \qquad\qquad (4\text{-}15)$$

where

k = initial modulus of subgrade reaction from API sand criteria,

c_σ = correction factor for overburden effects,

σ_{ref}' = reference stress at which k was calibrated, taken as 50 kPa.

k* = corrected modulus of subgrade reaction.

4.2.2.4 *Effect of liquefaction on p-y relations in sand*

The effect of liquefaction or excess pore water pressure on the p-y behavior of saturated sand was approximated by combining certain elements of previous studies. Wilson et al. (1998, 2000) first showed that dynamic p-y behavior exhibits the inverted s-shaped behavior that is characteristic of the stress-strain behavior of dilatant sands. This behavior was subsequently observed by a number of different researchers, who consistently found that the dynamic capacity of a p-y material can be larger than the drained capacity computed from static relations (e.g. API 1993). Furthermore, the shape of the drained relation is displacement softening (i.e. tangent modulus decreases with displacement) while the dynamic undrained relation is displacement hardening. The complex undrained p-y behavior cannot be reasonably captured in a static analysis because the p-y behavior depends on complex factors such as load history, dilatancy of the sand induced by shaking of the ground, dilatancy if the sand induced by strains from the pile, load rate, excess pore pressure ratio, and others.

The recommendations in this dissertation are intended to be used in conjunction with static p-y relations available in the literature, and the fact that these recommendations are crude representations of a complex reality is acknowledged from the outset. The emphasis was on providing a simple, rational framework that would enable inclusion of first-order effects of relative density and free-field peak excess pore pressure ratio. Recommended p-multipliers to use for static-seismic analysis of pile foundations in liquefied and laterally spreading ground are summarized in Table 4-1.

Table 4-1: p-multipliers, m_p, to account for liquefaction.

$(N_1)_{60\text{-CS}}$	m_p
< 8	0 to 0.1
8-16	0.1 to 0.2
16-24	0.2 to 0.3
>24	0.3 to 0.5

Analyses of the pile foundations in this study indicated that the predicted bending moments and pile cap displacements were not very sensitive to the selection of m_p within the range selected in Table 4-1. In many cases, the response of the pile foundation will be dominated by the loads from the nonliquefied spreading crust layer, and accuracy in modeling subgrade reaction in the liquefied sand layers becomes unimportant compared with modeling subgrade reaction in the nonliquefied crust layer.

The effect of excess pore pressure ratio (r_u) was approximated as producing a linear transition between the p_u value at $r_u = 0\%$ ($p_{u,0}$) and the p_u value at $r_u = 100\%$ ($p_{u,1}$), as

shown in Fig. 4-5, This relation is based on the results by Dobry et al. (1995) and can be written as:

$$p_u = p_{u,0} - r_u(p_{u,0} - p_{u,1})$$
(4-16)

where

$p_{u,0}$ = value of p_u at $r_u = 0$

$p_{u,1}$ = value of p_u at $r_u = 1.0$

This expression is based on the free-field r_u whereas the excess pore pressures adjacent to the pile may be significantly different due to the shear strains induced on the soil by its interaction with the pile. The pore pressures adjacent to the pile could be greater or smaller than free-field values depending on the soils' D_r and the loading history. It is known that fine sand around a pile will not be "drained" during dynamic loading (i.e. the drained monotonic backbone might not accurately represent the undrained or partially drained behavior, even with the free-field $r_u = 0$). But, in the absence of better information, the $p_{u,0}$ has been approximated as the drained monotonic capacity from API recommendation. It is recognized that the local variations in r_u introduce additional uncertainties in the subsequent analyses.

4.2.3 t-z relations

Like p-y relations, t-z relations were also defined for pile caps, piles in clay, for piles in nonliquefied sand, for piles in fully-liquefied sand (i.e. when peak r_u-values reach 1.0), and for piles in sand with intermediate free-field peak r_u-values (i.e. $0 < r_u < 1$).

4.2.3.1   t-z relations on pile caps

The t-z elements on the pile caps represent vertical friction at the contact between the pile caps and the crust. Friction forces along the sides and back face of the caps are shown in Table 4-4. The force on the back of the cap was represented using at-z elements attached to back of the cap, and the side forces were distributed into t-z elements geometrically dispersed along the length of the cap. The geometric distribution of t-z elements allows the vertical side friction exerted on the pile cap to resist rocking as the cap rotates during lateral loading.

4.2.3.2   t-z relations in clay

The properties of the t-z elements attached to the pile segments in the clay layer between the base of the pile cap and the top of the liquefiable loose sand were calculated as:

$$t_u = \alpha \cdot s_u \cdot p \tag{4-17}$$

where,

t_u = ultimate resistance of t-z element

α = adhesion coefficient

s_u = undrained shear strength of clay

p = pile perimeter

The shape of the t-z curves in clay approximated the relation defined by Reese and O'Neill (1987) for drilled shafts. The stiffness of the materials was set such that the ultimate resistances were mobilized at a displacement of about 0.5% of the pile diameter.

4.2.3.3   t-z relations in sand without liquefaction

The frictional strength at the interface between the pile and the sand was calculated as:

$$t_u = K_o \cdot \sigma_v{}' \cdot p \cdot \tan(\delta) \qquad\qquad (\ 4\text{-}18\ )$$

where,

t_u = ultimate resistance of t-z element

K_o = coefficient of earth pressure at rest [set equal to 0.4 as in LPile (Reese et al. 2000)]

$\sigma_v{}'$ = vertical effective stress

p = pile perimeter

δ = interface friction angle between the sand and the pile

The shape of the t-z relations approximated the relation proposed by Mosher (1984) for piles in sand. The stiffness of the t-z relations was set such that the ultimate resistance was mobilized at a displacement of about 0.5% of the pile diameter.

The concept of a limiting depth, below which frictional capacity remains constant in spite of increasing overburden stress (e.g. Meyerhof 1976) was not used to limit t_u along the piles. Vertical pile load test data, from which the limiting depth concept was derived, were often interpreted without accounting for residual stresses induced during pile

driving that were locked in prior to load testing. Fellenius (1972) first developed the neutral plane concept, wherein shaft friction is fully mobilized below the neutral plane and acts upward, and also fully mobilized above the neutral plane and acts downward. Since the frictional capacity below the neutral plane is already mobilized in the upward direction, it will appear to contribute little to resisting the head load imposed on the pile if initial stresses are not accounted for in interpreting the test data, which is consistent with the limiting depth concept. The piles in the centrifuge tests were driven at 1-g, and initial stresses are believed to be very small compared with capacity at high g-levels. Hence, the limiting depth concept has not been used in the study.

4.2.3.4 *Effect of liquefaction on t-z relations in sand*

Skin friction stresses between piles and liquefied sand are poorly understood. For lack of a better method, the skin friction in fully-liquefied soil (i.e. $r_u = 1.0$) was computed by treating the p-multipliers in Table 4-1 as being appropriate to use as t-multipliers. Hence the backbone curve computed for the drained condition was scaled by an appropriate t-multiplier to account for the influence of liquefaction. The shape of the fully-liquefied curves were assumed to be the same as for the nonliquefied curves, with the capacity being mobilized at a displacement of 0.5% of the pile diameter. Skin friction in partially-liquefied sand (i.e. $0 < r_u < 1$) was linearly interpolated in the same manner as for the p-y behavior.

4.2.4   Q-z relations

The drained end-bearing resistance for the sand layer were represented using the bearing capacity factors given by Meyerhof (1976). The bearing factor, N_q, is often tabulated in a figure for a range of friction angles, and embedment depths, and can be found in many foundation engineering text books. The effect of liquefaction on the Q-z capacity was modeled by assuming that the p-multipliers in Table 4-1 are appropriate to use for Q-z capacity as well. The influence of free-field excess pore pressure ratios intermediate between 0 and 1.0 was treated by linear interpolation in the same way as for the p-y behavior. The shape of the Q-z relations was modeled after Vijayvergiya's (1977) relation for piles in sand. The stiffness of the Q-z materials was set such that the ultimate resistance was reached when tip displacements were about 5% of the pile diameter.

4.2.5   Ground surface displacements and displacement profiles

The free-field soil deformation profile is required as an input parameter for a BNWF static-seismic analysis. Obtaining the displacement profile involves first estimating the ground surface displacement, and second estimating the displaced shape of the ground.

4.2.5.1   Ground surface displacement

Ground surface displacements were estimated using a sliding block analysis (e.g. Newmark 1965). The free-body diagram describing the sliding-seismic analysis is shown in Fig. 4-6. Example analyses are presented for the four base motions from test SJB03 in Fig. 4-7. The displacements become very large as the residual strength of the liquefied sand layer approaches the static driving stress imposed by the sloping nonliquefiable

crust (about 3 kPa) because the yield acceleration becomes zero. Note that the crust layer in the centrifuge test was not an infinite slope, and unequal forces would be expected to act on the sides of the slice in the free-body diagram in Fig. 4-6 (as they did in the load transfer model for lateral spreading presented in Chapter 3). However, the clay crust exhibited cracks that subsequently filled with ejected liquefied sand, so the forces on the sides of the slices are therefore difficult to determine. Furthermore, there is significant uncertainty in the selection of s_r. Hence, the infinite slope analysis has been used in this study with the understanding that much of the mechanics of the problem are neglected.

In the range of residual strengths plotted in Fig. 4-7, the corresponding ground surface displacements range from very large (i.e. more than 6 m at $s_r = 3$ kPa) to quite small (i.e. a few centimeters at $s_r = 12$ kPa). Representing undrained shear strength of liquefied sand using a constant s_r value ignores our fundamental understanding of the undrained response of sands being dependent on important factors such as dilatancy, load rate, stress history and load path. It is therefore no surprise that s_r values selected for the purpose of estimating ground displacements do not correlate well with penetration resistance, and one should expect significant uncertainty in predicting ground displacements using a constant s_r. The approach adopted in this dissertation is to consider a range of possible ground displacements for analysis of the pile foundation, and assess the sensitivity of the foundation response to the range of ground displacements. Adopted baseline ground displacements are shown for each ground motion in Table 4-14.

Numerous other methods exist for estimating the peak magnitude of earthquake-induced ground surface displacements in liquefying soils, but all of the methods involve significant uncertainty. For example, Tokimatsu (2003) recommends estimating shear

strains that will occur during the earthquake, then integrating the shear strains upward from a stiff layer to obtain ground surface displacement. Uncertainty in the shear strains induced by the earthquake, and the possible formation of a displacement discontinuity (as observed in the centrifuge tests), render the ground surface displacements difficult to accurately predict using this method. Regression analyses of data from measured lateral spreads can also be used to estimate ground surface displacements (e.g. Bartlett and Youd 1995). There is significant scatter in the prediction of ground displacement using these regression formulas, which is not surprising considering the range of different soils and boundary conditions contained within the data. Hence, accurately predicting ground displacements using the regression formulas is not likely, and again a range of values should be considered for design.

There is considerable scatter in the surface displacements recorded among the various centrifuge tests, which is an artifact of the differences in test variables. Peak crust displacements measured to the side of the pile group ranged from less than a meter to more than three meters for a large Kobe motion. The recorded displacements were consistent with boundary conditions along the contact between the crust and the container walls, and the undrained shear strength of the crust. A gap was cut along the sides of the crust and backfilled with bentonite slurry for some of the models, and these crusts exhibited larger displacements since friction along the sides was small. Crusts with smaller undrained shear strengths exhibited larger displacements. Cracking of the crust and filling of the cracks with sand ejecta likely influenced the measured crust displacements, though the influence of cracking could not be ascertained from the measurements that were made.

4.2.5.2   Shape of free-field ground displacement profile

The shape of the free-field ground displacement profile can influence the results of pushover analyses, yet many different ground displacement profiles have been observed in model tests, and ground displacement profiles are not obtained from field case histories of lateral spreading. The ground displacement profiles in the centrifuge tests were characterized by a displacement discontinuity that occurred when the clay crust slid on top of the loose sand layer. This displacement profile is attributed to upward-seeping pore water becoming trapped by the low-permeability crust layer, thereby increasing the void ratio near the top of the loose sand layer (Kulasingam et al. 2004; Malvick et al. 2004). The adopted ground displacement profile is presented in Table 4-15 and Fig. 4-8.

Centrifuge testing of piles in laterally spreading ground at RPI (e.g. Abdoun et al. 2003) showed that displacement discontinuities did not occur when cemented sand crusts were perforated to allow dissipation of excess pore pressures. In their tests, large ground surface displacements were attributed to large strains in the liquefied sand layer rather than to sliding of the nonliquefied crust on top of the liquefied layer. Considering the different displaced shapes that have been observed in different model tests, a range of different displaced shapes should be considered in design, and the influence of displaced shape should be observed.

4.2.6   Inertia forces

A very important, and often neglected step in the design of a pile foundation is to estimate the inertia forces that act in phase with the forces imposed by the laterally spreading ground. Designers often do not include inertia loads along with lateral

spreading loads because they feel that peak inertia loads occur during shaking, while peak lateral spreading loads occur after strong shaking when ground displacements are largest (e.g. Martin et al. 2002). However, the centrifuge test data showed that the transient, lurching component of the ground displacement can be sufficiently large to mobilize the peak lateral spreading loads during strong shaking, and that these loads may act in phase with the peak inertia loads. Estimating the inertia loads to use in combination with lateral spreading loads is therefore very important.

4.2.6.1 *Pile cap inertia forces*

Equating peak pile cap acceleration with peak ground acceleration in the absence of liquefaction is a clear, easy-to-implement approach, although it clearly neglects many of the fundamentals of site response and soil-structure-foundation interaction. Data from five of the centrifuge tests, summarized in the previous chapter, indicated that the peak pile cap acceleration was reasonably approximated as being equal to the ground acceleration that would be predicted in the absence of liquefaction. A linear regression of the data indicated the fit of predicted versus measured was 0.99, which is essentially unity for practical purposes. The computed coefficient of variation of the fit was 0.44, which is roughly ½ considering that the data set is sparse and does not conform to the law of large numbers (e.g. Christian 2004). The mechanics that control the magnitude of peak pile cap acceleration are not yet well understood, and the recommendation that the peak pile cap acceleration is equal to the peak ground acceleration may be used as an approximation with associated large uncertainty.

In addition to estimating the peak pile cap acceleration that will occur during a given earthquake, designers must also select the fraction of that acceleration that will occur simultaneously with the largest lateral spreading loads. For the tests with stiff 1.17-m diameter piles (SJB03, DDC01 and DDC02), the peak pile cap inertia force acted downslope at the same time as the peak lateral load from the nonliquefied crust, but for the tests with more flexible 0.73-m diameter piles (PDS03, SJB01, SJB02), the peak pile cap inertia force did not act at the same time as the peak lateral load from the nonliquefied crust. The reason for this behavior is not completely understood, but can likely be attributed to the different dynamic shaking characteristics of the pile groups related to the different pile group stiffnesses and pile cap masses. The guidelines presented in this chapter are intended to be used to design pile groups that are sufficiently stiff to exhibit reasonably small displacements as the soils spread past (i.e. like the 1.17-m diameter piles, not like the 0.73-m diameter piles). For such cases, the peak pile cap inertia should be assumed to act in phase with the peak crust load, with recognition given to the fact that this assumption may not be characteristic of pile foundations that exhibit large displacements.

4.2.6.2 *Superstructure inertia forces*

Several factors complicate the estimation of structural inertia forces in cases with lateral spreading. First, the influence of liquefaction on acceleration response spectra has not yet been accurately and reliably quantified. Second, inertia forces may cause the foundation to translate and rotate, thereby lengthening the natural period of the structure-foundation system, and the natural period of the system will vary throughout shaking due

to nonlinearity in the foundation response. Third, the laterally spreading crust exerts loads on the foundation that influence the motion of the pile cap and superstructure in addition to the influence of the base shaking.

Estimating ground motion in areas of liquefaction require site-specific analyses since liquefiable soils fall into site class F in building codes (e.g., ICC 2003). However, building codes do not provide guidance on how to conduct the site-specific analyses. Response spectra for class E sites are readily available and commonly used in design, but do not account for the influence of liquefaction. It is therefore useful to relate the structural accelerations observed in the centrifuge tests to response spectra for the estimated ground motion that would occur in the absence of liquefaction since (i.e. for a class E site). Such response spectra were computed from the ground surface motion predicted from the SHAKE analyses in this dissertation. Structural accelerations were predicted based on the spectral acceleration from the estimated response spectra associated with the fixed-base natural period of the structure. The measured versus predicted relation (Fig. 3-44) indicates a 40% over-prediction and coefficient of variation of about 0.5. However, the data set contains only eight points from tests DDC01 and DDC02 (four different motions and two different superstructures), and is so sparse that the results are not statistically reliable. For simplicity, the fit is assumed to be unity and coefficient of variation is assumed ½, just like for the pile cap acceleration.

The phasing of structural inertia loads and crust loads depended on the fixed-base natural period of the structure, with in-phase response observed for the short-period structure. This trend somewhat supported observations by Tokimatsu (2003) that if the predominant period of the ground motion is larger than the natural period of the structure,

the crust load will be out-of-phase with the inertia load. The predominant period of the crust motion was close to 2 seconds, but the T = 0.8 s structure did not observe entirely in-phase motion with the ground. Ongoing nonlinear dynamic finite element analyses (Chang et al. 2005) are being used to assess combinations of kinematic and inertia loading to use for design, and simplified methods for predicting the inertia loads will be developed. For this study, inertia forces were assumed to act in phase with crust loads regardless of structural fixed-base period.

4.2.6.3 Relative masses of pile caps and superstructures

In addition to inertia forces from the superstructures, pile cap inertia forces were significant for the pile groups in the centrifuge tests because large pile caps were used. For the tests with superstructures, the pile caps weighed about 7000 kN while the superstructures weighed 3300 kN (540 kN per pile). Typical pile foundations without any lateral spreading hazard have pile caps that are significantly lighter than the superstructure. The relative importance of superstructure and pile cap inertia forces clearly depends on their relative masses, so it is important to establish that the size of the pile caps and superstructures used in the centrifuge tests are in the reasonable range for field conditions so that the test results may be appropriately interpreted.

In a study to identify costs associated with different levels of ground motions, PEER researchers found bridge foundations that are not exposed to liquefaction and lateral spreading required pile caps with about 5% of the superstructure mass (4400 kN) for the 0.36 m diameter piles referenced in their study (Tom Shantz, personal communication). A reasonable range of mass ratios for such conditions would be about 4% to 8%. They

also found that larger pile caps were required to fix larger diameter piles (i.e. 0.61 m diameter) in areas with liquefaction and lateral spreading hazard, increasing the ratio of cap-to-superstructure mass to about 25%. A reasonable range of mass ratios for such conditions would be about 12% to 100%, though this range depended on the thickness of the crust used in their study (2 meters). For crusts thicker than the 2-m they considered, larger diameter piles and hence larger pile caps would be required to resist the imposed lateral loads. Hence, the mass ratio of 200% required for our centrifuge tests with 4.5-m thick strong clay crusts is on the upper end of what would be expected in the field. As crust thicknesses increase, the costs associated with constructing foundations to resist the loads they impose may become larger than the costs required to improve the ground to mitigate liquefaction and lateral spreading hazard.

4.2.7 Input parameters for analyses of centrifuge tests

This section presents the input parameter values that were used for the analyses presented in this dissertation.

Table 4-2: Soil properties for five centrifuge tests.

Test	Soil Layer	Depth of Layer Top (m)	Unit Weight, γ (kN/m^3)	Relative Density, D_R (%)	Friction Angle, ϕ' (deg)[b]	Undrained Shear Strength, s_u (kPa)[c]
	Clay	0.0	16	--	--	22
PDS03	Loose Sand	4.7	19	29	30	--
	Dense Sand	9.2	20	68	38	--
	Depth of groundwater table was approximately 1 meter at pile group location.					
	Clay	0.0	16	--	--	44
SJB01	Loose Sand	4.7	19	20	30	--
	Dense Sand	9.2	20	80	38	--
	Depth of groundwater table was approximately 1 meter at pile group location.					
	Monterey Sand	0.0	17	--[a]	36	--
	Clay	1.2	16	--	--	44
SJB03	Loose Sand	3.9	19	35	30	--
	Dense Sand	9.4	20	75	38	--
	Depth of groundwater table was approximately 2 meters at pile group location.					
	Monterey Sand	0.0	17	--[a]	36	--
	Clay	0.6	16	--	--	33
DDC01	Loose Sand	3.9	19	35	30	--
	Dense Sand	9.4	20	75	38	--
	Depth of groundwater table was approximately 2 meters at pile group location.					
	Monterey Sand	0.0	17	--[a]	36	--
	Clay	0.6	16	--	--	22
DDC02	Loose Sand	3.9	19	35	30	--
	Dense Sand	9.4	20	75	38	--
	Depth of groundwater table was approximately 2 meters at pile group location.					

[a] Minimum and maximum density data were not available for the Monterey sand
[b] Friction angle was estimated based on relative density
[c] Average undrained shear strength in clay layer based on T-bar measurements at 57.2 g before shaking was 40 kPa. Values have been increased by 10% to account for the roughly order of magnitude higher load rate during shaking than during the T-bar test.

Table 4-3: Properties of aluminum tubing used for model piles in centrifuge tests.

Test	tubing diameter	tubing wall thickness	pile diameter	cross-sectional area	moment of inertia	Young's modulus	Yield stress	Pile Length	Pile cap dimensions
	b_{tube} (m)	t (m)	b (m)	A (m^2)	I (m^4)	E (kPa)	σ_y (kPa)	L (m)	LxWxH (m)[a]
PDS03	0.73	0.034	0.78	0.42	0.0045	68,900,000	216,000	15.7	9.5 x 6.2 x 2.2
SJB01	0.73	0.034	0.78	0.42	0.0045	68,900,000	216,000	15.7	9.5 x 6.2 x 2.5[b]
SJB03	1.09	0.051	1.17	1.08	0.024	68,900,000	216,000	23.5	14.3 x 9.2 x 2.2
DDC01	1.09	0.051	1.17	1.08	0.024	68,900,000	216,000	23.5	14.3 x 9.2 x 2.2
DDC02	1.09	0.051	1.17	1.08	0.024	68,900,000	216,000	23.5	14.3 x 9.2 x 2.2

[a] Dimensions of the cofferdam that composed the outside edge of the pile cap that made contact with the soil after foundation installation. Length is the pile cap dimension oriented parallel to the direction of lateral spreading (north to south). At the south end of the pile cap, the pile cap elevation was the same as the soil surface elevation.

[b] The cofferdam thickness was 2.5 meters for test SJB01, but the pile cap height was only 2.2 meters. The bottom of the cofferdam extended 0.3 meters below the bottom of the pile cap around its perimeter, and the extra space was filled with soil such that the bottom of the cap was in contact with the clay crust.

Table 4-4: Summary of back-calculated lateral load components for pile groups in centrifuge tests.

Test	Undrained Shear Strength, c_u (kPa)	Adhesion Factor, α	Base Friction Reduction Factor, R_{base}[b]	Passive Force (kN)	Side Friction (kN)	Base Friction (kN)	Pile Segment Force (kN)	Total Crust Load (kN)	Peak Measured Crust Load (kN)	Load on Pile Cap (kN)[c]
PDS03	22	0.6	0.25	1093	494	170	620	2377	≈2530[a]	1757
SJB01	44	0.5	0.25	2315	954	347	1116	4732	4984	3617
SJB03	44	0.5	0.25	3500	452	688	2882	7526	6696	4640
DDC01	33	0.55	0.25	2604	651	568	2301	6123	6147	3823
DDC02	22	0.6	0.25	2093	477	413	1722	4705	4327	2983

[a] Pile cap acceleration was not measured for PDS03, so the pile cap inertia was assumed equal to that measured during the critical loading cycle in SJB01 (approximately 630 kN).

[b] Base friction force is defined as $F_{base} = \alpha \cdot R_{base} \cdot c_u \cdot A_{base}$. Average $R_{base} = 0.25$ for all five tests.

[c] Load on pile cap is the total crust load minus pile segment force.

Table 4-5: Properties of p-y materials on pile caps.

Test	p_u (kN/m)	y_{50} (m)
PDS03	799	0.2
SJB01	1644	0.2
SJB03	2109	0.2
DDC01	1738	0.2
DDC02	1356	0.2

Table 4-6: Properties for p-y materials on piles in clay layer.

Test	γ (kN/m^3)	b (m)	s_u (kPa)	J	y_{50} (m)
PDS03	16	0.78	22	0.5	0.2
SJB01	16	0.78	44	0.5	0.2
SJB03	16	1.17	44	0.5	0.2
DDC01	16	1.17	33	0.5	0.2
DDC02	16	1.17	22	0.5	0.2

Table 4-7: Properties for p-y elements on piles in loose sand layer.

Test	γ (kN/m^3)	b (m)	ϕ (deg)	$K_{(\sigma=50kPa)}$ (kN/m^3)	m_p	r_u
PDS03	19	0.78	30	12,500	0.05	1.0
SJB01	19	0.78	30	12,500	0.05	1.0
SJB03	19	1.17	30	12,500	0.05	1.0
DDC01	19	1.17	30	12,500	0.05	1.0
DDC02	19	1.17	30	12,500	0.05	1.0

Table 4-8: Properties for p-y materials on piles in dense sand layer.

Test	γ (kN/m^3)	b (m)	ϕ (deg)	$K_{\sigma=50kPa}$ (kN/m^3)	m_p	r_u
PDS03	20	0.78	38	55,500	0.3	0.6
SJB01	20	0.78	38	55,500	0.3	0.6
SJB03	20	1.17	38	55,500	0.3	0.6
DDC01	20	1.17	38	55,500	0.3	0.6
DDC02	20	1.17	38	55,500	0.3	0.6

Table 4-9: Properties for t-z materials on pile caps.

Test	t_u (kN/m)[a]	z_{50} (m)
PDS03	50	0.005
SJB01	100	0.005
SJB03	60	0.005
DDC01	90	0.005
DDC02	70	0.005

[a] t-z materials were distributed along the length of the pile cap such that they can resist cap rotations. Units of kN/m are force per horizontal unit length along the cap.

Table 4-10: Properties for t-z materials on piles in clay layer.

Test	γ (kN/m^3)	b (m)	s_u (kPa)	α	z_{50}/b (m)
PDS03	16	0.78	22	0.6	0.0006
SJB01	16	0.78	44	0.5	0.0006
SJB03	16	1.17	44	0.5	0.0006
DDC01	16	1.17	33	0.55	0.0006
DDC02	16	1.17	22	0.6	0.0006

Table 4-11: Properties for t-z materials on piles in loose sand layer.

Test	γ (kN/m^3)	b (m)	δ (deg)	m_t	r_u
PDS03	19	0.78	20	0.05	1.0
SJB01	19	0.78	20	0.05	1.0
SJB03	19	1.17	20	0.05	1.0
DDC01	19	1.17	20	0.05	1.0
DDC02	19	1.17	20	0.05	1.0

Table 4-12: Properties for t-z materials on piles in dense sand layer.

Test	γ (kN/m^3)	b (m)	δ (deg)	m_t	r_u
PDS03	20	0.78	30	0.3	0.6
SJB01	20	0.78	30	0.3	0.6
SJB03	20	1.17	30	0.3	0.6
DDC01	20	1.17	30	0.3	0.6
DDC02	20	1.17	30	0.3	0.6

Table 4-13: Properties for Q-z materials at pile tips.

Test	σ_v' (kPa)	A_{tip} (m^2)	ϕ (deg)	N_q	$Q_{u,0}$ (kN)	m_q	r_u	z_{50}/b
PDS03	169	0.42	38	209	15,000	0.3	0.6	0.00625
SJB01	169	0.42	38	209	15,000	0.3	0.6	0.00625
SJB03	256	1.08	38	209	60,000	0.3	0.6	0.00625
DDC01	256	1.08	38	209	60,000	0.3	0.6	0.00625
DDC02	256	1.08	38	209	60,000	0.3	0.6	0.00625

Table 4-14: Predicted ground surface displacements.

Motion	Ground Surface Displacement (m)
Small Santa Cruz	0.05
Medium Santa Cruz	0.2
Large Santa Cruz	1.2
Large Kobe	1.8

Table 4-15: Shape of ground displacement profile.

Depth (m) SJB03, DDC01, DDC02	Depth (m) PDS03, SJB01	Normalized Displacement (m)[a]
0	0	1
3.9	4.7	1
3.9	4.7	0.23
6.1	5.1	0.13
7.4	6.0	0.10
8.5	6.7	0.077
9.4	9.2	0.067
25.7	18.2	0.0

[a] Displacement at depth divided by ground surface displacement.

209

Table 4-16: Inertia forces used in analyses.

Test	Motion	Cap Inertia (kN)[a]	Structure Inertia (kN)[b]
PDS03	Small Santa Cruz	1100	--
	Medium Santa Cruz	1800	--
	Large Santa Cruz	1900	--
	Large Kobe	2200	--
SJB01	Small Santa Cruz	1100	--
	Medium Santa Cruz	1900	--
	Large Santa Cruz	2200	--
	Large Kobe 1	2300	--
	Large Kobe 2	2300	--
SJB03	Small Santa Cruz	2600	--
	Medium Santa Cruz	3600	--
	Large Santa Cruz	3600	--
	Large Kobe	4000	--
DDC01	Small Santa Cruz	2500	800
	Medium Santa Cruz	3300	2000
	Large Santa Cruz	3600	2700
	Large Kobe	3900	3900
DDC02	Small Santa Cruz	2500	2200
	Medium Santa Cruz	3400	2200
	Large Santa Cruz	3600	2300
	Large Kobe	4000	2200

[a] Cap inertia was computed based on estimate of peak ground acceleration from site response analyses in the absence of liquefaction.

[b] Structure inertia was computed based on estimate of 5% damped spectral acceleration at the fixed-base natural period of the structure from site response analyses in the absence of liquefaction.

4.3   NUMERICAL METHODS AND TOOLS

This section summarizes the numerical methods used in the static-seismic analyses, and the automation tools that were developed to build the finite element meshes and material properties. The numerical methods and tools were tailored for performing suites of analyses with different input parameters and assumptions using a single script file, which cannot be accomplished using most commercially-available software packages. These analyses and tools will hopefully be useful to other researchers and designers who find value in the sensitivity approach adopted in this dissertation.

4.3.1   OpenSees finite element platform

The analyses in this dissertation were performed using the Open System for Earthquake Engineering Simulation (OpenSees), which is a freely-distributed open-source finite element platform developed by the PEER Center (*http://opensees.berkeley.edu*). The analyses could have been performed using a number of different numerical modeling platforms, but OpenSees was selected for the following reasons:

1. Suites of many analyses can be easily accomplished using tcl, the scripting language that is used to control OpenSees, whereas most software packages do not facilitate the automation of the large number of analyses required to perform sensitivity studies.

2. Ongoing nonlinear dynamic analyses are being performed in OpenSees by Chang (e.g. Chang et al. 2005), and the static analyses provided a basis for the more complex dynamic analyses.

OpenSees has the additional benefit of containing a large library of geotechnical and structural materials, which facilitates performance-based design calculations involving coupled soil-foundation-structure systems in a single modeling platform.

4.3.2 Calculation tools developed for OpenSees BNWF analyses

Boulanger et al. (2003) described the p-y, t-z and q-z materials that were implemented into OpenSees for the purpose of performing BNWF analyses. Two additional OpenSees commands, PySimple1Gen and TzSimple1Gen, were developed in conjunction with the analyses performed in this dissertation to automate the generation of material properties for p-y and t-z materials. The new commands automatically calculate the capacities of the p-y and t-z materials based on input properties such as pile diameter, soil unit weight, and soil strength. The commands were constructed to save time and to prevent errors that could occur if the large number of material properties for each of the p-y and t-z materials were to be calculated by hand. Documentation of the commands can be found at the OpenSees website (*http://opensees.berkeley.edu*).

4.3.3 GiD mesh generator

The finite element meshes were generated using the pre- and post-processor GiD. An evaluation version can be downloaded free from *http://gid.cimne.upc.es*, and all of the

finite element meshes presented in this dissertation can be generated using the free evaluation version because the number of nodes and elements is relatively small. GiD was customized for performing BNWF analyses in OpenSees by defining a problem-type called OpenSees_py.gid, which outputs the various components of an OpenSees finite element analysis (nodes, elements, constraints, and recorders) as tcl files that can be sourced directly into OpenSees. Application of the problem-type is not restricted to pushover analyses; finite element meshes for dynamic analyses with soil elements and materials have also been constructed using OpenSees_py.gid by Chang et al. (2005). The output from the OpenSees_py.gid problem type are designed to be used with the PySimple1Gen and TzSimple1Gen commands.

4.3.4 Mesh configuration

A sample finite element mesh from test SJB03 is shown in Fig. 4-9 for the BNWF_SD and BNWF_LP analyses. Piles were modeled using elastic beam-column elements, and soil springs (p-y, t-z, and q-z) were densely located along the piles to represent soil-pile interaction. The analyses were two-dimensional (1x3 pile group), but the pile groups were three-dimensional (2x3 pile group). To account for the 2x3 pile group being modeled as a 1x3 pile group, the stiffness of the pile beam-column elements was doubled, and the stiffnesses and capacities of the p-y, t-z and q-z materials on the piles were doubled as well. The beam-column elements representing the pile cap were assigned very large stiffnesses such that the pile cap essentially translated and rotated as a rigid body. Soil springs on the pile cap were estimated based on the actual dimensions of the cap, so no correction was needed to transform 3-D pile cap loads for the 2-D problem.

4.3.5 Analysis solution method

The analyses were performed by first applying gravity loading, then by applying the lateral loading by linearly increasing the free field soil displacements (or limit pressures for a BNWF_LP analysis) while at the same time linearly increasing the inertia loads. The loads and displacements were applied incrementally using a load control integrator, with the number of required increments depending on the amount of nonlinearity in the pile foundation response. Generally, only one or two increments were required to converge on a solution for the small earthquake motions, while more than 50 increments were required for some of the large motions that induced significant cap displacements. An adaptive sub-incrementing algorithm was implemented into the tcl script such that increments were halved when convergence failure occurred, and then subsequently set to the original increment size after convergence was obtained. Force convergence was obtained using a norm displacement increment test wherein the solution converges when the norm of the displacement vector is smaller than a specified tolerance. Penalty constraints were used to enforce the prescribed displacement boundary conditions. Numbering of nodal degrees of freedom was performed using a reverse Cuthill-McKee algorithm, and the symmetric positive definite system of equations was set up and solved using a Newton-Raphson algorithm.

4.4 EXAMPLE ANALYSES OF TEST SJB03

Sample results from the BNWF analyses will be presented for test SJB03 to demonstrate the analysis procedures and output. Distributions of pile displacement, bending moment and subgrade reaction are compared with the measured distributions to

identify any differences between the analyses and the test data. For design, predicting the entire distribution of bending moment and pile displacement is likely not as important as predicting their peaks. Hence, distributions are presented only for test SJB03, with subsequent sections focusing on the peak bending moments and pile cap displacements from the other tests.

4.4.1   Results of BNWF_SD analyses

Distributions of pile displacement, bending moment, and subgrade reaction (p) for the BNWF_SD analysis of centrifuge test SJB03 are shown in Figs. 4-10 to 4-13 for the small, medium, and large Santa Cruz motions and for the large Kobe motion, respectively. Measured distributions are presented at the time that the peak bending moment was measured in the centrifuge test, and also at the time that the peak pile cap displacement was measured, for comparison with the BNWF analysis data. The peak bending moment and peak pile cap displacement did not occur at the same time during the centrifuge tests due to the complex dynamic loading mechanics. However, pushover analyses should be able to envelope both peak bending moments and peak pile cap displacements using a single set of "statically equivalent" loading conditions.

The distribution of bending moment predicted in the BNWF_SD analyses reasonably matches the measured distribution at shallow depth, but deviates significantly deeper in the soil profile where the predicted bending moments become significantly larger than the measured ones. The cause of this error is related to the liquefiable sand layer being models as soft and weak in the BNWF_SD analysis, but actually being stiff and strong during critical cycles in the centrifuge tests due to dilatancy As a result, the magnitude of

subgrade reaction in the loose sand layer is significantly under-predicted, while the magnitude of subgrade reaction in the dense sand layer is significantly over-predicted. The distributions of pile displacement also did not agree over the full pile length, with the analysis predicting a sharp curvature near the top of the dense sand layer, while the measured distributions vary more smoothly along the length of the pile.

While the predicted distributions exhibit some differences from the measured distributions, the peak values are likely more valuable parameters for design. Peak bending moments were predicted within -4% to +11% and cap displacements within 0% to -26% of the measured values, as summarized in Table 4-17. The predictions are quite reasonable considering the many sources of uncertainty, and would likely be considered sufficiently accurate for design. One reason for the good agreement between the predictions and the measured data is that the input parameters selected for the analyses match well with the observations from the centrifuge tests. The influence of changes in some of the input parameters on the results of the analysis is discussed in later sections.

Table 4-17: Summary of bending moments and pile cap displacements measured during centrifuge test SJB03, and those predicted by the BNWF_SD analyses.

Motion	Bending Moment (kN·m)			Pile Cap Displacement (m)		
	Measured peak	Predicted at depth = 2.7 m[a]	%Error[b]	Measured peak	Predicted	%Error[b]
Small Santa Cruz	-1551	-1412	-9	0.035	0.027	-23
Medium Santa Cruz	-3070	-2944	-4	0.06	0.06	0
Large Santa Cruz	-7082	-6791	-4	0.27	0.20	-26
Large Kobe	-8838	-9812	+11	0.48	0.38	-21

[a] The depth of the bending moment shear gauge was 2.7 meters, so the predicted bending moment is also at depth = 2.7 meters for compatibility. A larger value of bending moment was predicted in the analyses at the connection with the pile cap.
[b] Positive percent error indicates an over-prediction.

4.4.2 *Results of BNWF_LP analyses*

Distributions of pile displacement, bending moment, and subgrade reaction (p) for the BNWF_LP analysis of centrifuge test SJB03 are shown in Fig. 4-14 through 4-17 for the small, medium, and large Santa Cruz motions and for the large Kobe motion, respectively. The distributions of bending moments and pile displacements are different from the measured distributions, in part for the same reasons as for the BNWF_SD analyses that were mentioned previously. However, significant systematic errors arise in the BNWF_LP analyses for two separate reasons: (1) Ground displacements were assumed sufficiently large to mobilize the ultimate pressures in laterally spreading layers, whereas measured ground displacements for the small and medium motions were not

sufficient to mobilize ultimate pressures, and (2) free-field displacements in the dense sand layer were assumed to be zero.

Table 4-18 summarizes the predicted and measured bending moments and pile cap displacements. The bending moments and cap displacements were over-predicted by 306% and 115% for the small Santa Cruz and medium Santa Cruz motions, respectively, because free-field ground displacements were not large enough to mobilize the full downslope passive pressures of the laterally spreading layers for those motions. The bending moment predictions are more reasonable for the large motions (+8% to +12%) because the limit pressures more closely simulate the loads transferred in those motions due to the large observed ground displacements.

The pile cap displacements were significantly over-predicted for the small and medium motions (+243% and +117%, respectively) for the same reason that bending moments were over-predicted for these motions. Cap displacements were under-predicted by 41% and 58% for the large Santa Cruz and large Kobe motions, respectively, because the free-field displacement of the dense sand layer was assumed to be equal to zero. Displacements could theoretically be applied to deep nonliquefiable layers in BNWF_LP analyses to avoid these displacement prediction errors, but the difficulty associated with imposing displacement boundary conditions is the reason why BNWF_LP analyses are used in the first place. If one undertakes the effort of imposing displacements in the dense sand layer, one might as well impose displacements in the lateral spreading layers as well.

Table 4-18: Summary of bending moments and pile cap displacements measured during centrifuge test SJB03, and those predicted by the BNWF_LP analyses.

Motion	Bending Moment (kN·m)			Pile Cap Displacement (m)		
	Measured peak	Predicted at depth = 2.7 m[a]	%Error[b]	Measured peak	Predicted	%Error[b]
Small Santa Cruz	-1551	-6302	+306	0.035	0.12	+243
Medium Santa Cruz	-3070	-6607	+115	0.06	0.13	+117
Large Santa Cruz	-7082	-7949	+12	0.27	0.16	-41
Large Kobe	-8838	-9536	+8	0.48	0.20	-58

[a] The depth of the bending moment shear gauge was 2.7 meters, so the predicted bending moment is also at depth = 2.7 meters for compatibility. A larger value of bending moment was predicted in the analyses at the connection with the pile cap.
[b] Positive percent error indicates an over-prediction in magnitude.

4.5 ANALYSES OF FIVE CENTRIFUGE TESTS USING BASELINE INPUT PARAMETERS

In this section, results of analyses of pile foundations from five centrifuge tests (PDS03, SJB01, SJB03, DDC01 and DDC02) are presented for all of the earthquake motions applied to each of the models. The detailed presentation of the test results in the preceding section for test SJB03 was designed to demonstrate the analysis procedures and typical analytical results. The plots of distributions of bending moments and pile displacements demonstrate some of the differences in loading mechanics between the measured data and the analysis results, but the distributions themselves are not as important for design as the peak bending moment and displacement values. Hence, results of the analyses for all of the different earthquake motions for the different tests are

presented graphically in terms of predicted versus measured peak bending moments and pile cap displacements, but distributions of bending moments and pile displacements are not presented.

Quantifying the bias and dispersion in the predictions is a simple, systematic method of assessing accuracy and uncertainty for design. Bias in bending moment, for example, will be represented by the slope of a least squares fit of a line with 0,0 for an intercept through data points of predicted moment versus measured moment. Slopes greater than 1 indicate an average over-prediction of bending moment or cap displacement and slopes less than 1 indicate an average under-prediction. Dispersion in bending moment, for example, will be represented as a coefficient of variation of predicted bending moment versus measured bending moment about the least-squares fit. The slope of the least-squares fit will be designated by the variable FIT, and the coefficient of variation will be called COV, with a subscript M representing bending moment and Δ representing cap displacement. The data set is sparse, therefore statistical analysis of the data is prone to error. Using the rule of thumb that the potential error in computed standard deviations is equal to the standard deviation divided by the square root of the sample size (Christian 2004), then errors of about 20% can be expected in the coefficients of variation based on the sample size of 21 data points in the analyses. However Christian (2004) notes that this rule of thumb is not always correct and caution should be used when statistically analyzing sparse data sets.

4.5.1   BNWF_SD Analyses

Fig. 4-18 shows the results of BNWF_SD analyses for each earthquake motion for all five centrifuge tests that were analyzed using the baseline set of input parameters. The slope of the best fit for bending moment (FIT_M) is 1.14 and for cap displacement (FIT_Δ) it's 0.73. Hence, bending moments are over-predicted on average by 14% while cap displacements are under-predicted on average by 27%. Small cap displacements were more accurately predicted than large cap displacements, which can be attributed in part to cyclic ratcheting as discussed later. The coefficient of variation for bending moment (COV_M) was 0.26 and for cap displacement (COV_Δ) was 0.36. The bias and dispersion in these relations is very reasonable considering the simplifying assumptions involved in deriving the input parameters. The reasonable prediction is not surprising since many of the design guidelines used to estimate the input parameters were based on measurements from the centrifuge test data.

4.5.2   BNWF_LP Analyses

Fig. 4-19 shows the results of BNWF_LP analyses for each earthquake motion for all five centrifuge tests that were analyzed. The prediction exhibits significantly more bias and dispersion compared with the BNWF_SD analyses with $FIT_M = 1.57$, $FIT_\Delta = 0.76$, $COV_M = 0.54$ and $COV_\Delta = 0.77$ (versus 1.14, 0.26, 0.73 and 0.36 for the BNWF_SD analyses, respectively). Regarding bending moments, the BNWF_LP analysis results indicated some significant conservative bias at small bending moment values, but was reasonably accurate at large values of bending moment. The reason for this bias is that

the BNWF_LP analysis assumes that the crust displacement is large enough to mobilize the ultimate loads against the pile foundation, which was not true for the smaller motions that generated the smaller bending moments. Regarding pile cap displacements, the BNWF_LP analyses tended to over-predict cap displacements for the small and medium motions, and under-predict for the large motions. Hence, the average prediction is reasonable, but clearly there is bias in the method. The under-prediction for the large motions is caused primarily by the assumption of zero free-field displacement in the dense sand layer. BNWF_LP should be used only when ground displacements will be large enough to mobilize ultimate pressures, and when deep nonliquefiable layers will exhibit very small strains.

4.5.3   *Influence of cyclic ratcheting*

One source of systematic bias that was not considered in the BNWF analyses was cyclic ratcheting that occurs as the pile cap accumulates downslope displacements during progressive loading cycles. The influence of cyclic ratcheting was observed by conducting BNWF_SD analyses using a cyclic ground displacement pattern for test SJB01 for a large Kobe motion with 3 meters of ground surface displacement. Inertia forces and strain in the dense sand layer were removed from the analyses to isolate the influence of cyclic ratcheting on accumulated pile cap displacement. The p-y springs on the pile cap had direction-dependent capacities, with downslope loading being the sum of passive loads and friction loads, and the upslope capacity being the sum of only the friction loads. This direction-dependence simulates the gap that existed on the downslope face of the pile cap prior to the large Kobe motion. The drag coefficient for

the p-y springs on the piles in the clay layer was set to 0.1, such that the load capacity for a pile moving through an open gap was equal to 10 percent of p_u. The analyses were first conducted first for a case with small axial pile tip capacity in which axial deformations of the pile tips were significant (i.e. more than 100 mm) and then were repeated with large axial tip capacity such that axial deformations were limited to less than about 5 mm.

Fig. 4-20a shows that the ground surface displacement pattern consisted of 5.25 sinusoidal displacement cycles with 0.5-m amplitude, and a static increase such that the final displacement was 3.0 meters. The pile cap displacement was 0.36 meters for the cyclic load path, compared with 0.34 meters for a linear load path of imposed ground displacement with the same 3.0 meters of surface displacement.

Fig. 4-20b shows how the pile cap accumulates displacements during repeated loading cycles due to cyclic ratcheting. Loading during the first quarter of a sinusoidal cycle follows the same path as for the linear load series. The second loading cycle that follows the first unloading cycle causes the pile cap displacement to exceed the previous displacement that occurred during the first loading cycle. Each subsequent loading cycle is accompanied by an increase in cap displacement compared with the previous cycle due to cyclic ratcheting.

The analyses were repeated with the axial capacities of the pile tips set to a large value that limited the axial deformation of the tips to less than 5 mm. Fig. 21 shows that the pile cap displacement at the end of the load series is about 0.24 meters for both the cyclic and linear load paths. The influence of cyclic ratcheting was much smaller when axial pile tip capacity was sufficient to prevent significant axial plunging and pullout of the piles.

Additional load paths consisting of 1.25, 10.25, 15.25 and 20.25 sinusoidal cycles with 0.5-m amplitude, all with a final displacement of 3.0 meters, were analyzed for the case with small axial capacity and with large axial capacity. Fig. 4-22 shows that as the number of cycles increases, so does the final pile cap displacement for the case with small axial capacity. With 20.25 cycles, the pile cap displacement is 0.42 meters, which is about 25% larger than the cap displacement for the linear load path. Clearly cyclic ratcheting occurs when significant pile tip displacements occur. In contrast, the final pile cap displacement did not vary much for the case when the axial pile capacity was large.

4.5.3.1 *Implications of cyclic ratcheting*

The influence of cyclic ratcheting is expected to be largest for large-magnitude, long duration ground motions combined with axial failure at pile tips. The pile groups in the centrifuge tests were subjected to a large number of loading cycles during a sequence of four or five earthquake motions, and the large cap rotations measured for the 0.73-m diameter pile groups indicated that axial failure of the pile tips occurred. Cyclic ratcheting was probably a big effect on pile groups with large measured pile cap displacements, and a small effect on pile groups with small measured pile cap displacements. This observation is supported by the fact that the small pile cap displacements were more accurately predicted than the large pile cap displacements using the linear load path in the BNWF_SD analyses.

Comparing total measured pile cap displacements with predicted cap displacements might be considered unfair because the influence of cyclic ratcheting is unrealistically large in the measured values. It is therefore useful to explore whether incremental pile

cap displacements might be a fairer measure of the predictive capabilities of the analysis methods. Table 4-19 shows the predictions of pile cap displacement compared with the total cap displacement at the end of each motion, and also with the peak incremental pile cap displacement (peak cap displacement minus initial cap displacement for a given motion). The errors are similar for the incremental pile cap displacements compared with the total pile cap displacements because while incremental displacements reduce errors associated with cyclic ratcheting, they introduce errors caused by neglecting stress history. For example, the incremental displacement for the large Kobe motion for SJB03 was 0.21 meters, but would likely have been larger if the large Kobe motion was not preceded by the three previous motions that locked in some loads on the foundation. Hence, in this dissertation, predicted pile cap displacements will be compared with total measured pile cap displacements, with acknowledgment given to the fact that cyclic ratcheting is not being modeled in the analyses.

Table 4-19: Summary of total and incremental pile cap displacements compared with BNWF_SD analysis results for SJB03.

Motion	Total Cap Displacement			Incremental Cap Displacement	
	Predicted	Measured peak (m)	%Error[a]	Incremental peak (m)	%Error[a]
Small Santa Cruz	0.027	0.035	-23	0.035	-23
Medium Santa Cruz	0.06	0.06	0	0.06	0
Large Santa Cruz	0.20	0.27	-26	0.24	-17
Large Kobe	0.38	0.48	-21	0.29	+31

[a] Positive percent error indicates an over-prediction in magnitude.

4.6   ANALYSES WITH ALTERNATIVE APPROXIMATIONS AND ASSUMPTIONS

Different designers are likely to make different approximations and assumptions when selecting input parameters for static-seismic design of pile foundations in liquefied and laterally spreading ground. Some of the baseline input parameters used in this dissertation would be widely accepted as reasonable even though they do not match trends observed in the centrifuge tests. For example, p-y materials in the liquefied sand layer were assigned small capacities, as is commonly done in design, but contrastingly large subgrade reaction loads were measured in the centrifuge test. Conversely, some of the input parameters used in this dissertation might be deemed unreasonable or excessively conservative even though they do match trends observed in the centrifuge tests. For example, inertia loads and lateral spreading loads were assumed to act in phase in this dissertation, but are commonly assumed to act out-of-phase (e.g. TRB 2002).

The purpose of this section is to present the impact of alternative approximations or assumptions on the predictive accuracy of the BNWF_SD method. The analyses were repeated with various deviations from the baseline set of input parameters developed in the previous section, and the effect on the analysis results were quantified.

4.6.1 *Measured quantities used as input parameters*

Fig. 4-23 shows the predicted versus measured peak bending moments and pile cap displacements for analyses in which the measured ground displacement profile, measured crust load, and measured inertia forces were used in lieu of the baseline estimates. All other parameters were the same as for the baseline set. The results were $FIT_M = 0.99$, $COV_M = 0.18$, $FIT_\Delta = 0.63$ and $COV_\Delta = 0.47$. The prediction of bending moment is significantly improved compared with the baseline case, and dispersion is reduced ($COV_M = 0.18$ versus 0.26). The prediction of cap displacement is worse than it was for the baseline case ($FIT_\Delta = 0.63$ versus 0.73), which supports the previous hypothesis that the errors in estimating pile cap displacements were systematic, arising from limitations of the static analysis method (i.e. the inability to model cyclic ratcheting) rather than errors in selecting the input parameters. Table 4-20 summarizes the bias and dispersion in analysis predictions for all of the analyses performed in this section.

Table 4-20: Summary of bias and dispersion in analysis predictions.

Analysis Identification	$FIT_M{}^1$	$COV_M{}^2$	$FIT_\Delta{}^1$	$COV_\Delta{}^2$
BNWF_SD Baseline	1.14	0.26	0.73	0.36
BNWF_LP Baseline	1.57	0.54	0.76	0.77
Measured Inputs	0.99	0.18	0.63	0.47
No Inertia Loads	0.62	0.34	0.58	0.34
No Lateral Spreading	0.42	0.65	0.10	1.14
Reduced Crust Load, No Inertia Loading	0.51	0.32	0.52	0.36
Pile Tips Fixed	1.15	0.26	0.72	0.37
Static p-y Relation in Crust	1.27	0.33	0.79	0.36
Pile Heads Fixed into Cap	1.28	0.27	0.66	0.36
Continuous Soil Displacement Profile	1.17	0.26	0.76	0.35

[1] FIT is the slope of the least squares linear regression of predicted versus measured with intercept at 0,0. Subscript M is for bending moment and subscript Δ is for cap displacement

[2] COV is the coefficient of variation of the predicted data about the least-squares fit, and represents the dispersion of the data about the median trend.

4.6.2   *No inertia loading (lateral spreading only)*

Fig. 4-24 presents the results of the BNWF_SD analyses using the baseline parameter set, but with the inertia loads from the pile caps and superstructures set to zero. The results were $FIT_M = 0.62$, $COV_M = 0.34$, $FIT_\Delta = 0.58$ and $COV_\Delta = 0.34$. Bending moments were under-predicted by an average of 38% when the inertia forces were excluded, whereas they were over-predicted by an average of 14% with the inertia forces

excluded (FIT_M = 0.62 versus 1.14). Inertia forces are a very important components that must be included in static-seismic design of pile foundations that are designed to exhibit limited cap displacements in lateral spreads. Furthermore, large-diameter piles that are often required to limit pile cap displacements in lateral spreads are often connected by massive pile caps that can contribute significant inertia loads onto the piles.

4.6.3   No lateral spreading (inertia only)

Fig. 4-25 shows the results of BNWF_SD analyses using the baseline parameter set, but with no imposed free-field ground displacements (i.e. inertia loading only). The results were FIT_M = 0.42, COV_M = 0.65, FIT_Δ = 0.10 and COV_Δ = 1.14. Bending moments were under-predicted by about 60%, and pile cap displacements were under-predicted by about 90% or more. Clearly the ground displacements significantly influenced the response of the pile foundations. Failing to identify lateral spreading potential could result in dangerously unconservative designs.

4.6.4   Reduced crust load and no inertia loading

Fig. 4-26 shows the results of BNWF_SD analyses using the baseline parameter set, but with no applied inertia loading, and no contribution from friction loading to the capacities of the p-y materials on the pile caps. This case was included because these assumptions would likely be considered reasonable by the standards of today's design practice [e.g. JRA (2002) implies passive loading from nonliquefied crusts but no friction loads, and TRB (2002) states that inertia forces need not be included with lateral

spreading loads]. The results were $FIT_M = 0.51$, $COV_M = 0.32$, $FIT_\Delta = 0.52$ and $COV_\Delta = 0.36$ (versus 1.14, 0.26, 0.73 and 0.36 for the baseline case, respectively). Both bending moments and cap displacements were under-predicted by an average factor of about 2. Clearly friction forces and inertia loads were important for the pile foundations in the centrifuge tests, and should be included in design computations. For the case with no inertia loading but with the friction forces on the pile cap included, $FIT_M = 0.62$ and $FIT_\Delta = 0.58$, with the difference being attributed to the friction forces on the pile cap.

4.6.5   Pile tips fixed (no base rocking)

Axial displacements at the pile tips might potentially be excluded to simplify analytical computations using the justification that the factor of safety against axial failure is sufficient to prevent significant rocking of the foundation. Fig. 4-27 shows the results of BNWF_SD analyses performed using the baseline set of input parameters, but with the pile tips fixed in the vertical direction. The results were $FIT_M = 1.15$, $COV_M = 0.26$, $FIT_\Delta = 0.72$ and $COV_\Delta = 0.37$. The predicted bending moments increased by less than 1% compared with the baseline set of parameters ($FIT_M = 1.15$ versus 1.14), and the predicted cap displacements decreased slightly ($FIT_\Delta = 0.72$ versus 0.73). Allowing axial deformations at the tips of the piles from the centrifuge tests was not very important because most of the pile foundations did not exhibit axial failure, and because cyclic ratcheting is not included in monotonic linear load paths, as discussed previously. However, neglecting axial deformations at the pile tips could cause a more significant under-prediction of pile cap displacements if the axial loads do induce bearing failure.

4.6.6 *Stiffness of p-y materials in nonliquefied crust layer set to higher values characteristic of non-liquefied soil profiles*

Fig. 4-28 shows the results of BNWF_SD analyses performed using the baseline set of input parameters, but with the y_{50} of the p-y materials between the nonliquefied crust and the pile group set to 10% of the values from the baseline parameter set such that the stiffness of the relations was characteristic of load transfer in nonliquefied soil profiles. The results were $FIT_M = 1.27$, $COV_M = 0.33$, $FIT_\Delta = 0.79$ and $COV_\Delta = 0.36$ (versus 1.14, 0.26, 0.73 and 0.36 for the baseline case, respectively). Results were similar to those for the baseline case for the large earthquake motions because ground displacements were large enough to mobilize the ultimate loads in the crust and the stiffness of the p-y materials did not matter. However, larger errors occurred for the small and medium motions because ground displacements were not sufficient to mobilize the ultimate capacities in the centrifuge tests, whereas they did mobilize ultimate loads in the analyses. Hence, including the softening of the load transfer behavior in the nonliquefied crust caused by the underlying liquefied layer is important when moderate ground displacements are expected (i.e. centimeters), but becomes unimportant when ground displacements are expected to be large (i.e. meters).

4.6.7 *Pile heads fixed into cap (no rotation at cap to pile connection)*

Designers commonly assume that pile caps provide rigid connections at the heads of piles such that the rotation of the pile cap and the rotation of the pile head are the same. However, some rotational flexibility was observed in the centrifuge tests, and also exists for real piles and pile caps. Fig. 4-29 shows the results of BNWF_SD analyses with the

piles fixed into the pile cap, but otherwise identical input parameters with the baseline case. The results were $FIT_M = 1.28$, $COV_M = 0.27$, $FIT_\Delta = 0.66$ and $COV_\Delta = 0.36$ (versus 1.14, 0.26, 0.73 and 0.36 for the baseline case, respectively). Compared with the baseline case, predicted bending moments were larger and predicted pile cap displacements were smaller when the pile tips were fixed into the cap rather than using a flexible connection. Neglecting rotational flexibility at the pile to pile cap connection could cause an under-prediction of pile cap displacements and should therefore be included in design of foundations where excessive pile cap deformation would be problematic.

4.6.8   Continuous soil profile

To determine the influence of the shape of the free-field ground displacement on analysis results, BNWF_SD analyses were performed using the baseline set of parameters, except that the shear strain in the sand layer was increased such that there was no displacement discontinuity, which is similar to observations of centrifuge tests by Abdoun et al. (2003) with a perforated high-permeability crust layer. The formation of a displacement discontinuity is difficult to predict in practice, and other design procedures (e.g. Tokimatsu 2003) do not attempt to include this mechanism. The ground surface displacements and strains in the dense sand layers were kept the same as in the baseline case. Fig. 4-30 shows the results of BNWF_SD analyses with a continuous free-field soil displacement profile. The results were $FIT_M = 1.17$, $COV_M = 0.26$, $FIT_\Delta = 0.76$ and $COV_\Delta = 0.35$ (versus 1.14, 0.26, 0.73 and 0.36 for the baseline case, respectively). The analyses with the continuous soil displacement profile were slightly more conservative than the analyses with the baseline set of input parameters because the loose sand layer

provided a small downslope loading throughout its depth using the continuous soil profile, whereas the a portion of the loose sand layer provided an upslope resisting load using the discontinuous baseline displacement profile. However, the magnitude of these loads was small, hence the changes in predicted bending moment and cap displacement were relatively small as well. The relatively small influence of ground displacement shape in the analysis is related to the small capacities assigned to the p-y materials in the loose sand layer. If the p-y capacities had been stiffer and stronger to represent the dilatant conditions that were measured in the centrifuge tests, the analysis would likely have been very sensitive to the displaced shape of the ground profile.

4.7 SENSITIVITY STUDY

In this section, the influence of variations in the input parameters is examined to identify the parameters whose uncertainty and variability most significantly influences the analysis results.

4.7.1 Approach

The sensitivity approach adopted in this study has been used by researchers at the PEER center (e.g. Porter et al. 2002), and is commonly utilized in decision-making (NRC 2001). In general, the procedure consists of an output variable that is studied in a variety of deterministic tests consisting of computations utilizing different input variables. In this case, the output variables are peak pile bending moment and pile cap displacement, and the input variables include inertia forces, crust load magnitude, ground

displacements, and others discussed later. The analysis proceeds by selecting a baseline set of best-guess input parameters, and a minimum and maximum value for each parameter. One of the input parameters is set to its minimum value while the other inputs are assigned their baseline values, and the outputs are computed. Then that input parameter is assigned its maximum value while the other inputs are assigned baseline values, and the outputs are computed. The absolute value of the difference in these two outputs is called the swing. The swing is computed for each maximum/minimum pair of input parameters, and the inputs are subsequently sorted by swing and represented as a bar diagram, called a tornado diagram, stacked top to bottom in order of decreasing swing. These diagrams exhibit the characteristic shape of a tornado, hence their name.

The number of total analyses required is equal to 2N+1, where N is the number of input parameters to be varied. For example, 10 input parameters were selected for the sensitivity study in this dissertation, so 21 analyses were performed for each ground motion. Considering the widespread use of computers, the bulk of time required to perform design computations is in setting up the analysis, while actually running the analysis requires significantly less time. Hence, running 21 analyses instead of just one would typically require only a modest increase in effort (e.g. Duncan 2000).

In selecting a reasonable range of values for each input parameter, one should try to specify a range for each parameter that corresponds to the same probability (i.e. the likelihood that a given parameter lies within the selected range should be constant for all of the parameters). Otherwise some parameters could unfairly appear to influence the analysis results more than they actually do. Typically we do not have sufficient data to formally characterize the variability in a given input parameter. Christian (2004)

provided an example in which an erroneous distribution was obtained from a small data set, and showed that dispersion is often under-estimated from small data sets and cautioned against assuming that small data sets conform to the "Law of Large Numbers". In the absence of sufficient data to reliably estimate statistical properties of a given parameter, judgment and approximations must be used. General coefficients of variation can be found for a number of common geotechnical properties, which can aide in developing reasonable ranges of site-specific input parameters for sensitivity studies. Duncan (2000) explained the "three-sigma" rule, in which the maximum and minimum possible perceived values of a parameter typically correspond to plus and minus three standard deviations from the mean.

The effort exerted in estimating a reasonable range for each input parameter for a sensitivity study should be congruous with the sophistication of the sensitivity approach. The purpose is to obtain some idea of which input parameters are important and which are unimportant. One's inability to obtain statistically reliable measures of dispersion in the input parameters should not paralyze the sensitivity evaluation process. Rather, the sensitivity analysis can proceed with rough estimates of standard deviations, and may lead to the conclusion that uncertainty in some parameters is unimportant because that particular parameter does not participate significantly in the mechanics of the problem. Conclusions from such a sensitivity study can subsequently serve as the foundation for a more robust probabilistic analysis or reliability analysis, with care taken to accurately characterize the dispersion in the most important parameters while efficiently neglecting the dispersion in the unimportant parameters.

The following limitations should be considered in performing a sensitivity analysis:

1. Results from a sensitivity study of a given problem cannot be generalized to other problems; separate sensitivity studies are required for each problem.

2. The sensitivity approach neglects correlations between input parameters. For example, for his BNWF_SD analyses of single piles in lateral spreads, Singh (2002) found that soil layers assigned large shear strains were generally soft and should be assigned small ultimate capacities for subgrade reaction. Hence, subgrade reaction and ground displacement are correlated, yet each parameter is varied independently in the sensitivity analysis.

3. The sensitivity approach depends on the values selected for the baseline input parameters. Reasonable but different selections of baseline input parameters could drastically influence the sensitivity results.

4. The approach evaluates the sensitivity of the analysis method to variations in input parameters, and is therefore bound to the same limitations and assumptions inherent to the analysis method. The static approach adopted in this dissertation does not capture many of the fundamentals that actually occur, so there could be a mismatch between the input parameters that are identified as important in the sensitivity study, and the properties that are actually important in the field.

4.7.2   Ranges assigned to input parameters

The following input parameters were each assigned a range of values for the sensitivity study:

1. The ultimate capacities of the p-y materials in the nonliquefied crust layer.

2. The ultimate capacities of the p-y materials in the liquefied sand layer.

3. The ultimate capacities of the p-y materials in the dense sand layer.

4. The magnitude of the displacement of the nonliquefiable crust layer.

5. The magnitude of the displacement of the liquefiable loose sand layer.

6. The magnitude of the displacement of the nonliquefiable dense sand layer.

7. The pile cap (and structure when appropriate) inertia loads.

8. The axial capacity of the piles (i.e. the capacities of the t-z and q-z materials).

9. The stiffness of the p-y materials on the pile caps.

10. The rotational stiffness of the connection between the pile heads and the pile cap.

The range assigned to each parameter is ± a factor of two, which will be shown in the paragraphs that follow to correspond to about ± 1 ½ standard deviations. Minus a factor of two is Parameter set A, and plus a factor of two is Parameter set B. Justification for the ± a factor of two assumption are provided first for input parameters with the largest data sets, with subsequent estimates of input parameters requiring progressively more and more judgment and approximations.

Bartlett and Youd (1995) presented a database of nearly 500 data points of lateral spreading ground displacements, and they calibrated a multiple linear regression model to the data. They found that their model provided reasonable estimates of lateral spreading displacements to within plus or minus a factor of two. They did not explicitly state the coefficient of variation associated with their model's predictive capabilities, but plus or minus a factor of two corresponds roughly with 1 ½ standard deviations (σ's) in their

model for ground displacements in the range of interest for this dissertation of smaller than about 3 meters (dispersion is smaller for ground displacements larger than 3 meters). The observation of 1 ½ standard deviations was made qualitatively by noting that about 80% to 90% of the data lies inside of the 2:1 and 1:2 range, and that about 87% of the data would lie within the ±1.5σ range.

Dispersion in predicting pile cap acceleration as being equal to the ground surface acceleration predicted in the absence of liquefaction was presented in Chapter 3. The coefficient of variation was found to be 0.46, and using the ± factor of two rule of thumb would correspond to about ± 2.0 σ. The data set had only 15 points, so the actual coefficient of variation can be anticipated to be larger than based on statistical analysis. Hence, the ± factor of two rule of thumb will be assumed to correspond to ± 1.5 σ.

Curras et al. (2001) analyzed lateral load test data from large-diameter cast in drilled hole (CIDH) shafts, and presented p-multipliers that were required to accurately predict the measured pile response. The coefficient of variation of their sparse data set (11 data points) was 0.59, and using the ± factor of two rule of thumb would correspond to about ± 1.2 σ. However, the data set is sparse, so the rigorous statistical analysis is merely an approximation. The ± factor of two rule of thumb could reasonably correspond to ± 1.5 σ.

Gilbert et al. (2005) observed that axial capacity of offshore piles is log-normally distributed with coefficients of variation ranging from about 0.3 to 1.0. TRB (2004) observed a smaller range in c.o.v. of 0.29 to 0.62. These observations were derived from static axial load test data of piles in non-liquefied ground. Material properties and soil stratigraphy in the centrifuge tests were better known than in the field test cases since the

models were constructed in a laboratory, but liquefaction of the loose sand and significant pore pressure buildup in the dense sand complicates the prediction of axial pile capacity in the centrifuge tests. A reliable measure of dispersion in the prediction of axial capacity cannot be obtained, so the ± factor of two rule of thumb will be assumed to correspond to ± 1.5 σ. While this assumption cannot be completely justified, it at least falls within the ranges of c.o.v. observed by Gilbert et al. (2005) and by TRB (2004).

Of the ten parameters being varied in the sensitivity study, ranges for two of them have yet to be established: 1. the stiffness of the p-y materials in the nonliquefiable crust, and 2. the rotational stiffness of the connection between the piles and the pile cap. Very little data is available to reliably establish measures of dispersion for these parameters. Curras et al. (2001) systematically varied the stiffness of the p-y materials used for the large-diameter CIDH piles, and found slightly more dispersion in stiffness than in capacity (c.o.v. of 0.65 for stiffness compared with 0.59 for capacity). Given the errors associated with the small data set, it is reasonable to assume that the dispersion for the two parameters is similar. Extrapolating their observations from static load tests in non-liquefied ground to p-y stiffness in lateral spreading ground is problematic because the loading mechanisms are different (Chapter 3). Nevertheless, a range of stiffness values must be selected for the sensitivity study. For simplicity, the ± factor of two rule of thumb will be assumed to correspond to ± 1.5 σ for p-y stiffness in the laterally spreading crust. Rotational stiffness at the connection between piles and pile caps is a structural engineering problem that is beyond the scope of this dissertation. Again, for simplicity and uniformity, the ± factor of two rule of thumb will be assumed to correspond to ± 1.5 σ for rotational stiffness of these connections as well.

4.7.3 Tornado diagrams for SJB03

The tornado diagrams for the large Kobe motion for test SJB03 are plotted in Fig. 4-31 for bending moment. The most influential parameter was the capacity of the p-y materials in the nonliquefiable crust layer, followed by pile cap inertia force, followed by free-field displacement in the dense sand layer. The least influential parameter was axial capacity of the piles, though many other parameters were nearly equally un-influential. The tornado diagram for pile cap displacement for the large Kobe motion for test SJB03 is shown in Fig. 4-32. The three parameters that most influenced bending moments also most influence cap displacement, though the order is different. Free-field displacement in the dense sand most influenced cap displacement, followed by the capacity of the p-y materials in the nonliquefied crust, followed by inertia forces. The same five parameters were least influential for bending moments and cap displacements.

Tornado diagrams for the remaining motions for test SJB03 are shown in Figs. 4-33 to 4-38. Capacity of the p-y materials in the nonliquefied crust and inertia forces were influential parameters for bending moments and cap displacements for all four motions. Axial pile capacity, the capacity of the p-y materials in the loose sand layer, and the free-field ground displacement in the loose sand layer did not significantly influence bending moments nor cap displacements for any of the motions.

Bending moments and cap displacements for the large motions tended to be dominated by two or three highly influential parameters, while the influence was distributed among four or five parameters for the smaller motions. The reason for this is that the stiffnesses of the p-y materials and crust displacement did not matter much for the large motions because the ground displacements were sufficiently large to drive them to their ultimate

capacities. However, the stiffness of the materials and the ground displacements for the smaller motions was more important because the moderate ground displacements did not drive the p-y materials to their ultimate loads. Different observations for different levels of shaking demonstrates that different problems will exhibit different influential input parameters, and that sensitivity studies should be performed for each problem separately.

4.7.4 Summary plots from sensitivity study for all tests

The tornado diagrams provide a detailed presentation of the results of the sensitivity study for each test, but it is difficult to compare the importance of the various parameters across the entire suite of tests. In this section, the results from the tornado plots are summarized in histograms that show the number of times a given parameter was the most influential, second most influential, and so on. The tornado diagrams for each motion for each test are in Appendix C, and the data for the histogram summaries was taken directly from those tornado diagrams.

The summary histograms are presented in Figs. 4-39 to 4-41. The capacity of the p-y materials in the nonliquefied crust layer and the inertia forces were the two most dominant input parameters across the entire suite of tests for predicting both bending moments and pile cap displacements (i.e. the bars of the histogram are clustered to the left side, where influence is high). The two sources of downslope loading on the pile group are the crust load and the inertia forces, so it is not surprising that these two properties significantly influenced the predicted cap displacements and bending moments. The capacity of the p-y materials in the loose sand, and the free-field displacement of the loose sand never significantly influenced the analysis results. This

observation is related to the fact that very small capacities were assigned to the p-y materials in the loose sand layer to represent the influence of liquefaction. Since the capacities were small, doubling them or halving them did little to change the response of the pile foundation. While the p-y materials in the loose sand were unimportant in the sensitivity study, the dynamic response of the sand layer contributed significantly to the actual loading mechanics observed in the centrifuge tests. Hence, there is a mismatch between the predicted and observed importance of subgrade reaction in the liquefied sand layer.

A number of parameters exhibited a bi-modal distribution of influence, meaning that they were highly influential for some analyses but not influential for others. For example, the axial capacity of the piles did not exhibit significant influence on most of the analyses, but exhibited a heavy influence on others. The explanation for this observation is that either the piles failed under axial loading due to plunging or pullout, or they did not fail. Axial failure of the piles tends to considerably decrease bending moments and considerably increase pile cap displacements, but when axial loads do not exceed the capacity of the piles, the influence on bending moments and cap displacements is small. A similar bi-modal distribution of influence was observed for the stiffness of the p-y materials in the nonliquefiable crust layer because either the ultimate capacities of the p-y materials were mobilized or they were not. For cases when ground displacements were large enough to mobilize the capacities, the shape of the p-y curves did not matter because the crust load was controlled by the capacity of the materials. For smaller ground displacements associated with the small and medium motions, the shape

of the p-y curve was important because the crust load was controlled by a point on the p-y curve that was smaller than the ultimate load.

4.8   SUMMARY

In this chapter, static-seismic analyses of pile groups in liquefied and laterally spreading ground that utilized a set of baseline guidelines and input parameters were performed in OpenSees. Pre-existing guidelines were adopted for the baseline set of input parameters, and subsequently modified to account for the effects of liquefaction. Centrifuge test observations were utilized to characterize the influence of liquefaction in developing the baseline set of input parameters. Detailed results of the analyses were compared with centrifuge test data for one of the tests, and summary results of predicted peak bending moment and peak pile cap displacement were compared with five centrifuge tests. The impact of alternative sets of design guidelines, assumptions and approximations was explored by systematically changing the various input parameters and subsequently observing the influence on peak bending moments and pile cap displacements. The influence of uncertainty in ten of the input parameters was explored in a sensitivity study.

Peak bending moments for test SJB03 were predicted within -9% to +11%, while pile cap displacements were predicted within -26% to 0% for the BNWF_SD analyses, wherein lateral spreading was modeled as displacements on the free-ends of the soil springs. In the BWNF_LP analyses, wherein lateral spreading was modeled using limit pressures imposed on the pile, bending moments were predicted within +8% to +306% while pile cap displacements were predicted within -58% to +243%. BNWF_LP

analyses resulted in larger errors than the BNWF_SD analyses because 1. ground displacements were not sufficiently large to mobilize limit pressures against the piles for the small and medium motions, and 2. free-field ground displacements were not imposed in the dense sand layer for the BNWF_LP analyses whereas some small displacements were imposed in the BNWF_SD analyses.

Peak bending moments for five centrifuge tests were over-predicted by an average of 14% using the baseline set of input parameters. The source of this bias is not entirely understood, but is quite reasonable considering the various sources of uncertainty in the input parameters (i.e. estimating inertia forces, crust load magnitudes and ground displacements). Furthermore, bending moments were over-predicted, and some built-in conservatism is often desirable for simple design methods.

Pile cap displacements for five centrifuge tests were under-predicted by an average of 37% using the baseline set of input parameters, with the primary cause being attributed to cyclic ratcheting. Cyclic load paths imposed on an example pile group foundation showed that cyclic ratcheting during repeated loading cycles can cause larger pile cap displacements than a single monotonic linear load path if axial failure occurs at the pile tips. 25% more displacement was accumulated for a sinusoidal load path of 20.25 cycles of ground displacement compared with a monotonic push with the same final ground displacement when pile tip displacements were about 100 mm. However, the influence was negligible when pile tip displacements were reduced to less than about 5 mm.

The BNWF_SD analyses were repeated with alternative assumptions and approximations that were different from the baseline set of input parameters. Many of the alternative assumptions have been recommended in various design guidelines, and

others could potentially be considered as reasonable approximations. The additional analyses showed that:

- including inertia forces and lateral spreading displacements simultaneously was required to accurately predict bending moments and pile cap displacements. Many design guidelines assume that the two loads occur at different times and can therefore be treated separately (e.g. TRB 2002). However, analyses of the centrifuge tests showed that the inertia loads were critical components, and that static-seismic design codes that recommend uncoupling inertia loads from lateral spreading loads should never be used to design stiff pile groups that perform well in lateral spreads because such an approach is potentially inaccurate and unconservative. Including superstructure and pile cap inertia loads is a critical for obtaining safe and reliable bridge foundations,

- lateral loads exerted by nonliquefiable crusts include friction components that had to be included in the analyses to accurately predict peak bending moments and pile cap displacements. These friction components are not explicitly required in many design codes (e.g. JRA 2002), and could therefore potentially be neglected,

- softening the p-y relations in the nonliquefiable crust layer to account for the influence of the underlying liquefied sand is important for cases where moderate ground displacements are anticipated, or when a large number of cycles can soften the response through cyclic degradation, but becomes

unimportant when large ground displacements cause mobilization of the ultimate crust load,

- including rotational flexibility at the connection between the pile and pile cap can be important if excessive displacements of the pile cap are an issue,

- using a continuous soil profile instead of imposing a displacement discontinuity only slightly changed the predicted bending moments and pile cap displacements because the only change was the direction of loading in the liquefied sand layer where the capacities of the soil springs were very small. More flexible piles that move along with the ground would likely be influenced more by the displaced shape of the free-field soil.

A suite of BNWF_SD analyses were performed to assess the sensitivity of predicted pile bending moments and pile cap displacements on uncertainty in the input parameters. The most influential parameters for this type of analysis were the capacity of the p-y materials in the nonliquefied crust layer and the inertia forces. The least influential input parameters were the capacity of the p-y materials in the liquefied sand layer and the free-field displacement of the liquefied sand. The predicted influence of the liquefied sand was smaller than the influence observed in the centrifuge tests because the liquefied sand was modeled as soft and weak in the BNWF analyses whereas the measured subgrade reaction loads were significantly larger. Free-field displacement of the nonliquefiable crust layer and axial capacity of the piles were important for some tests, but not for others. For example, free-field displacement of the crust was not important when the ground displacements were large enough to drive the p-y materials in the crust layer to

their ultimate capacities, but became important for smaller crust displacements where loads from the crust were defined by the intermediate range of the p-y materials.
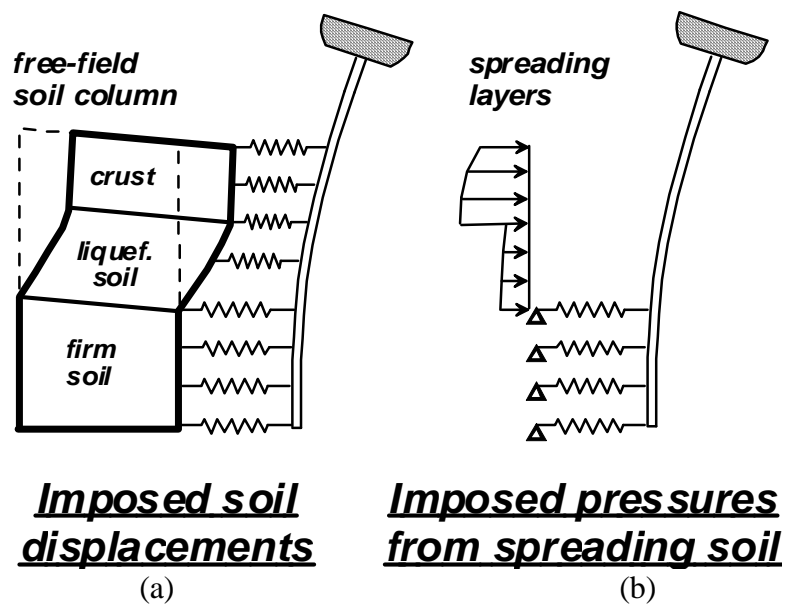
Figure 4-1: Schematic of (a) BNWF_SD analysis with imposed soil displacements, and (b) BNWF_LP analysis with imposed limit pressures.

Figure 4-2: Six-pile group from test SJB03 during excavation after shaking.
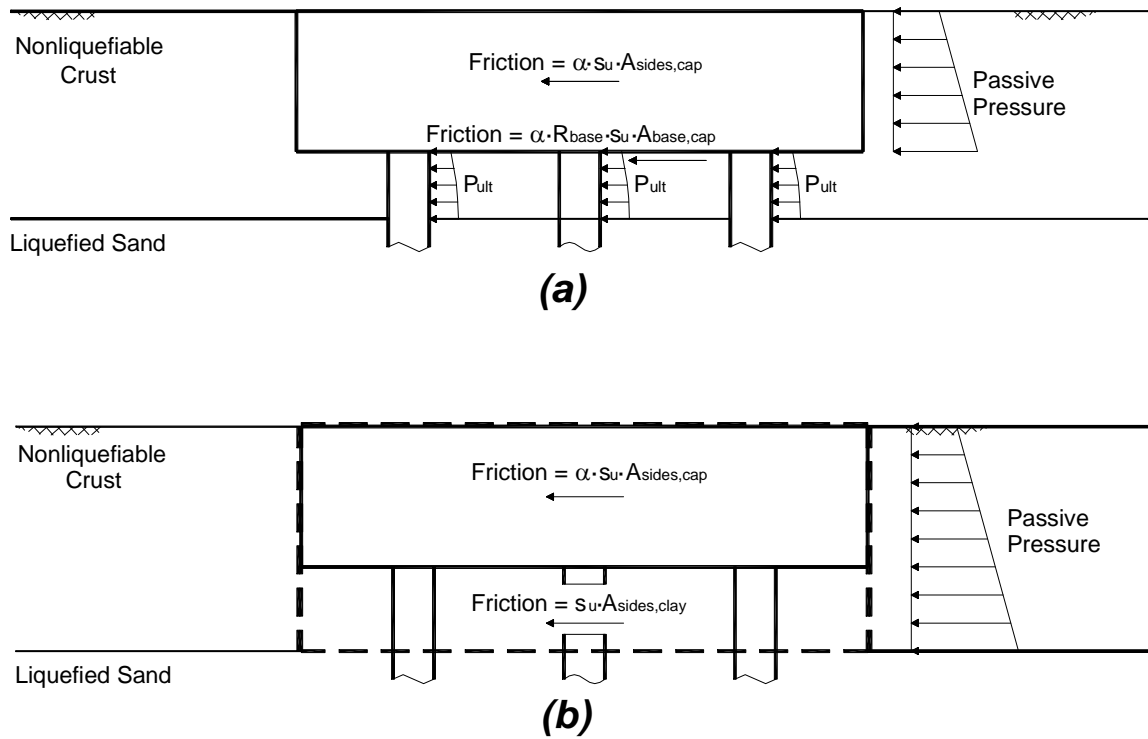
Figure 4-3: Free-body diagram of loads from nonliquefiable crust for (a) mechanism in which clay flows around piles beneath the pile cap, and (b) "equivalent block" mechanism in which the clay becomes trapped between the piles beneath the pile cap.
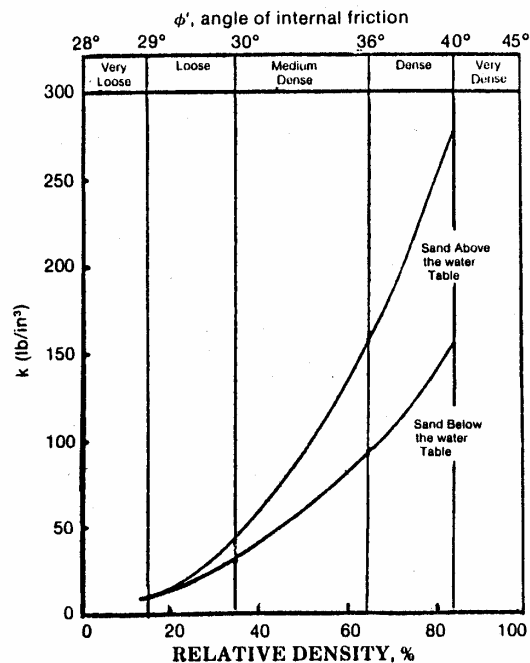
Figure 4-4: Coefficient of subgrade reaction versus relative density (Reese et al. 2000).
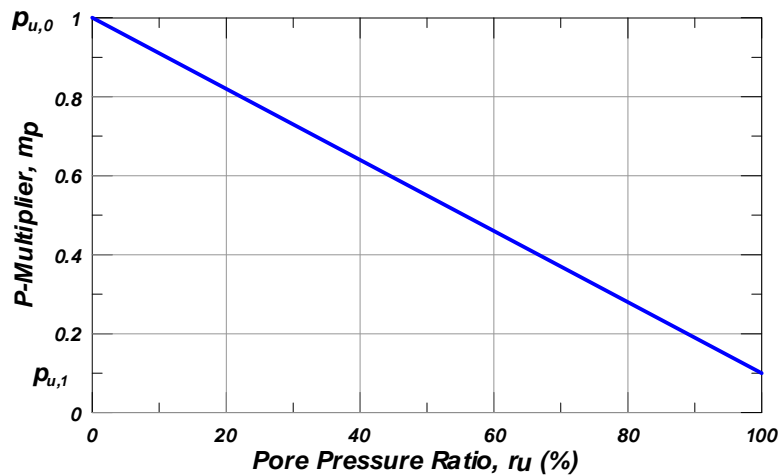
Figure 4-5: Influence of excess pore pressure in the free-field on ultimate lateral resistance, pu (After Dobry et al. 1995).

Figure 4-6: Free-body diagram to calculate yield acceleration for an infinite slope.
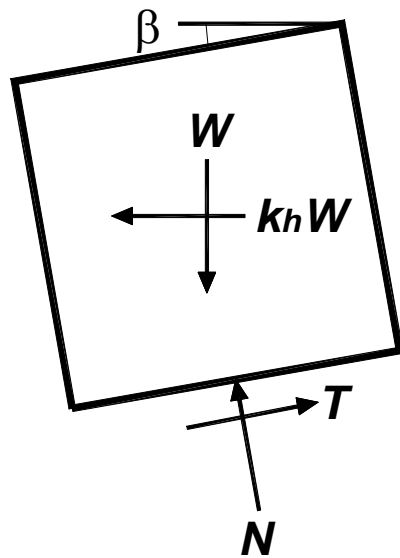
$$\sum F_V = 0$$

$$-W + T \cdot \sin(\beta) + N \cdot \cos(\beta) = 0$$

$$N = \frac{W - T \cdot \sin(\beta)}{\cos(\beta)}$$

$$\sum F_H = 0$$

$$-k_H \cdot W + T \cdot \cos(\beta) - N \cdot \sin(\beta) = 0$$

$$k_H = \frac{T - W \cdot \sin(\beta)}{W \cdot \cos(\beta)}$$
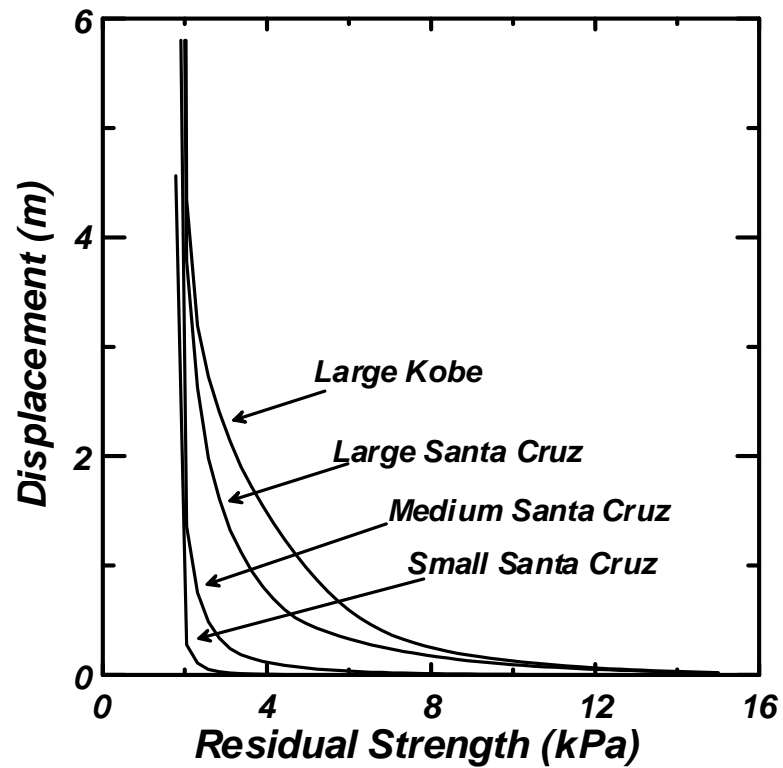
Figure 4-7: Results of sliding block analysis for nonliquefied crust layer in centrifuge test for SJB03.
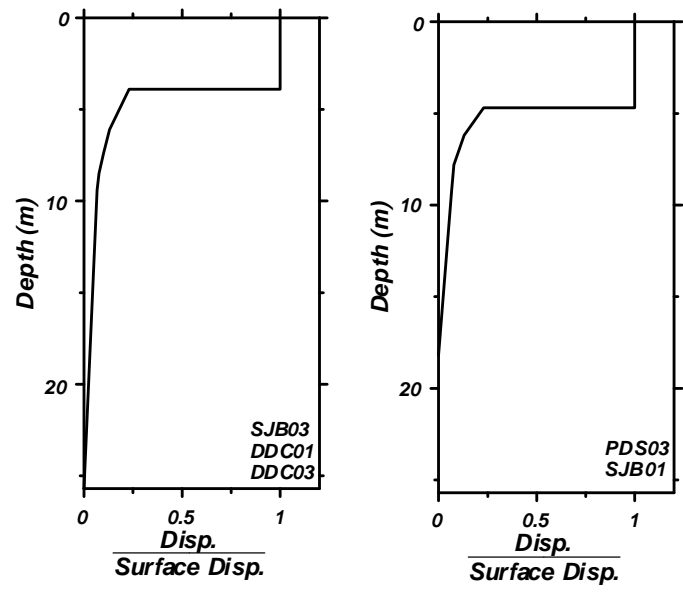
Figure 4-8: Free-field ground displacement profiles.

(a) *(b)*

Figure 4-9: Element configurations used in (a) BNWF_SD and (b) BNWF_LP analyses. Green lines are beam-column elements, and each number represents the location of the p-y and t-z elements.
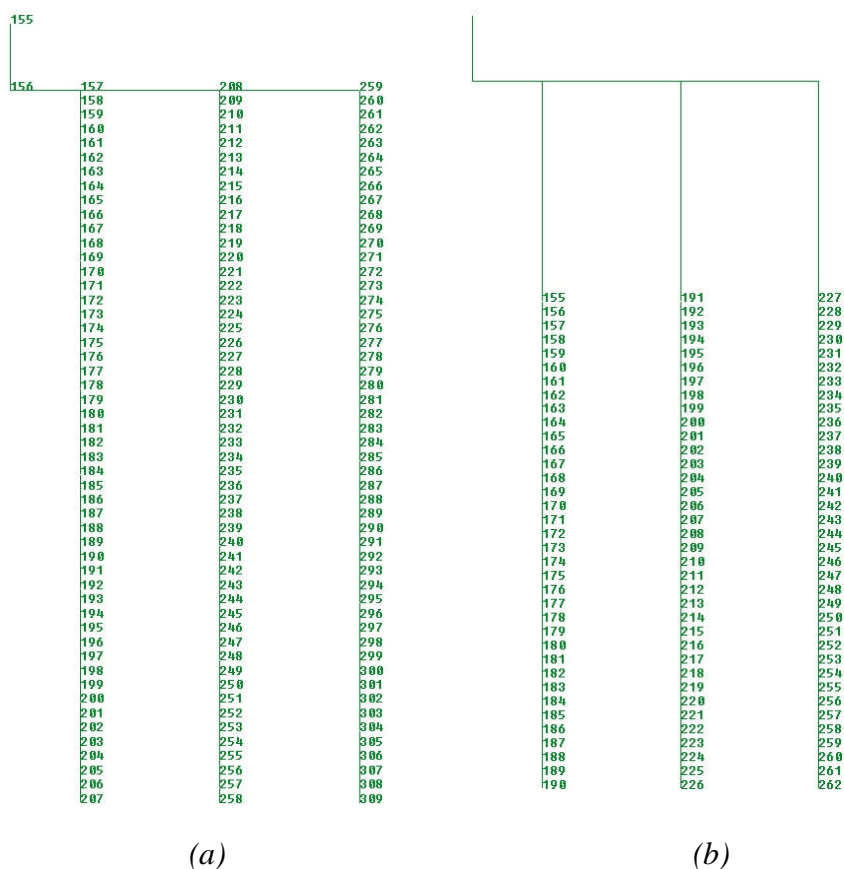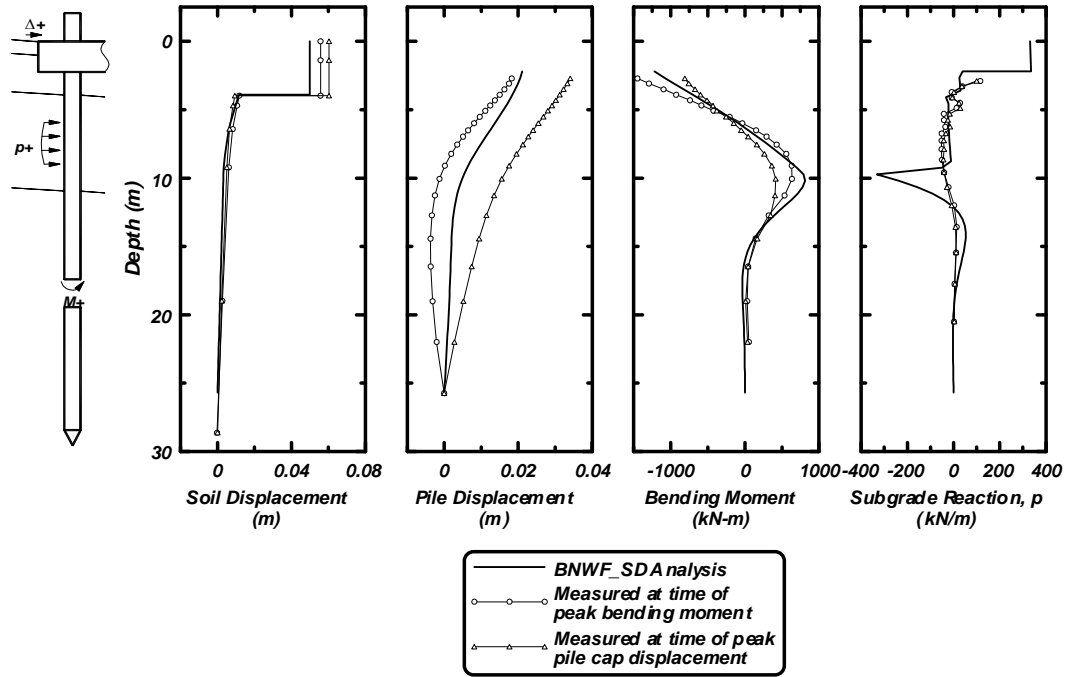
Figure 4-10: Results of BNWF_SD analysis of centrifuge test SJB03 for the small Santa Cruz motion.

255
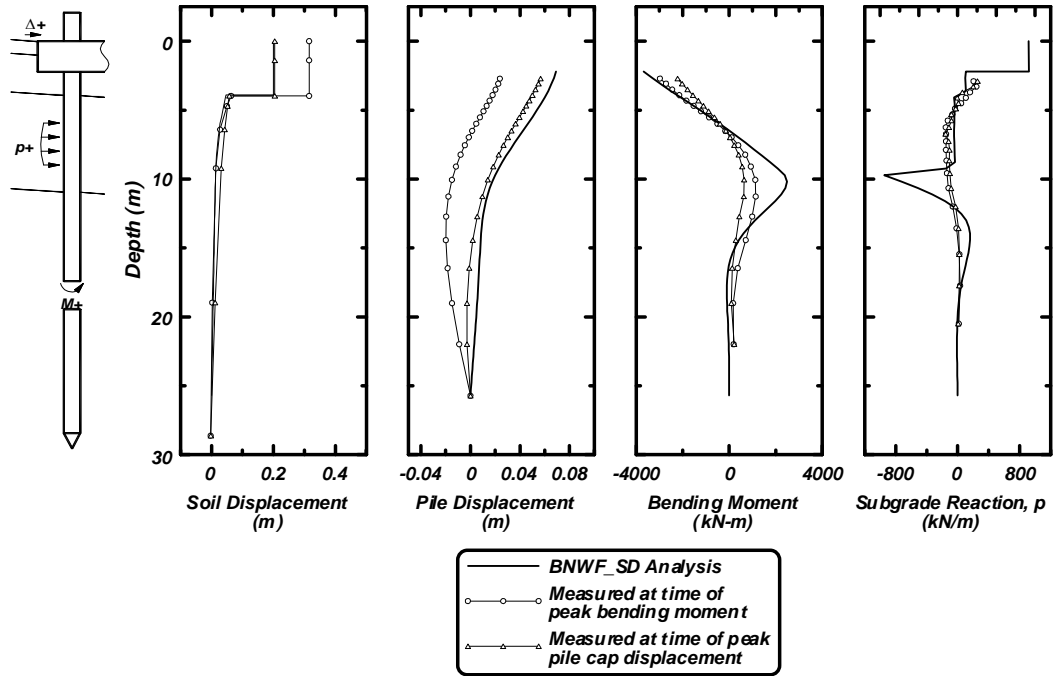
Figure 4-11: Results of BNWF_SD analysis of centrifuge test SJB03 for the medium Santa Cruz motion.
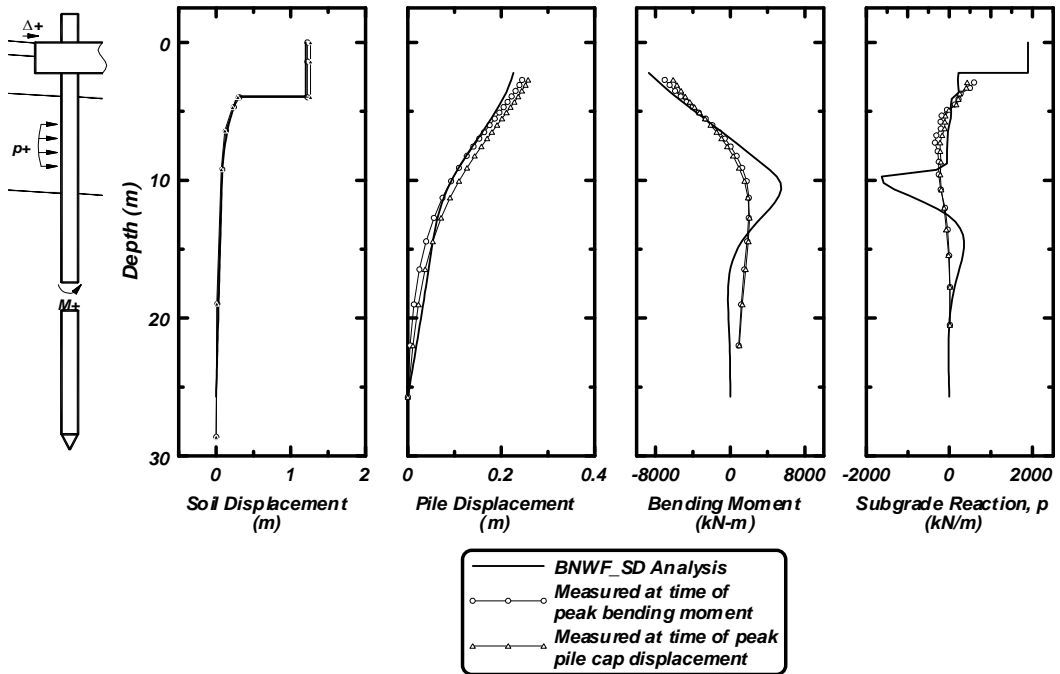
Figure 4-12: Results of BNWF_SD analysis of centrifuge test SJB03 for the large Santa Cruz motion.
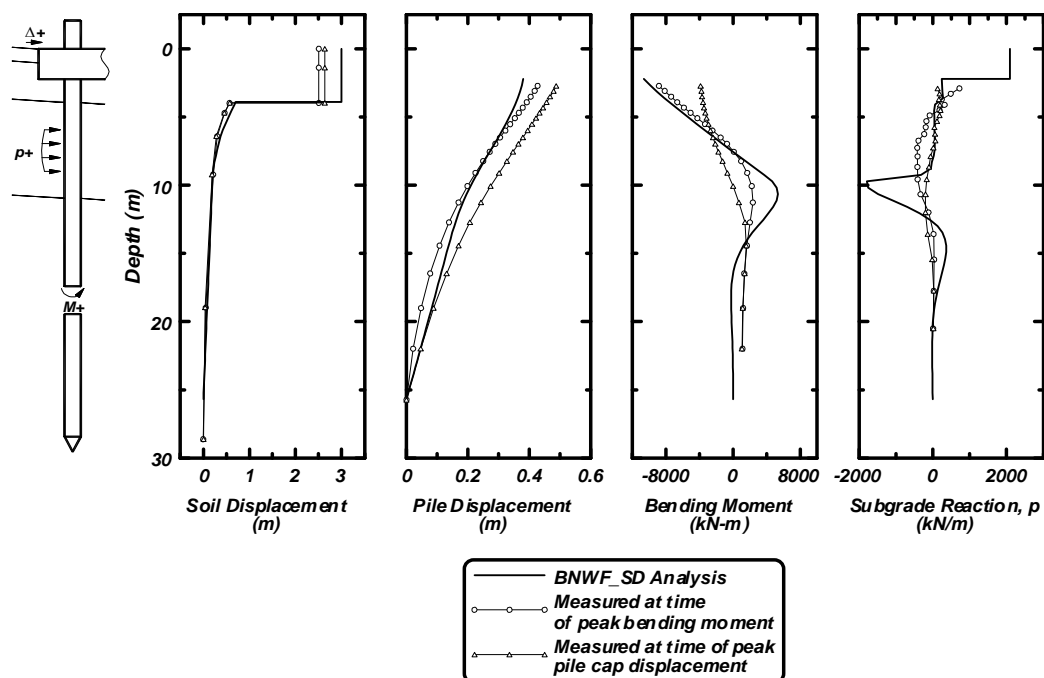
Figure 4-13: Results of BNWF_SD analysis of centrifuge test SJB03 for the large Kobe motion.
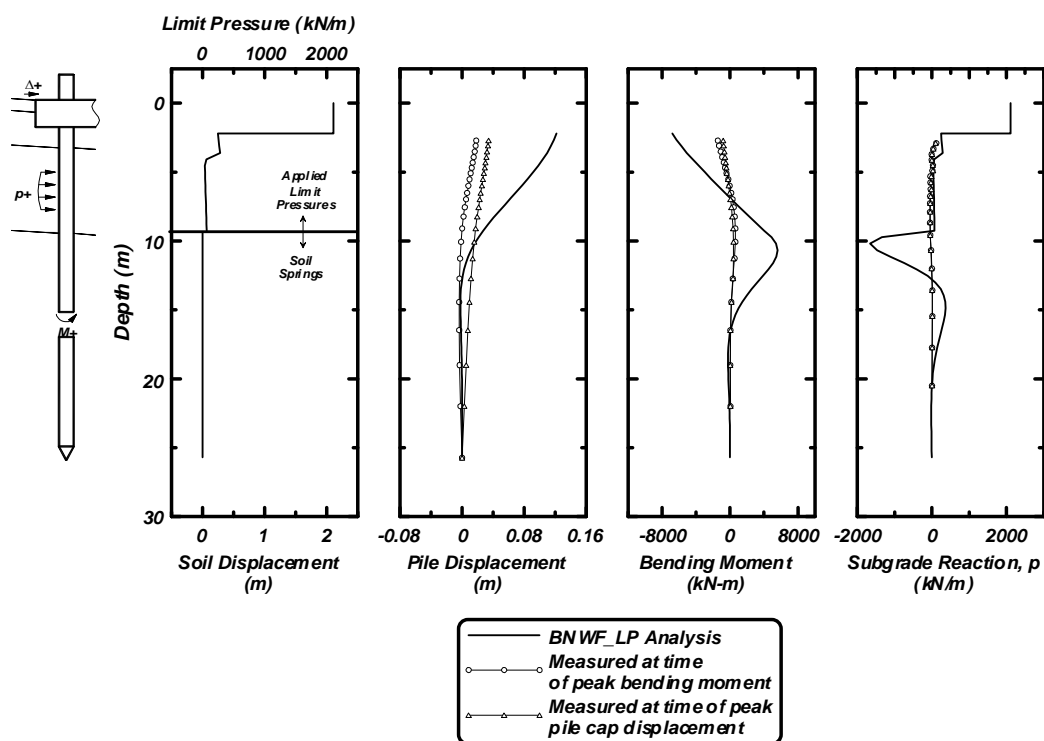
Figure 4-14: Results of BNWF_LP analysis of centrifuge test SJB03 for the small Santa Cruz motion.
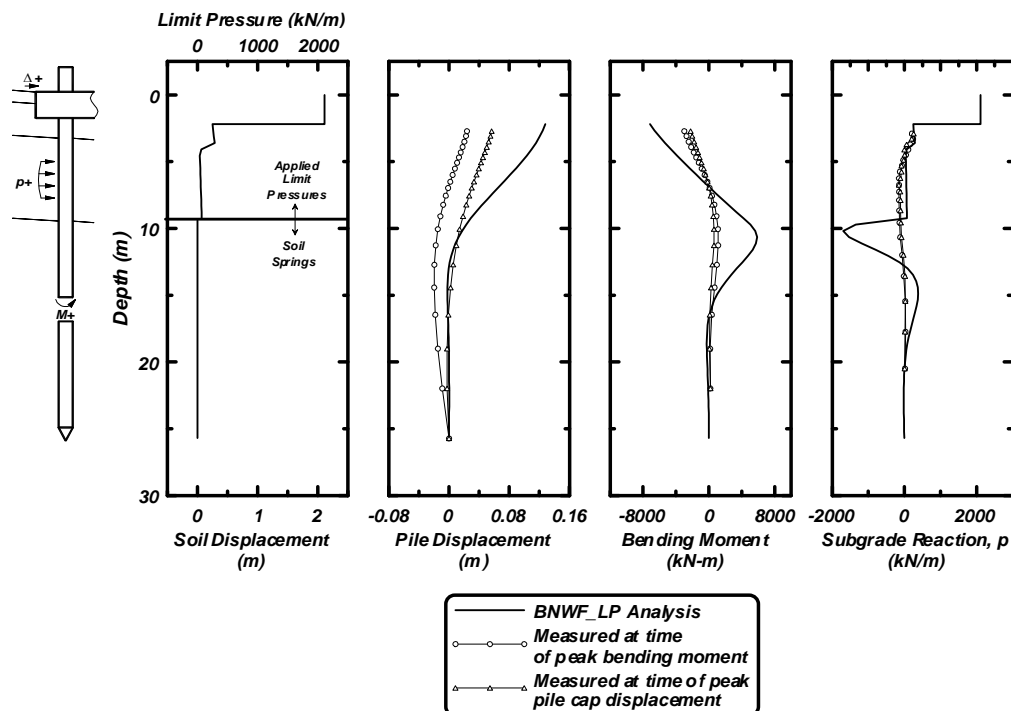
Figure 4-15: Results of BNWF_LP analysis of centrifuge test SJB03 for the medium Santa Cruz motion.
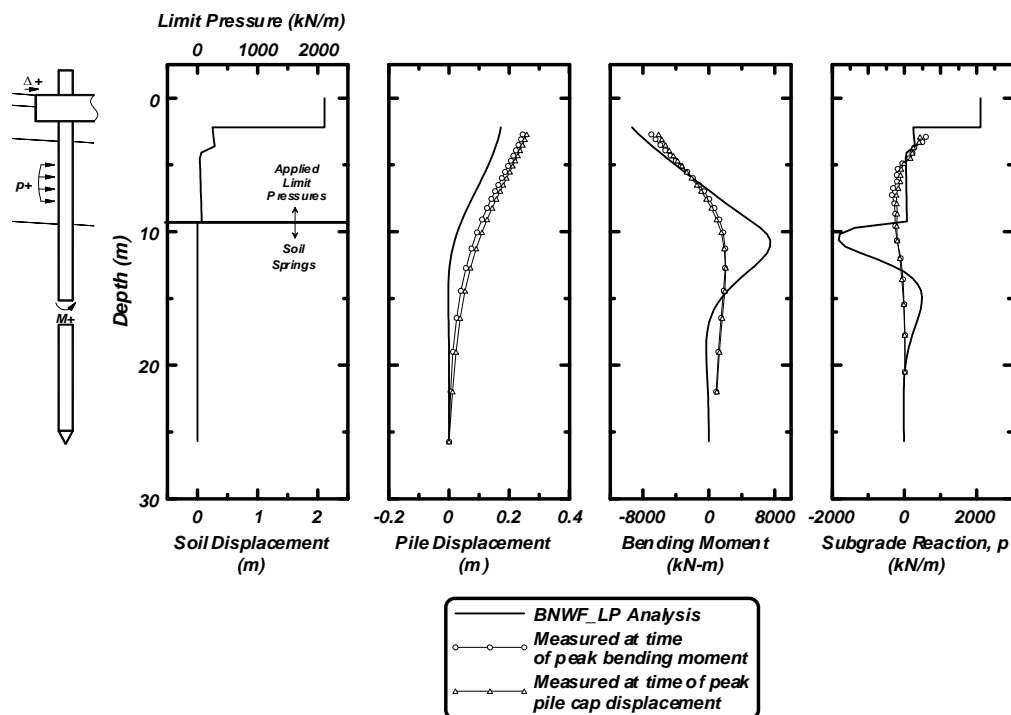
Figure 4-16: Results of BNWF_LP analysis of centrifuge test SJB03 for the large Santa Cruz motion.
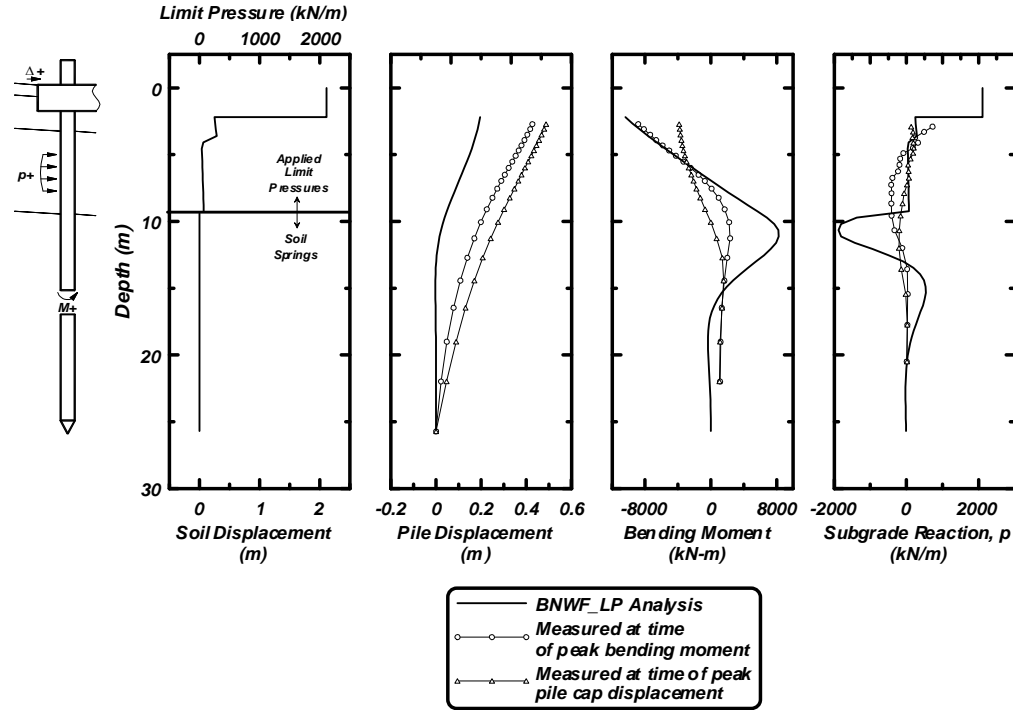
Figure 4-17: Results of BNWF_LP analysis of centrifuge test SJB03 for the large Kobe motion.
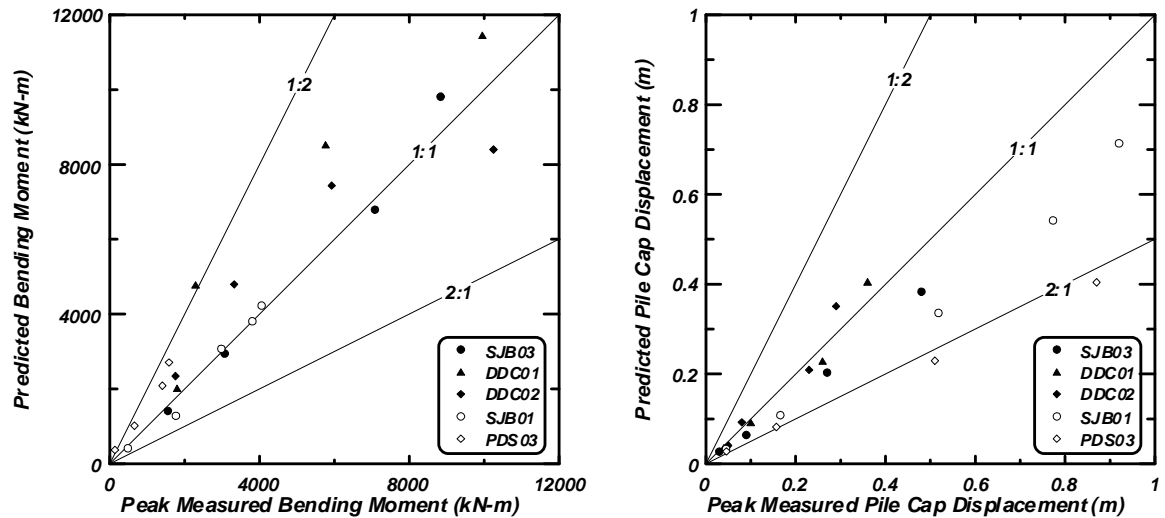
Figure 4-18: Predicted versus measured values of bending moment and pile cap displacement for BNWF_SD analyses of each shake for five centrifuge tests.
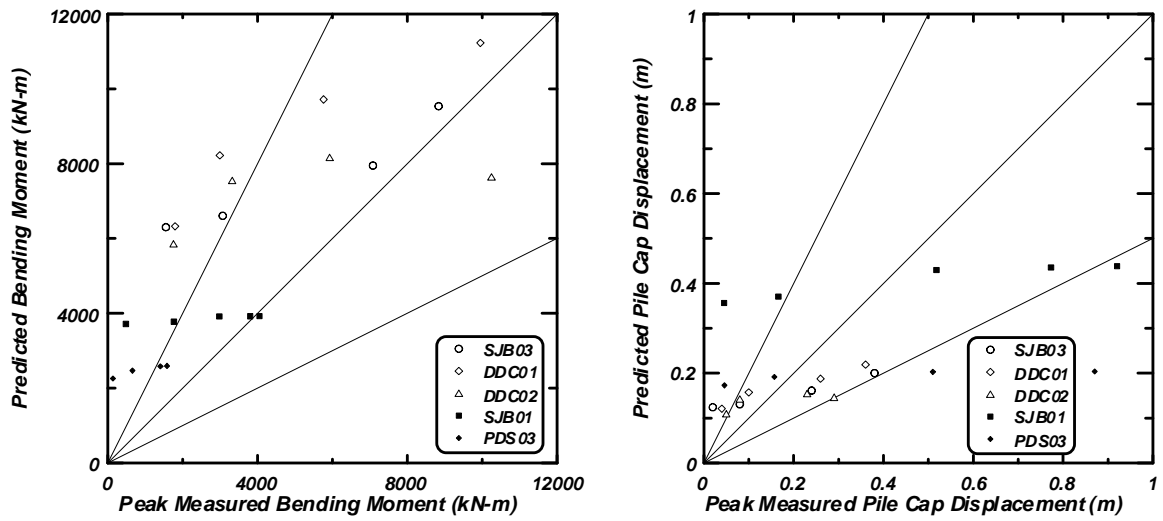
Figure 4-19: Predicted versus measured values of bending moment and pile cap displacement for BNWF_LP analyses of each shake for five centrifuge tests.

(a)   (b)
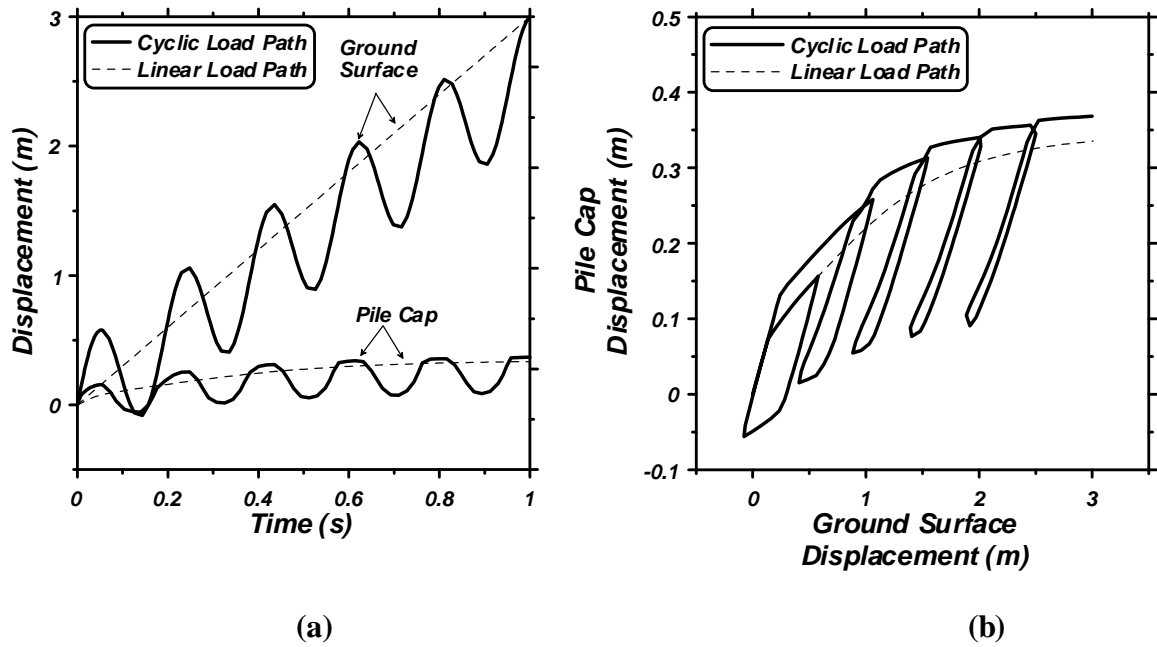
Figure 4-20: BNWF_SD analyses comparing a linear load path with a sinusoidal load path consisting of 5 ¼ cycles. The axial capacity of the piles was insufficient to prevent significant plunging and pullout of the piles.

(a)   **(b)**
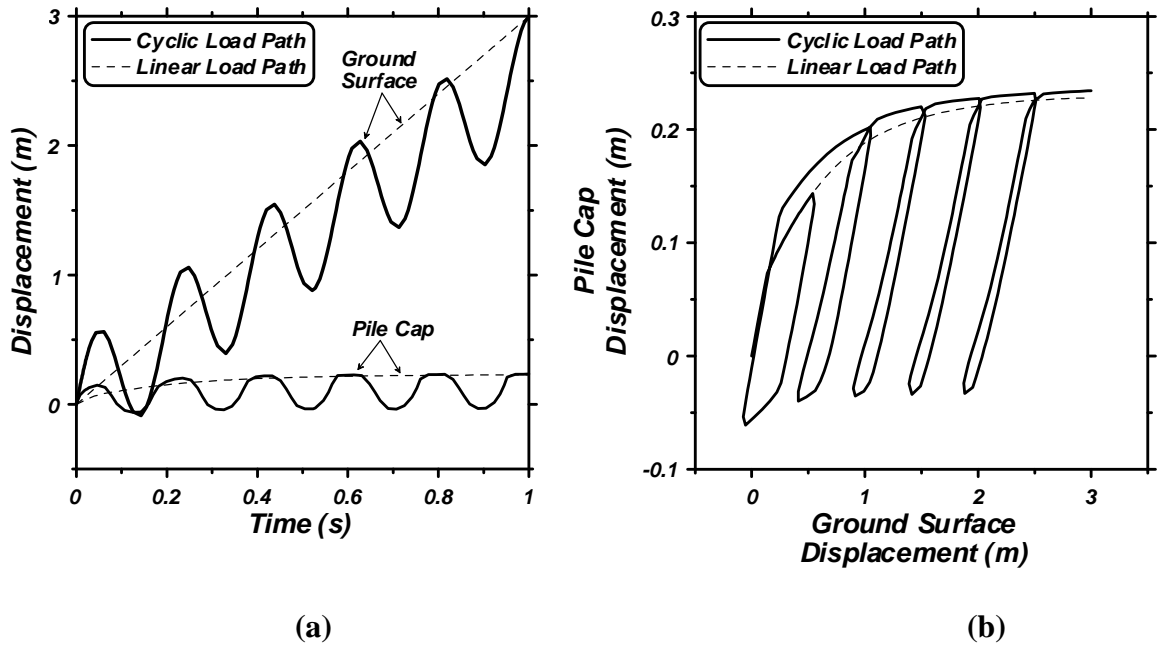
Figure 4-21: BNWF_SD analyses comparing a linear load path with a sinusoidal load path consisting of 5 ¼ cycles. The axial capacity of the piles was large enough to prevent significant plunging and pullout of the piles, thereby limiting the influence of cyclic ratcheting.
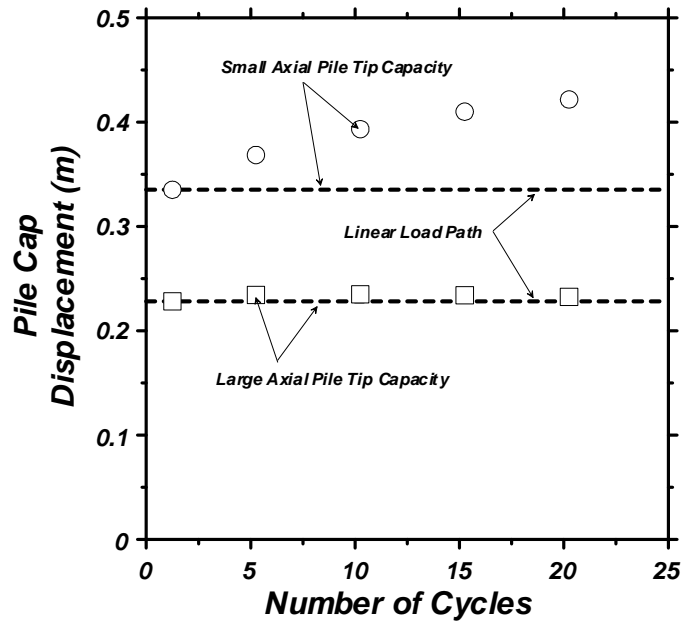
Figure 4-22: Influence of number of loading cycles on accumulation of pile cap displacements.
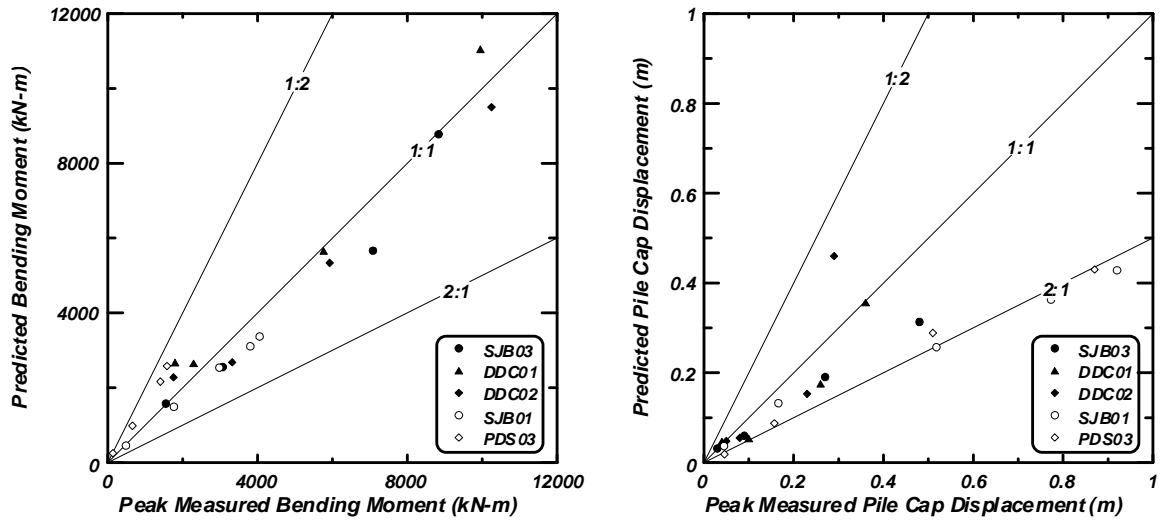
Figure 4-23: Predicted versus measured values of bending moment and pile cap displacement for BNWF_SD analyses using the measured ground surface displacement, crust load and inertia loads as input parameters.
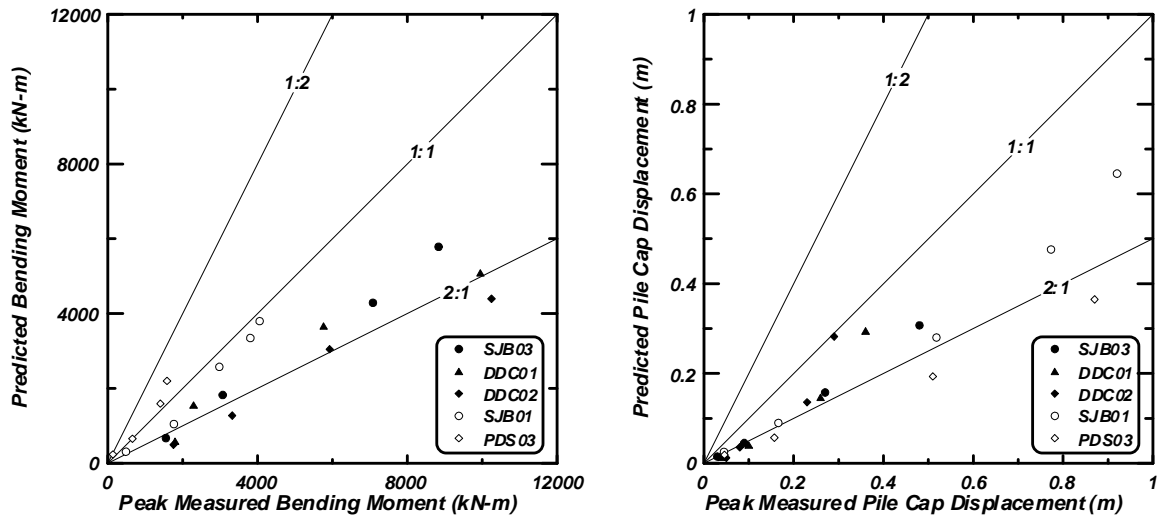
Figure 4-24: Predicted versus measured values of bending moment and pile cap displacement for BNWF_SD analyses using the baseline input parameters, but with zero pile cap and superstructure inertia loading.
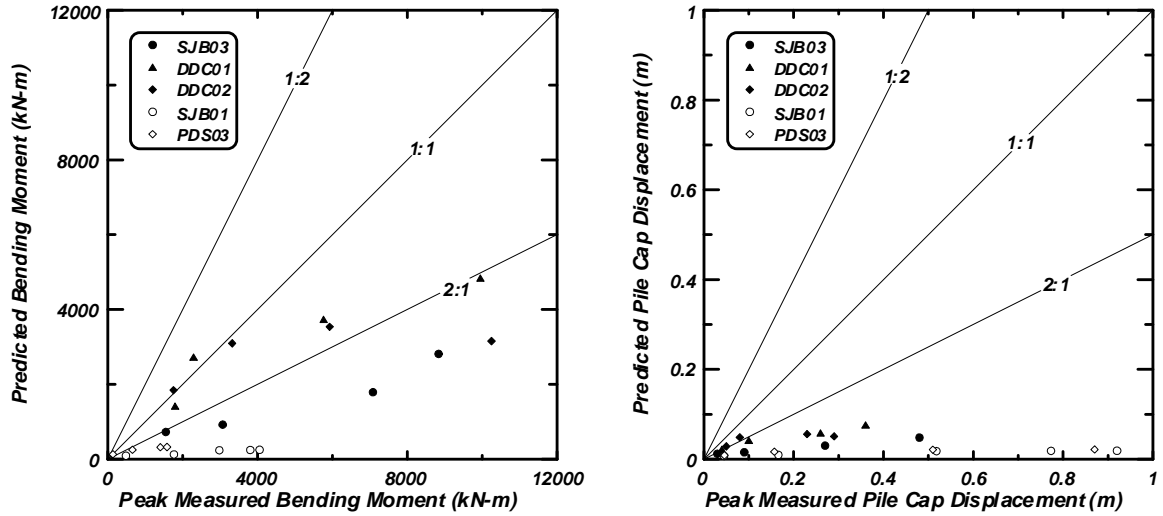
Figure 4-25: Predicted versus measured values of bending moment and pile cap displacement for BNWF_SD analyses using the baseline input parameters, but with zero free-field ground displacement.
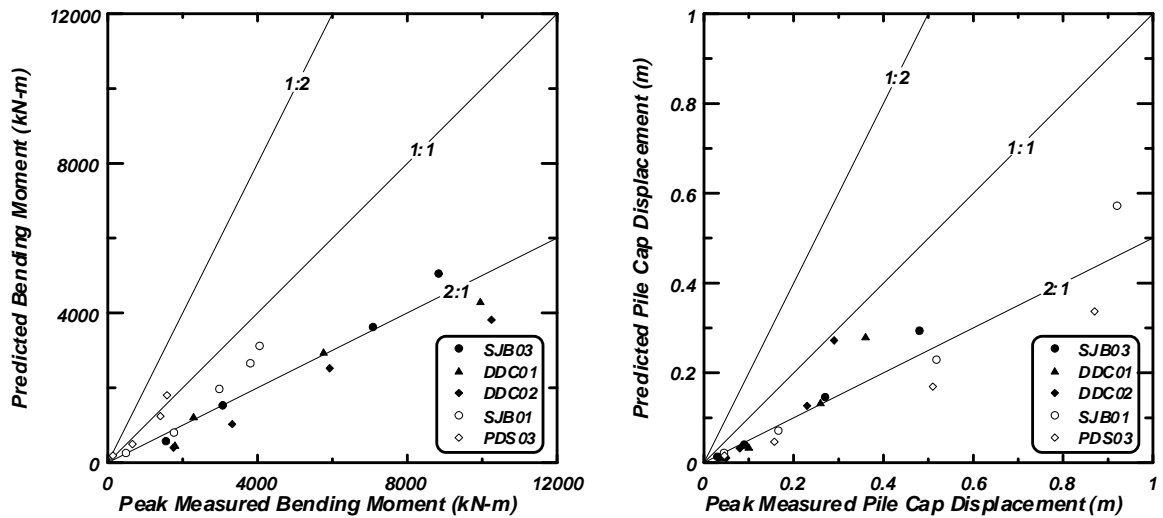
Figure 4-26: Predicted versus measured values of bending moment and pile cap displacement for BNWF_SD analyses using the baseline input parameters, but with no inertia loading and no friction loading between the pile cap and laterally spreading crust.
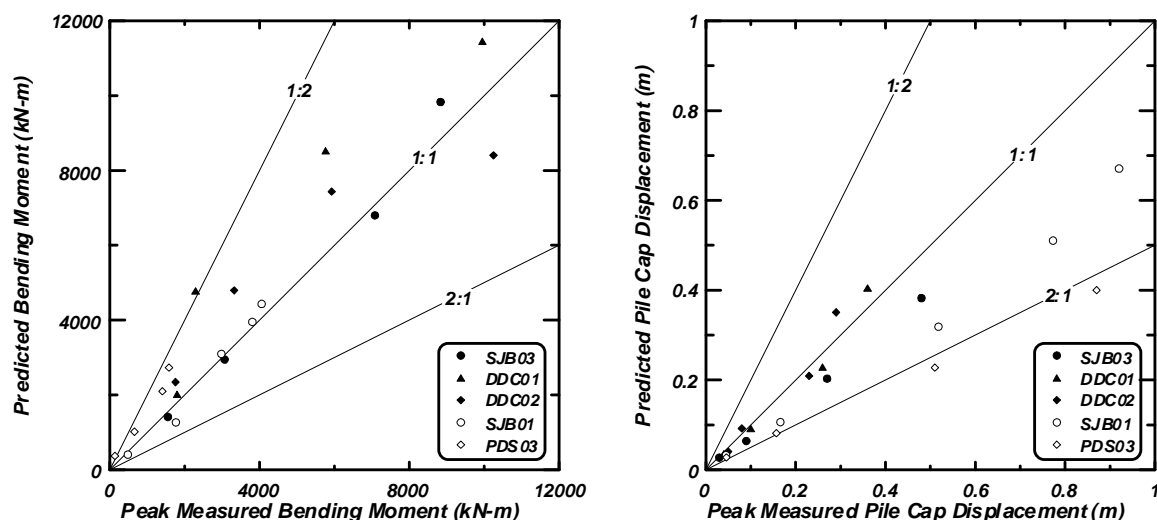
Figure 4-27: Predicted versus measured values of bending moment and pile cap displacement for BNWF_SD analyses using the baseline input parameters, but with the pile tips fixed in the vertical direction.
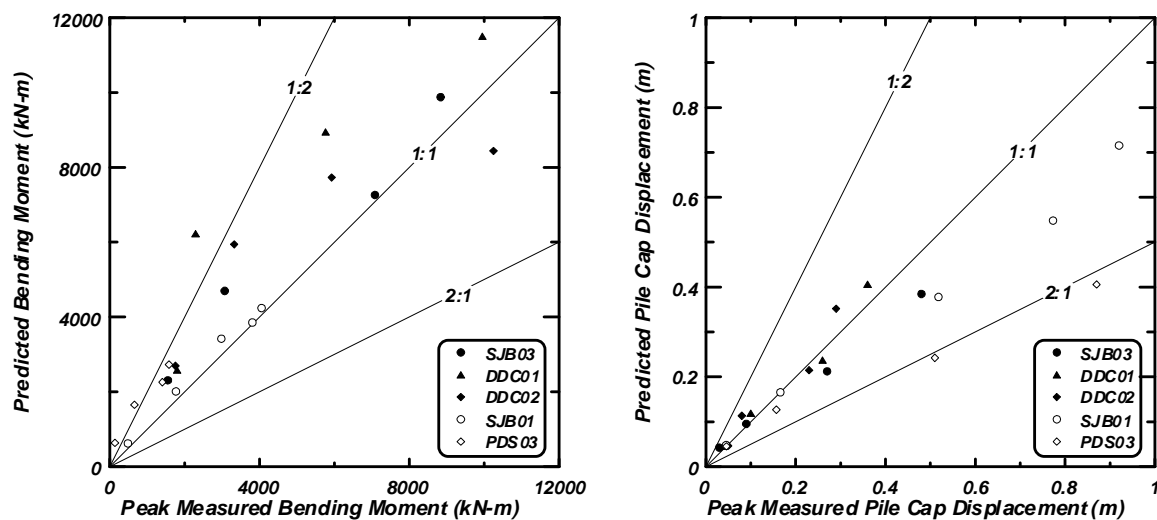
Figure 4-28: Predicted versus measured values of bending moment and pile cap displacement for BNWF_SD analyses using the baseline input parameters, but with ten times higher stiffness on p-y materials in nonliquefied crust.
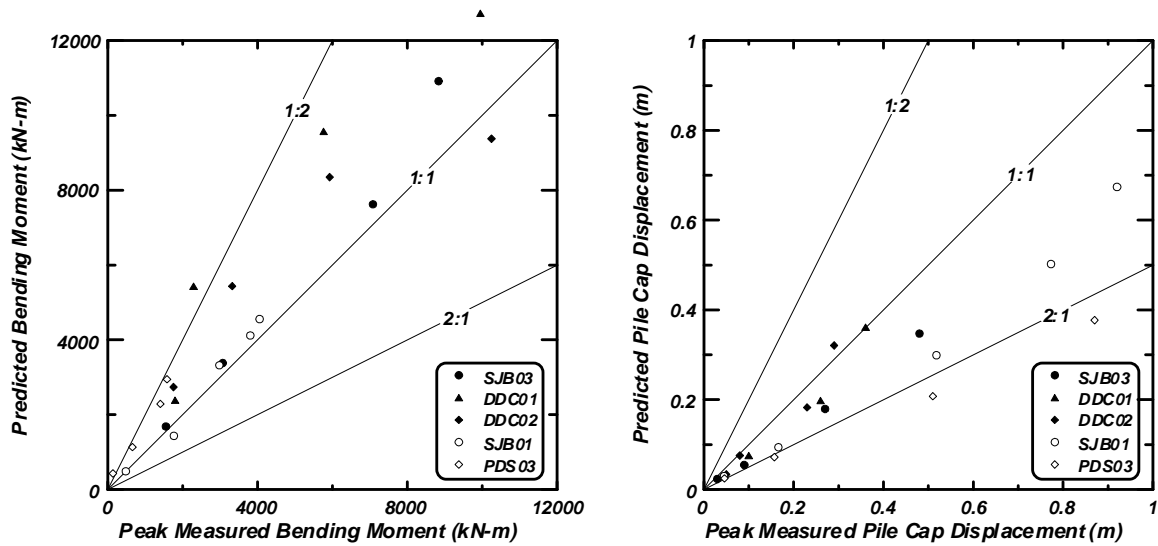
Figure 4-29: Predicted versus measured values of bending moment and pile cap displacement for BNWF_SD analyses using the baseline input parameters, but with the pile heads fixed at the connection with the pile cap.
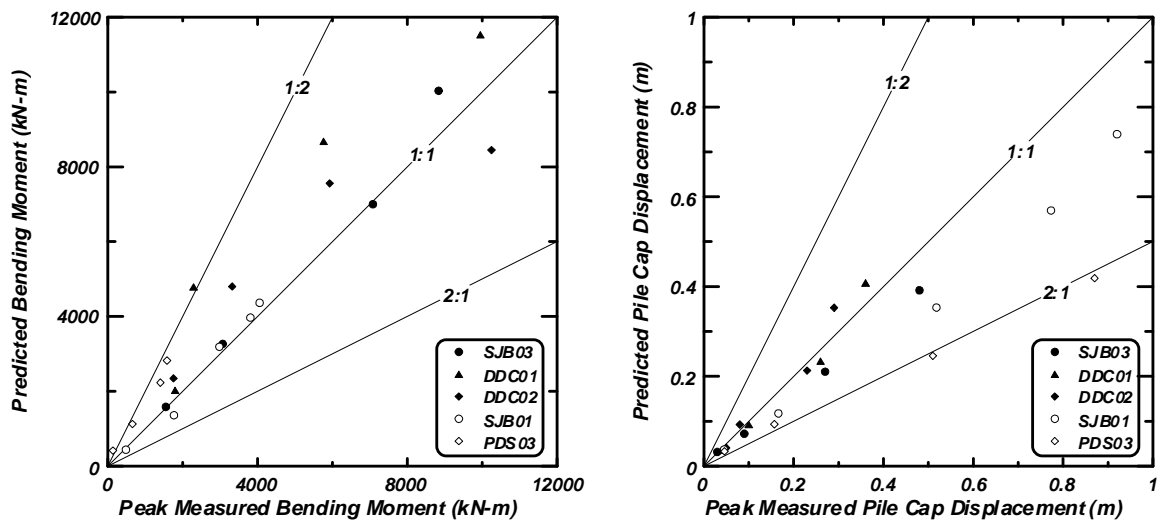
Figure 4-30: Predicted versus measured values of bending moment and pile cap displacement for BNWF_SD analyses using the baseline input parameters, but with a continuous free-field soil displacement profile.
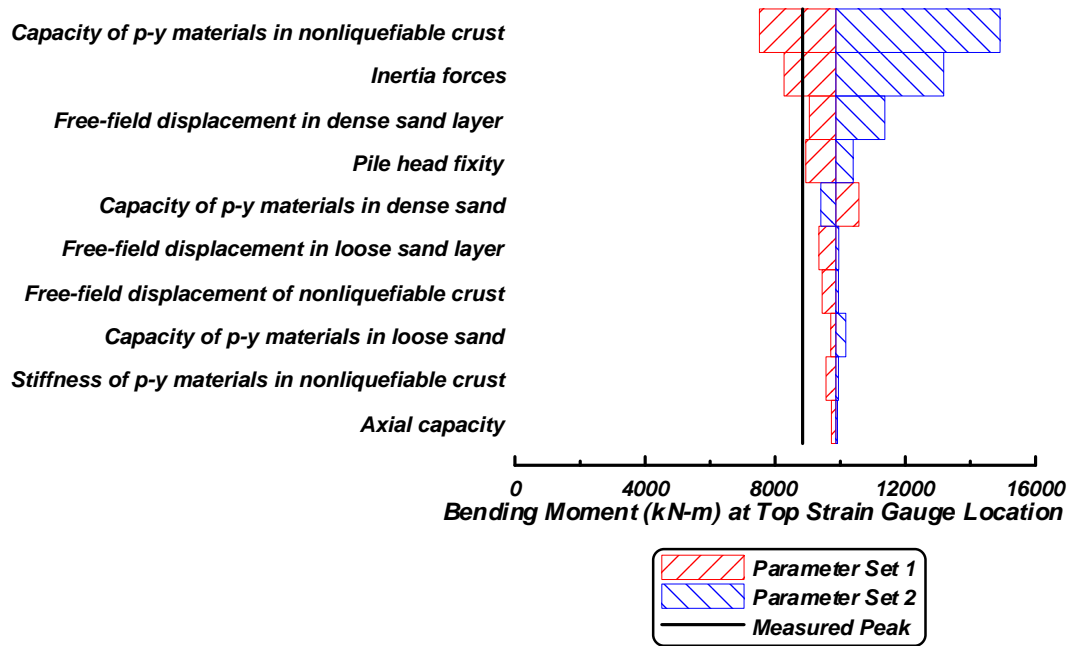
Figure 4-31: Bending moment tornado diagram for BNWF_SD analyses of the large Kobe motion for SJB03.
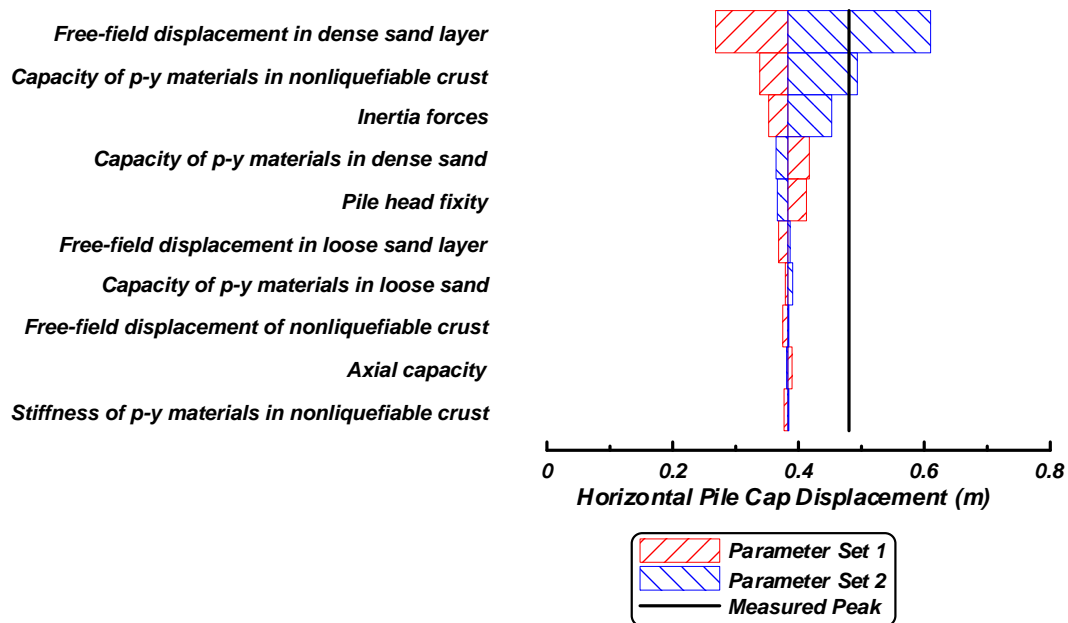
Figure 4-32: Pile cap displacement tornado diagram for BNWF_SD analyses of the large Kobe motion for SJB03.
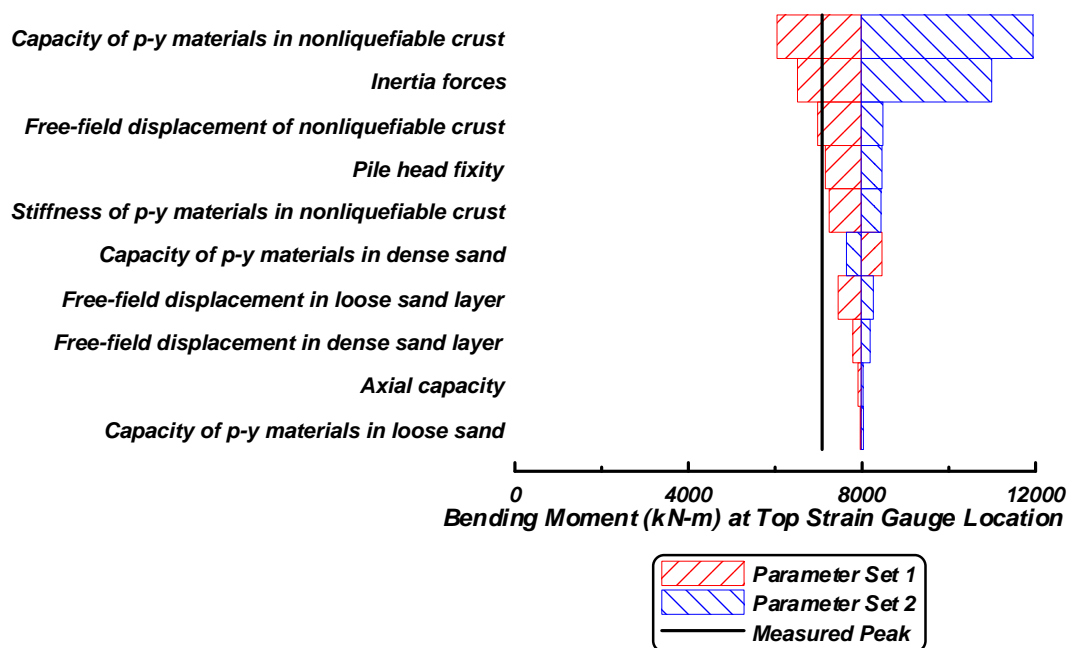
Figure 4-33: Bending moment tornado diagram for BNWF_SD analyses of the large Santa Cruz motion for SJB03.
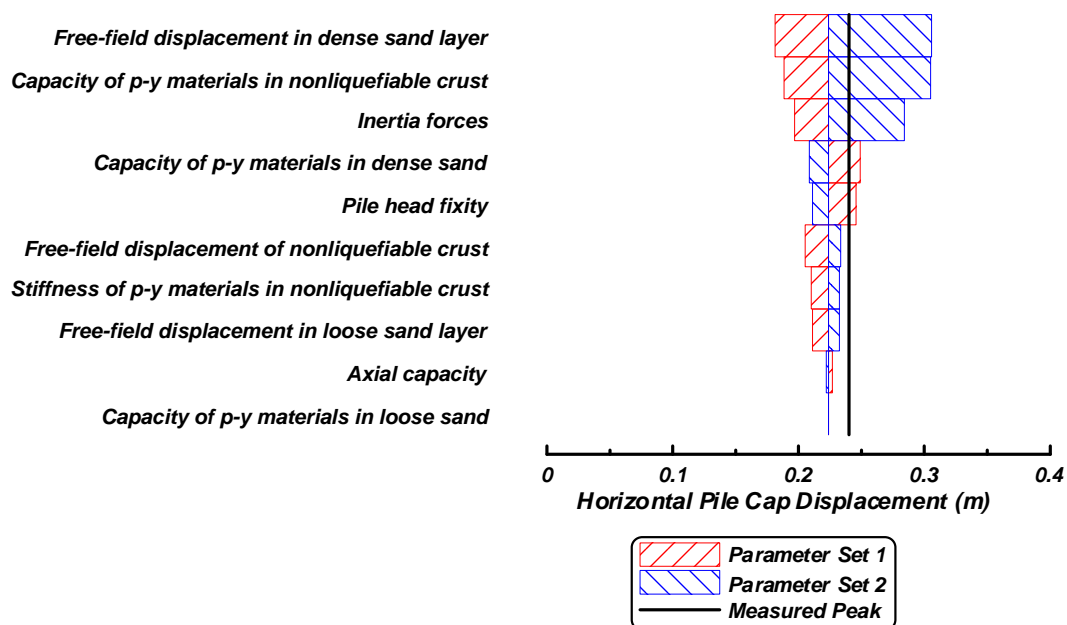
Figure 4-34: Pile cap displacement tornado diagram for BNWF_SD analyses of the large Santa Cruz motion for SJB03.
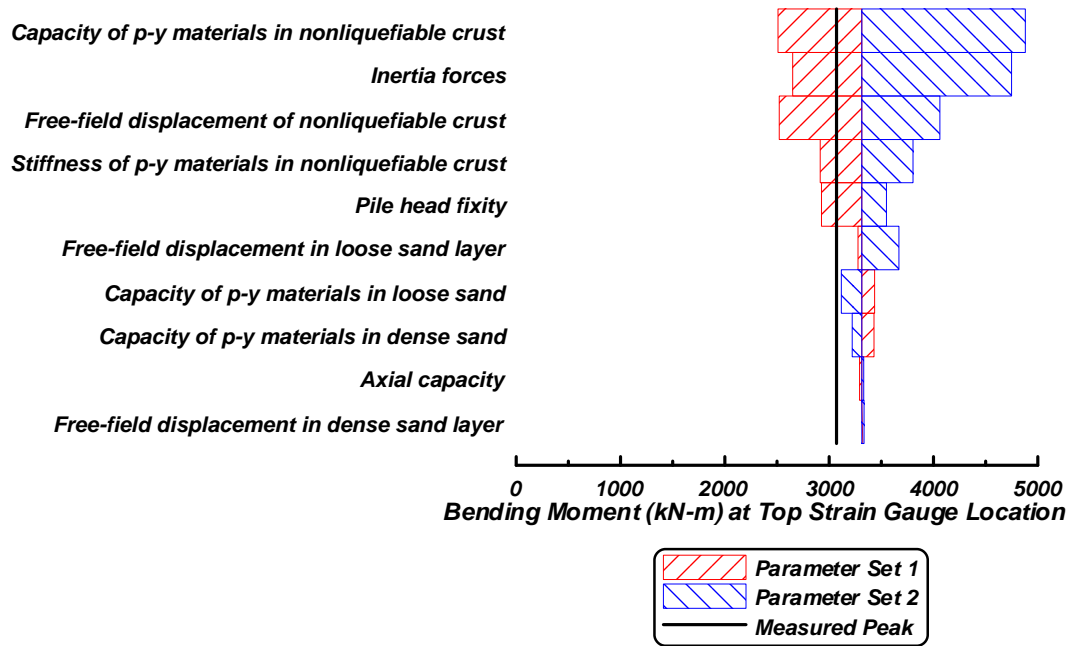
Figure 4-35: Bending moment tornado diagram for BNWF_SD analyses of the medium Santa Cruz motion for SJB03.
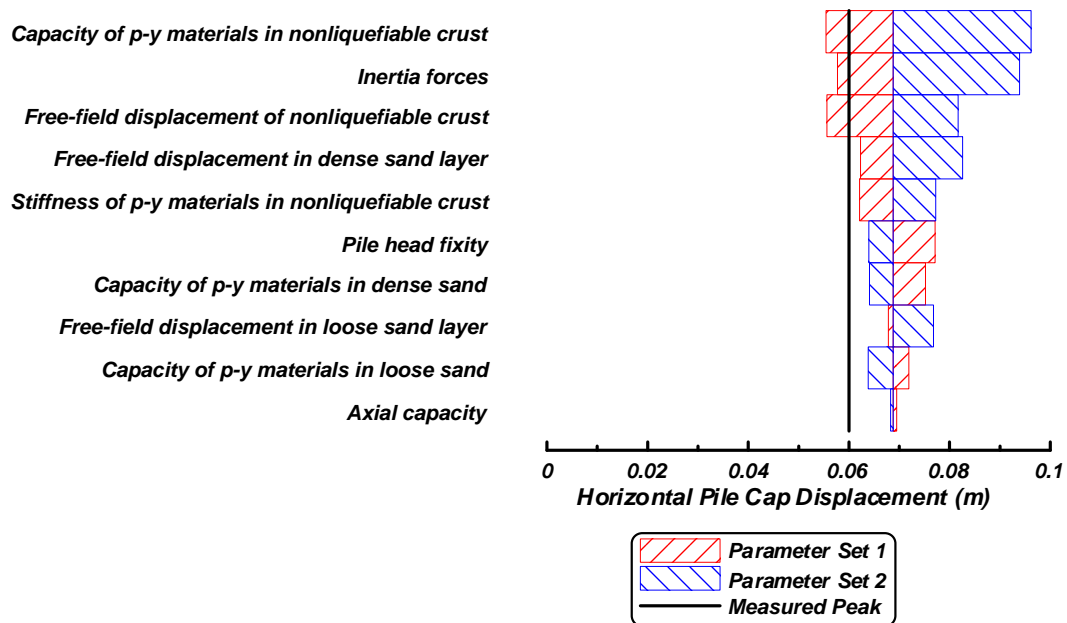
Figure 4-36: Pile cap displacement tornado diagram for BNWF_SD analyses of the medium Santa Cruz motion for SJB03.
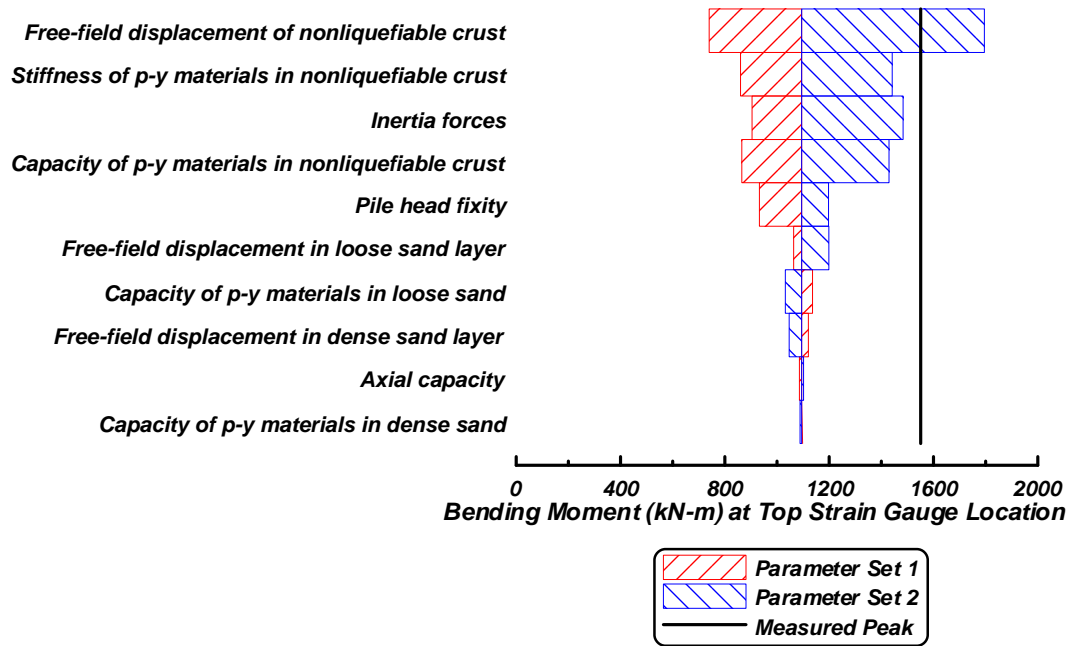
Figure 4-37: Bending moment tornado diagram for BNWF_SD analyses of the small Santa Cruz motion for SJB03.
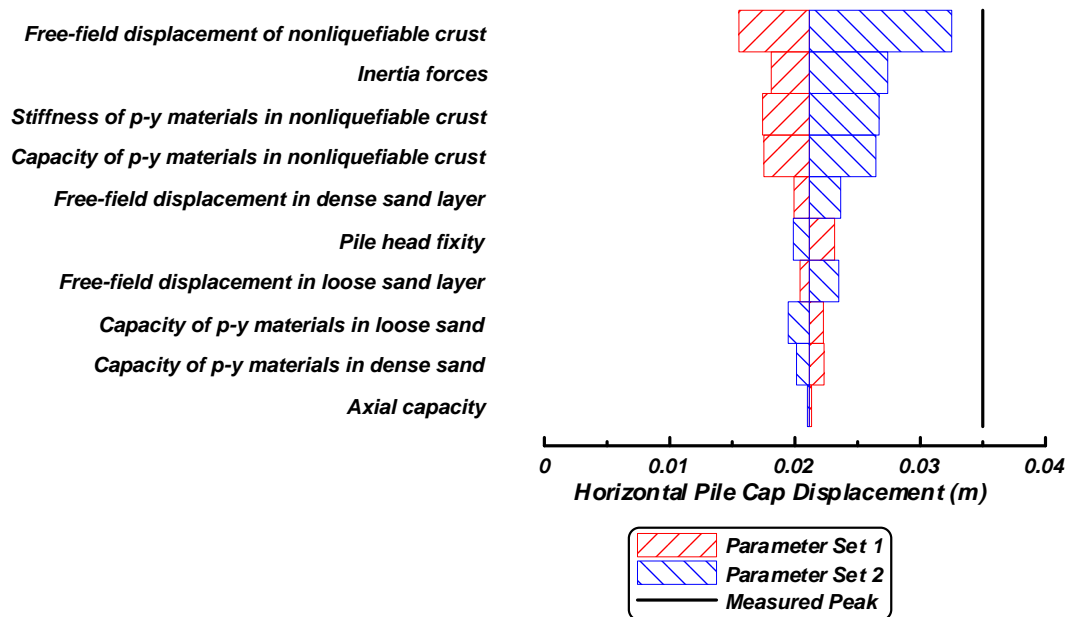
Figure 4-38: Pile cap displacement tornado diagram for BNWF_SD analyses of the small Santa Cruz motion for test SJB03.
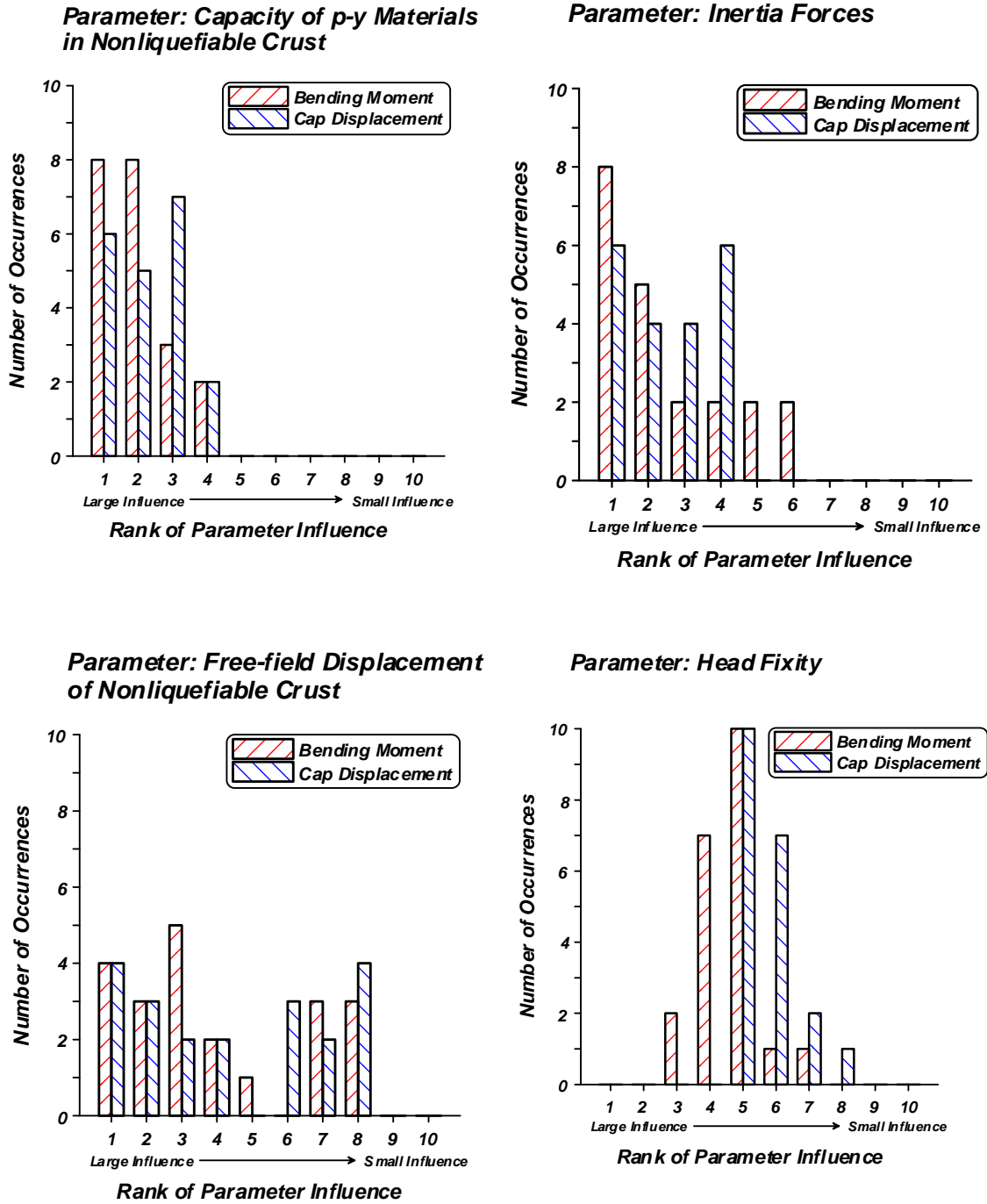
Figure 4-39: Histograms showing influence of input parameters on BNWF_SD analyses.
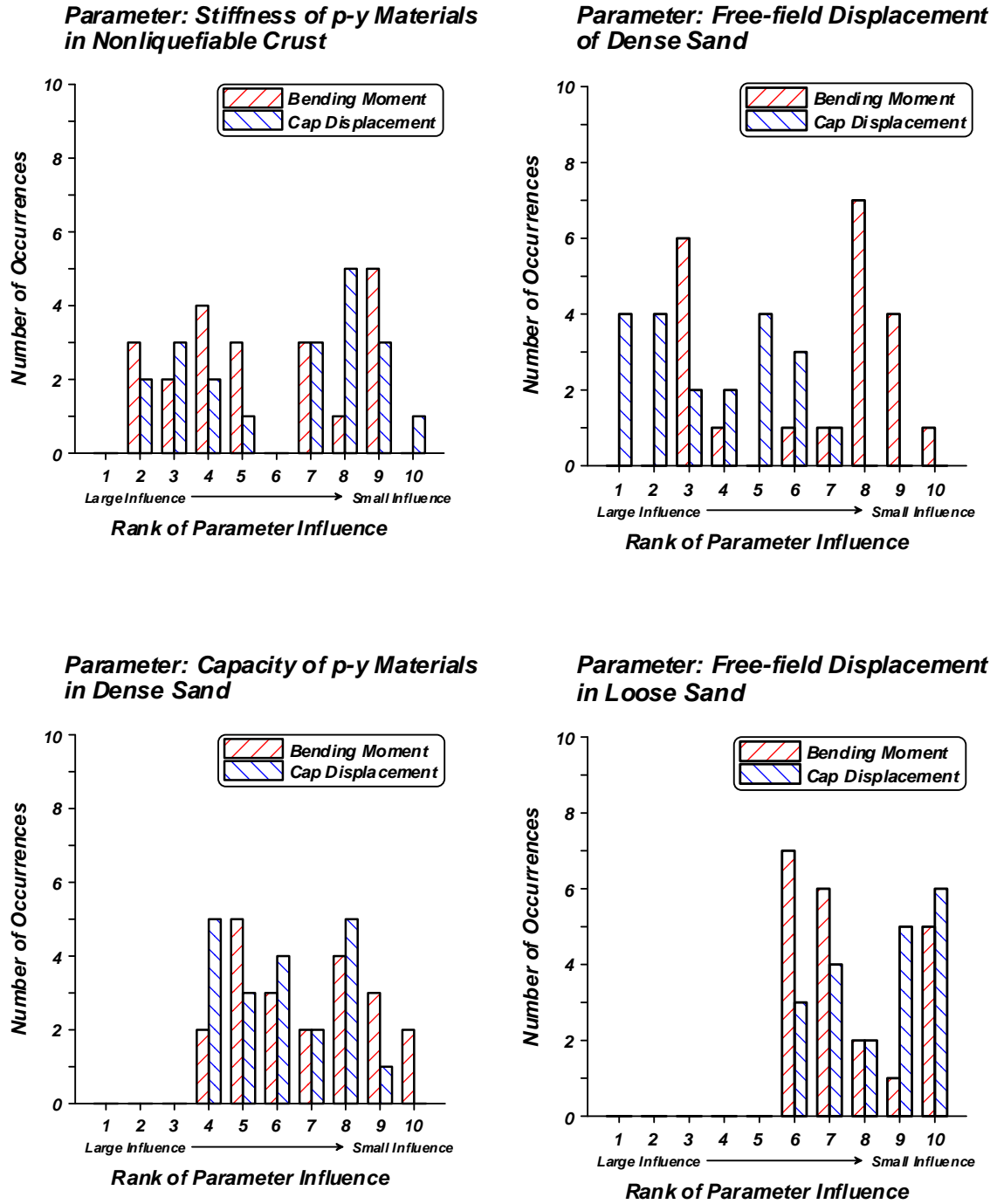
Figure 4-40: Histograms showing influence of input parameters on BNWF_SD analyses.
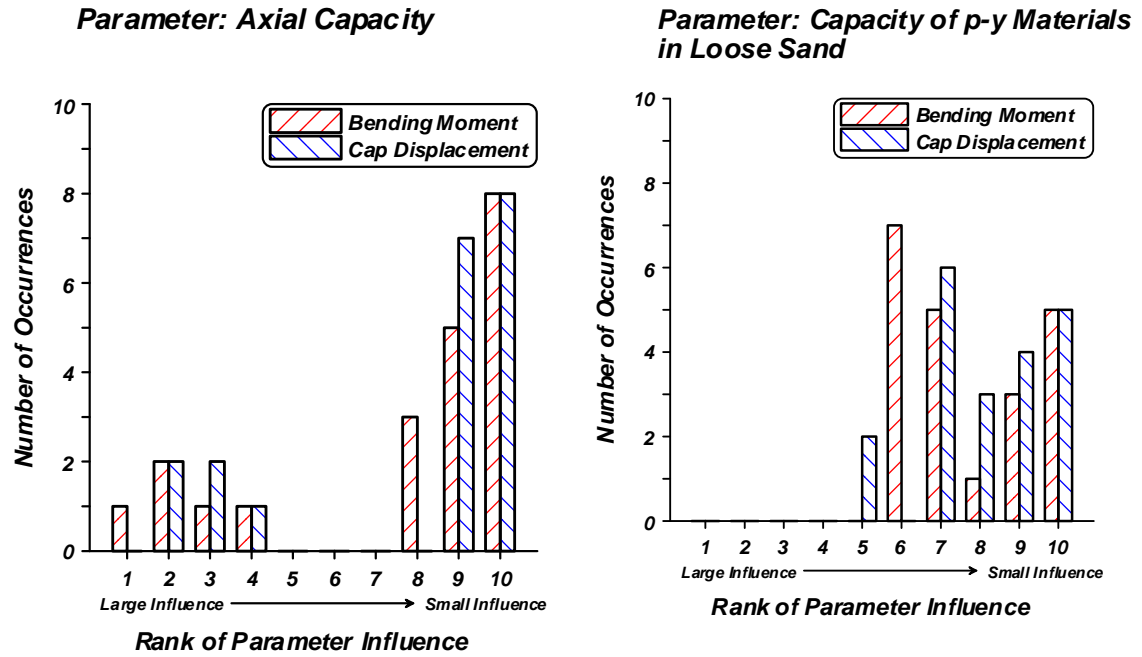
Figure 4-41: Histograms showing influence of input parameters on BNWF_SD analyses.

CHAPTER FIVE

5. SUMMARY AND CONCLUSIONS, AND FUTURE WORK

5.1 SUMMARY AND CONCLUSIONS

This dissertation consisted of the following three components: 1. A series of dynamic centrifuge tests of pile foundations in liquefied and laterally spreading ground, 2. back-calculation of fundamental engineering behaviors from the raw recorded data and subsequent observations and comparisons with theories, and 3. a suite of static-seismic analyses that a) utilized a single set of recommendations and guidelines for comparison with centrifuge test results, b) explored the influence of alternative assumptions and approximations and c) assessed the sensitivity of analysis results to variations in the input parameters.

5.1.1 Dynamic centrifuge tests

A series of eight dynamic centrifuge tests was performed at the Center for Geotechnical Modeling at UC Davis to study the behavior of pile foundations in liquefied and laterally spreading ground. The soil profiles consisted of a gently-sloping nonliquefiable predominantly clay crust over liquefiable loose sand over dense sand. Pile foundations were embedded in the soil profiles, with the pile tips penetrating deep into

the dense sand layer. Simulated earthquakes were applied to each of the models, and the large base motions caused liquefaction of the loose sand layer, and subsequent lateral spreading of the nonliquefiable crust toward an open channel carved at the downslope end of the crust layer.

Data were collected from about 100 sensors placed in each model to measure accelerations, pore pressures, displacements, bending moments, axial forces and shear forces. A portion of the data was presented in this dissertation, and full data archives are available at http://nees.ucdavis.edu. Pore pressure records showed that the loose sand layer liquefied (i.e. r_u reached 1.0) for the large earthquake motions and exhibited dilatancy behavior in which the pore pressures transiently dropped as the sand layer became temporarily stiff and strong. The dilatancy behavior is also evident in the high-frequency large acceleration spikes that occurred simultaneously with the drops in pore pressure. Peak bending moments occurred at the connection with the pile cap, and the bending moment profile exhibited the reverse curvature characteristic of deeply-embedded fixed-head piles in lateral spreads.

Measurements of the model geometries taken before and after testing identified a displacement pattern in which the clay crust slid on top of the liquefiable sand layer. This discontinuity was caused by upward-seeping pore water becoming trapped beneath the low-permeability clay crust layer, thereby causing an increase in the void ratio of the sand underlying the crust layer (e.g. Kulasingam et al. 2004). The weakened interface allowed the crust to slide downslope, creating a displacement discontinuity. In contrast, a continuous displacement profile was not seen in other centrifuge studies by Abdoun et al. (2003) in which the crust had a high permeability, which supports the hypothesis that

void redistribution occurs when a low-permeability layer impedes water flowing from higher-permeability underlying liquefied layers.

5.1.2   *Observations from raw and processed centrifuge test data*

Observations and interpretations of raw and processed data provided insights into fundamental engineering behaviors of soil-foundation interaction during liquefaction and lateral spreading. Methods used to compute subgrade reaction loads, crust loads, pile displacements and soil displacements were presented. Validation for the differentiation and data processing techniques applied to bending moment data was provided by the close agreement between shear forces measured directly using shear gauges, and shear forces obtained by single differentiation of bending moment distributions. Time series of subgrade reaction loads from double-differentiation of bending moment gauges that were densely populated along one pile, when considered along with excess pore pressures, ground deformations, and foundation stiffness, helped explain the fundamental loading mechanics of soil-pile interaction in liquefied laterally spreading ground.

Subgrade reaction loads in the liquefiable sand layer were found to act in the opposite direction as the loads from the spreading nonliquefied crust during critical loading cycles (i.e. when the peak bending moments were measured in the piles). This is contrary to the downslope loading direction commonly assumed in design, and the magnitude of the observed peak loads was an order of magnitude larger than commonly assumed in static design approaches. The fundamental mechanisms that caused this behavior were 1. the direction of pile displacement compared with free-field soil displacement, and 2. the dilatancy response of the sand layers during critical cycles. Piles that displaced

downslope through the liquefiable layer (i.e. piles that were flexible relative to the soil profile) attracted upslope restraining forces from the liquefiable layer. Liquefied sand flowed around the piles that were stiff relative to the soil profile, thereby exerting a downslope load. The liquefiable sand layer exhibited transient drops in pore pressure caused by dilatancy, and the associated increase in strength and stiffness of the liquefiable layer resulted in the potential for large-magnitude subgrade reaction loads.

Peak crust loads were observed during strong shaking rather than at the end of shaking, when ground displacements were largest. This is contrary to the typical shape assigned to p-y materials in which load increases as the total relative displacement between the pile foundation and the spreading crust increases. Incremental displacements that occurred when the crust lunged downslope during strong shaking were sufficiently large to mobilize the peak crust loads, while crust loads did not return to these large values after strong shaking when incremental displacements were smaller.

Lateral loads exerted on the single piles by the laterally spreading crust layer were reasonably predicted using Matlock's (1970) static bearing factors for piles in soft clay. His relations for cyclic loading were found to significantly under-predict the measured subgrade reaction loads, and are not appropriate to use in lateral spreading loading conditions.

The components of loading exerted on the pile groups by laterally spreading crusts were 1. passive force on the upslope face of the pile cap, 2. friction forces between the sides of the pile cap and the spreading crust, 3. friction forces between the base of the pile cap and the spreading crust, and 4. loads on the pile segments in the spreading crust beneath the pile cap. Forces along the base of the pile cap were multiplied by a base

friction reduction factor to account for loss of soil contact along the base of the cap, and interaction between friction stresses and lateral stresses on the pile segments beneath the cap. Friction along the sides and base of the pile caps were observed to contribute significantly to the lateral loading, which is contrary to the common assumption that passive force on the upslope face is the dominant component.

Ultimate lateral crust loads were mobilized at relative displacements (between the pile group and "free-field" spreading crust) that were about an order of magnitude larger than commonly observed for static loading conditions. Horizontal strains were distributed through a large zone of crust soil upslope from the pile group. Since relative displacement is the integral of horizontal strain through the zone of influence, the spreading of significant strains throughout a large zone of crust soil was associated with large relative displacements. The large zones of influence were caused by small friction stresses along the base of the crust due to liquefaction of the underlying sand layer, and cyclic degradation and gap formation of the crust material. Simple models were developed to envelope the influence of underlying liquefiable sand on load transfer behavior between pile groups and nonliquefied laterally spreading crusts, and reasonably captured the centrifuge test results.

Pile cap inertia forces were often at or near their peak downslope values at the same time that the crust load values were at or near their peak values. This is contrary to design guidelines that assume inertia forces and lateral spreading forces do not act simultaneously (e.g. TRB 2002). Pile foundation stiffness was observed to contribute to the magnitude and phasing of pile cap accelerations for the ground motions applied in the centrifuge tests. Groups of 1.17-m diameter piles exhibited cap accelerations that were

in-phase with crust loads, while more flexible 0.73-m diameter pile groups exhibited cap inertia forces that were a smaller fraction of their peak values during peak crust loads. Pile cap accelerations were reasonably estimated as being equal to the peak ground surface acceleration predicted in the absence of liquefaction from an equivalent-linear site response analysis. Superstructure accelerations were reasonably predicted as the spectral acceleration associated with the natural period of the superstructure. Uncertainty in both predictions was quantified.

5.1.3   *Static-seismic analyses*

Static-seismic analyses of pile groups in liquefied and laterally spreading ground that utilized a set of baseline guidelines and input parameters were performed using OpenSees. Pre-existing guidelines for static loading conditions were adopted for the baseline set of input parameters, and subsequently modified to account for the effects of liquefaction. Detailed results of the analyses were compared with centrifuge test data for one of the tests, and summary results of predicted peak bending moment and peak pile cap displacement were compared with five centrifuge tests. The impact of alternative sets of design guidelines, assumptions and approximations was explored by systematically changing the various input parameters and subsequently observing the influence on peak bending moments and pile cap displacements. The influence of uncertainty in ten of the input parameters was explored in a sensitivity study.

Peak bending moments for five centrifuge tests were over-predicted by an average of 14% using the baseline set of input parameters for the BNWF_SD analyses (with imposed soil displacement), and by 57% for the BNWF_LP analyses (with imposed limit

pressures). The bias in the BNWF_LP analysis results is caused by the inherent assumption that ground displacements are large enough to mobilize ultimate downslope pressures, and the assumption of zero strain in the deep nonliquefied layer. In the centrifuge tests, moderate ground displacements for the small and medium motions did not mobilize ultimate loads, and some small strains in the dense sand layer affected the pile foundation response.

Pile cap displacements for five centrifuge tests were under-predicted by an average of 37% using the baseline set of input parameters for the BNWF_SD analyses and by an average of 34% for the BNWF_LP analyses. However, the dispersion for the BNWF_LP analyses was much larger (COV_Δ of 0.77 compared with 0.36) because cap displacements were significantly over-predicted for the small and medium motions, and significantly under-predicted for the large motions due to the assumption of zero displacement in the deep nonliquefied layer. Hence, the BNWF_SD analyses provided a more reliable prediction of cap displacements.

Cyclic ratcheting of the pile foundation during repeated ground displacement cycles contributed significantly to some of the measured cap displacements, but this effect is not included in a monotonic static-seismic analyses. The influence of cyclic ratcheting was observed by imposing different cyclic ground displacement time series, all of which ended with the same ground displacement profile, on an example pile group foundation. Cyclic ratcheting was observed to significantly influence cap displacements when the axial capacity at the pile tips was too small to prevent significant axial deformations, but did not significantly influence cap displacements for pile groups with little axial pile tip displacements.

The BNWF_SD analyses were repeated with alternative assumptions and approximations that were different from the baseline set of input parameters. Many of the alternative assumptions have been recommended in various design guidelines, and others could potentially be considered as reasonable approximations. The additional analyses showed that:

- including inertia forces and lateral spreading displacements simultaneously was required to accurately predict bending moments and pile cap displacements. Many design guidelines assume that the two loads occur at different times and can therefore be treated separately (e.g. TRB 2002). However, analyses of the centrifuge tests showed that the inertia loads were critical components, and that static-seismic design codes that recommend uncoupling inertia loads from lateral spreading loads should never be used to design stiff pile groups that perform well in lateral spreads because such an approach is potentially inaccurate and unconservative. Including superstructure and pile cap inertia loads is a critical for obtaining safe and reliable bridge foundations,

- lateral loads exerted by nonliquefiable crusts include friction components that had to be included in the analyses to accurately predict peak bending moments and pile cap displacements. These friction components are not explicitly required in many design codes (e.g. JRA 2002) and could therefore easily be neglected,

- softening the p-y relations in the nonliquefiable crust layer to account for the influence of the underlying liquefied sand is important for cases where

moderate ground displacements are anticipated, or where many loading cycles can cause a softening of the response due to cyclic degradation, but becomes unimportant when large ground displacements cause mobilization of the ultimate crust load,

- including rotational flexibility at the connection between the pile and pile cap can be important if excessive displacements of the pile cap are an issue,

- using a continuous soil profile instead of imposing a displacement discontinuity only slightly changed the predicted bending moments and pile cap displacements because the only change was the direction of loading in the liquefied sand layer where the capacities of the soil springs were very small. More flexible piles that move along with the spreading ground would likely be more sensitive to the displaced shape of the free-field ground.

A suite of BNWF_SD analyses were performed to assess the sensitivity of predicted pile bending moments and pile cap displacements on uncertainty in the input parameters. The most influential parameters for this type of analysis were the capacity of the p-y materials in the nonliquefied crust layer and the inertia forces. The least influential input parameters were the capacity of the p-y materials in the liquefied sand layer and the free-field displacement of the liquefied sand. Free-field displacement of the nonliquefiable crust layer and axial capacity of the piles were important for some tests, but not for others. For example, free-field displacement of the crust was not important when the ground displacements were large enough to drive the p-y materials in the crust layer to

their ultimate capacities, but became important for smaller crust displacements where loads from the crust were defined by the intermediate range of the p-y materials.

5.2 TOPICS FOR FUTURE RESEARCH

Recent research has begun to clarify some of the fundamental aspects of lateral loading between pile groups and liquefied, laterally spreading ground, yet many important topics have been left unexplored. This section presents some ideas for future research topics.

Values of inertia loads to use in static-seismic analyses were found to be important in the sensitivity study, yet are often neglected in design. Pile foundation stiffness, crust load magnitude, pile cap mass, and superstructure properties contributed to the magnitude and phasing of the inertia loads, but the influence of these properties is not yet understood well enough to formulate reliable design guidelines. Additional model studies, both centrifuge and 1-g shake table, are required to collect sufficient data to obtain reliable design guidelines for a range of different soil properties, foundation properties and superstructure properties. Dynamic finite element studies can be calibrated to test data, and exercised to fill in gaps that are too costly to fill by performing model studies.

Static design procedures are not sensitive to many features that affect subgrade reaction behavior between piles and liquefied sand (i.e. the influence of dilatancy behavior, rate dependence, etc.) because the capacities of the soil springs are artificially set to small values. However, dilatancy behavior of the sand was shown to contribute significantly to the loading mechanisms in the centrifuge tests, with large upslope resisting loads observed during critical loading cycles. There is a mismatch between the

sensitivity of static analysis results to subgrade reaction in the liquefiable sand, and the actual influence observed in the centrifuge tests, hence there is a need to re-assess sensitivities using a more robust analysis method that can capture more of the real loading mechanisms. A sensitivity study using dynamic finite element analyses with various complexities added to the p-y behavior in the liquefied sand layer can help identify which issues most directly impact the response of the foundation and superstructure.

Evaluation of the static-seismic design recommendations against a set of case histories could verify whether the bias and dispersion quantified for the centrifuge models in this dissertation is applicable to field cases. Case histories that exhibited poor performance and good performance would be required.

Constructing the large-diameter pile foundations required to limit cap displacements to reasonable levels in lateral spreads can be costly, particularly when the nonliquefied crust layer is thick and/or strong. Ground modification will likely be used to mitigate liquefaction hazard in areas where a structural solution (i.e. large pile group) is too costly. If sands are densified to mitigate liquefaction hazard, then the behavior of piles is well understood since there are many case studies of piles in nonliquefied ground. However, other methods of ground improvement, which may be more economical than densification, have an unknown influence on pile foundation response. For example, deep soil mixed (DSM) panels can be used to contain liquefied soil, thereby limiting ground displacements, but the influence of DSM panels near pile foundations is not yet understood. Centrifuge studies of pile groups in ground improved by DSM could provide an understanding of the fundamental loading mechanisms, laboratory tests would be

required to characterize the properties of the DSM material, and subsequent three-dimensional finite element modeling could assess the performance of bridges on piles in liquefiable soil improved by deep soil mixing.

The influence of pile yielding on structural performance should be thoroughly examined, particularly since many of the observations presented in this dissertation will tend to increase design loads on pile foundations compared with existing design methods in which these loads are often currently neglected. Static-seismic analyses and dynamic finite element analyses with nonlinear pile behavior can identify the influence of ductility in the piles on the response of the system. This is important for retrofit computations since many existing pile foundations will likely yield when exposed to design ground motions because they were not designed with realistic loading conditions. It is also important for new designs, where sizing piles to remain elastic under large, rare design ground motions may be excessively conservative and costly. Designers should keep in mind the case of the Niigata Family Courthouse Building (Meyersohn et al. 1992), which suffered extensive damage to its pile foundation during the 1964 Niigata earthquake. The building remained in service during 20 years in which the damage had not yet been discovered. The building may not have needed piles in the first place since many of the piles suffered extensive failures at shallow depths, but the case history nevertheless shows that pile damage may be acceptable in certain cases.

Probabilistic studies should be performed as a follow up to the sensitivity studies performed in this dissertation. Appropriate factors of safety cannot be obtained from the sensitivity studies because a probability of failure is not quantified. Equating probability of failure with some measure of factor of safety for a range of different conditions could

provide guidance on selecting factors of safety given the importance of the structure and the desired performance. The probabilistic analyses could also provide a template and example for performing such analyses in design, and could help make the probabilistic approach to performance-based design more transparent.

Assessing the performance of an entire bridge system is ultimately the goal when performing computations for designing or retrofitting a bridge. The influence of loads and displacements transmitted from the pile foundation to the superstructure and vice-versa should be observed to obtain an understanding of how each piece influences the whole. OpenSees is an excellent tool for conducting such a study since it contains a wide range of geotechnical and structural materials. Collaborative analytical research should be conducted among geotechnical and structural engineers to obtain this holistic understanding.

APPENDIX A

A. REFERENCES

Abdoun, T., Dobry, R., O'Rourke, T. D., and Goh, S. H. (2003). ''Pile response to lateral spreads: Centrifuge modeling.'' *J. Geotech. Geoenviron. Eng., ASCE.* 129(10), 869–878.

American Petroleum Institute (API). (1993). *Recommended Practice for Planning, Design, and Constructing Fixed Offshore Platforms.* API RP 2A - WSD, 20th ed., American Petroleum Institute.

Arulnathan , R., Boulanger, R.W., Kutter, B.L. and Sluis, W.K. (2000) "New tool for shear wave velocity measurements in model tests." *Geotechnical Testing Journal*, GTJODJ, 23(4), pp. 444-453.

Ashford, S. A., and Rollins, K. M. (2002). *TILT: The Treasure Island Liquefaction Test: Final Report*, Report SSRP-2001/17, Department of Structural Engineering, University of California, San Diego.

Ashford, S.A., and Juirnarongrit, T. (2005). "Push-over analyses of piles in laterally spreading soil." Simulation and Performance of Pile Foundations in Liquefied and Laterally Spreading Ground, Geotechnical Special Publication, ASCE, in press.

Bartlett, S. F., and Youd, L. T. (1995). "Empirical prediction of liquefaction-induced lateral spread." *J. Geotech. Geoenviron. Eng., ASCE.* 121(4) pp 316-329.

Bhattacharya, S., and Bolton, M. D. (2004). "A fundamental omission in seismic pile design leading to collapse." Proc., 11th Int. Conf. Soil Dynamics Earthquake Eng., and 3rd Int. Conf. Earthquake Geotechnical Eng., University of California, Berkeley, CA, January, 2004.

Boulanger, R.W., Chang, D., Gulerce, U., Brandenberg, S.J., and Kutter, B.L. (2005). "Evaluating pile pinning effects on abutments over liquefied ground." Simulation and Performance of Pile Foundations in Liquefied and Laterally Spreading Ground, Geotechnical Special Publication, ASCE, in press.

Boulanger, R.W., and Brandenberg, S.J. (2004). "Neutral plane solution for liquefaction-induced downdrag on vertical piles." Proceedings ASCE Geo-Trans Conference, Los Angeles, CA, July 27-31, 2004.

Boulanger, R. W., Kutter, B. L., Brandenberg, S. J., Singh, P., and Chang, D. (2003). Pile foundations in liquefied and laterally spreading ground during earthquakes: Centrifuge experiments and analyses. Report UCD/CGM-03/01, Center for Geotechnical Modeling, Univ. of California, Davis, CA.

Brandenberg, S. J., Boulanger, R. W., Kutter, B. L., Wilson, D. W., and Chang, D. (2004). "Load transfer between pile groups and laterally spreading ground during earthquakes." 13th World Conference on Earthquake Engineering, Vancouver, B.C., Paper 1516.

Brandenberg, S. J., Chang, D., Boulanger, R. W., and Kutter, B. L. (2003). "Behavior of piles in laterally spreading ground during earthquakes – centrifuge data report for SJB03." UCD/CGMDR-03/03, Center for Geotechnical Modeling, Department of Civil Engineering, University of California, Davis.

Brandenberg, S. J., Singh, P., Boulanger, R. W., and Kutter, B. L. [2001 (a)]. "Behavior of piles in laterally spreading ground during earthquakes – centrifuge data report for SJB01." Report No. UCD/CGMDR-01/02, Center for Geotechnical Modeling, Department of Civil Engineering, University of California, Davis.

Brandenberg, S. J., Singh, P., Boulanger, R. W., and Kutter, B. L. [2001 (b)]. "Behavior of piles in laterally spreading ground during earthquakes – centrifuge data report for SJB02." Report No. UCD/CGMDR-01/06, Center for Geotechnical Modeling, Department of Civil Engineering, University of California, Davis.

Chang, D., Boulanger, R. W., Kutter, B. L. and Brandenberg, S. J. (2005) "Experimental observations of inertial and lateral spreading loads on pile groups during earthquakes." Submitted to *GeoFrontiers 2005, Austin Texas.* Jan. 24 – 25, 2005.

Chen, Y. R. (1995). "Behavior of Fine Sand in Triaxial, Torsional and Rotational Shear Tests," Ph.D Thesis, University of California, Davis.

Christian, J. T. (2004). "Geotechnical engineering reliability: How well do we know what we are doing?" *J. Geotech. Geoenviron. Eng., ASCE.* 130(10) pp 985-1003.

Cruz, R. D. (1995). "Rate Dependent Shear and Consolidation of Remolded San Francisco Bay Mud," Ph.D Thesis, University of California, Davis.

Curras, C. J., Hutchinson, T. C., Boulanger, R. W., Chai Y. H., and Idriss, I. M. (1999). "Lateral Loading & Seismic Response of CIDH Pile Supported Bridge Structures." Foundations and Ground Improvement. Geotechnical Special Publication No. 113, ASCE.

Dobry, R., Abdoun, T., O'Rourke, T. D., and Goh, S. H. (2003). "Single Piles in Lateral Spreads: Field Bending Moment Evaluation." *J. Geotech. Geoenviron. Eng.,* ASCE, Vol. 129(10), 879-889.

Dobry, R., Taboada, V, and Liu., L. (1995). "Centrifuge modeling of liquefaction effects during earthquakes." *Proc. 1st Intl. Conf. On Earthquake Geotechnical Engineering*, K. Ishihara, ed., Tokyo, Japan, Vol. 3, pp. 1291-1324.

Duncan, M. J., and Mokwa, R. L. (2001). "Passive earth pressures: Theories and tests." *J. of Geotechnical and Geoenviron. Eng.,* ASCE, Vol. 127(3), pp. 248-257.

Duncan, M. J. (2000). "Factors of safety and reliability in geotechnical engineering." *J. of Geotechnical and Geoenviron. Eng.,* ASCE, Vol. 126(4), pp. 307-316.

Electric Power Research Institute (EPRI). (1993), *Guidelines for Determining Design Basis Ground Motions*, Palo Alto, CA, Electric Power Research Institute, Vol. 1, EPRI TR-102293.

Elgamal, A., Yang, Z., Lai, T., Kutter, B.L., and Wilson, D.W. (2005). "Dynamic Response of Saturated Dense Sand in Laminated Centrifuge Container." *J. Geotech. Geoenviron. Eng., ASCE.* 131(5) pp 598-609.

Fellenius, B. H. (1972). "Downdrag on long piles in clay due to negative skin friction," Canadian Geotechnical Journal, 9(4), 323-337.

Gilbert, R. B., Najjar, S. S., and Choi, Y. J. (2005). "Incorporating Lower-Bound Capacities into LRFD Codes for Pile Foundations." Contemporary Issues in Foundation Engineering, Geotechnical Special Publication No. 131, ASCE.

Haigh, S. K. (2002). "Effects of earthquake-induced liquefaction on pile foundations in sloping ground." Ph.D. dissertation, Cambridge University, UK.

Iai, S. (2002). "Analysis of soil deformation around a cylindrical rigid body." Proc. U.S.-Japan Seminar on Seismic Disaster Mitigation in Urban Area by Geotechnical Engineering, I. Towhata and R. W. Boulanger, eds., Anchorage, Alaska, June.

Idriss, I. M. and Sun, J. I. (1992). "SHAKE91: a computer program for conducting equivalent linear seismic response analyses of horizontally layered soil deposits," *User's Guide,* University of California, Davis, 13pp.

Japan Road Association (JRA). (2002). *Seismic design specifications for highway bridges.* English Version, prepared by Public Works Research Institute (PWRI) and Ministry of Land, Infrastructure and Transport, Tokyo, Japan.

Kulasingam, R., Malvick, E.J., Boulanger, R.W., and Kutter, B.L. (2004). "Strength Loss and Localization at Silt Interlayers in Slopes of Liquefied Sand." *J. Geotech. Geoenviron. Eng.,* ASCE, Vol. 130(11), 1192-1202.

Kutter, B.L. and Wilson, D.W. (1999). "De-Liquefaction Shock Waves", Proc. 7th U.S.-Japan Workshop on Earthquake Resistant Design of Lifeline Facilities and Countermeasures Against Soil Liquefaction, Seattle, August, 1999, Technical Report MCEER-99-0019 (O'Rourke, Bardet, and Hamada eds.), pp. 295-310, November 1999.

Ladd, C.C., and Foott, R. (1974). "New Design Procedure for Stability of Soft Clays." *J. of Geotech. Eng. Division,* ASCE, Vol. 100(GT7), 769-786.

Lai, T., Elgamal, A., Wilson, D.W., and Kutter, B.L. (2001). "Numerical modeling for site seismic response in laminated centrifuge container." Proc. 1st Albert CAQUOT Int. Conf., Paris.

Malvick, E.J., Kutter, B.L., Boulanger, R.W., and Feigenbaum, H.P. (2004). "Post-shaking failure of sand slope in centrifuge test." Proc., 11th International Conference on Soil Dynamics and Earthquake Engineering, and 3rd International Conference on Earthquake Geotechnical Engineering, D. Doolin et al., eds., Stallion Press, Vol 2, 484-491.

Matlock, H. (1970). "Correlations of design of laterally loaded piles in soft clay." *Proc. Offshore Technology Conference*, Houston, TX, Vol 1, No.1204, pp. 577-594.

Martin, G. R., March, M. L., Anderson, D. G., Mayes, R. L, and Power, M. S. (2002). "Recommended design approach for liquefaction induced lateral spreads." Proc. 3rd National Seismic Conference and Workshop on Bridges and highways, MCEER-02-SP04, Buffalo, NY.

Meyerhof G.G. (1976). "Bearing capacity and settlement of pile foundations," *Journal of the Geotechnical Engineering Division,* ASCE. Vol. 102(GT3), pp. 197-228.

Meyersohn, W. D., O'Rourke, T. D. and Miura, F., (1992). "Lateral spread effects on reinforced concrete pile foundations." *Proc. 5th US-Japan Workshop on Earthquake Disaster Prevention for Lifeline Systems*, Tsukuba, pp. 173-196.

Mokwa, R. L., and Duncan, J. M. (2001). "Experimental evaluation of lateral-load resistance of pile caps." *J. Geotech. Geoenviron. Eng., ASCE.* 127(2) pp. 185-192.

Mokwa, R. L., and Duncan, J. M. (2000). "Investigation of the resistance of pile caps and integral abutments to lateral loading." *A report of research performed under sponsorship of the Virginia Transportation Research Council*, Virginia Tech, Blacksburg, VA

Mononobe, N. and Matsuo, H. (1929). "On the determination of earth pressures during earthquakes." *Proceedings, World Engineering Congress, 9 p.*

Mosher, R. L. (1984). "Load Transfer Criteria for Numerical Analysis of Axial Loaded Piles in Sand." US Army Engineering Waterways Experimental Station, Automatic Data Processing Center, Vicksburg, Mississippi, January.

National Research Council (NRC) (2001). "Theoretical Foundations for Decision Making in Engineering Design." Board on Manufacturing and Engineering Design, National Academies Press, 68 p.

Newmark, N. M. (1965). ''Effects of earthquakes on dams and embankments.'' *Geotechnique*, London, 15(2), 139–160.

Okabe, S. (1926). "General theory of earth pressures." *Journal of the Japan Society of Civil Engineering*, Vol. 12(1).

Ovesen, N. K. (1964). "Anchor slabs, calculation methods and model tests." *Bulletin No. 16*, The Danish Geotechnical Institute, Copenhagen.

Porter, K.A., Beck, J.L., and Shaikhutdinov, R.V. (2002). "Investigation of Sensitivity of Building Loss Estimates to Major Uncertain Variables for the Van Nuys Testbed." Report No. PEER 2002/03. Pacific Earthquake Engineering Research (PEER) Center. Berkeley, CA.

Reese, L. C. and O'Neill, M.W. (1987). "Drilled Shafts: Construction Procedures and Design Methods." Report No. FHWA-HI-88-042, U.S. Department of Transportation, Federal Highway Administration, Office of Implementation, McLean, Virginia.

Reese, L. C., Wang, S. T., Isenhower, W. M., Arrelaga, J.A., and Hendrix, J. A. (2000). *LPILE Plus Verion 4.0m,* Ensoft, Inc. Austin, TX.

Rollins, K. M., and Sparks, A. (2002). "Lateral resistance of full-scale pile cap with gravel backfill." *J. Geotech. Geoenviron. Eng., ASCE.* 128(9), 711-723.

Seed, H. B. and Idriss I. M. (1970). "Soil moduli and damping factors for dynamic response analyses," *Report EERC 70-10,* Earthquake Engineering Research Center, University of California, Berkeley.

Sheahan, T. C., Ladd, C., and Germaine, J. T. (1996). "Rate-Dependent Undrained Shear Behavior of Saturated Clay." *J. Geotech. Geoenviron. Eng.,* ASCE, Vol. 122(2), 99-108.

Singh, P. (2002). "Behavior of piles in earthquake-induced lateral spreading." MS thesis, University of California, Davis.

Singh, P., Brandenberg, S. J., Boulanger, R. W., and Kutter, B. L. (2001). "Behavior of piles in laterally spreading ground during earthquakes – centrifuge data report for PDS03." Report No. UCD/CGMDR-01/01, Center for Geotechnical Modeling, Department of Civil Engineering, University of California, Davis.

Singh, P., Subramanian, P. K., Boulanger, R. W., and Kutter, B. L. [2000 (a)] "Behavior of piles in laterally spreading ground during earthquakes – centrifuge data report for PDS01." Report No. UCD/CGMDR-00/05, Center for Geotechnical Modeling, UC Davis.

Singh, P., Boulanger, R. W., and Kutter, B. L. [2000 (b)]. "Behavior of piles in laterally spreading ground during earthquakes – centrifuge data report for PDS02." Report No. UCD/CGMDR-00/06, Center for Geotechnical Modeling, Department of Civil Engineering, University of California, Davis.

Stewart, D. P. and Randolph, M. F. (1991). "A New Site Investigation Tool for the Centrifuge," Proc., Centrifuge ′91, H.-Y. Ko and F. G. McLean, eds., Balkema, Rotterdam, 531-538.

Terzaghi, K., Peck, R.B., and Mesri, G. (1996). "Soil Mechanics in Engineering Practice, 3rd Edition." John Wiley & Sons, Inc., New York. 592 pp.

Terzaghi, K. (1936). "A fundamental fallacy in earth pressure computations." *J. of the Boston Society of Civil Engineers.* April.

Tokimatsu, K. (2003). "Behavior and design of pile foundations subjected to earthquakes." Proc., *12th Asian Regional Conference on Soil Mechanics and Geotechnical Engineering*, Singapore, August $4^{th} – 8^{th}$.

Tokimatsu, K., Suzuki, H., and Suzuki, Y. (2001). "Back-calculated p-y relation of liquefied soils from large shaking table tests." *Fourth International Conference on Recent Advances in Geotechnical Earthquake Engineering and Soil Dynamics*, S. Prakash, ed, University of Missouri – Rolla, paper 6.24.

Tokimatsu, K. and Asaka, Y. (1998). "Effects of liquefaction-induced ground displacements on pile performance in the 1995 Hyogoken-Nambu earthquake." Soils and Foundations, Special Issue, 163-177.

Tokimatsu, K., Mizuno, H., and Kakurai, M. (1996). "Building damage associated with geotechnical problems." *Special Issue of Soils and Foundations*, Japanese Geotechnical Society, 219-234.

Transportation Research Board (TRB). (2002). Comprehensive Specification for the Seismic Design of Bridges. National Cooperative Highway Research Program (NCHRP) Report 472, National Research Council, 47 pp.

Transportation Research Board (TRB). (2004). Load and Resistance Factor Design (LRFD) for Deep Foundations. National Cooperative Highway Research Program (NCHRP) Report 507, National Research Council, 76 pp.

Uchida, A., and Tokimatsu, K. (2005). "Comparison of Current Japanese Design Specifications for Pile Foundations in Liquefiable and Laterally Spreading Ground." Simulation and Performance of Pile Foundations in Liquefied and Laterally Spreading Ground, Geotechnical Special Publication, ASCE, in press.

Uzuoka, R., Sento, N., and Kazama, M. (2005). "Numerical Analysis of Rate-Dependent Reaction of Pile in Saturated or Liquefied Soil." Simulation and Performance of Pile Foundations in Liquefied and Laterally Spreading Ground, Geotechnical Special Publication, ASCE, in press.

Vijayvergiya, V. N. (1977). "Load-Movement Characteristics of Piles." Proceedings, Ports 77 Conference, American Society of Civil Engineers, Long Beach, California, March.

Vucetic, M. and Dobry, R. (1991). "Effect of Soil Plasticity on Cyclic Response," Journal of Geotechnical Engineering, ASCE. 117(1) pp. 89-107.

Wilson, D. W., Boulanger, R. W., and Kutter, B. L. (2000). "Seismic lateral resistance of liquefying sand." *J. of Geotechnical & Geoenvironmental Engrg.,* ASCE, Vol. 126, No.10, pp. 898-906.

Wilson, D. W., Boulanger, R. W., and Kutter, B. L. (1998). "Signal processing for and analyses of dynamic soil-pile-interaction experiments." Proceedings, Centrifuge 98, Kimura, Kusakabe and Takemura, eds., Balkema, Rotterdam, 1: 135-140.

Wilson, D. W. (1998). "Soil-Pile-Superstructure interaction in liquefying sand and soft clay." Ph.D. dissertation, University of California, Davis.

Yasuda, S., and Berril, J. B. (2000). "Observations of the earthquake response of foundations in soil profiles containing saturated sands." *Proc. GeoEng 2000 Conf.*, Melbourne, Australia, CD Rom

APPENDIX B

B. TIME SERIES OF REPRESENTATIVE DATA FROM FIVE TESTS

This appendix contains time series of raw and processed data from tests SJB03, SJB01, PDS03, DDC01 and DDC02. The information supplements many of the conclusions made in the body of the dissertation, particularly in Chapter 3, but it was not critical for arriving at those conclusions so it has been placed in this appendix. Data processing for tests DDC01 and DDC02 was performed by Dongdong Chang, and the figures in this appendix are used with her permission.
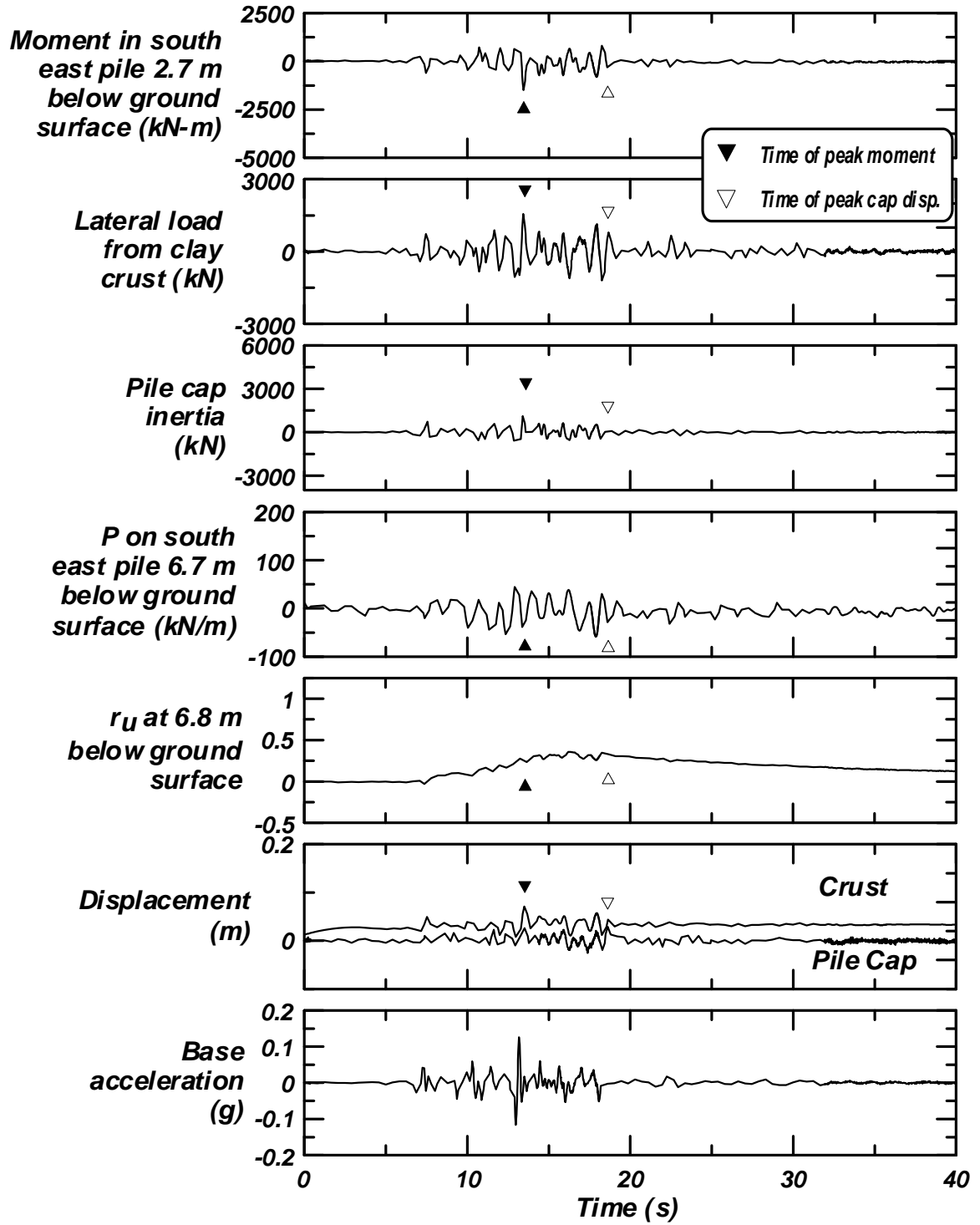
Figure B-1: Time series from test SJB03 for the small Santa Cruz motion.
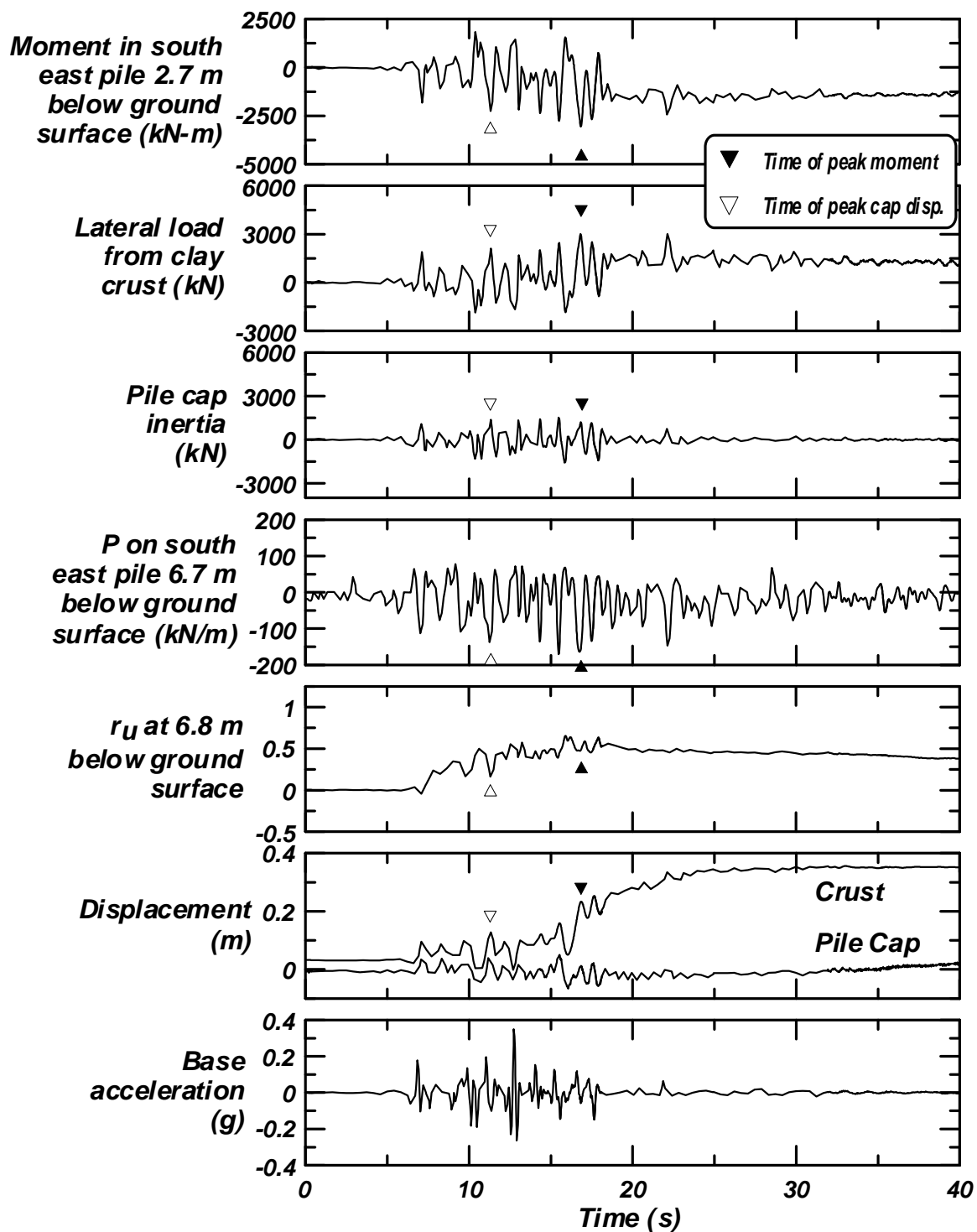
Figure B-2: Time series from test SJB03 for the medium Santa Cruz motion.
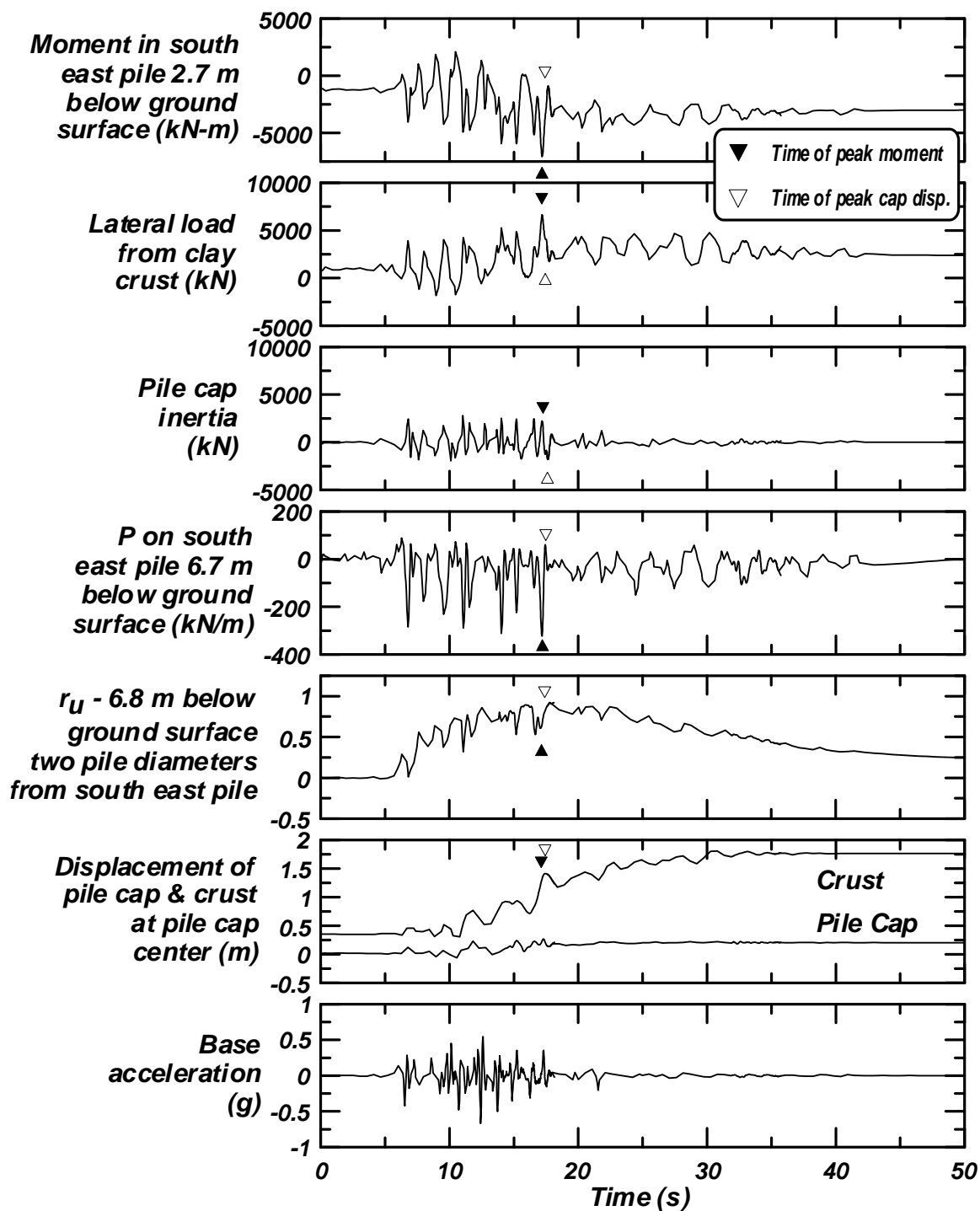
Figure B-3: Time series from test SJB03 for the large Santa Cruz motion.
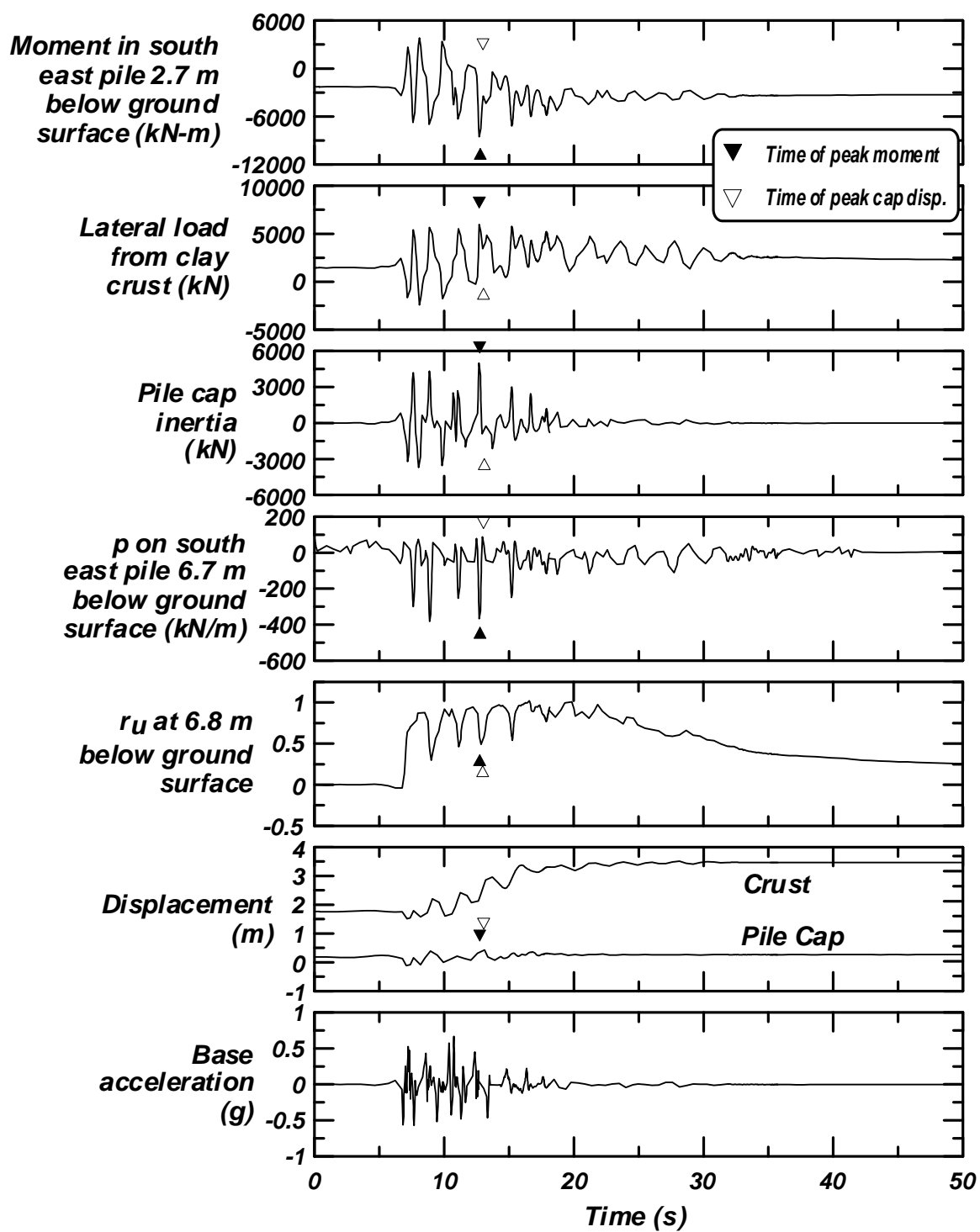
Figure B-4: Time series from test SJB03 for the large Kobe motion.
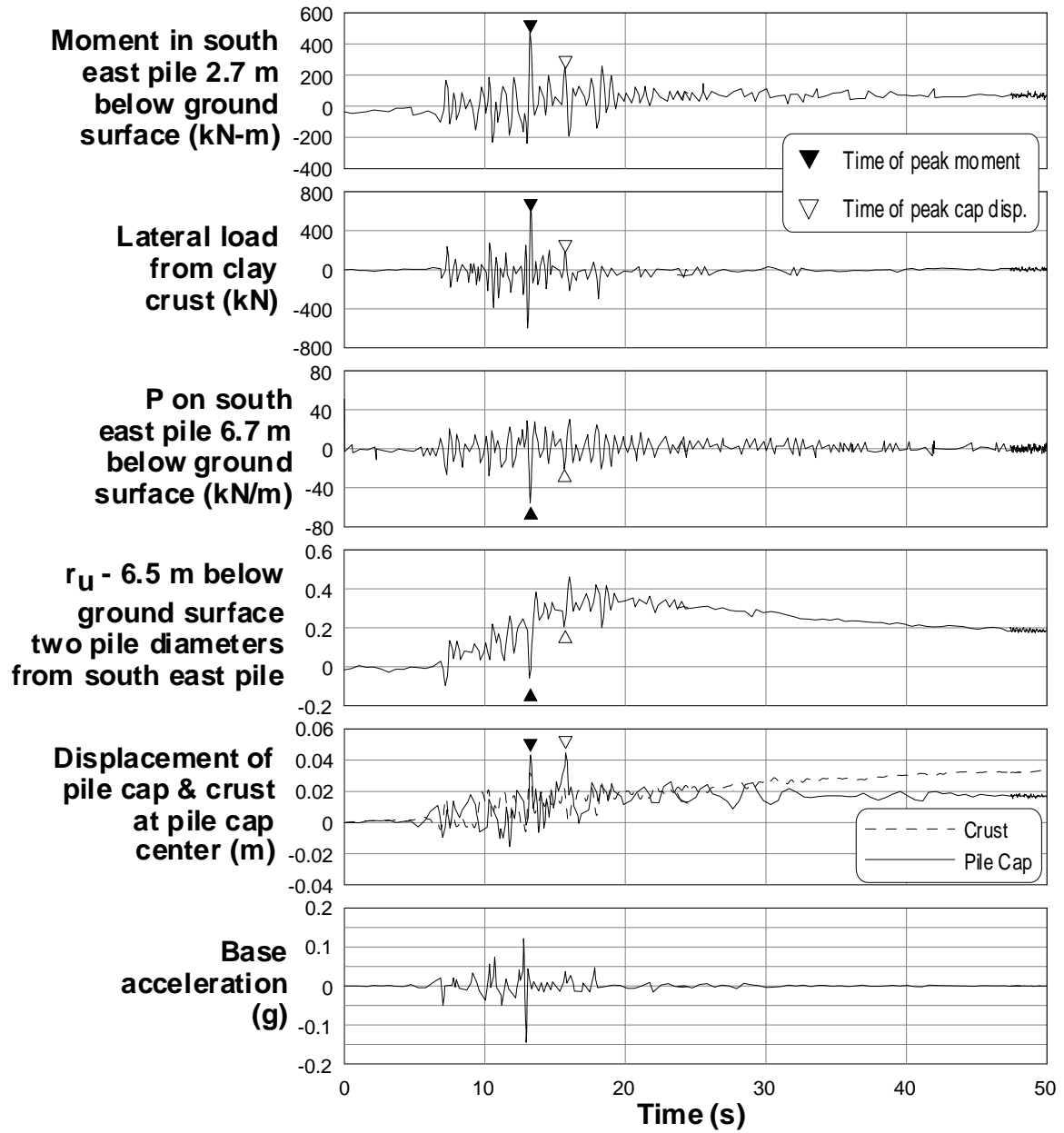
Figure B-5: Time series from test SJB01 for the small Santa Cruz motion.
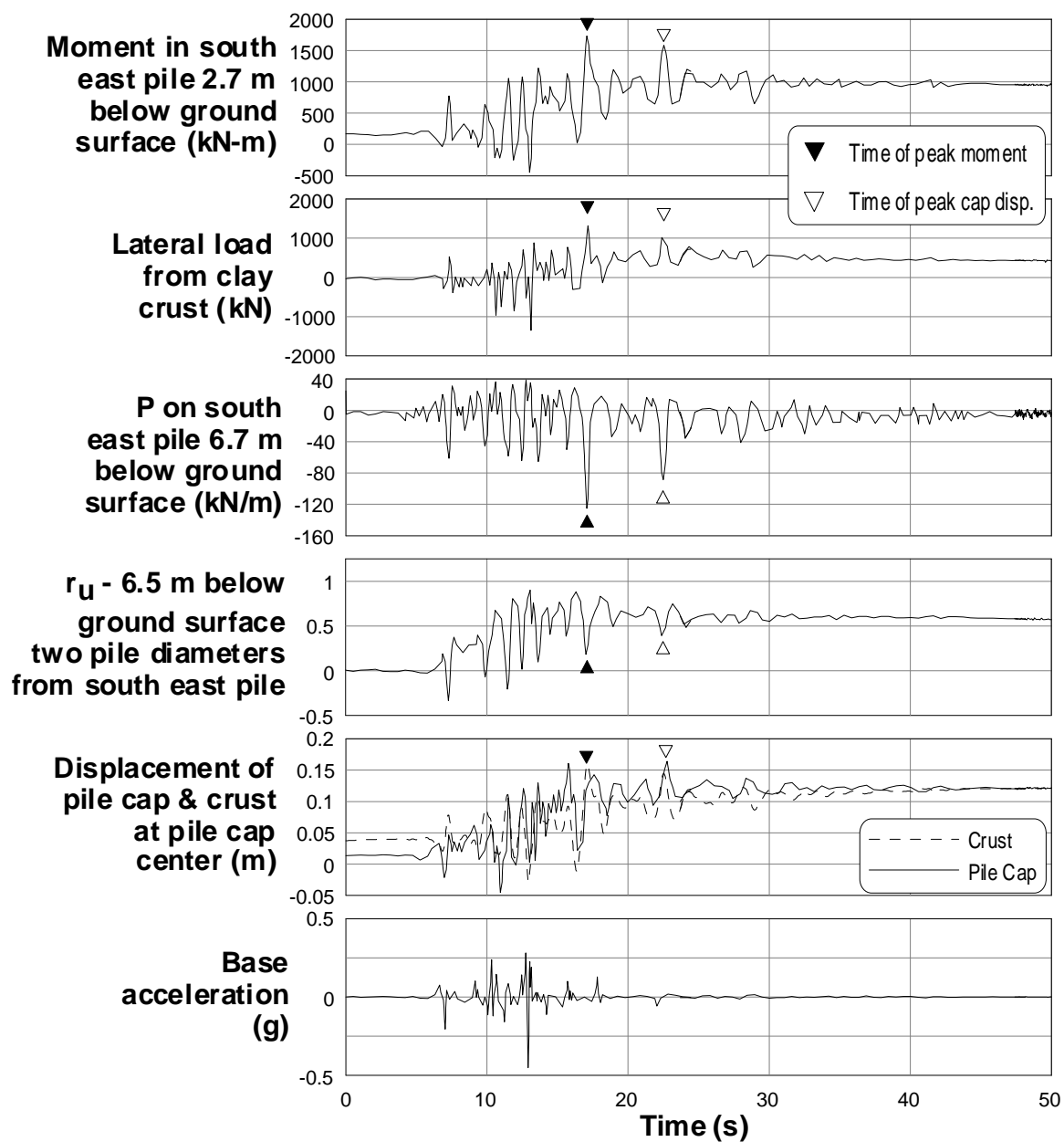
Figure B-6: Time series from test SJB01 for the medium Santa Cruz motion.
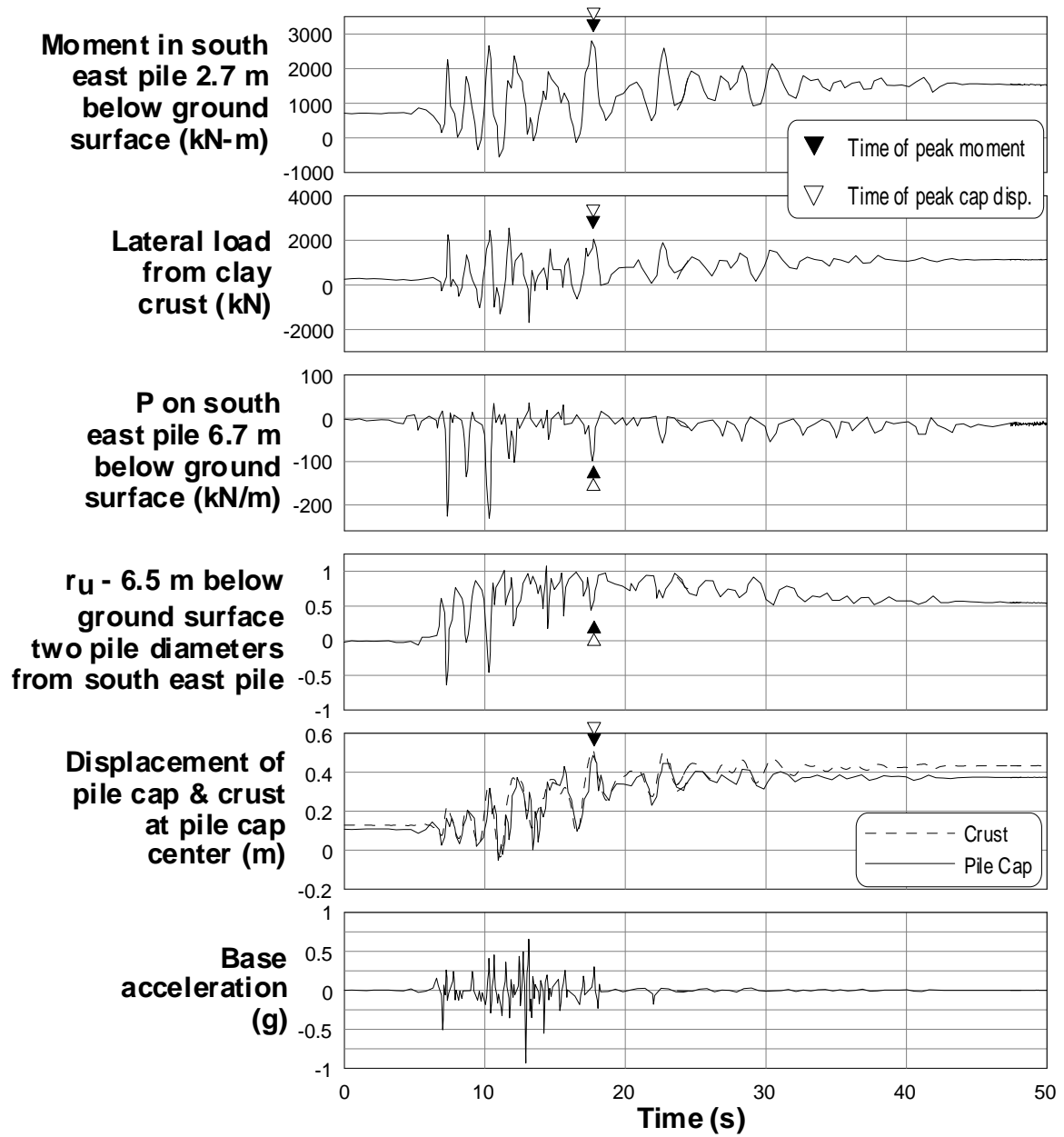
Figure B-7: Time series from test SJB01 for the large Santa Cruz motion.
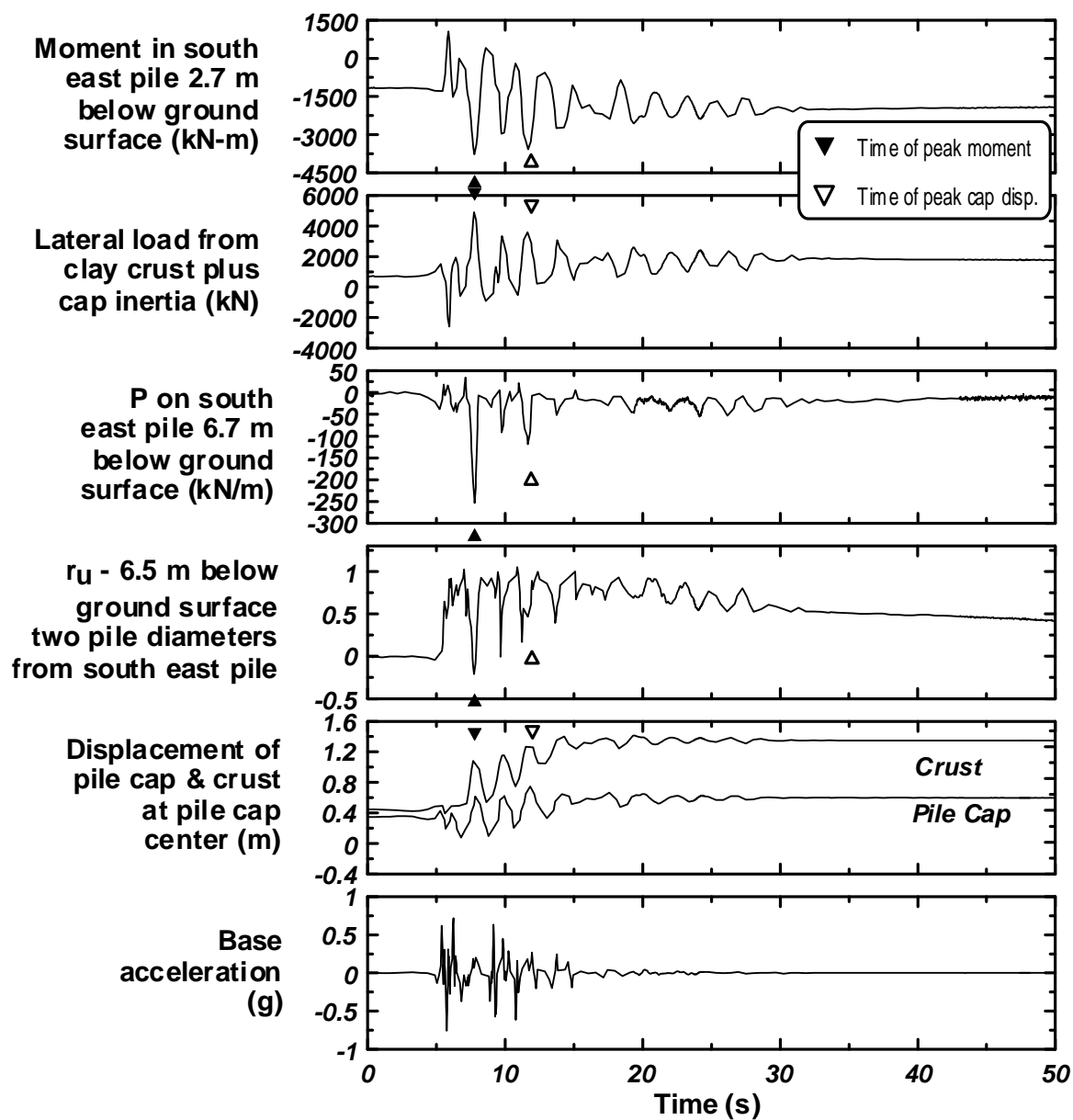
Figure B-8: Time series from test SJB01 for the first large Kobe motion.
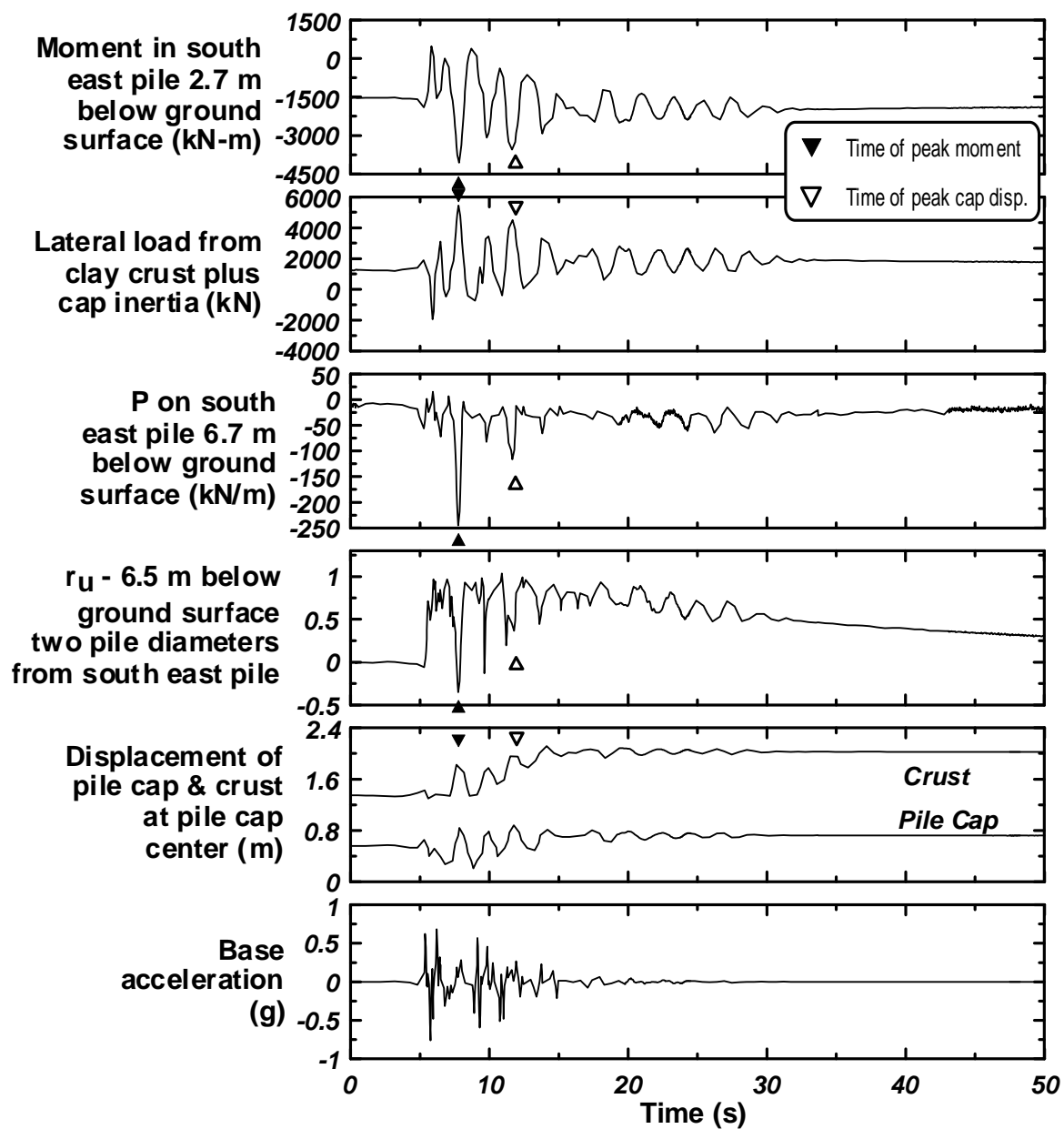
Figure B-9: Time series from test SJB01 for the second large Kobe motion.
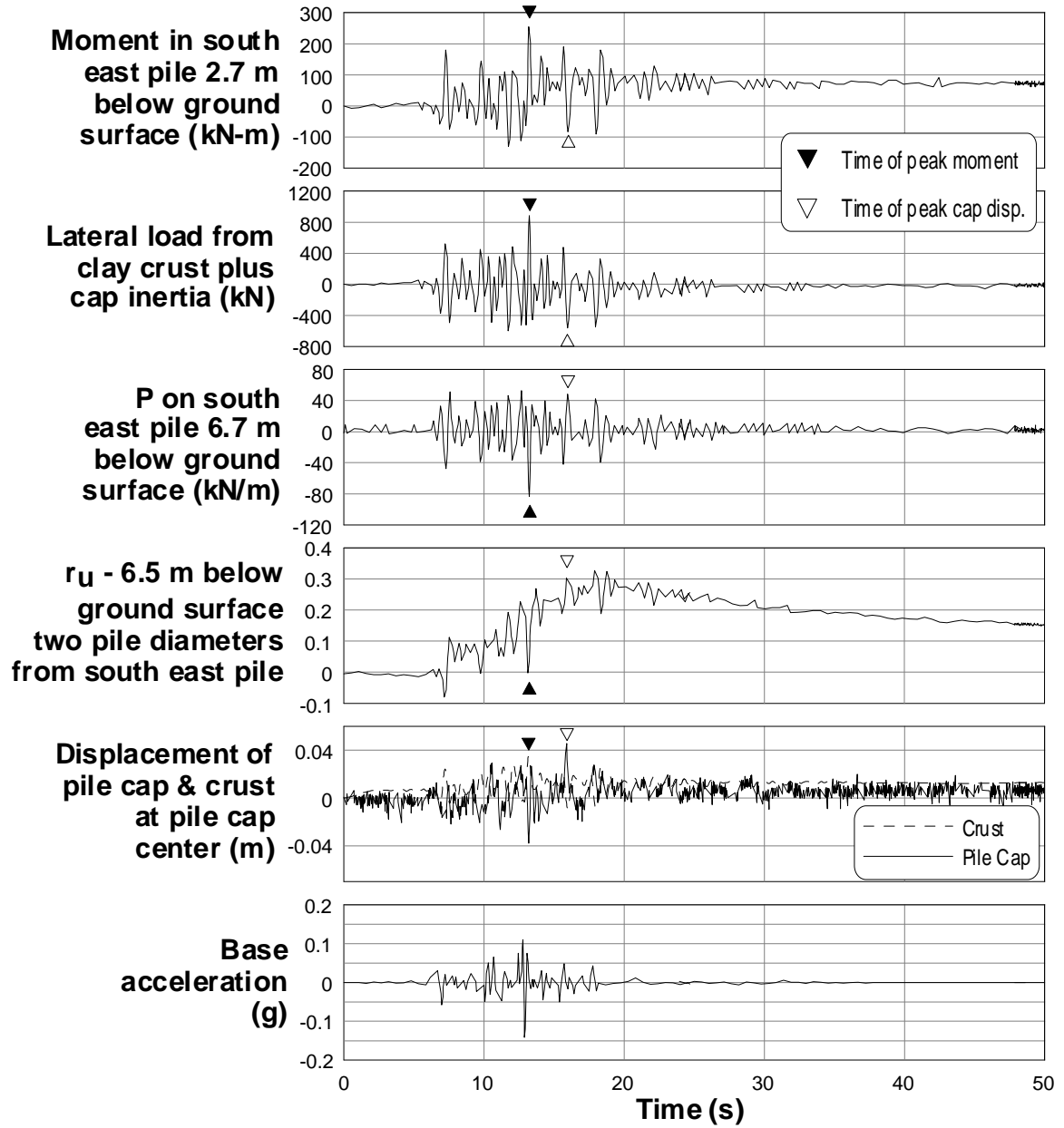
Figure B-10: Time series from test PDS03 for the small Santa Cruz motion.
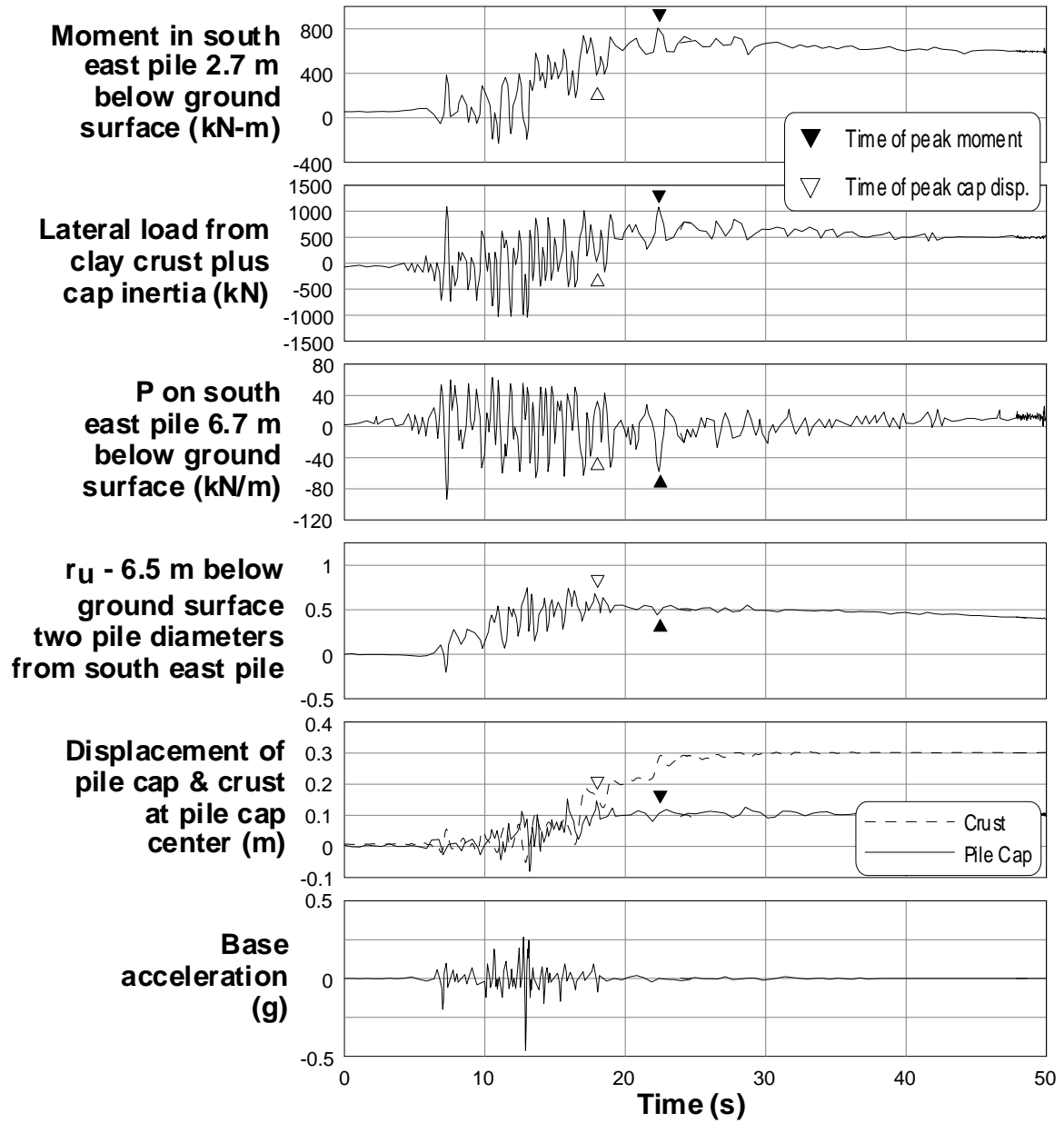
Figure B-11: Time series from test PDS03 for the medium Santa Cruz motion.
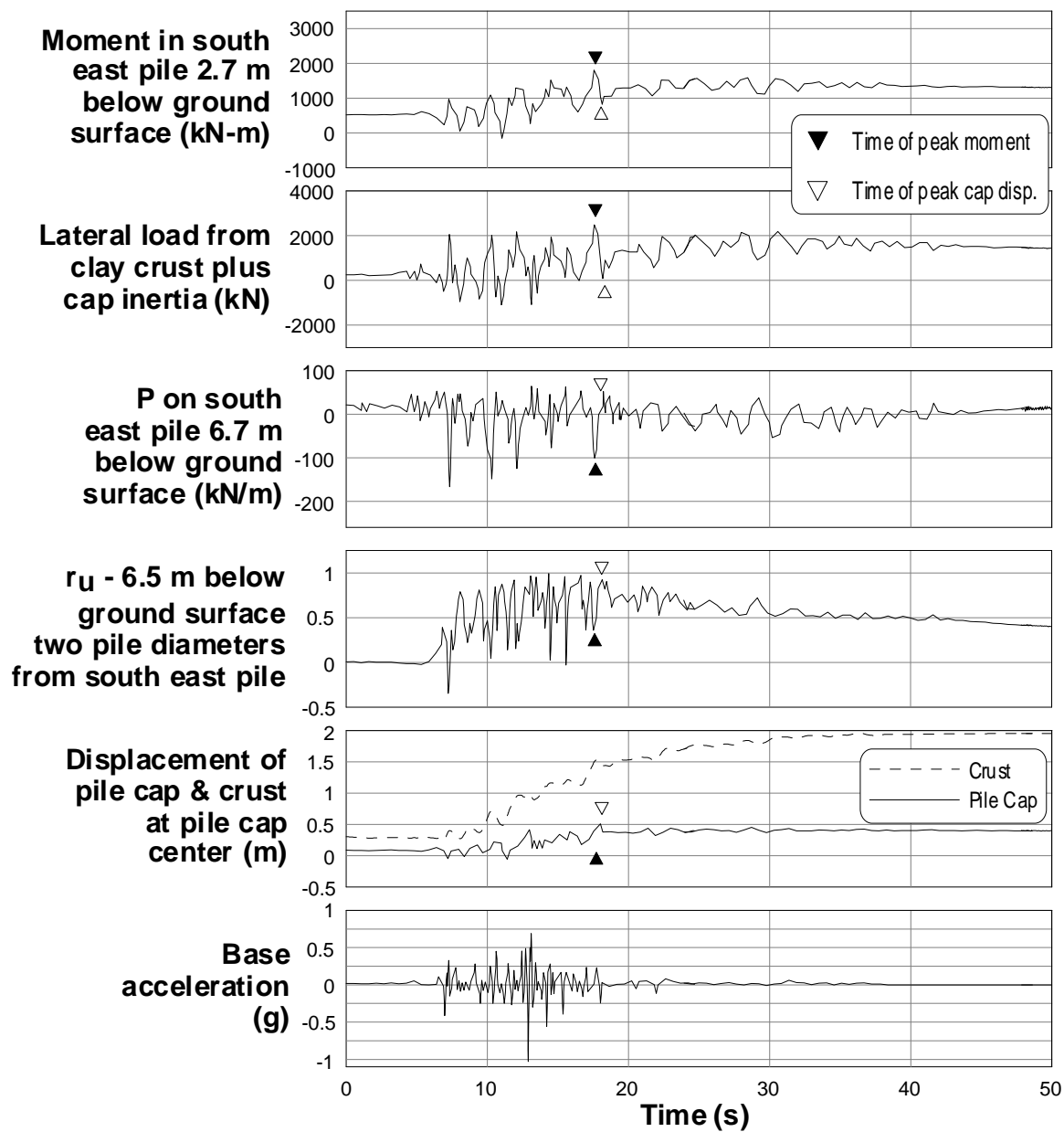
Figure B-12: Time series from test PDS03 for the large Santa Cruz motion.
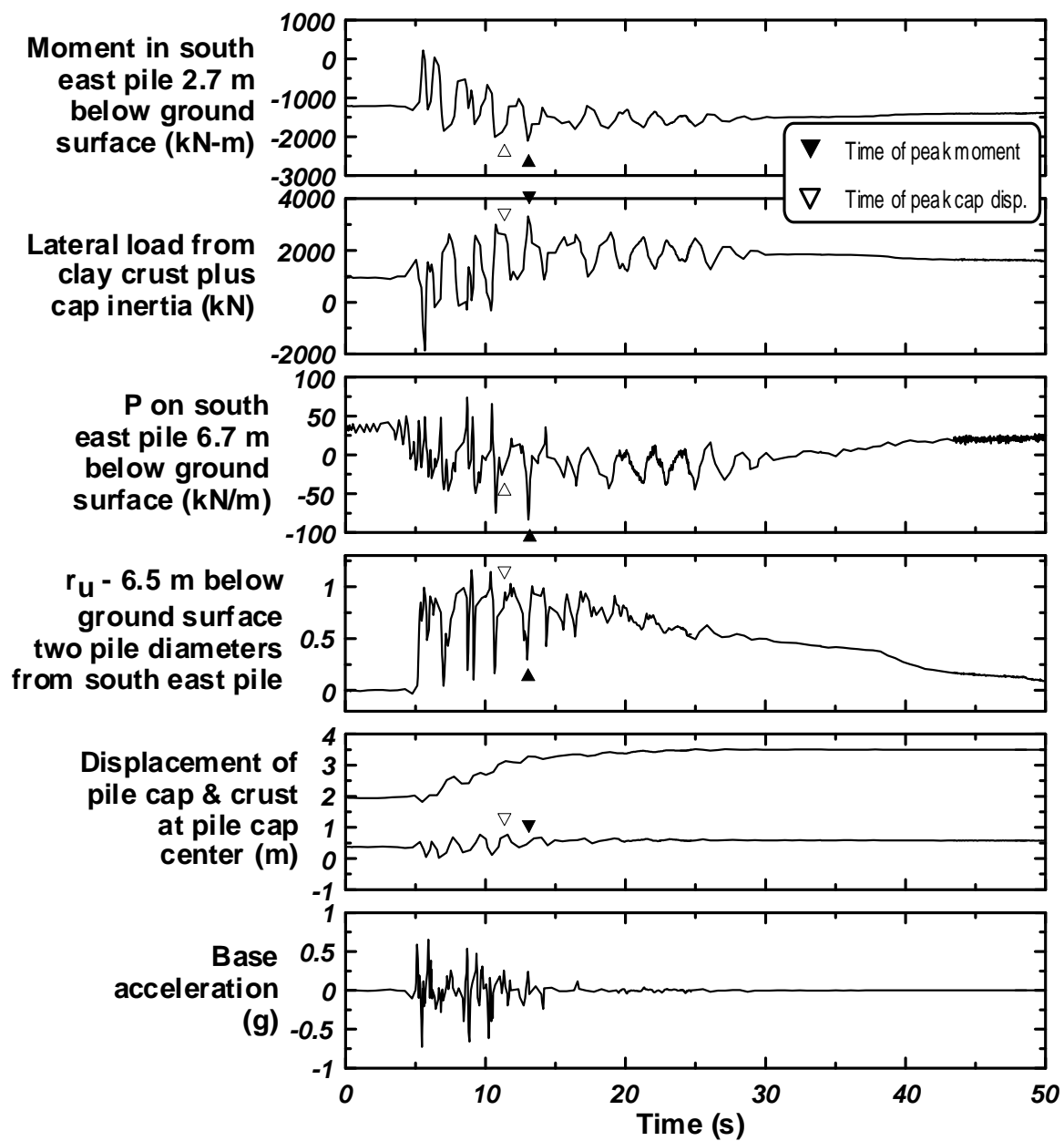
Figure B-13: Time series from test SJB03 for the large Kobe motion.
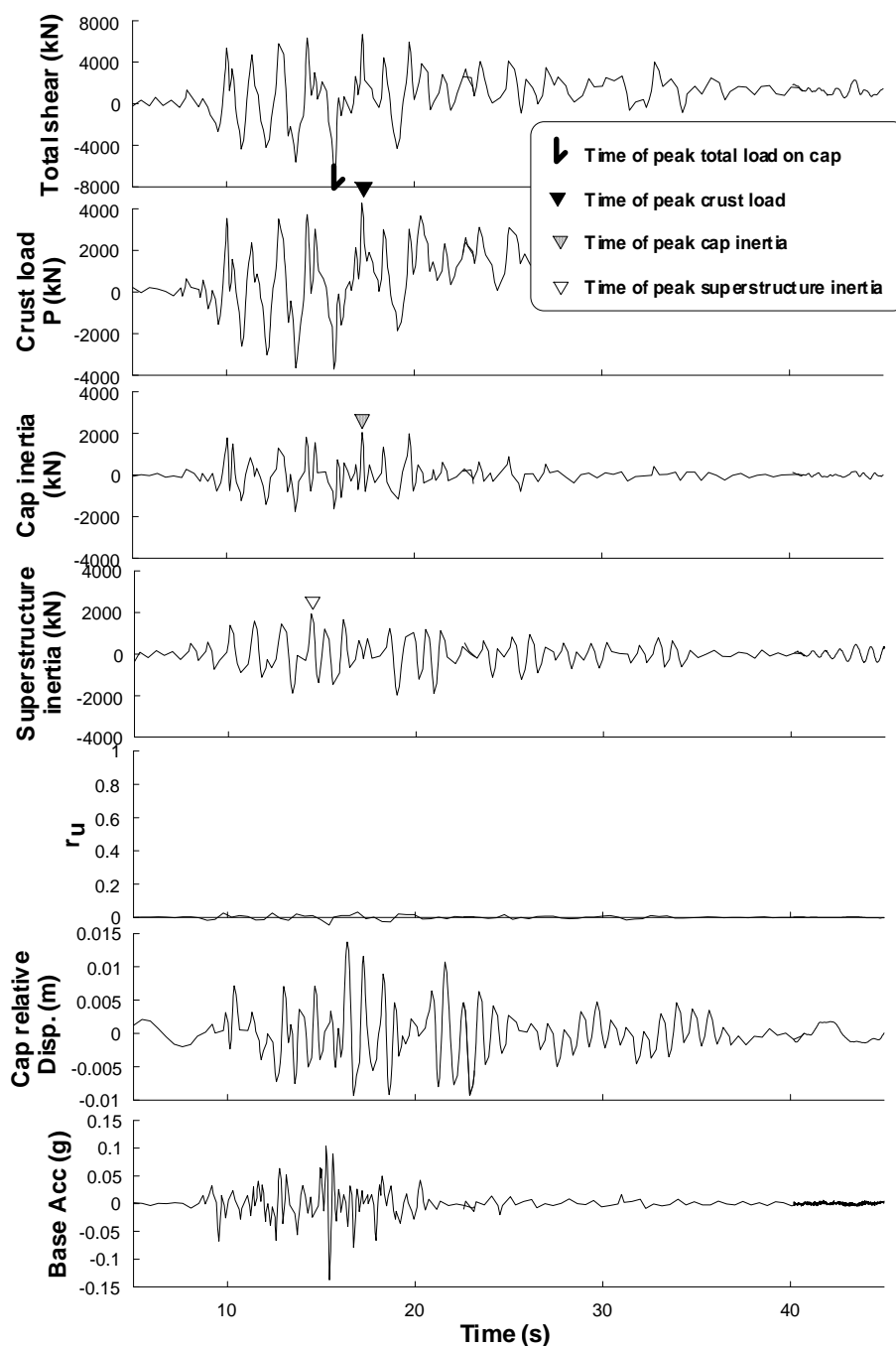
Figure B-14: Time series from test DDC01 for the large Santa Cruz motion.
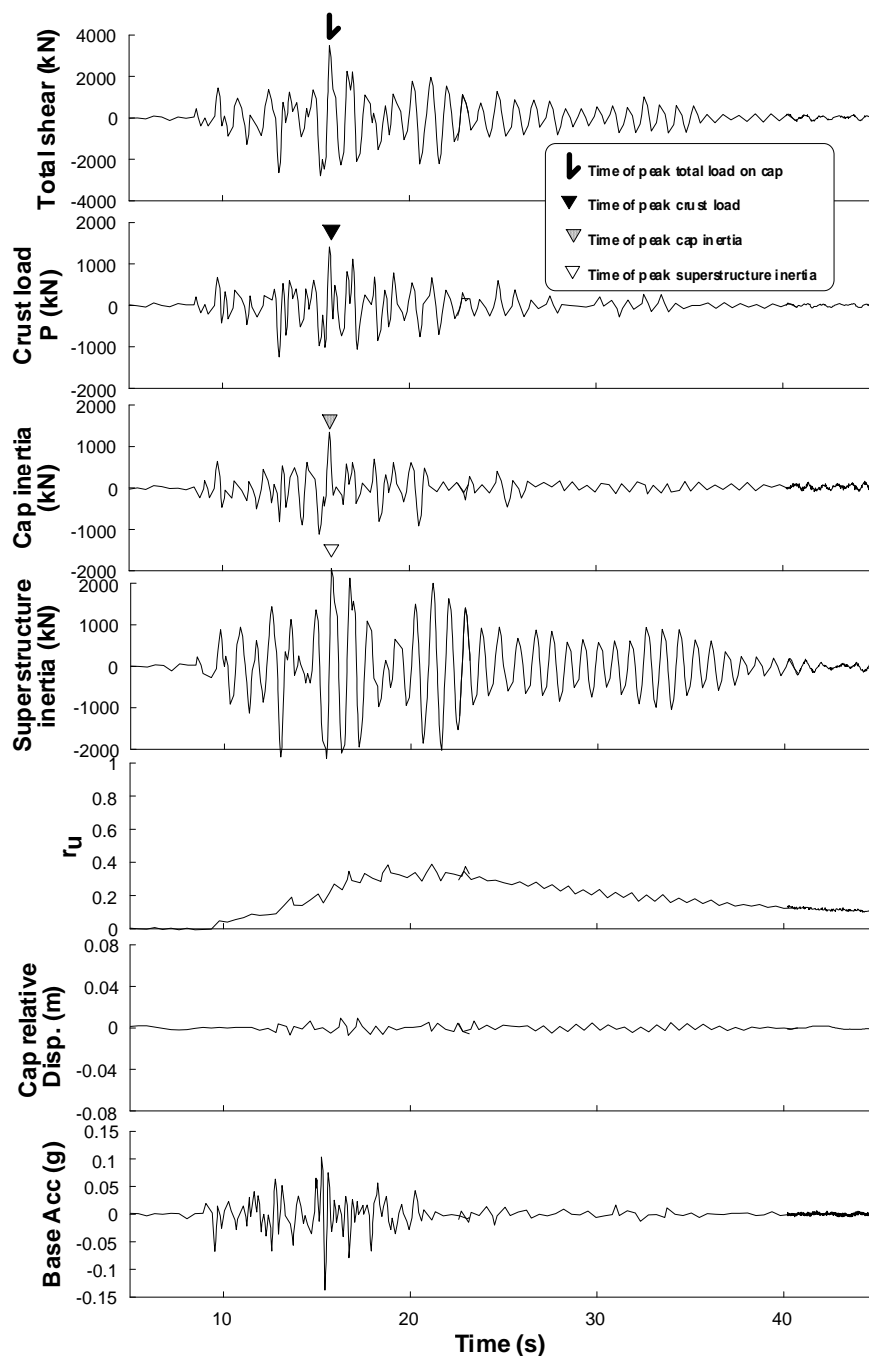
Figure B-15: Time series from test DDC01 for the medium Santa Cruz motion.

313
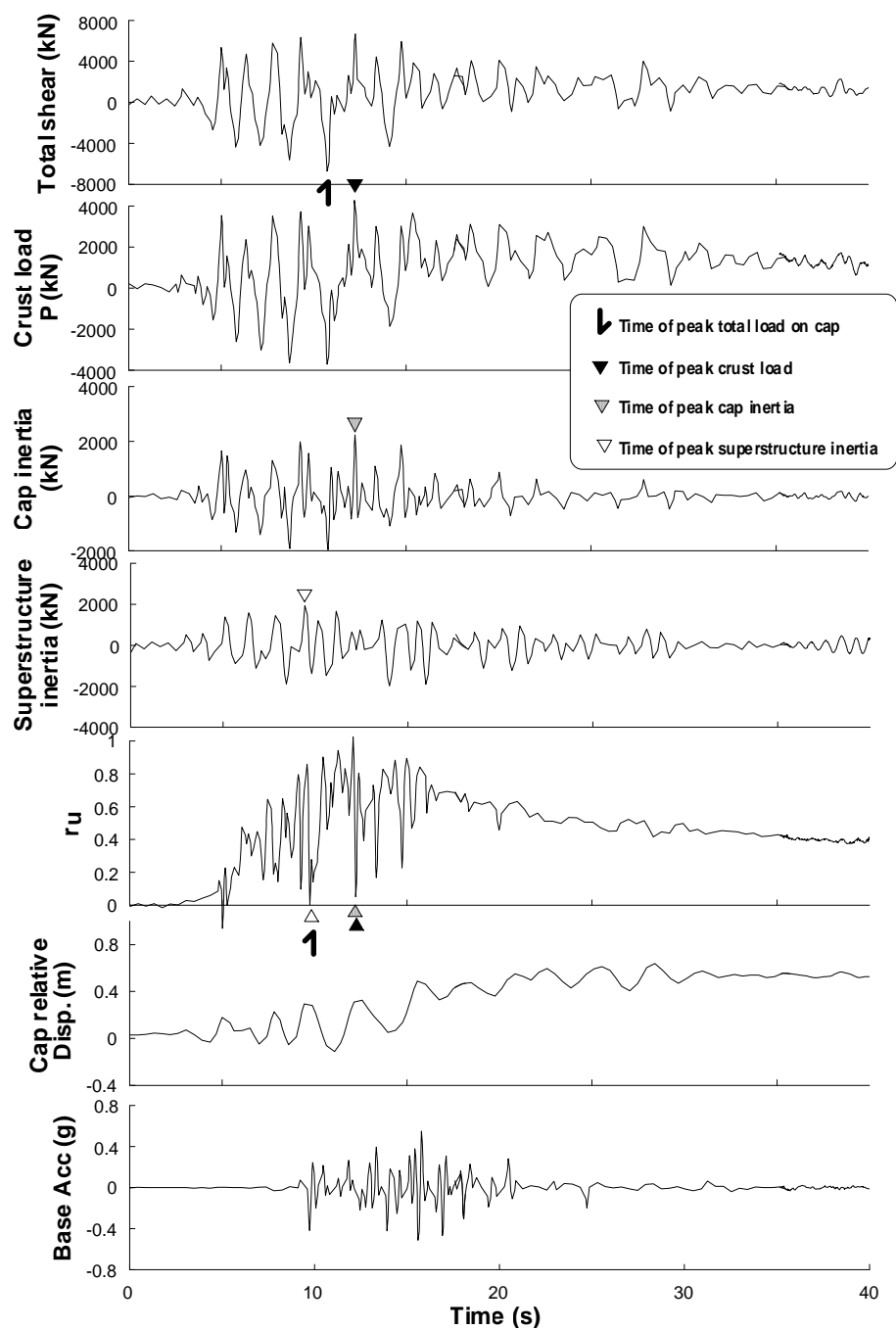
Figure B-16: Time series from test DDC01 for the large Santa Cruz motion.
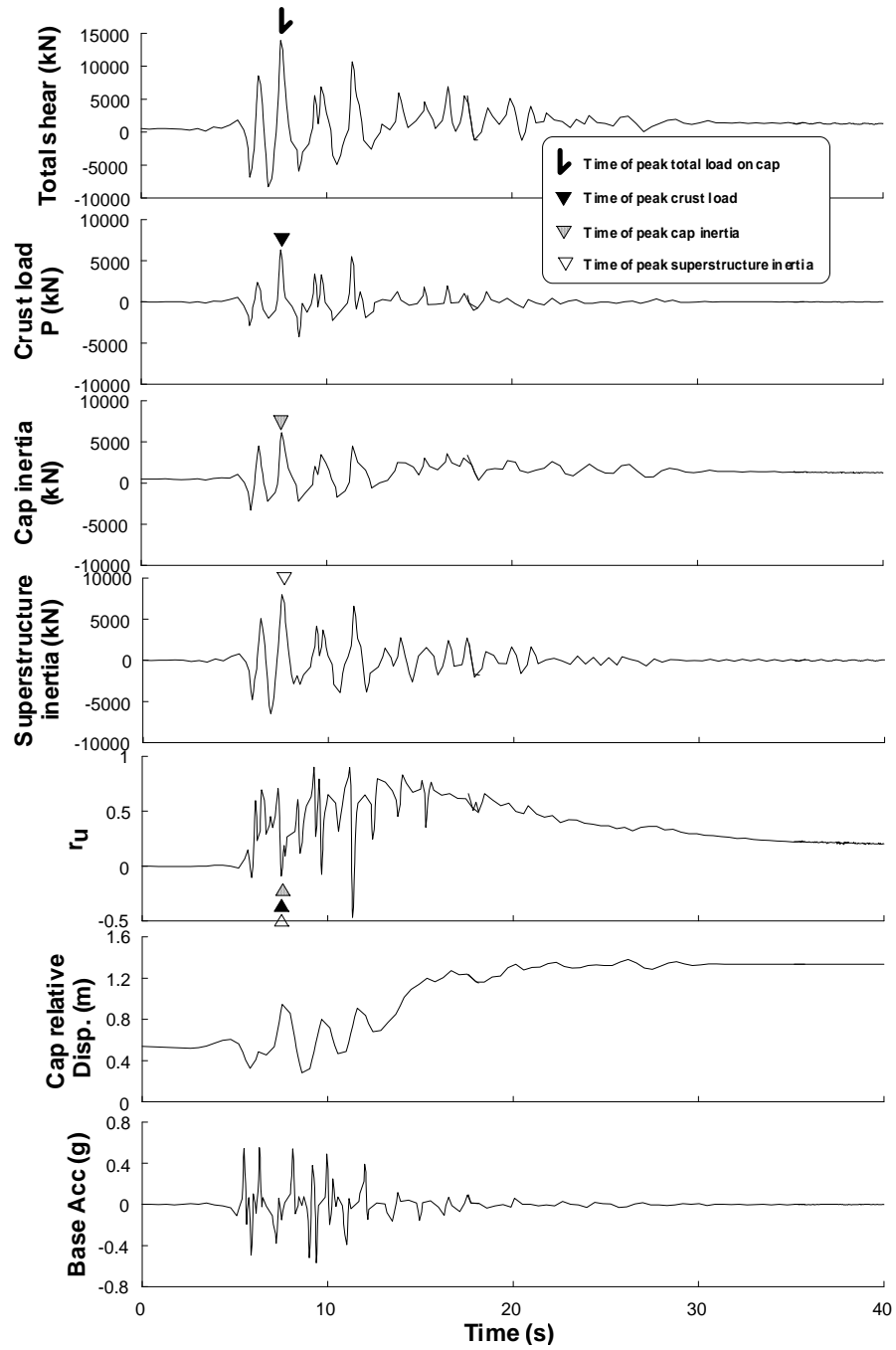
Figure B-17: Time series from test DDC01 for the large Kobe motion.
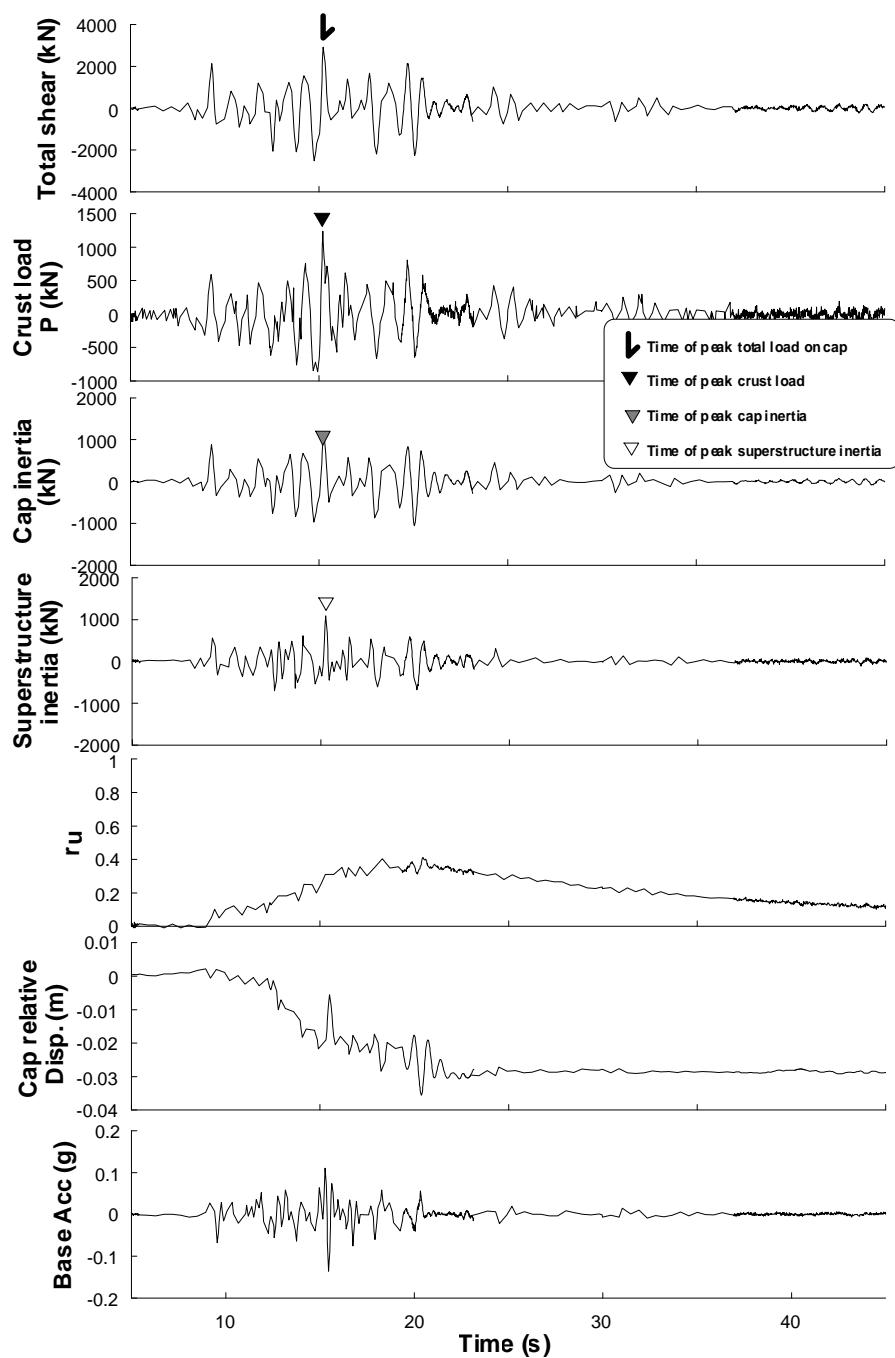
Figure B-18: Time series from test DDC02 for the small Santa Cruz motion.
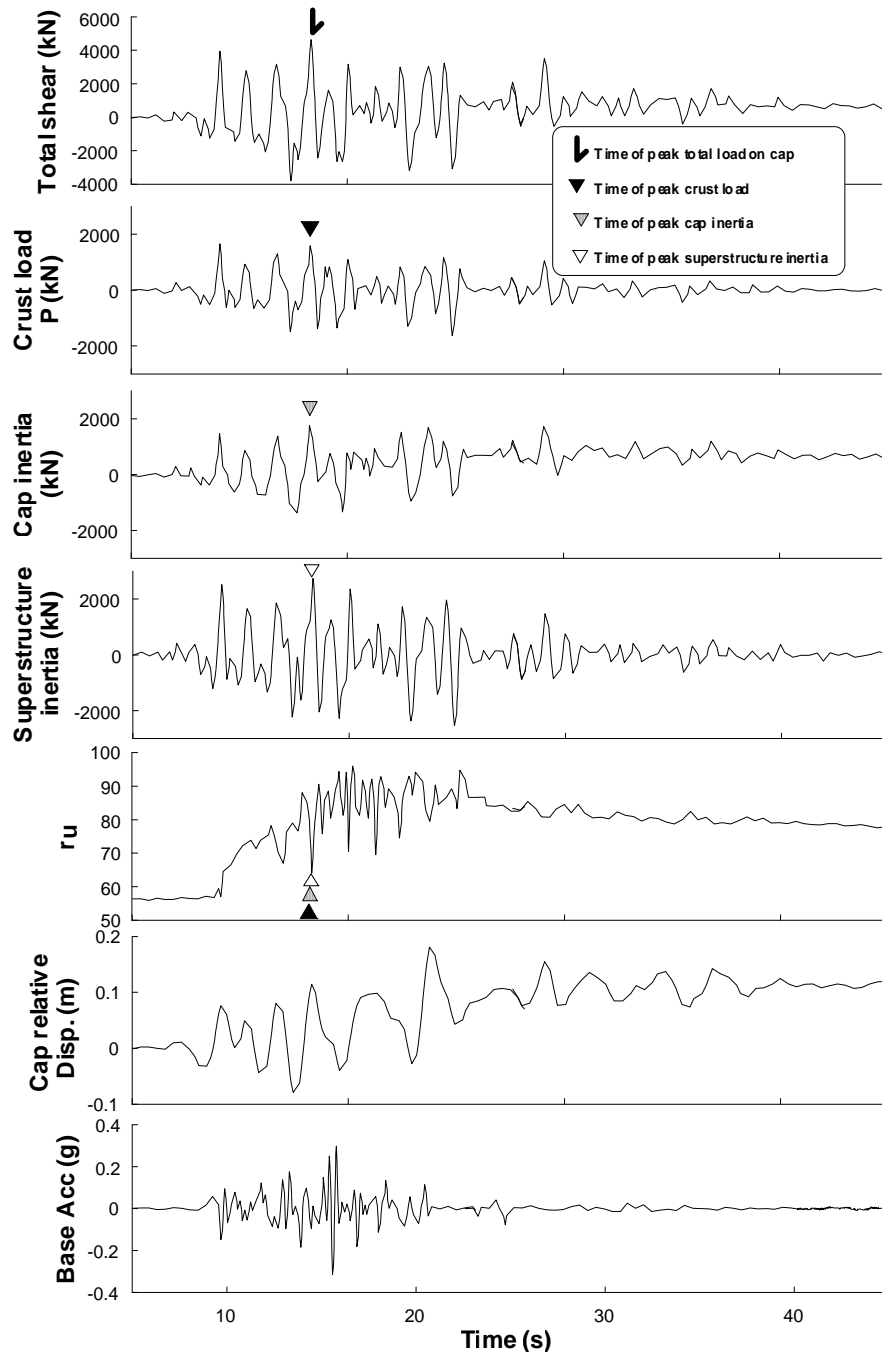
Figure B-19: Time series from test DDC02 for the medium Santa Cruz motion.
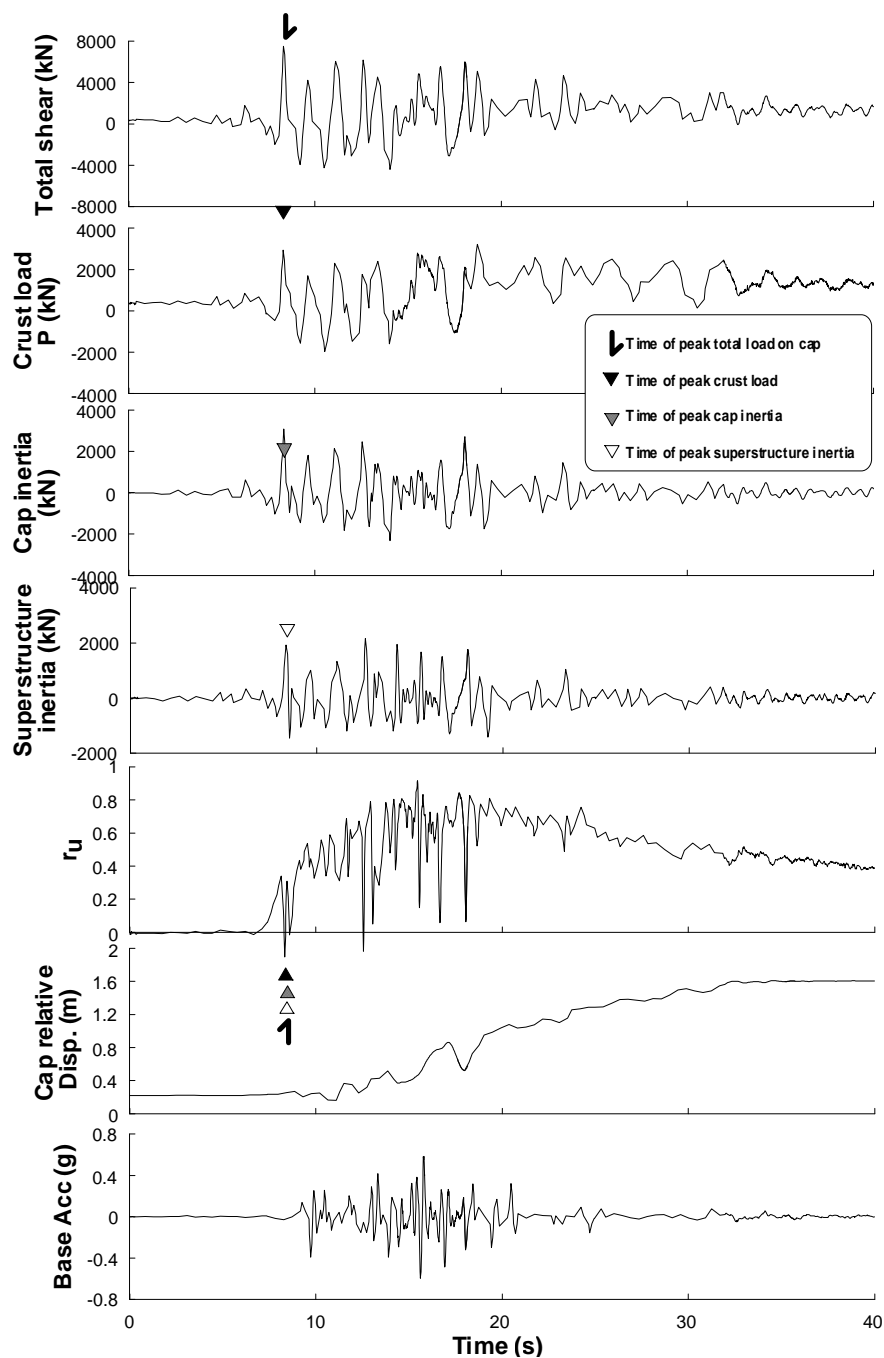
Figure B-20: Time series from test DDC02 for the large Santa Cruz motion.

318
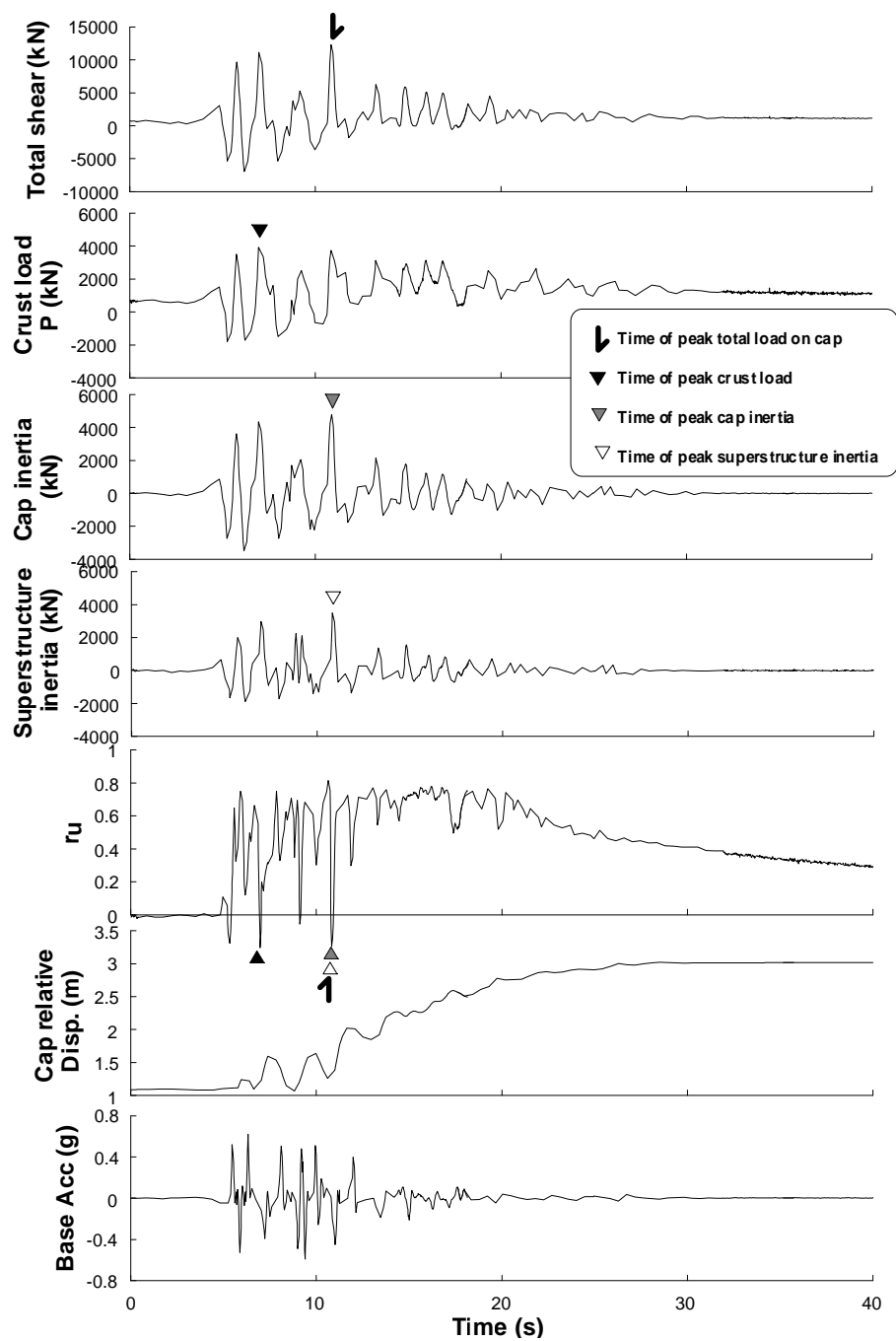
Figure B-21: Time series from test DDC02 for the large Kobe motion.

APPENDIX C

C. TORNADO DIAGRAMS

This appendix contains tornado diagrams that summarize the sensitivity study performed in Chapter 4 of this dissertation. The results of these tornado diagrams were represented more concisely but less completely in Chapter 4 using histograms. The tornado diagrams in this appendix supplement the conclusions made in Chapter 4, and disclose information about individual analyses in the sensitivity study that readers might find valuable. Each tornado diagram was formed by performing 21 analyses (required to systematically vary 10 different input parameters to their min. and max. values), and tabulating the recorded bending moments and pile cap displacements for each analysis. The range between the minimum and maximum response (peak bending moment or pile cap displacement) was then computed for each input parameter, and the input parameters were sorted in order of the range in the response caused by the variation in the parameter. Finally, the ranges were plotted as a bar diagram with the most influential parameter on top, the second most influential parameter immediately below, and so on to the least influential parameter on the bottom. These diagrams typically exhibit the characteristic shape of a tornado, hence their name.
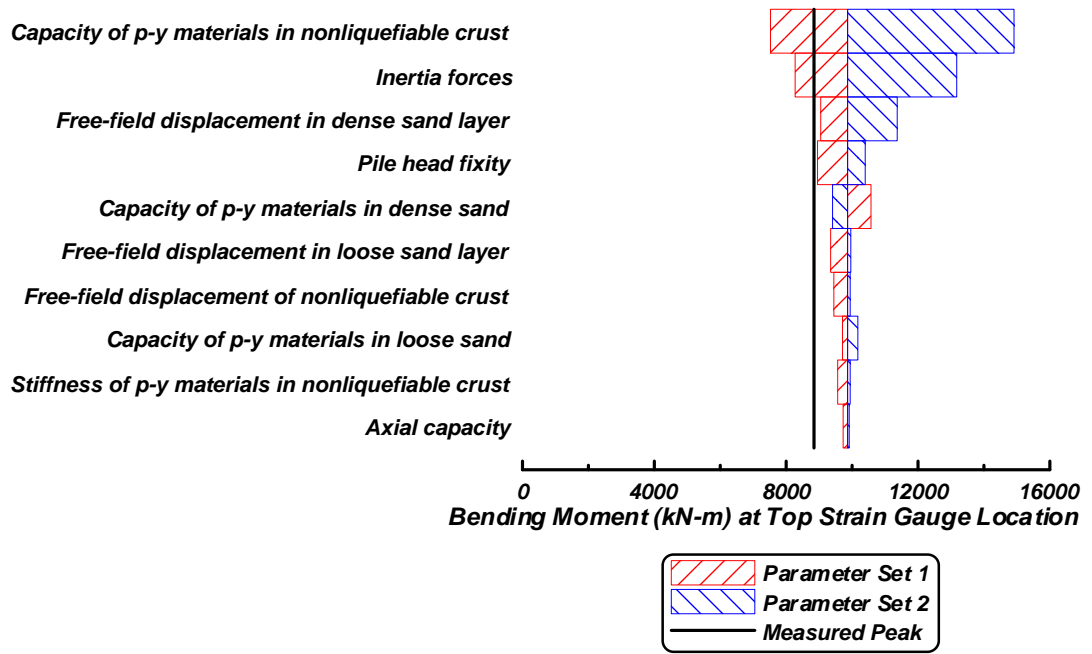
Figure C-1: Bending moment tornado diagram for BNWF_SD analyses of the large Kobe motion for
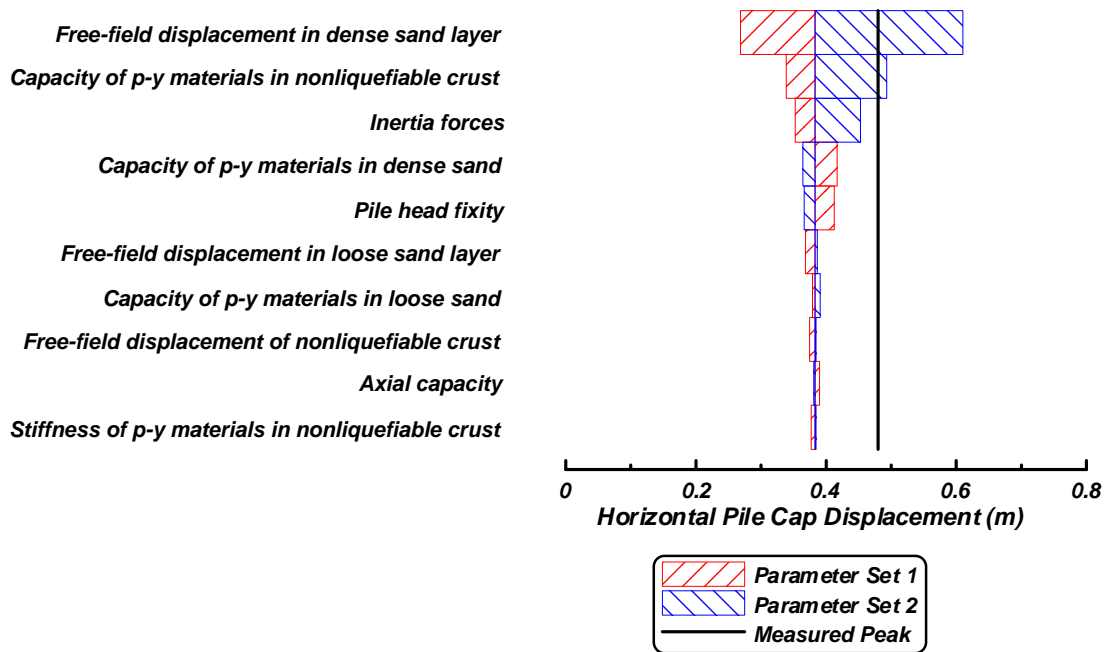
test SJB03.

Figure C-2: Pile cap displacement tornado diagram BNWF_SD analyses of the large Kobe motion for
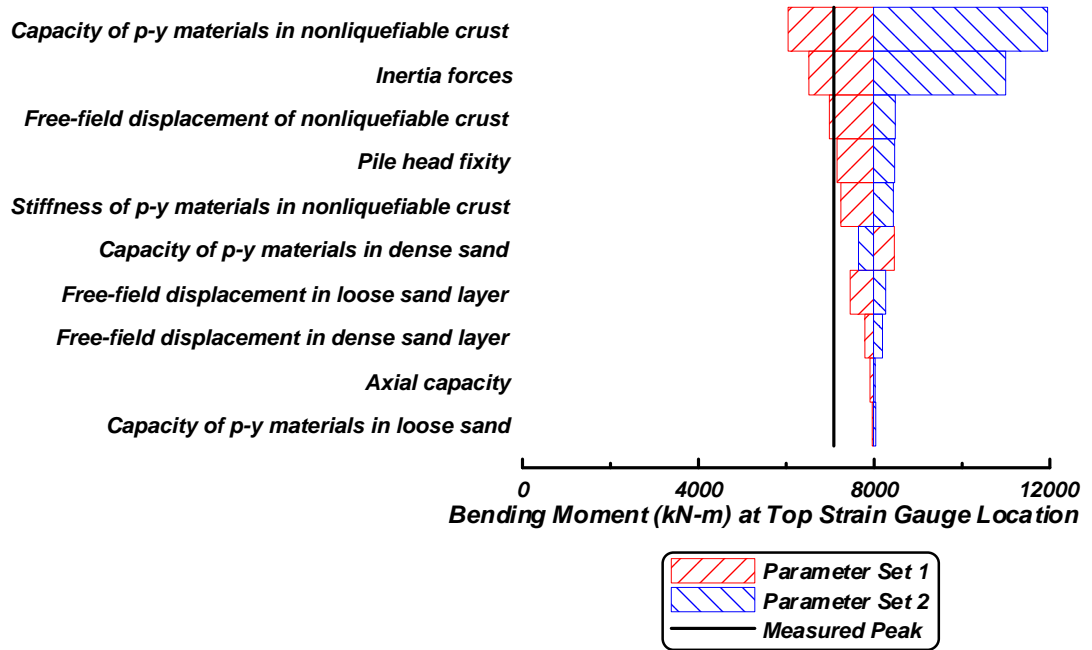
test SJB03.

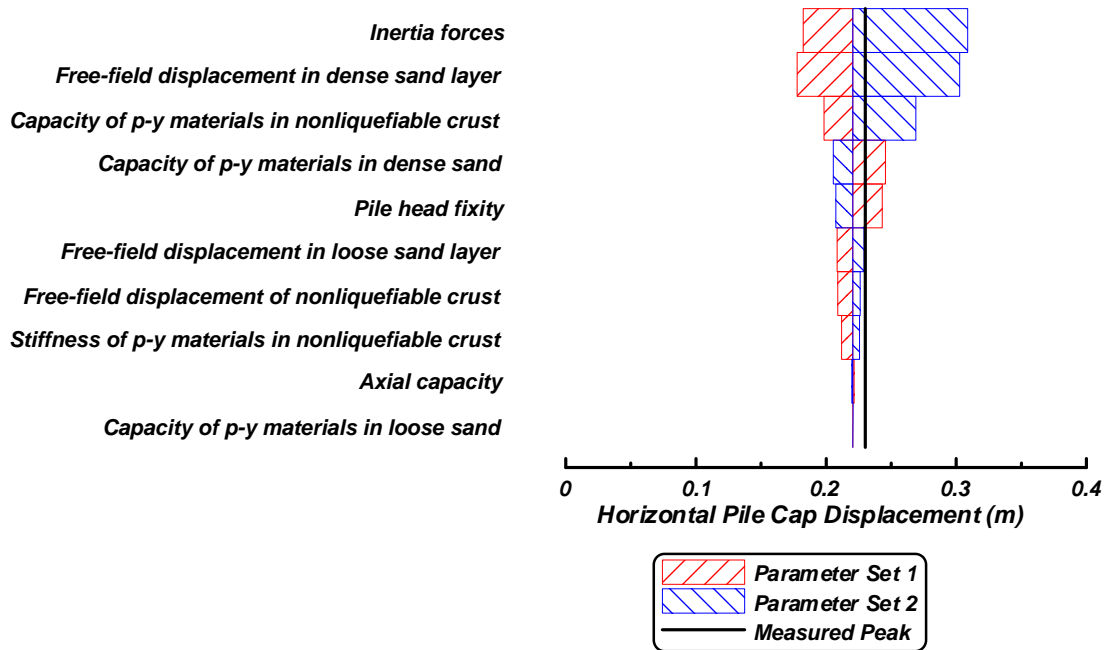Figure C-3: Bending moment tornado diagram for BNWF_SD analyses of the large Santa Cruz motion
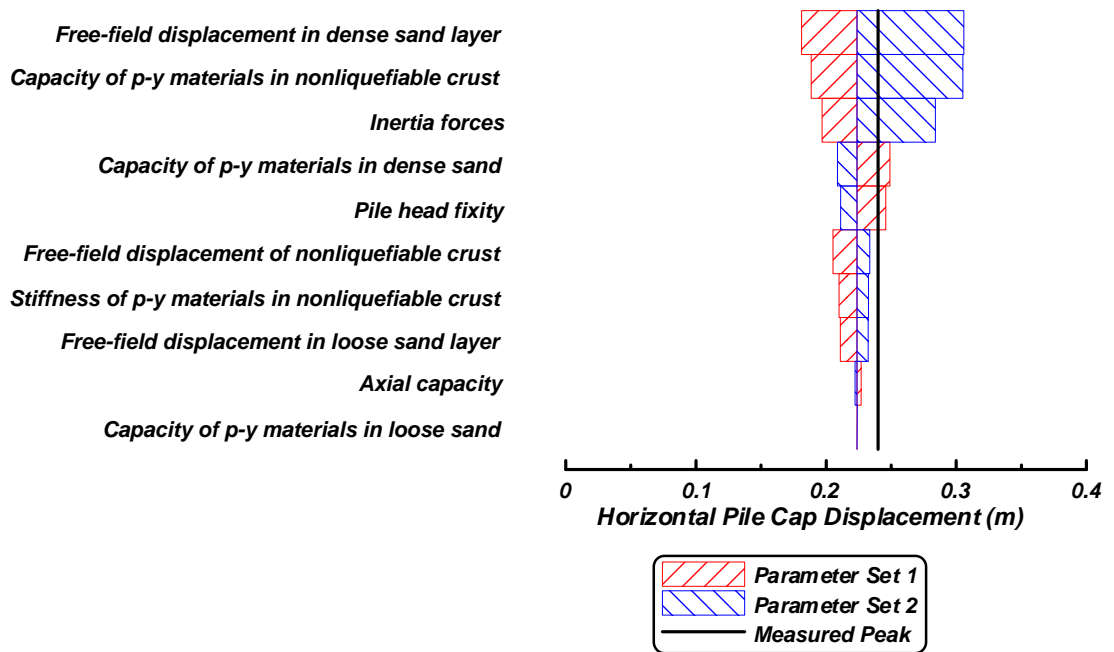
for test SJB03.

Figure C-4: Pile cap displacement tornado diagram for BNWF_SD analyses of the large Santa Cruz
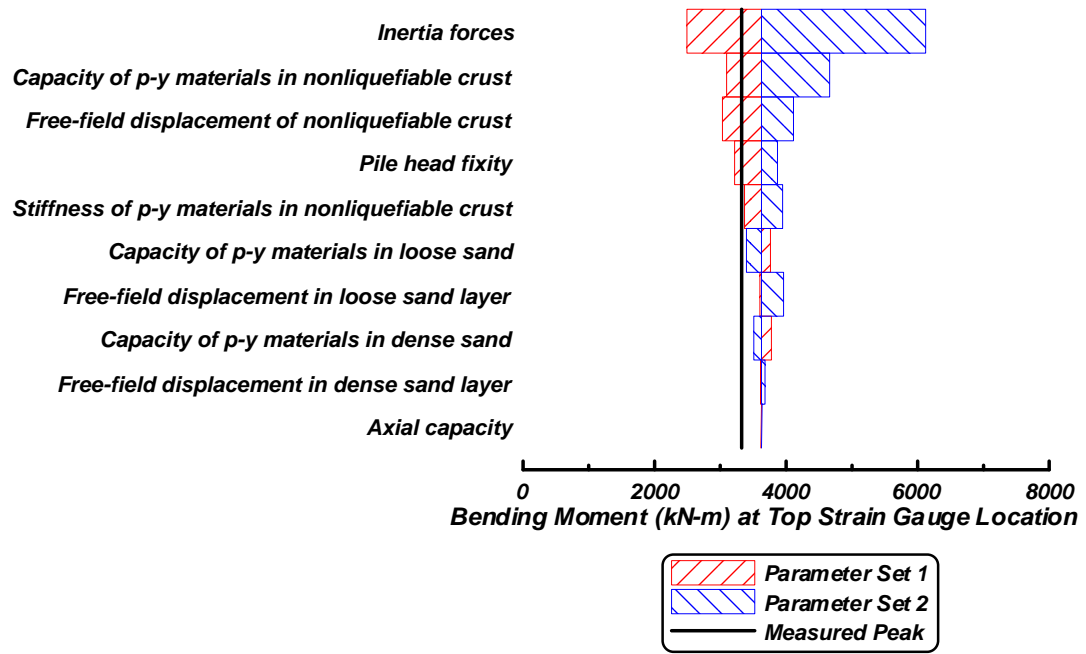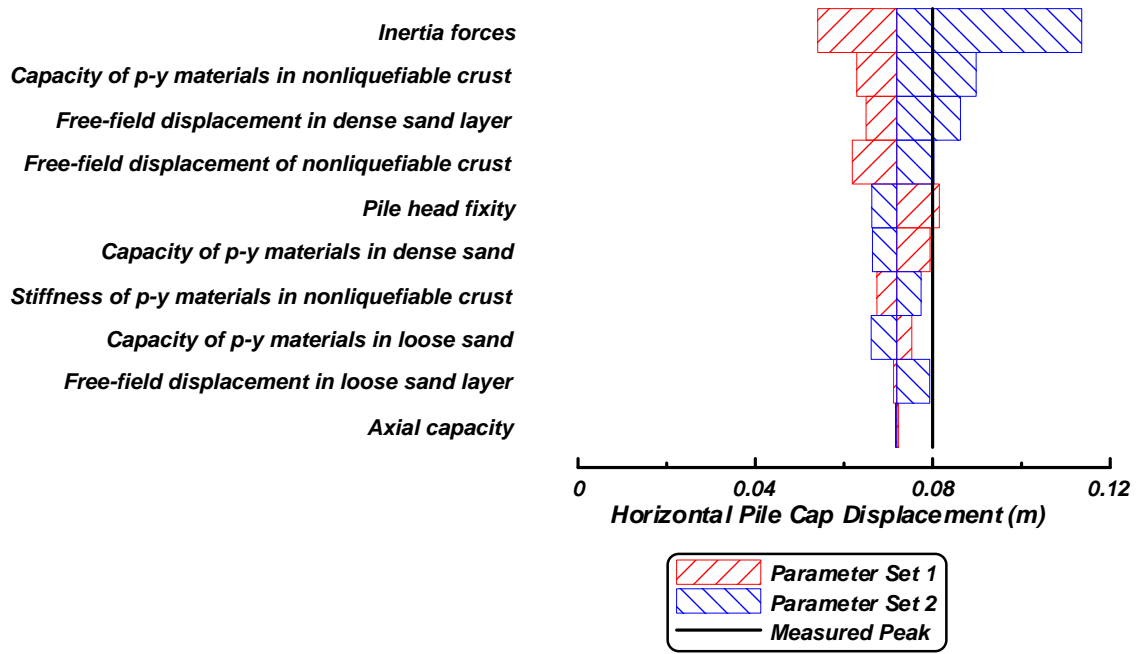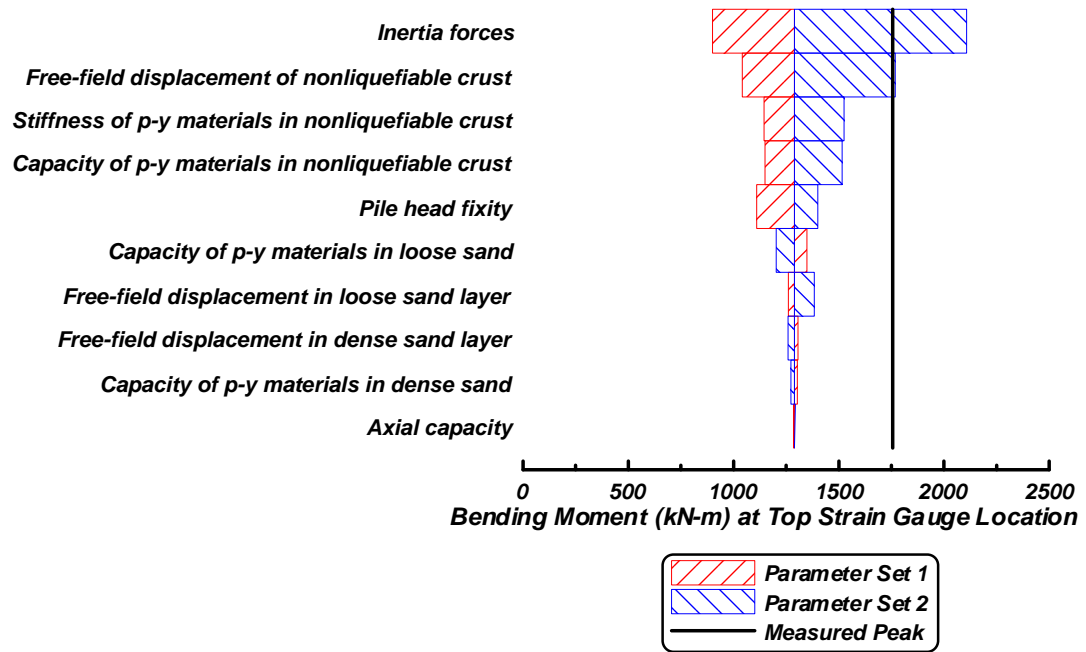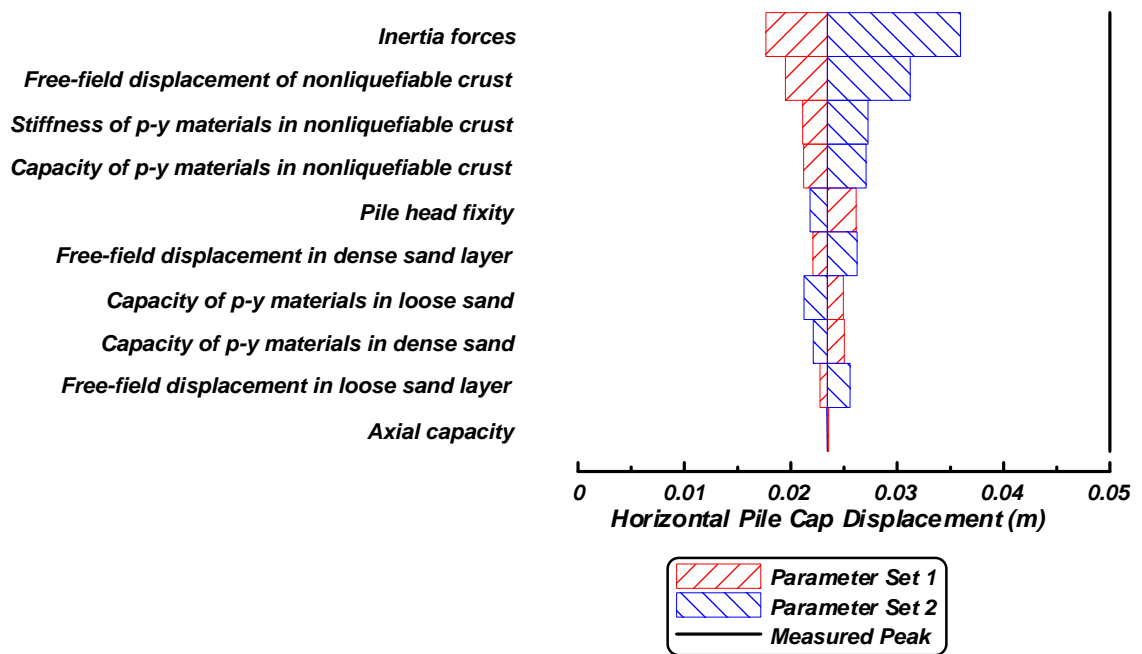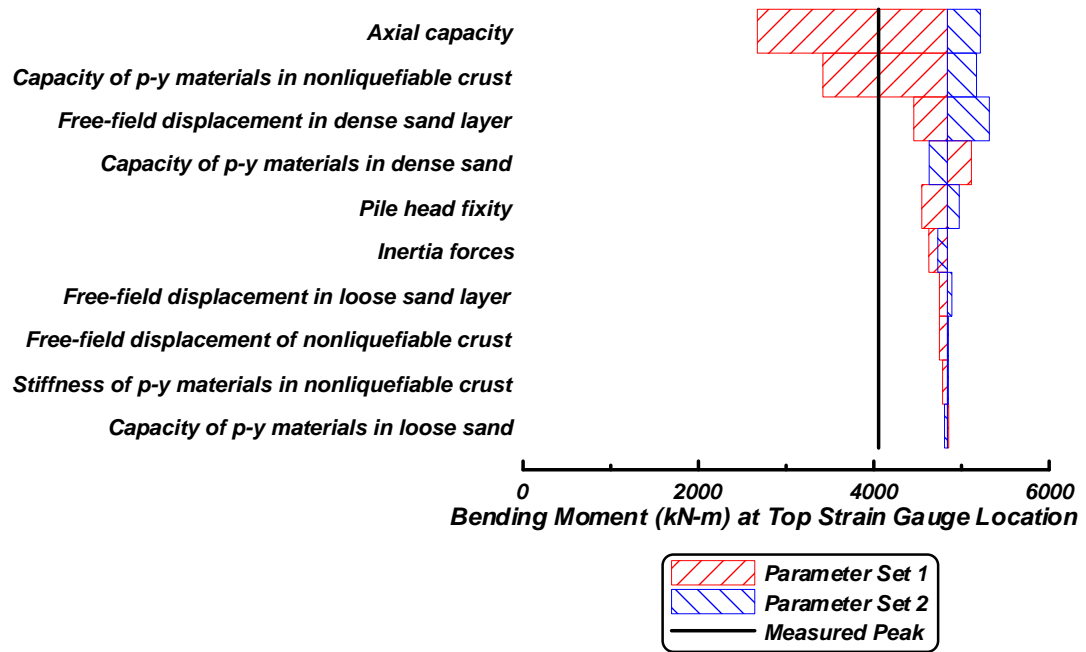
motion for test SJB03.
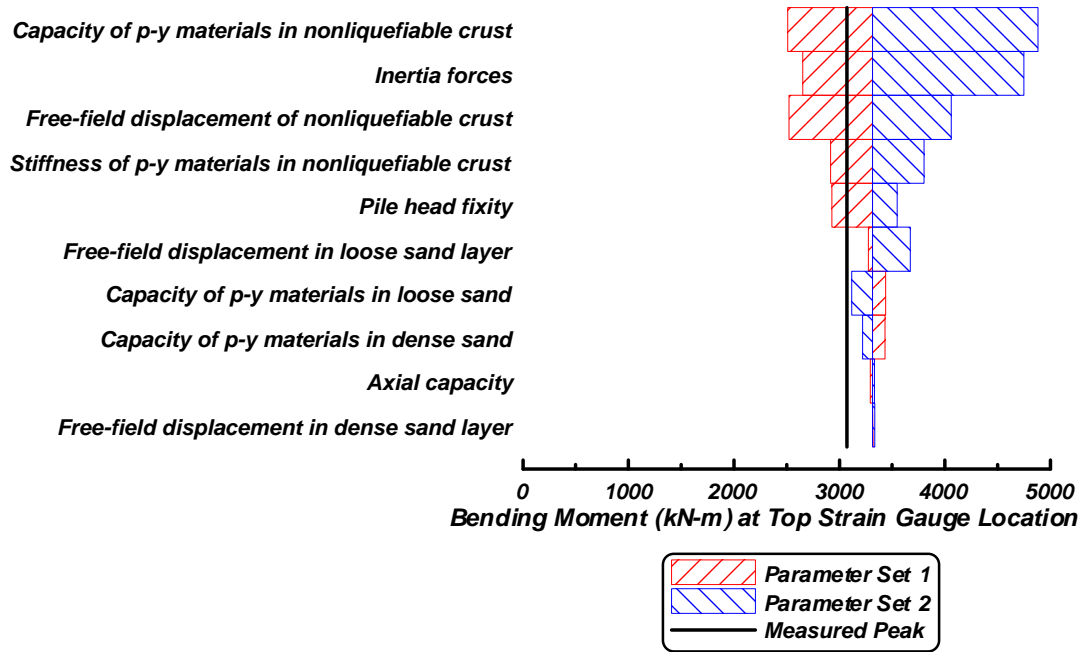
Figure C-5: Bending moment tornado diagram for BNWF_SD analyses of the medium Santa Cruz
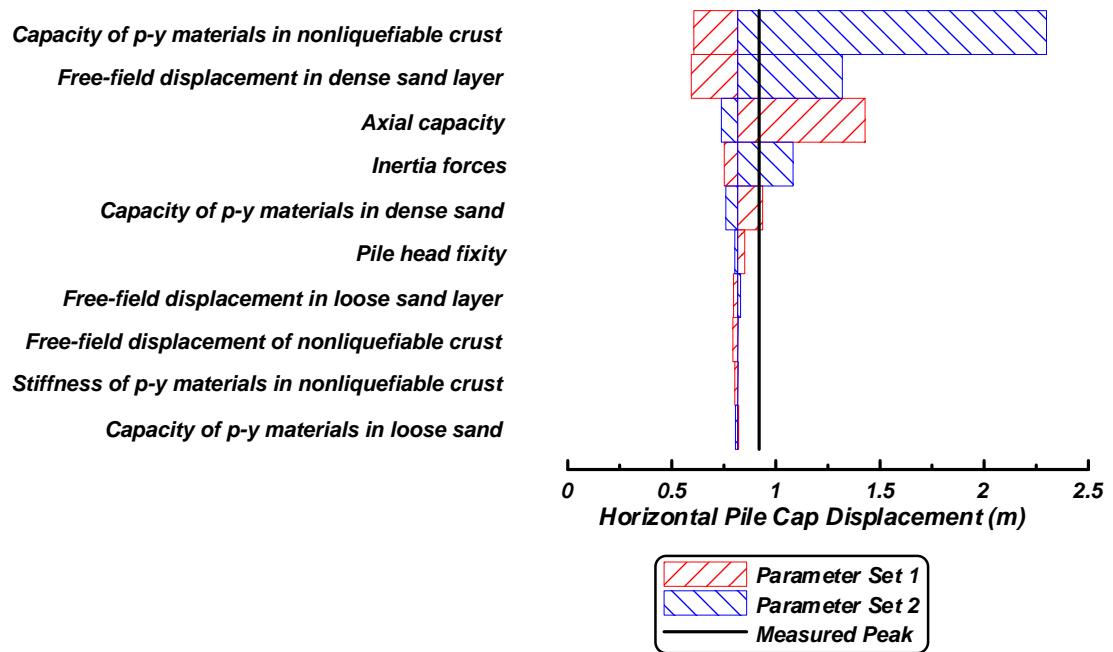
motion for test SJB03.
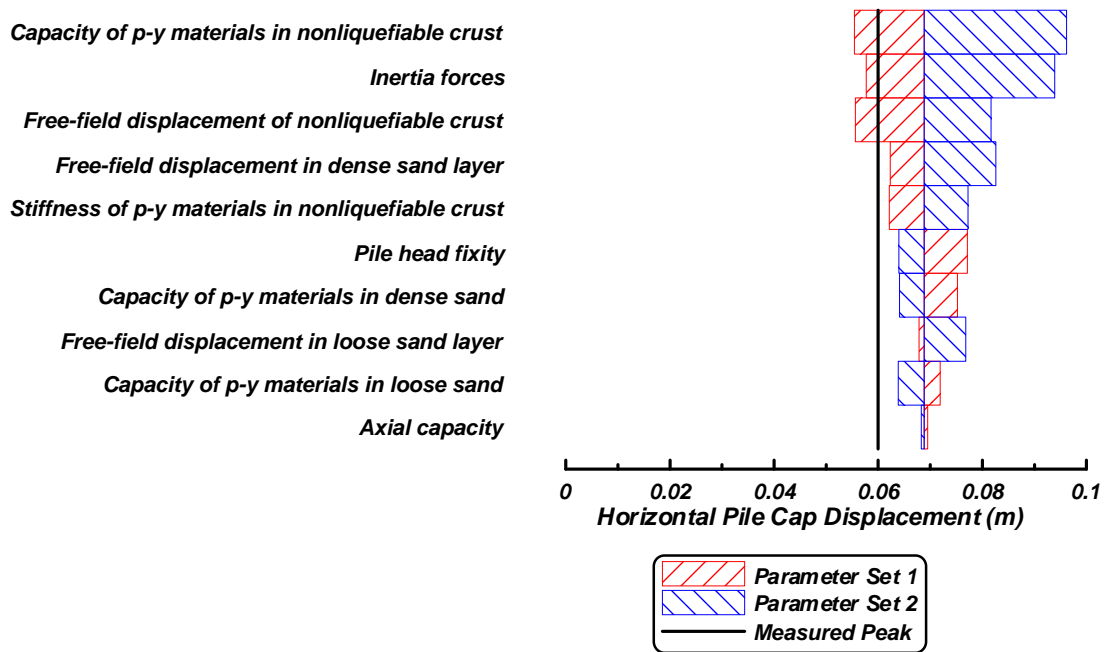
Figure C-6: Pile cap displacement tornado diagram for BNWF_SD analyses of the medium Santa Cruz

motion for test SJB03
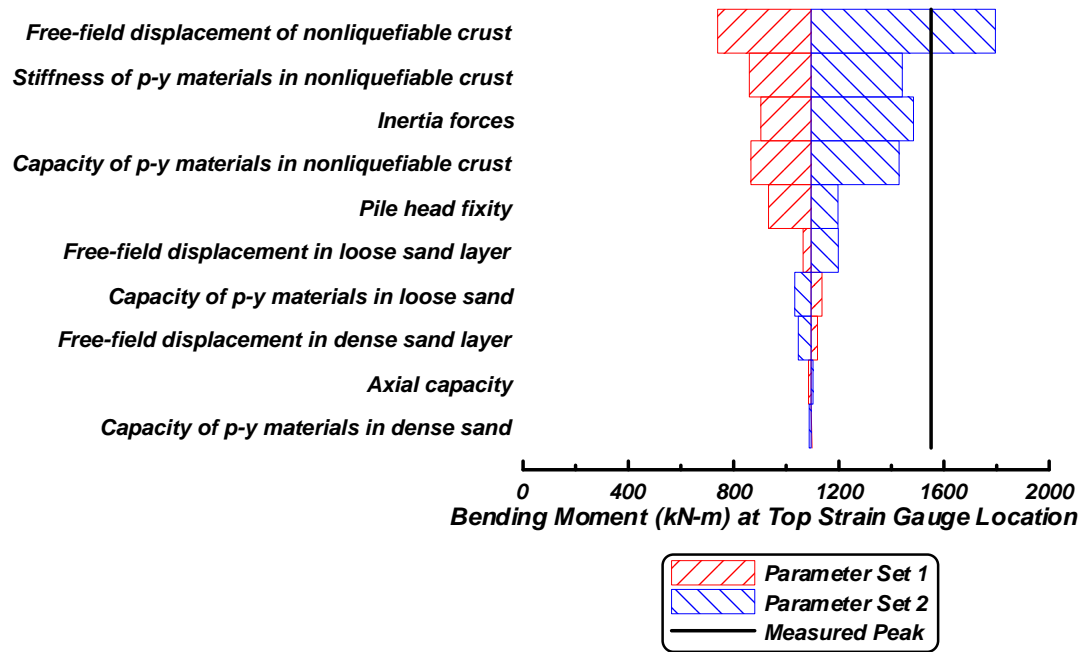
Figure C-7: Bending moment tornado diagram for BNWF_SD analyses of the small Santa Cruz motion
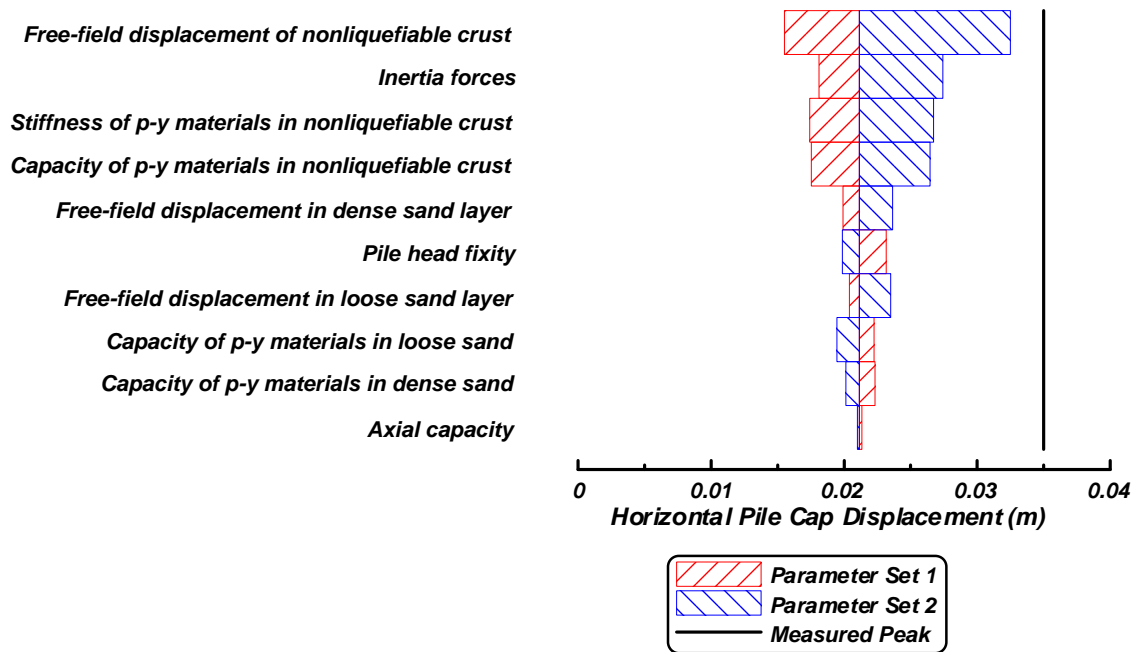
for test SJB03.

Figure C-8: Pile cap displacement tornado diagram for BNWF_SD analyses of the small Santa Cruz
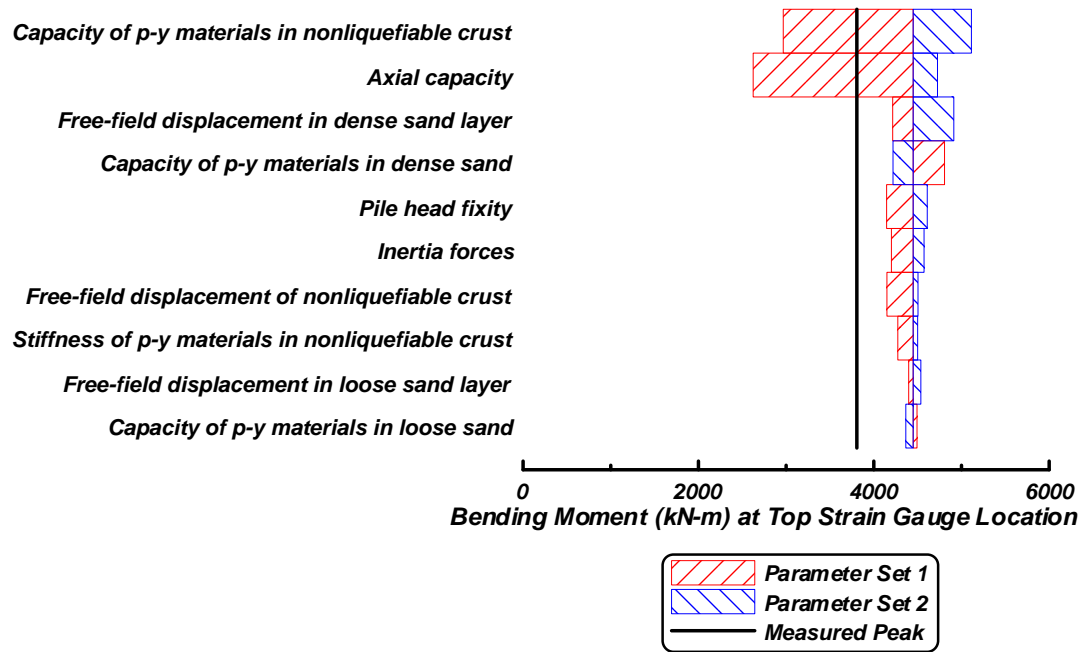
motion for test SJB03.
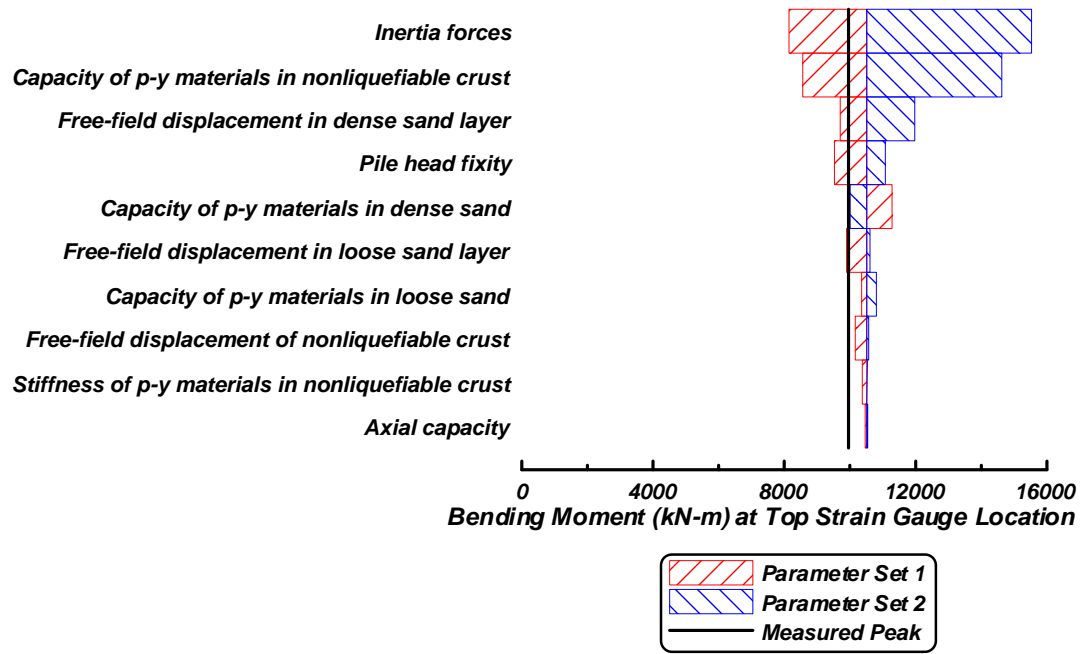
Figure C-9: Bending moment tornado diagram for BNWF_SD analyses of the large Kobe motion for
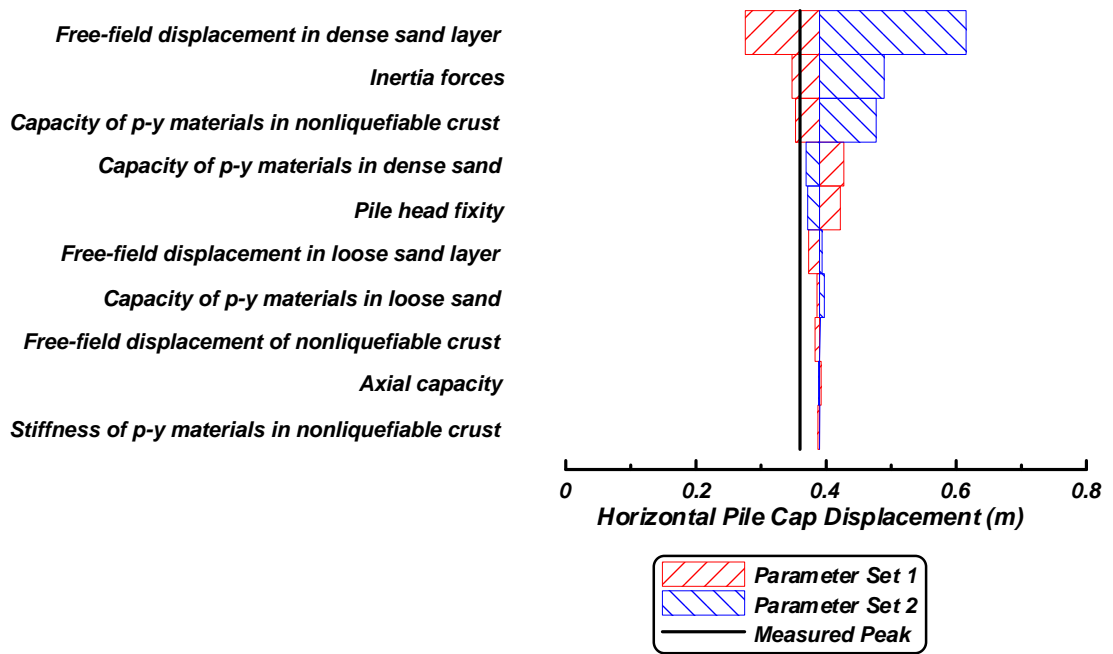
test DDC01.
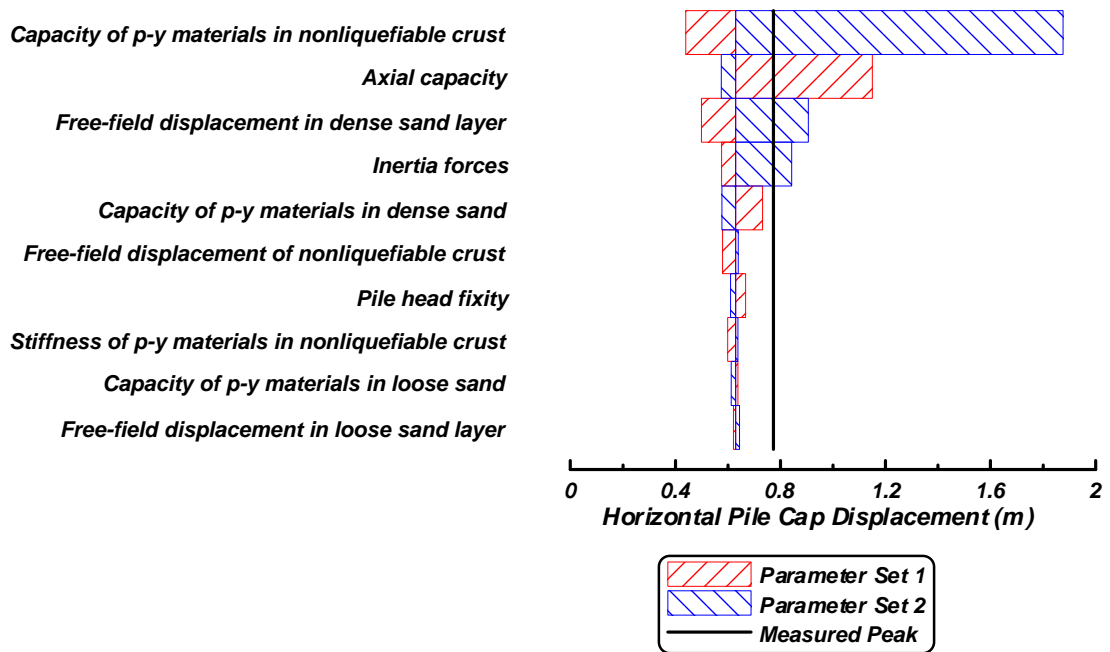

Figure C-10: Pile cap displacement tornado diagram for BNWF_SD analyses of the large Kobe motion
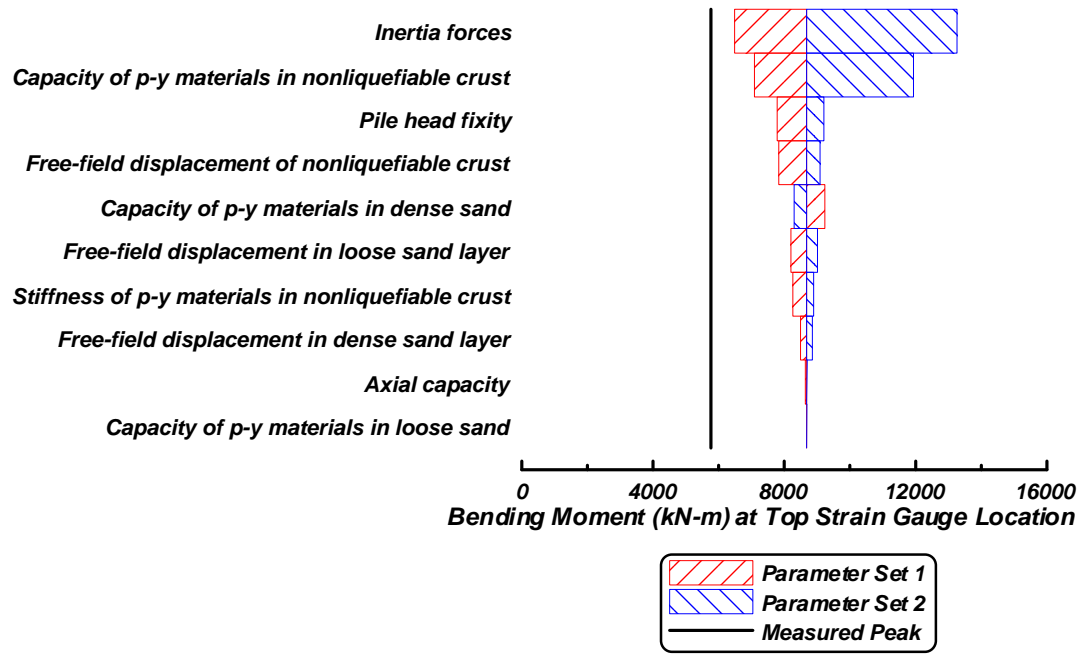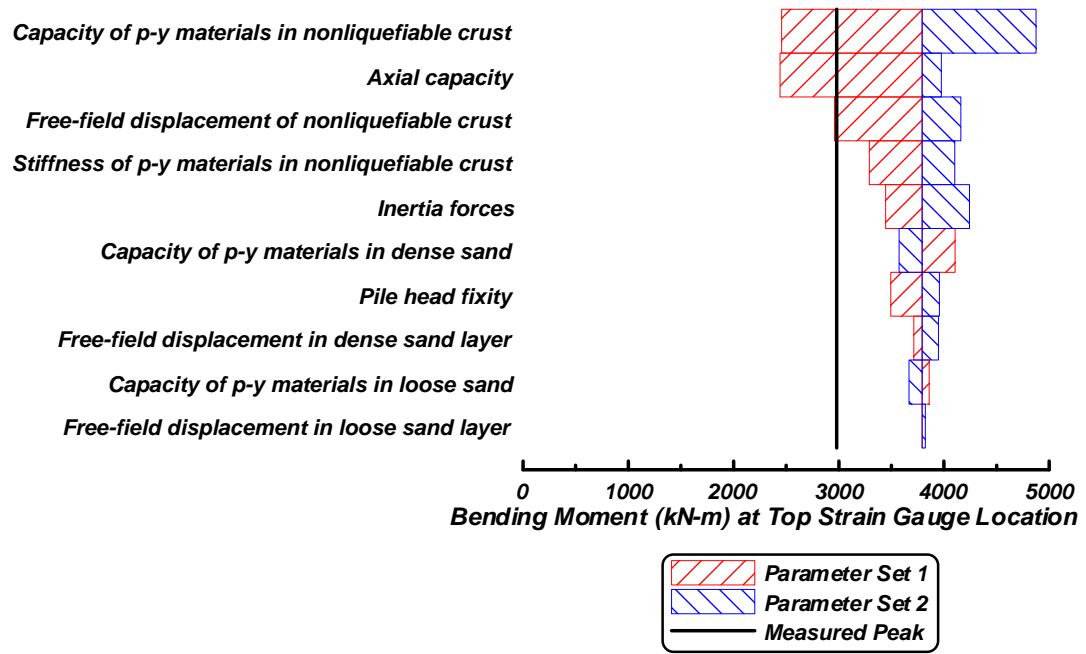
for test DDC01.

Figure C-11: Bending moment tornado diagram for BNWF_SD analyses of the large Santa Cruz motion
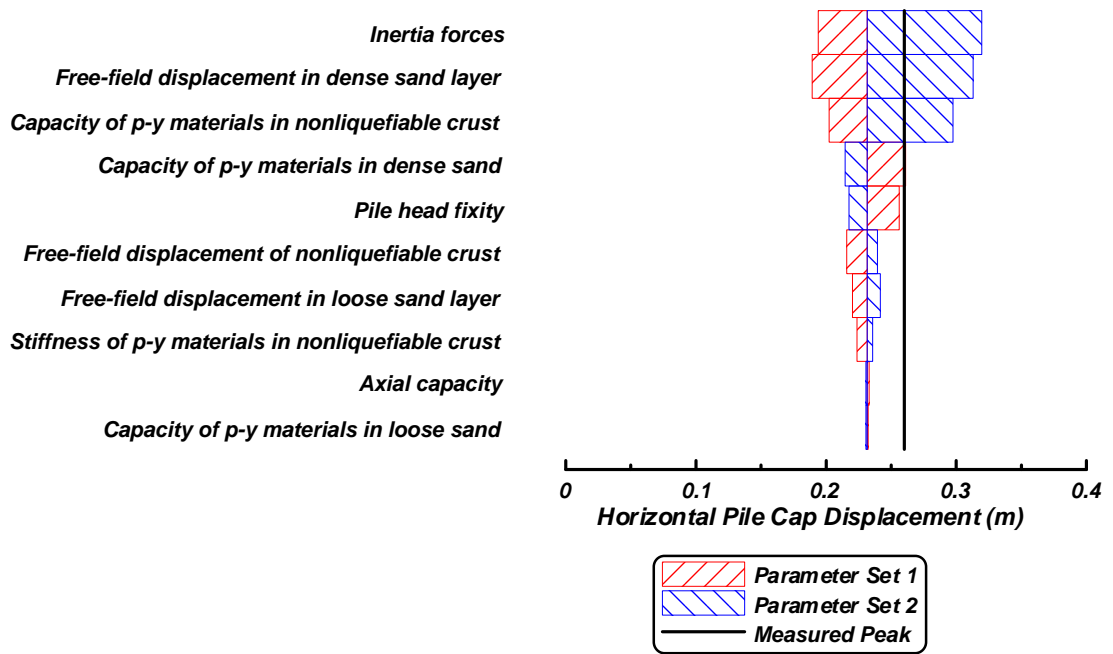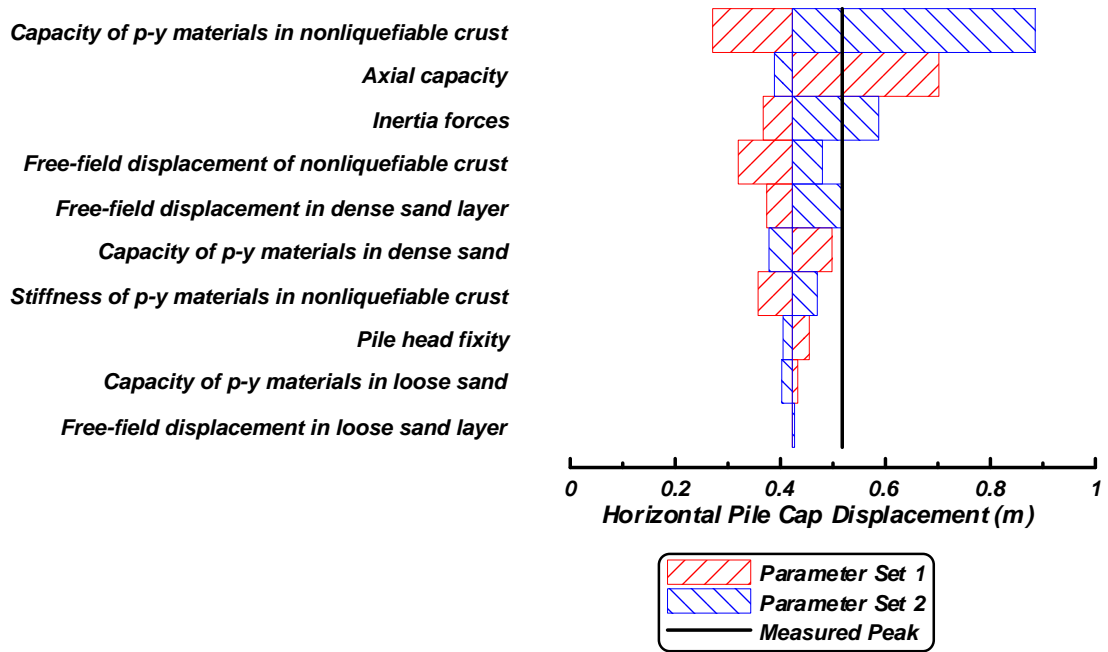
for test DDC01.

Figure C-12: Pile cap displacement tornado diagram for BNWF_SD analyses of the large Santa Cruz

motion for test DDC01.
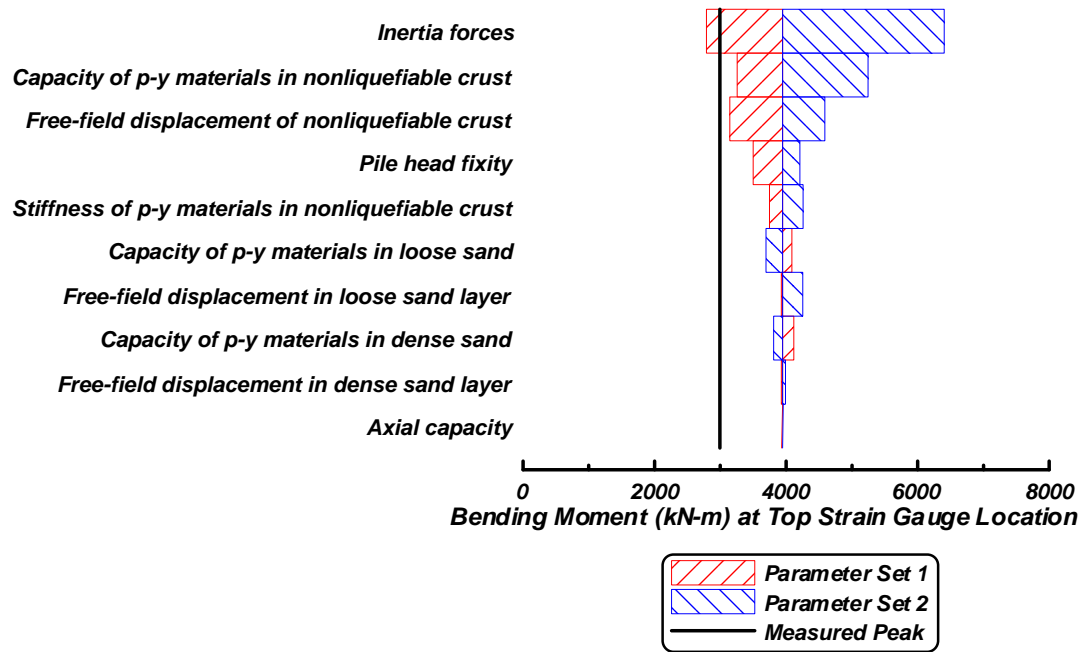
Figure C-13: Bending moment tornado diagram for BNWF_SD analyses of the medium Santa Cruz

motion for test DDC01.
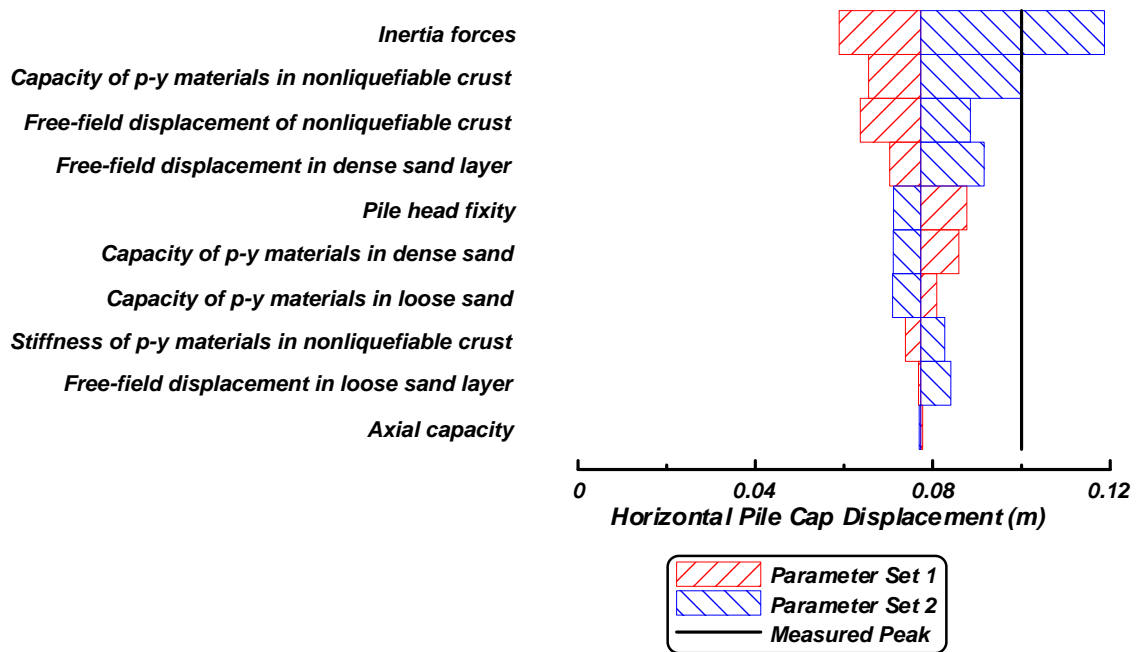
Figure C-14: Pile cap displacement tornado diagram for BNWF_SD analyses of the medium Santa Cruz

motion for test DDC01.
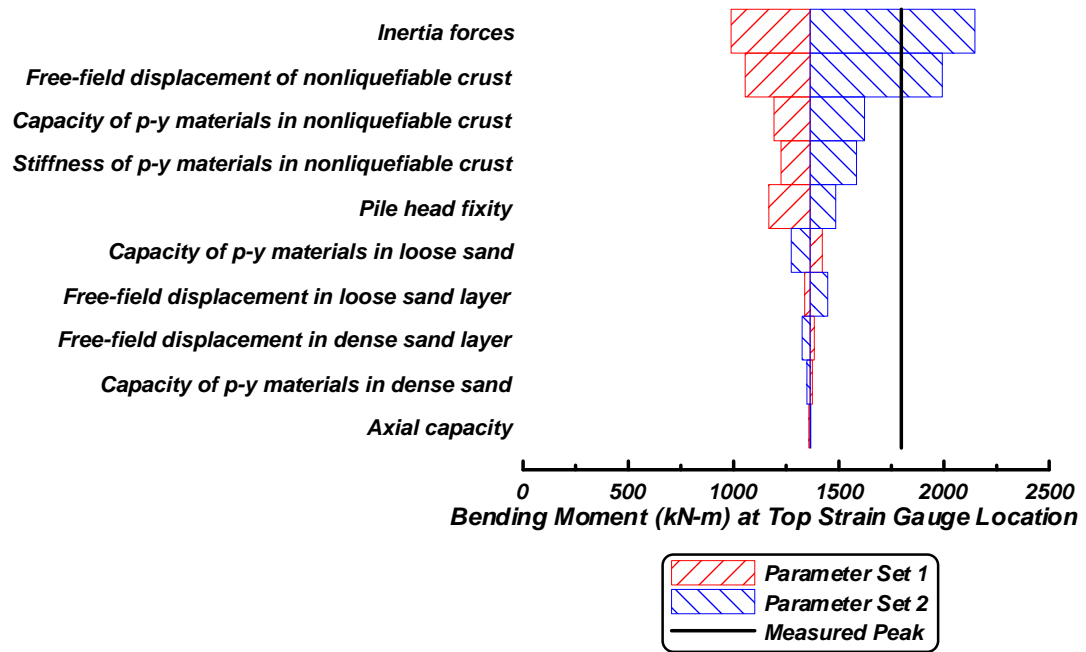
Figure C-15: Bending moment tornado diagram for BNWF_SD analyses of the small Santa Cruz

motion for test DDC01.
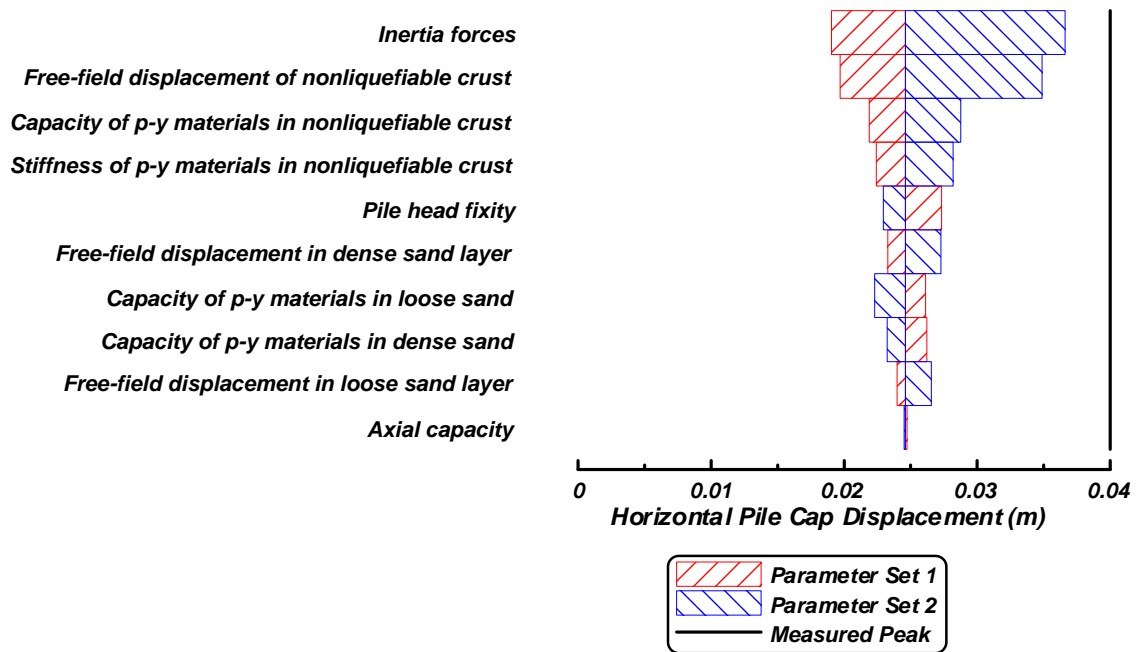
Figure C-16: Pile cap displacement tornado diagram for BNWF_SD analyses of the small Santa Cruz

motion for test DDC01.
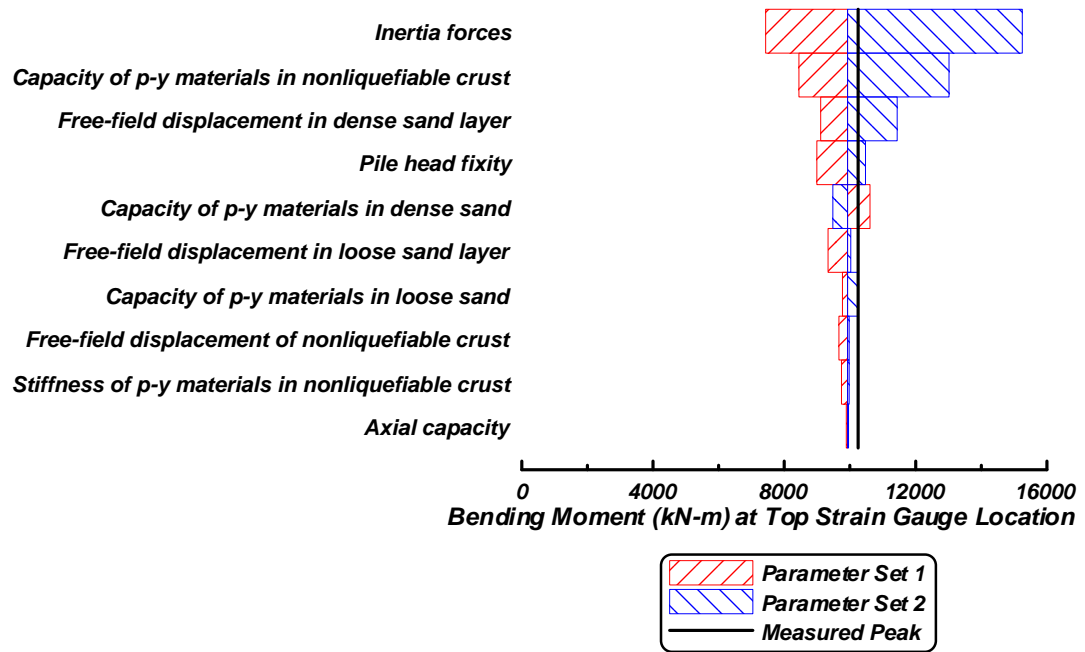
Figure C-17: Bending moment tornado diagram for BNWF_SD analyses of the large Kobe motion for
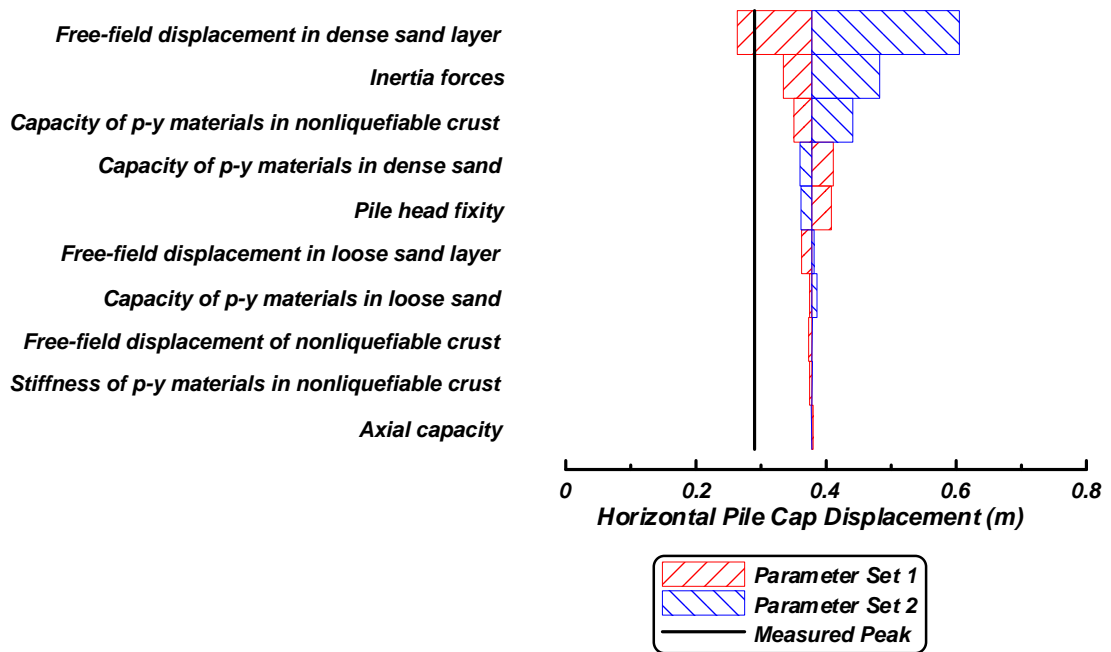
test DDC02.

Figure C-18: Pile cap displacement tornado diagram for BNWF_SD analyses of the large Kobe motion
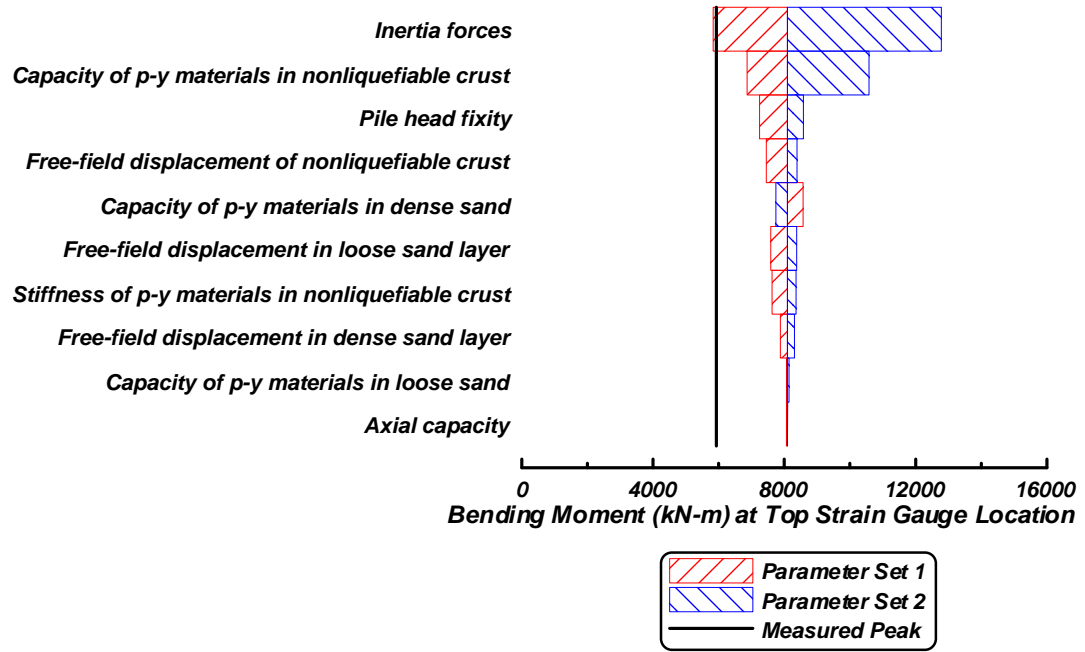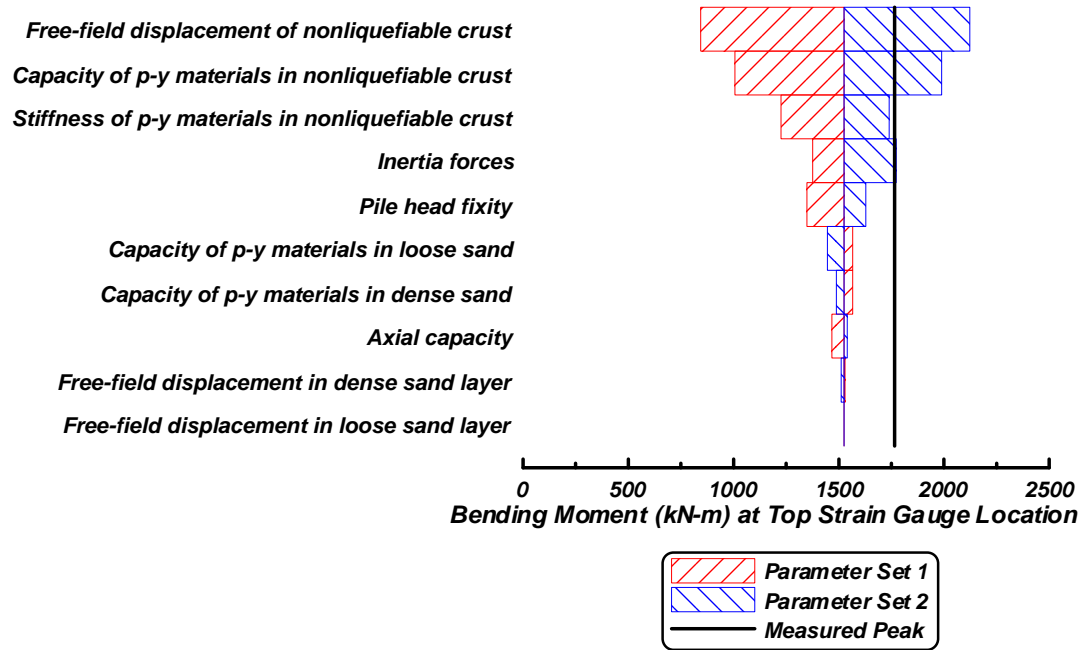
for test DDC02.

Figure C-19: Bending moment tornado diagram for BNWF_SD analyses of the large Santa Cruz motion

for test DDC02.

Figure C-20: Pile cap displacement tornado diagram for BNWF_SD analyses of the large Santa Cruz

motion for test DDC02.

Figure C-21: Bending moment tornado diagram for BNWF_SD analyses of the medium Santa Cruz
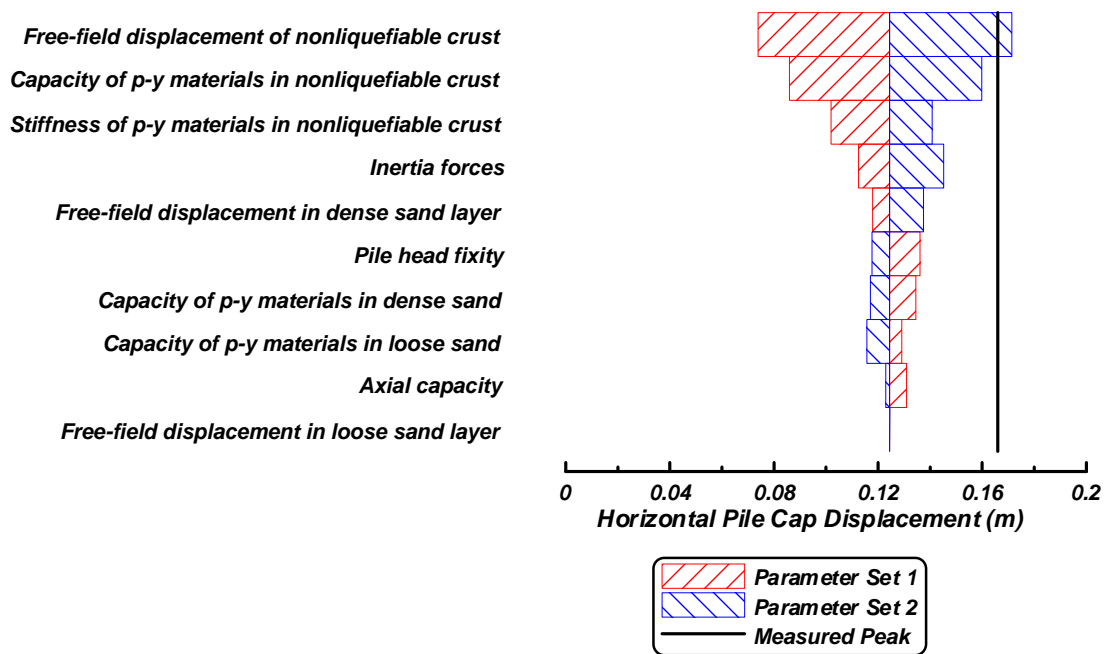
motion for test DDC02.

Figure C-22: Pile cap displacement tornado diagram for BNWF_SD analyses of the med. Santa Cruz
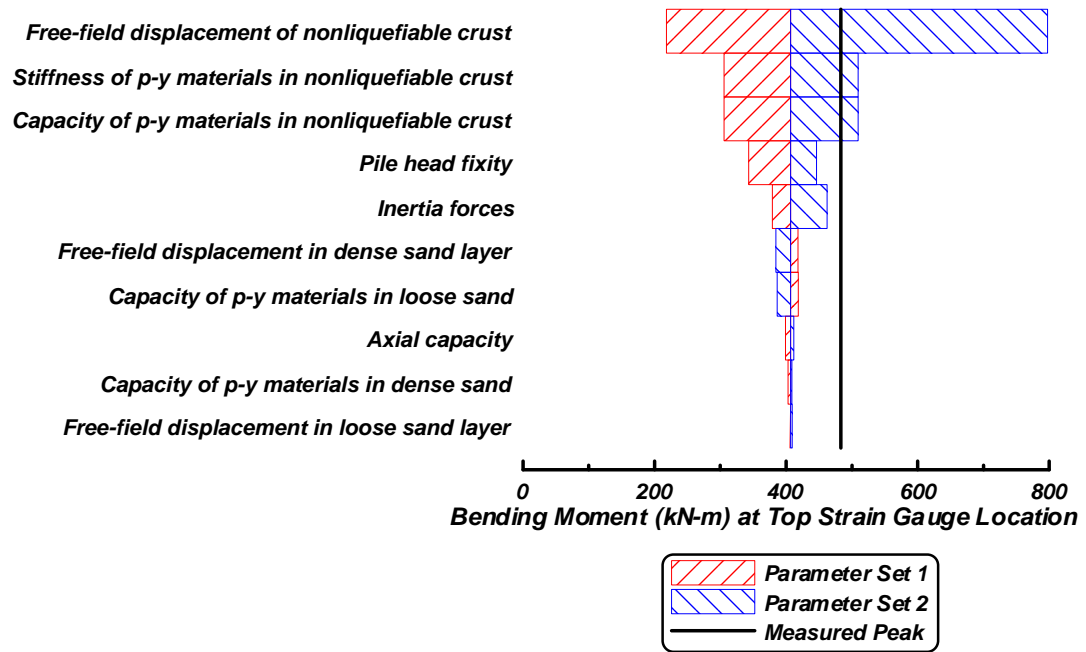
motion for test DDC02.

Figure C-23: Bending moment tornado diagram for BNWF_SD analyses of the small Santa Cruz
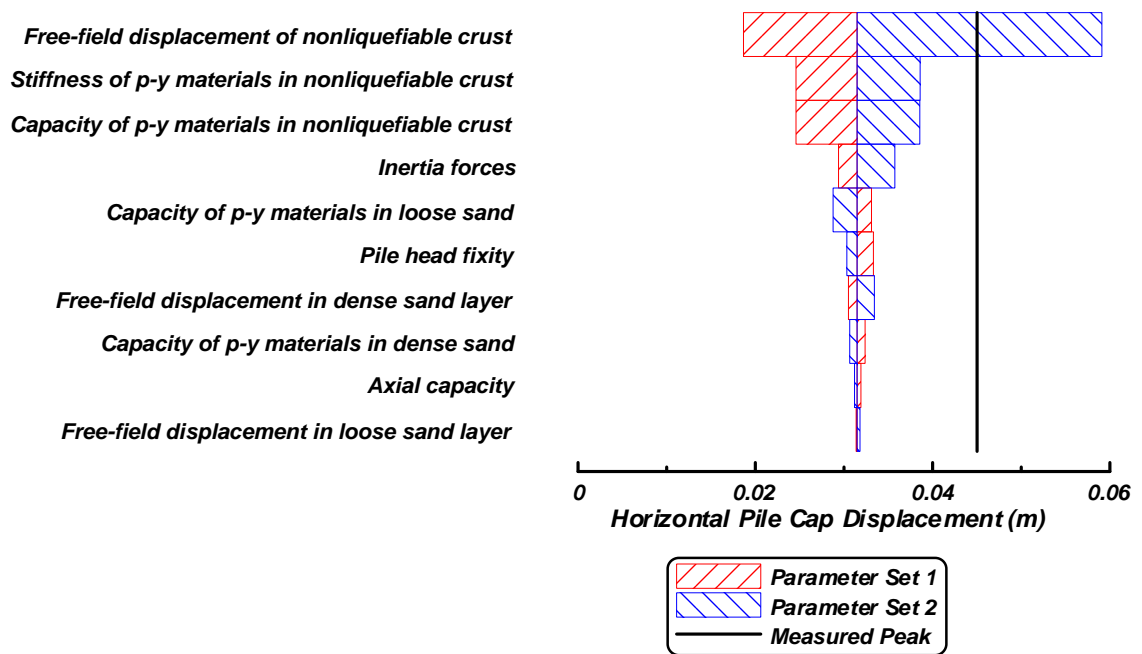
motion for test DDC02.

Figure C-24: Pile cap displacement tornado diagram for BNWF_SD analyses of the small Santa Cruz
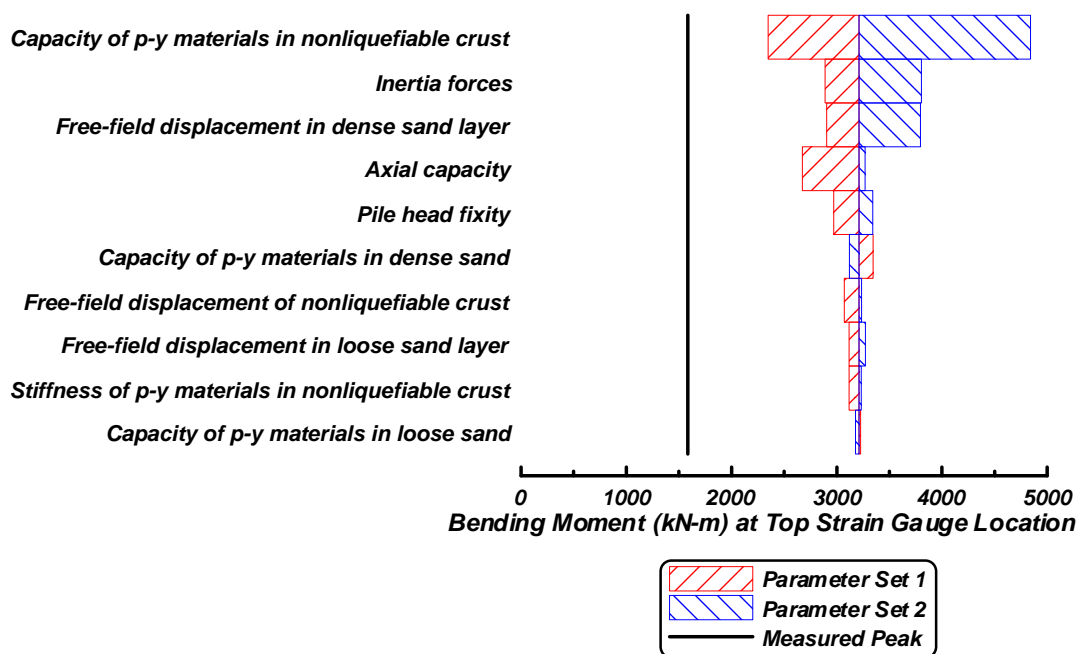
motion for test DDC02.

Figure C-25: Bending moment tornado diagram for BNWF_SD analyses of the second large Kobe
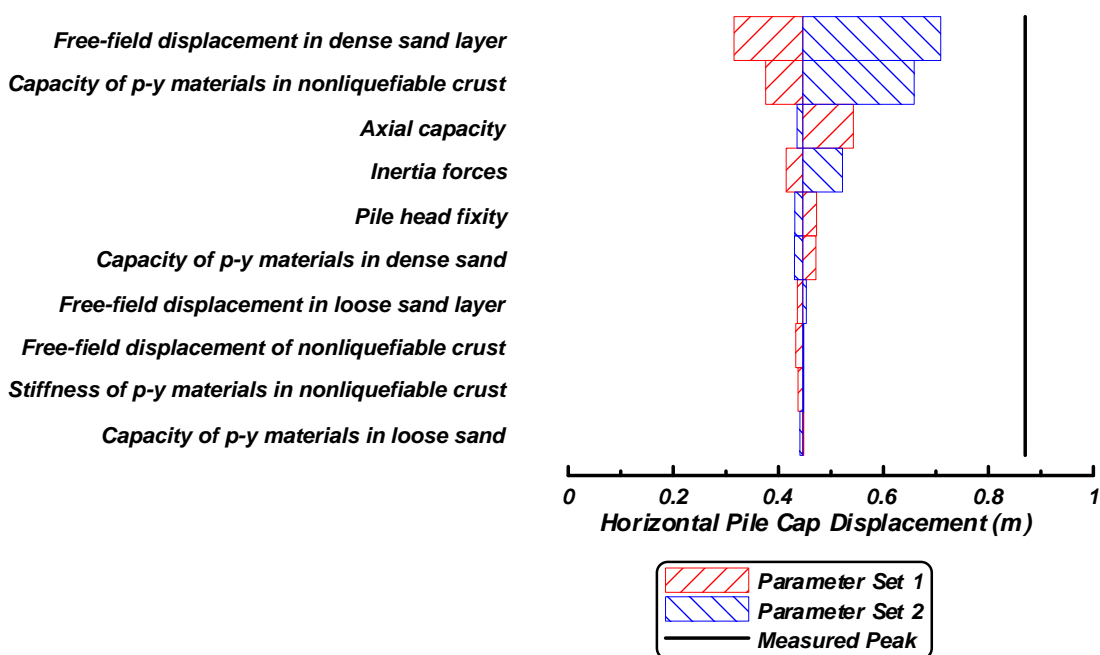
motion for test SJB01.

Figure C-26: Pile cap displacement tornado diagram for BNWF_SD analyses of the second large Kobe

motion for test SJB01.

Figure C-27: Bending moment tornado diagram for BNWF_SD analyses of the first large Kobe motion

for test SJB01.

Figure C-28: Pile cap displacement tornado diagram for BNWF_SD analyses of the first large Kobe

motion for test SJB01.

Figure C-29: Bending moment tornado diagram for BNWF_SD analyses of the large Santa Cruz motion

for test SJB01.

Figure C-30: Pile cap displacement tornado diagram for BNWF_SD analyses of the large Santa Cruz
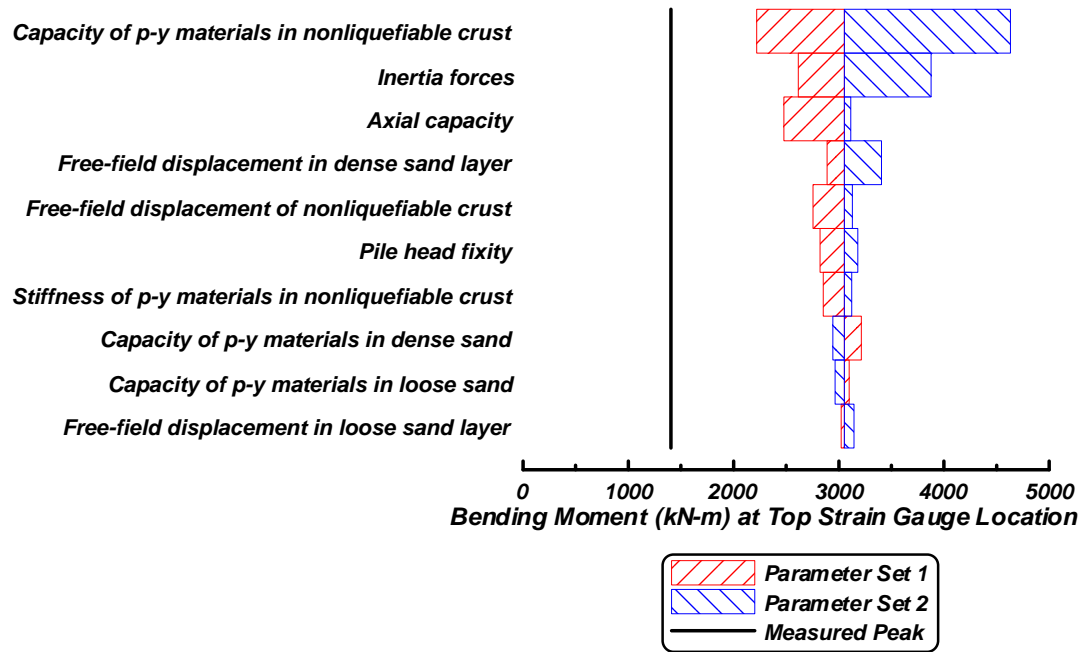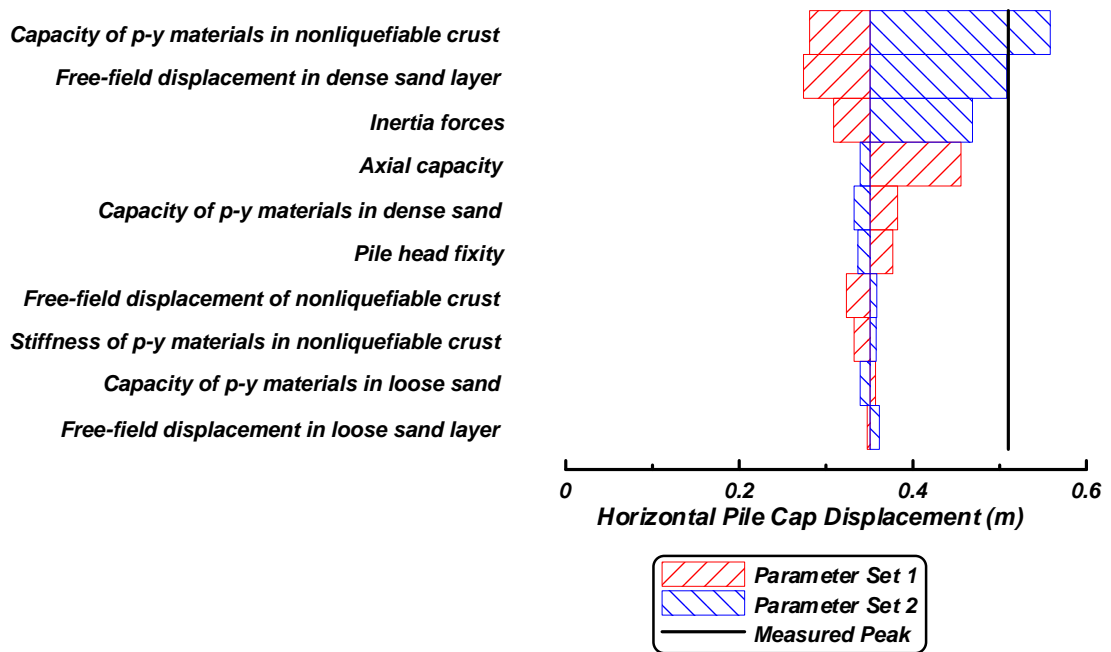
motion for test SJB01.

Figure C-31: Bending moment tornado diagram for BNWF_SD analyses of the medium Santa Cruz

motion for test SJB01.

Figure C-32: Pile cap displacement tornado diagram for BNWF_SD analyses of the medium Santa Cruz
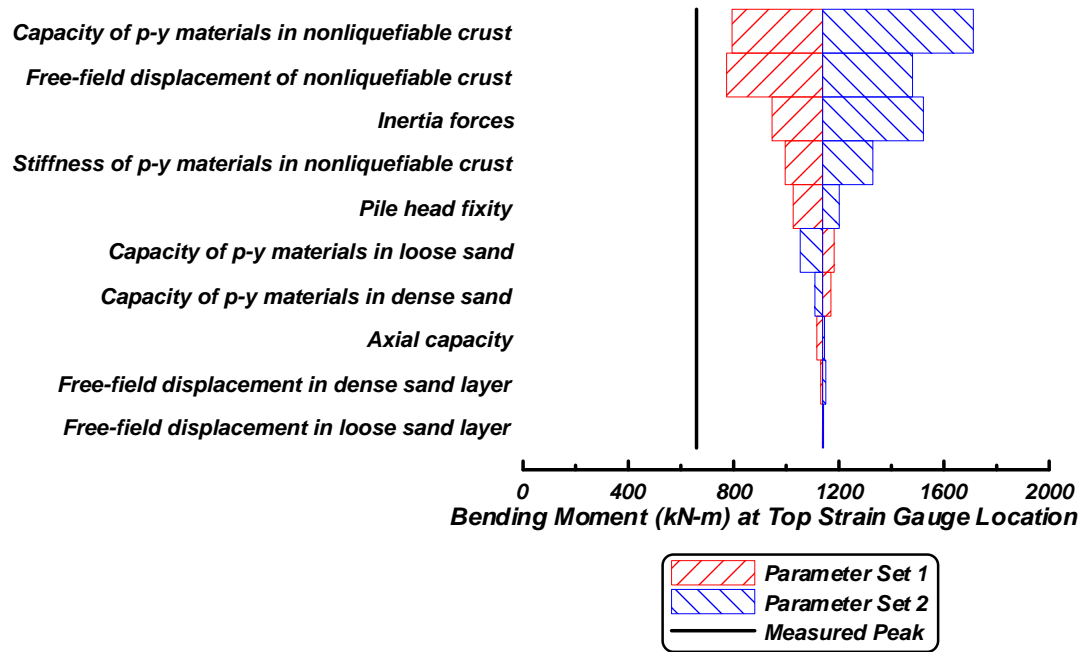
motion for test SJB01.

Figure C-33: Bending moment tornado diagram for BNWF_SD analyses of the small Santa Cruz

motion for test SJB01.

Figure C-34: Pile cap displacement tornado diagram for BNWF_SD analyses of the small Santa Cruz

motion for test SJB01.

Figure C-35: Bending moment tornado diagram for BNWF_SD analyses of the large Kobe motion for

test PDS03.

Figure C-36: Pile cap displacement tornado diagram for BNWF_SD analyses of the large Kobe motion

for test PDS03.

Figure C-37: Bending moment tornado diagram for BNWF_SD analyses of the large Santa Cruz motion

for test PDS03.

Figure C-38: Pile cap displacement tornado diagram for BNWF_SD analyses of the large Santa Cruz

motion for test PDS03.

Figure C-39: Bending moment tornado diagram for BNWF_SD analyses of the medium Santa Cruz
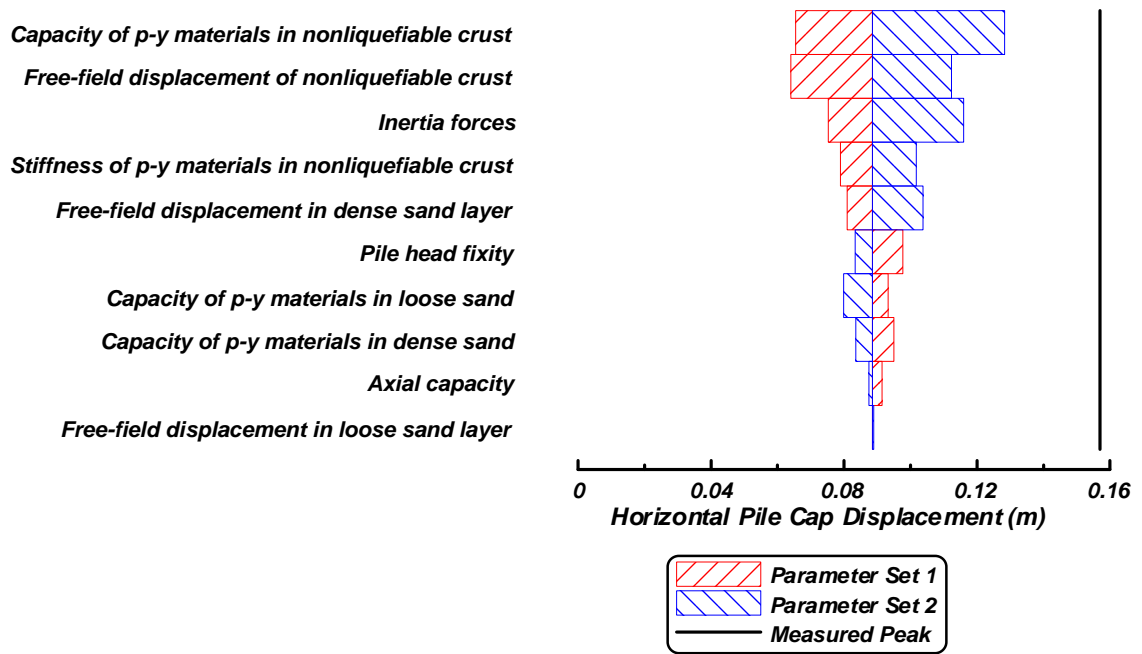
motion for test PDS03.

Figure C-40: Pile cap displacement tornado diagram for BNWF_SD analyses of the medium Santa Cruz
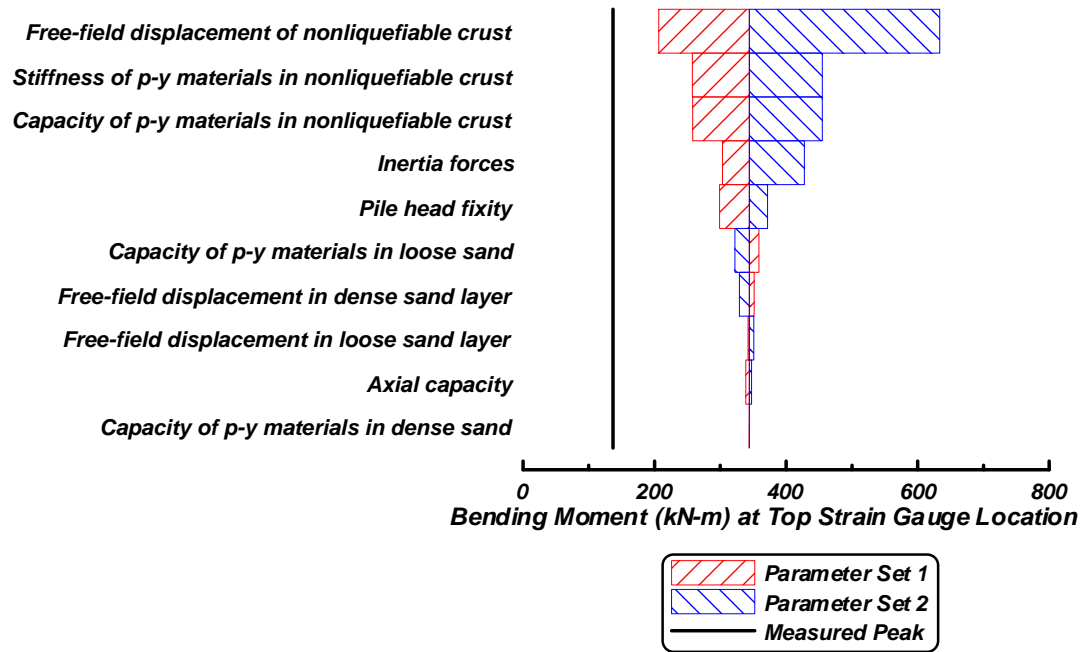
motion for test PDS03.

Figure C-41: Bending moment tornado diagram for BNWF_SD analyses of the small Santa Cruz
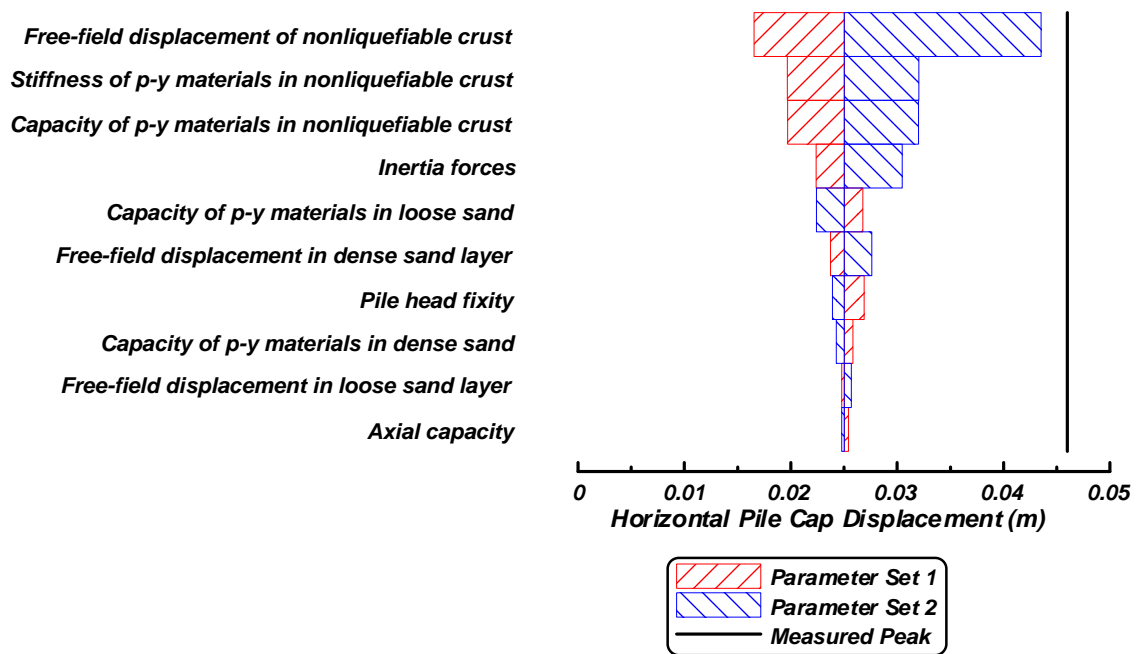
motion for test PDS03.

Figure C-42: Pile cap displacement tornado diagram for BNWF_SD analyses of the small Santa Cruz

motion for test PDS03.